HIGH SENSITIVITY ELECTROKINETIC ASSAYS BASED ON PROPAGATION AND INTERACTION OF ION CONCENTRATION SHOCK WAVES

A DISSERTATION
SUBMITTED TO THE DEPARTMENT OF MECHANICAL ENGINEERING
AND THE COMMITTEE ON GRADUATE STUDIES
OF STANFORD UNIVERSITY
IN PARTIAL FULFILLMENT OF THE REQUIREMENTS
FOR THE DEGREE OF
DOCTOR OF PHILOSOPHY

Supreet Singh Bahga

January 2013

© 2013 by Supreet Singh Bahga. All Rights Reserved.

Re-distributed by Stanford University under license with the author.

This work is licensed under a Creative Commons Attribution-Noncommercial 3.0 United States License.
http://creativecommons.org/licenses/by-nc/3.0/us/

This dissertation is online at: http://purl.stanford.edu/jf985py3082

I certify that I have read this dissertation and that, in my opinion, it is fully adequate in scope and quality as a dissertation for the degree of Doctor of Philosophy.

Juan Santiago, Primary Adviser

I certify that I have read this dissertation and that, in my opinion, it is fully adequate in scope and quality as a dissertation for the degree of Doctor of Philosophy.

Sanjiva Lele

I certify that I have read this dissertation and that, in my opinion, it is fully adequate in scope and quality as a dissertation for the degree of Doctor of Philosophy.

Ali Mani

Approved for the Stanford University Committee on Graduate Studies.

Patricia J. Gumport, Vice Provost Graduate Education

This signature page was generated electronically upon submission of this dissertation in electronic format. An original signed hard copy of the signature page is on file in University Archives.

Abstract

The advent of microfluidics has ushered a renewed interest in electrokinetic transport phenomenon for controlling, mixing, concentrating, and separating a wide variety of charged species. This dissertation focuses on two electrokinetic techniques, capillary zone electrophoresis (CZE) and isotachophoresis (ITP), each of which enables detection of charged analytes based on their differential migration velocities under applied electric fields. CZE is a linear electrokinetic technique wherein analytes separate into distinct zones under a uniform electric field and while diffusing over time. Whereas ITP leverages nonlinear electrokinetic transport to generate propagating ion-concentration shock waves which counter diffusion of analytes and enable analyte focusing and separation. This dissertation deals with theoretical and experimental studies to explore new regimes of shock wave propagation and interaction in electrokinetics which enable higher performance of microchip ITP and CZE.

We begin by presenting a quasi one-dimensional (1-D) model based on averaging of the 3-D equations along the local cross-sectional area, and an associated numerical scheme to simulate nonlinear electrokinetic processes in channels with non-uniform cross-sectional area. Our approach uses techniques of lubrication theory to approximate electrokinetic flows in channels with arbitrary variations in cross-section; and we include chemical equilibrium calculations for weak electrolytes, Taylor-Aris type dispersion due of non-uniform bulk flow, and the effects of ionic strength on species mobility and on acid-base equilibrium constants. To solve the quasi 1-D governing equations, we provide a finite volume scheme with limited numerical dissipation, coupled with an adaptive grid refinement algorithm to improve accuracy. Simulations of nonlinear electrokinetic problems, including ITP and electromigration-dispersion effects in CZE show that our approach yields fast, stable and high resolution solutions using an order of magnitude less grid points compared to the existing dissipative schemes. We have also validated our simulations with a wide range of data from ITP and CZE experiments.

We then use our model and simulations to design and optimize two methods for increasing detection sensitivity of ITP. The first method employs axial variations in channel cross-sectional area to elongate analyte zones in ITP and thereby increase

sensitivity. We show that using strongly convergent channels can result in large increase in sensitivity and simultaneous reduction in assay time, compared to uniform cross-section channels. Using our model, we develop simple analytical relations for dependence of zone length and assay time on geometric parameters of strongly convergent channels. We have validated our theoretical predictions with detailed experiments by varying channel geometry and analyte concentrations, and demonstrated indirect fluorescence detection with a sensitivity of 100 nM.

In the second method for increasing sensitivity of ITP, we use bidirectional ITP to create a concentration cascade of leading electrolyte (LE) in ITP. In bidirectional ITP, we set up simultaneous shock waves between anions and cations such that these waves approach each other and interact. This shock interaction causes a sudden decrease in the LE zone concentration in the region ahead of the focused anions and a corresponding decrease in analyte zone concentrations. This readjustment of analyte zone concentrations is accompanied by a corresponding increase in their zone lengths, in accordance to conservation laws. We have developed an analytical scaling relation for the gain in analyte zone length due to shock interaction, verified it with detailed simulations, and validated it with experimental visualizations of bidirectional ITP zones.

Lastly, we present a method to enhance resolution of detection by coupling ITP and CZE via shock interaction in bidirectional ITP. In this method, we use anionic ITP to focus anionic sample species prior to shock interaction. The interaction of the counter-propagating anionic and cationic ITP shocks then changes the local pH (and ionic strength) of the focused analyte zones and the trailing anion zone. Under this new condition, the analytes no longer focus and begin to separate electrophoretically. We illustrate the technique with numerical simulations, validate theoretical predictions with experimental visualization of bidirectional ITP zones. We then show the effectiveness of the technique by coupling ITP preconcentration and high resolution separation of a 1 kbp DNA ladder via shock interaction in bidirectional ITP. We also demonstrate applicability of this coupled ITP-CZE method for rapid, sequence-specific detection of multiple DNA fragments. For these experiments, we leverage the high preconcentration ability of ITP to accelerate slow, second-order DNA hybridization kinetics, and the high resolving power of CZE to separate and identify reaction products.

Acknowledgments

I would like to express my sincere gratitude to my adviser Prof. Juan G. Santiago for his mentorship and support. I feel fortunate to have spent time with an adviser having unmatched passion for science and exemplary dedication to students. Importantly, and to my benefit, he has been successful in programming me by a slow irreversible process to become an experimentalist, while still encouraging me to work on theory and computation. I also wish to thank my dissertation reading committee members, Prof. Sanjiva Lele and Prof. Ali Mani, and the defense committee members, Prof. Antony Jameson and Prof. Gianluca Iaccarino, for their valuable time and suggestions.

I wish to thank my colleagues at the Stanford Microfluidics Laboratory for creating a vibrant atmosphere in the laboratory. A very special thanks to my colleagues and friends, Govind Kaigala, Viktor Shkolnikov, Denitsa Milanova, and Prof. Hirofumi Shintaku, for their wonderful company. I have highly benefited by interacting with them. Also a sincere thanks to Cecilia Gichane-Bell and Linda Huber for keeping me immune from administrative issues.

I have been fortunate to receive three fellowships at Stanford, namely the Stanford School of Engineering Fellowship, the Mayfield Stanford Graduate Fellowship, and the Kodak Corporation Fellowship. I am grateful to the fellowship donors. Their financial support allowed me to solely dedicate my efforts on research.

I have been blessed with a constellation of talented friends at Stanford, including Nikhil Ghare, Krishnamurthy Iyer, Arjun Sharma, Shrey Kumar Shahi, Kuldeep Lonkar, Amrita Lonkar, Bhupesh Chandra, Manu Bansal, Uzma Hussain Barlaskar, Srilakshmi Lingamneni, Satish Talluri, Shalin Shah, Sankaran Ramakrishnan, Ramsharan Rangarajan, and Apaar Sadhwani. I thank them for their support and making my days at Stanford so memorable. I also thank many more friends outside Stanford for their continuing support during my graduate studies. A very special thanks to Praveen Agarwal for lending a patient ear since my days at IIT Bombay.

I would also like to thank my previous advisers, Prof. Jagdeep B. Doshi (IIT Bombay), Prof. Johannes Zimmer (University of Bath), and Dr. Anandaroop

Bhattacharya, without whose support, motivation, and guidance I would not have been at Stanford in the first place.

I am indebted to the Johal and the Sandhar family for their continuing hospitality during my stay in California. I am grateful to my parents, brother, sister-in-law, and the extended family for their unconditional love and unwavering support. This dissertation is a culmination of my parents' vision, efforts, and sacrifice. To them I dedicate this dissertation.

Table of Contents

Abstract v

Acknowledgments vii

Table of Contents ix

List of Tables xii

List of Figures xiii

List of Abbreviations xvii

1 Introduction 1

- 1.1 Electrokinetic transport 2
- 1.2 Capillary zone electrophoresis (CZE) 4
- 1.3 Isotachophoresis (ITP) 6
- 1.4 Scope of thesis 12

2 Modeling and simulations of electrokinetic processes in variable cross-section channels 14

- 2.1 Introduction 14
- 2.2 Mathematical Model 19
- 2.3 Numerical Method 25
- 2.4 Results and discussion 34
- 2.5 Summary 46

3 Ionic strength effects on electrophoretic focusing and separations 49

- 3.1 Introduction 49
- 3.2 Materials and methods 57
- 3.3 Results and Discussions 59
- 3.4 Summary 70

4 High-sensitivity detection using isotachophoresis with variable cross-section geometry 71

- 4.1 Introduction 71
- 4.2 Theory 74

4.3 Materials and methods 83
4.4 Experiments 85
4.5 Summary 91
5 Concentration cascade of leading electrolyte using bidirectional isotachophoresis ..93
5.1 Introduction 93
5.2 Theory 96
5.3 Materials and Methods 110
5.4 Results and discussion 113
5.5 Summary 118
6 Coupled isotachophoretic preconcentration and electrophoretic separation using bidirectional isotachophoresis 120
6.1 Introduction 120
6.2 Theory 124
6.3 Materials and Methods 136
6.4 Experiments 138
6.5 Summary 143
7 Integration of rapid DNA hybridization and capillary zone electrophoresis using bidirectional isotachophoresis 145
7.1 Introduction 145
7.2 Coupling rapid ITP based DNA hybridization and CZE 146
7.3 Materials and Methods 149
7.4 Results and discussion 152
7.5 Summary 155
8 Conclusions and recommendations 156
8.1 Major Contributions 156
8.2 Conclusions 161
8.3 Recommendations for future work 164
Bibliography 168

A. Derivation of area-averaged species transport equations in variable cross-sectional area channels.....184
B. Necessary conditions for the stability of SLIP scheme.....198
C. Guidelines for choosing parameters for adaptive grid refinement.....202
D. Derivation of regulating functions for weak univalent electrolyte systems.....206
E. Benchmark of ionic strength correction calculations with PeakMaster.....210
F. Calculation of species concentrations in ITP zones using diffusion-free model.....211
G. Dependence of sensitivity and assay time on geometry of variable cross-sectional area channels.....215
H. Calculation of species concentrations in bidirectional ITP zones using diffusion-free model.....223
I. Method for preconcentrating and separating weak acids using bidirectional ITP.....226
J. User's Manual to the Stanford Public Release Electrophoretic Separation Solver (SPRESSO).....230
K. Practically useful electrolyte buffers for anionic and cationic ITP.....247

List of Tables

Table 4.1: Geometric parameters of the five microchannel geometries used in this study……………………………………………………………………………………...84
Table 5.1: Possible cationic ITP buffer systems which are compatible with bidirectional, cascade ITP……………………………………………………………………………….105
Table 6.1: Possible cationic buffer systems for coupled preconcentration and separation of anions using bidirectional ITP…………………………………….…………………129
Table E.1: Benchmark of ionic strength correction calculation of SPRESSO with PeakMaster……………………………………………………………………………...210
Table I.1: Possible cationic buffer systems for coupled preconcentration and separation of weakly acidic anions using bidirectional ITP……………………………………......228
Table J.1: Important variables in SPRESSO data file corresponding to various physicochemical quantities……………………………………………………..……244

List of Figures

Figure 1.1: Schematics illustrating isotachophoretic focusing and separation of two analytes using finite and semi-infinite injection schemes. ……………………….………………8

Figure 2.1: Schematic summarizing various physical features of the current simulation code.………………………………………………………………………………...20

Figure 2.2: Simulations of electromigration dispersion in CZE using the upwind, sixth-order compact, and current SLIP spatial differencing schemes.…………………...37

Figure 2.3: Simulation results of focusing and separation of aniline and pyridine in plateau mode ITP……………………………………………………………….……..39

Figure 2.4: Comparison of six numerical schemes in predicting zone boundary thickness between aniline and pyridine zones in ITP.…………………………………………...41

Figure 2.5: Simulation showing focusing and separation of pyridine and aniline in plateau mode ITP as it approaches and travels through a converging channel with 5-fold cross-sectional area reduction.………………………………………………………………44

Figure 2.6: Simulation showing effect of variable channel cross-section on peak-mode ITP……………………………………………………………………………………..46

Figure 3.1: Mobility dependence of several binary electrolytes on ionic strength…………………………………………………………………………………...54

Figure 3.2: Effect of ionic strength on activity coefficient for varying ion valence……..56

Figure 3.3: Effect of ionic strength on ionic mobility of Fluorescein at two pH values……..61

Figure 3.4: Influence of ionic strength dependence on a divalent analyte focusing in peak mode isotachophoresis (with univalent TE)……………………………………………..64

Figure 3.5: Comparison of numerical and experimental results of separation and detection of sample analytes, using NFT and fluorescent mobility markers at high (a-d) and low ionic strength (e-h)…………………………………………………………………………67

Figure 3.6: Experiments from Harrold et al. and our respective simulations showing the effect of ionic strength dependence on electropherograms (from CZE) of four ions………………………………………………………………………………………69

Figure 4.1: Schematic illustrating the effect of varying channel cross-section on sensitivity of isotachophoretic separation and detection………………………………...74

Figure 4.2: Comparison of our diffusion free model (d-f) with a full numerical simulation (a-c), for the case of plateau mode ITP with semi-infinite injection of analyte (i.e., analyte mixed homogenously with TE)……………………………………………………..80

Figure 4.3: ITP injection protocol and variation of analyte zone length along the separation channel...…………………………………………………………......86

Figure 4.4: Effect of analyte concentration and channel geometry on zone length……………...88

Figure 4.5: Comparison of experimentally observed analyte zone length in ITP in variable cross-section channels with predictions using a diffusion-free model and the current quasi 1-D model……………………………………………………...……..89

Figure 4.6: Indirect fluorescence detection of 100 nM bistris using non-focusing tracer technique with variable area geometry channel……………………………………....90

Figure 5.1: Schematic illustrating increase in analyte zone length upon shock interaction in bidirectional ITP……………………………………..……………..……97

Figure 5.2: Simulation showing increase in zone length of anionic analytes using concentration cascade of LE- in bidirectional ITP……………………………………..108

Figure 5.3: Numerical simulation and experimental visualization of increase in analyte zone length due to interaction of anionic and cationic ITP shocks……………………..110

Figure 5.4: Protocol for visualizing increase in analyte zone lengths due to shock interaction in bidirectional ITP……………………………………………………112

Figure 5.5: Effect of the leading electrolyte composition on gain in analyte zone lengths due to shock interaction…………………………………………………………...115

Figure 5.6: Indirect fluorescence detection of 5 µM 2,4,6-trichlorophenol (TCP) using the NFT technique with concentration cascade of LE-……………………………………..117

Figure 6.1: Schematic illustrating focusing and separation of analytes using bidirectional ITP………………………………………………………………………………127

Figure 6.2: Simulation showing focusing and separation of species using bidirectional ITP………………………………………………………………………………131

Figure 6.3: Numerical simulation and experimental visualization of interacting anionic and cationic ITP shocks…………………………………………………………...133

Figure 6.4: Simulations comparing unidirectional transient ITP-CZE (tITP-CZE) and bidirectional ITP…………………………………………………………………..136

Figure 6.5: Protocol for DNA separations using bidirectional ITP leveraging channel cross-sectional area reduction for increased sensitivity……………………………...141

Figure 6.6: Experimental preconcentration and separation of 1 kb dsDNA ladder using bidirectional ITP………………..……………………………………………………142

Figure 7.1: Schematic of preconcentration and hybridization of nucleic acids followed by electrophoretic separation of reaction products using bidirectional ITP……………….148

Figure 7.2: Protocol for performing coupled ITP-based hybridization and CZE separation using bidirectional ITP…………………………………………………………….151

Figure 7.3: Experimental visualization of preconcentration and hybridization of nucleic acids followed by electrophoretic separation using bidirectional ITP………………….153

Figure 7.4: Multiplexed sequence-specific detection of two target oligonucleotides (39 and 90 nt) including the same 27 bases complementary to the molecular beacon probe……………………………………………………………………………………154

Figure A.1: Schematic of a variable cross-section area channel considered for the lubrication theory analysis…………………………………………………………...184

Figure B.1: Schematic showing characteristic equation for eigenvalues of an arbitrary electrokinetics system………………………………………………………………..201

Figure C.1: Comparison of the accuracy of SLIP scheme with varying degree of grid adaptation and the sixth-order compact scheme with analytical solution of a model single-interface ITP problem……………………………………………………………..205

Figure G.1: Effect of cross-sectional area ratio (A_L / A_D) and the length of loading section (L_L) on plateau zone length and interface thickness for fixed voltage operation……...219

Figure G.2: Effect of cross-sectional area ratio (A_L / A_D) and length of loading section (L_L) on signal-to-noise ratio (SNR) and assay time, for fixed voltage operation…………………………………………………………………………..220

Figure G.3: Variation of zone length, SNR and assay time with cross-sectional area ratio (A_L / A_D) and loading length (L_L), for fixed current operation……………………..222

Figure H.1: Comparison of predicted gains in zone length due shock interaction using analytical model, diffusion-free model and SPRESSO……………………………...225

Figure I.1: Simulation showing focusing and separation of two amino acids (cysteine and serine) using bidirectional ITP…………………………………………….....……..229

Figure J.1: Graphical user interface of SPRESSO code……………………………..230

Figure J.2: Screenshot of SPRESSO GUI showing typical parameters for performing fast and approximate ITP simulations……………………………………………………241

Figure J.3: Screenshot of SPRESSO GUI showing typical parameters for performing a high-fidelity simulation of ITP using compact scheme……………………………...…243

List of Abbreviations

AF	Alexa Fluor
AMR-CESE	Adaptive mesh refinement conservation element solution element
BGE	Background electrolyte
Bistris	2-[Bisamino]-2-1,3-propanediol
CCD	Charge-coupled device
CE	Capillary electrophoresis
CESE	Conservation element solution element
CI	Counter-ion
CZE	Capillary zone electrophoresis
DNA	Deoxyribonucleic acid
dsDNA	Double stranded deoxyribonucleic acid
EDL	Electric double layer
EOF	Electroosmotic flow
FASS	Field amplified sample stacking
HEPES	2-[4-(2-hydroxyethyl)piperazin-1-yl]ethanesulfonic acid
HIRAG	High resolution adaptive grid
ITP	Isotachophoresis
LE	Leading electrolyte
LE-	Anionic leading electrolyte ion
LE+	Cationic leading electrolyte ion
LED	Light emitting diode
LIF	Laser-induced fluorescence
MB	Molecular beacon
MOPS	3-morpholinopropane-1-sulfonic acid
NFT	Nonfocusing tracer
OGCA	Oregon Green carboxylic acid
PCR	Polymerase chain reaction
PLPE1	Phoenical low phase error-1

PVP	Polyvinylpyrrolidone
R6G	Rhodamine 6G
rRNA	Ribosomal ribonucleic acid
SLIP	Symmetric limited positive
SNR	Signal to noise ratio
SPRESSO	Stanford public release electrophoretic separation solver
ssDNA	Single stranded deoxyribonucleic acid
TCP	Trichlorophenol
TE	Trailing electrolyte
TE-	Anionic trailing electrolyte ion
TE+	Cationic trailing electrolyte ion
tITP	Transient Isotachophoresis
Tris	Trisaminomethane
UV	Ultra-violet

1 Introduction

Some of the contents of this chapter (Sections 1.2 and 1.3) are based on a review article by S.S. Bahga and J.G. Santiago [1] in *Analyst*, and are reproduced here with minor modifications.

Microfluidics deals with transport of fluid, mass and energy at micron scale, and has witnessed enormous growth over past fifteen years [2,3]. Microfluidic research spans across numerous disciplines and seeks to miniaturize, integrate and automate a wide range of physical, chemical and biological processes. While majority of efforts in microfluidics research have focused on developing "lab-on-a-chip" type systems for chemical and biological sensing, unique physical regimes at micron scale have also lead to advances in thermal management [4], energy generation [5], and optics [6].

The current work deals with developing lab-on-chip techniques for high-sensitivity detection of chemical species. Typical steps involved in chemical analysis may include mixing, concentrating reagents, chemical reactions, and subsequent separation and detection of reaction products. A convenient way of integrating the above processes in microfluidic devices is through electrokinetic transport, i.e., electric field driven transport of fluid and ionic species. Electrokinetic transport can exhibit complex phenomenon in form of propagating, nonlinear ion-concentration waves, including shock [7], expansion [7], and solitary waves [8]. The current work deals with ion-concentration shock waves, and leverages their propagation and interaction to dramatically enhance the performance two important electrokinetic techniques, capillary zone electrophoresis (CZE) [9] and isotachophoresis (ITP) [9].

This chapter first introduces fundamental concepts pertaining to fluid and ion-transport under applied electric field. This is followed by a brief review of CZE and ITP, focusing on their relative advantages and limitations. The scope and main contributions of the thesis are presented at the end of the chapter.

1.1 Electrokinetic transport

Electrokinetic transport deals with motion of bulk fluid and charged species under applied electric field. The principle electrokinetic phenomena that drive bulk fluid and charged species are termed electroosmosis and electrophoresis, respectively. The physics, modeling and applications of these processes are reviewed at length by several texts, including those by Hunter [10], Lyklema [11], Probstein [12], and Bruus [13]. Here we provide a brief discussion of these transport processes.

1.1.1 Electroosmotic flow

The motion of bulk fluid relative to a charged surface under an applied electric field is termed electroosmotic flow (EOF). EOF results from body force on fluid induced by externally applied electric fields on mobile counter-ions which shield a charged surface. Nearly all solid surfaces acquire a charge when brought in contact with liquids. The most common mechanism for charging of a surface is through ionization of surface chemical groups in contact with liquid. For example, glass surface acquires a spontaneous negative surface charge upon contact with water due to ionization of silanol groups. In contact with electrolyte solutions, charged surfaces attract oppositely charge ions (counter-ions) and repel like-charged ions from solution to form a thin, charged boundary layer. This boundary layer of excess charges in solution is called the electric double layer (EDL). In typical microfluidic applications, the EDL is significantly thin compared to the channel thickness (order 10-100 µm). For example, 10 mM sodium chloride solution results in 3 nm thick EDL, while the majority of solution outside the EDL remains nearly perfectly electroneutral.

Upon application of external electric field, tangential to the charged surface, the mobile ions in EDL move and simultaneously drag the fluid along. The body force on fluid, therefore, is limited to the thin EDL near the charged surface and the fluid moves with a plug-like velocity profile with an apparent velocity slip at the surface. This slip velocity, or the velocity of fluid just outside the EDL, is given by Helmholtz-Smoluchowski relation [11] as,

$$u_{EOF} = \mu_{EOF} E = -\frac{\epsilon \zeta}{\eta} E. \tag{1.1}$$

Here, μ_{EOF} is the electroomostic mobility, E, the local tangential electric field, ϵ the electric permittivity of solution, η the dynamic viscosity of solution, and ζ the potential at the shear plane near the charged wall. In general, the "zeta potential" ζ is a function of pH and conductivity of the electrolyte solution; more details can be found in Lyklema [11].

1.1.2 Electrophoresis

Electrophoresis refers to migration of charged species under the influence of applied electric field. In the creeping flow regime, a charged particle subject to an external electric field attains a steady uniform velocity, termed electrophoretic or electromigration velocity. This steady electromigration velocity results from the balance of Coulomb force and Stokes drag, and is attained by the particle in a very short time (order 1 µs or less) after application of electric field. For an isolated spherical particle of radius a with charge q, balance of these forces yields a velocity relation of,

$$u_{EP} = \mu_{EP} E = \frac{q}{6\pi\eta a} E. \tag{1.2}$$

Here μ_{EP} denotes the electrophoretic mobility of particle. Though relation in eq. (1.2) is based on a continuum model, it is even valid for small ions [13]; the factor 6π may differ depending on the shape of ions. Also, for ions, the radius a in eq. (1.2) should be interpreted as the radius of solvated ion.

Electrophoretic mobility also depends on the degree of ionization of the species. Strong electrolyte species, such as sodium and chloride ions, are invariably fully-ionized and hence their mobilities are constants. In contrast, ionization fraction and therefore mobility of weak electrolyte species, such as HEPES and Tris, depend strongly on the local pH of solution. Mobility of weak electrolyte species is termed "effective mobility", and is defined as the average of mobilities of all ionization states, weighted by their respective ionization fractions.

Besides its dependence on the local pH, electrophoretic mobility also depends on the local ionic strength of solution. Electrophoretic mobility of species in high ionic strength solution is usually lower than their corresponding mobility in dilute solutions, and the relative decrease in mobility at high ionic strengths is demonstrably more pronounced for species with higher valence [14,15]. The reduction in mobility at high ionic strengths can be attributed primarily to two factors. First, an ion in solution attracts a cloud of counter-ions (ionic atmosphere) around itself, balancing local charge. Under an applied electric field, the ion and its counter-ionic cloud move in opposite direction and this causes a polarization (new counter-ions are recruited and old ions are rejected, but overall the ion and its ionic atmosphere polarize). This polarization has a finite relaxation time scale, and retards the motion of the central ion; this phenomenon is called the "relaxation effect". The second effect, called "electrophoretic effect", is associated with the drag force exerted by the moving counter-ion cloud ionic atmosphere on the central ion. Modeling of the relaxation and electrophoretic effects on electrophoretic mobility at finite ionic strength are discussed later in Chapter 3.

1.2 Capillary zone electrophoresis (CZE)

Capillary electrophoresis (CZE) is an analytical separation technique which enables separation and detection of ionic species based on their differential migration velocities under applied electric field [9,16]. CZE is widely used in a wide variety of fields including food analysis [17], molecular biology [18], and environmental monitoring [19] for the separation and detection of ionic species ranging from small ions to macromolecules and microorganisms [20]. Typical CZE experiments involve injection of a sample mixture as a short zone in a capillary or microchannel filled with a background electrolyte (BGE) with a concentration significantly higher than those of analytes, followed by application of electric field. Thereafter, analytes zones separate based on their differential electrophoretic mobilities. As the analyte zones separate they also disperse (including by molecular diffusion). Measured CZE signals are called electropherograms which quantify the relative heights, widths, and locations of peaks corresponding to separated analytes zones.

The ability of CZE to distinguish separated analyte zones is characterized by its resolution, the separation between neighboring peaks normalized by their thickness [21,22]. Peaks are said to be well-resolved if the separation between their maxima is significantly larger than their widths. The ability to identify a well-resolved analyte peak over background noise is termed detection sensitivity, and characterized by the height of peak relative to the fluctuation magnitude of the background signal [22]. The design of CZE experiments often poses a tradeoff between resolution and sensitivity: Longer separation times increase peak separation, but at a cost of lower sensitivity due to increased dispersion [22]. In general, CZE has very high resolving power, and in many cases higher than that of chromatographic techniques [23,24]. However, low sensitivity of CZE often limits its applicability for detection of trace species, particularly when detection modes other than fluorescence, such as conductivity and ultra-violet (UV) absorbance [25,26], are employed.

Several methods have been employed to increase the sensitivity of CZE, including use of high-sensitivity detectors, and off- and on-line sample preconcentration techniques. Direct laser-induced fluorescence (LIF) is the most sensitive method for detection in CZE, and has been used for single molecule detection (order 100 aM concentration) with on-line sample preconcentration [27]. However, in practice, many analytes of interest are either non-fluorescent or lack free chemical groups that can be derivatized with fluorophores. Even if fluorescent-labeling of analytes is possible, inefficiencies involved in derivatization of trace species can result in unwanted artifacts, including modification of analyte mobilities, and background signals resulting from unbound fluorophores and their degradation products [28,29]. Detection of many analytes using CZE with local conductivity or UV absorbance detection modes is limited to analytes to order 1-100 nM or greater concentrations [25,26].

Irrespective of the method of detection, detection sensitivity of CZE can be maximized by performing sample preconcentration prior to CZE. While offline preconcentration techniques such as liquid-liquid extraction and solid-phase extraction are routinely used for sample pretreatment, these methods are often laborious, are time consuming, can require significant experimental skills, and are difficult to automate. In contrast, electrophoresis based online preconcentration techniques, such as field-amplified stacking (FASS) [30,31], dynamic pH junction [32,33], and isotachophoresis (ITP) [33,34] are well suited for increasing sensitivity of CZE as they require little or no changes to existing CZE setups, and their coupling with CZE can be mostly or completely automated. All electrophoretic sample preconcentration techniques set up specific regions with spatial gradients in electromigration velocities of analyte ions, wherein analytes undergo a net accumulation. Such spatial gradients in electromigration velocity can be generated by creating corresponding gradients in local electric field or electrophoretic mobility. ITP is perhaps the most effective and robust among all electrophoretic preconcentration techniques, and this makes ITP well-suited for online preconcentration in CZE. Below, we review the physics, advantages and limitations of ITP. We present a brief review of methodologies for coupling ITP and CZE in Chapter 6.

1.3 Isotachophoresis (ITP)

ITP is an electrophoretic preconcentration technique which leverages discontinuous electrolyte system to preconcentrate and, in some cases, separate analytes based on their electrophoretic mobility [34,35]. ITP has been used in wide range of fields, including food analysis, pharmacology, and environmental monitoring [2,36,37], for simultaneous preconcentration and separation of analytes. In addition, ITP is one of the most preferred methods for online sample preconcentration in CZE due to its high preconcentration ability (more than million-fold preconcentration [38]) and its robustness to sample impurities and non-uniform bulk flow. Figure 1.1 shows a schematic of an ITP experiment for preconcentration of two model analytes S1 and S2. A sample mixture consisting of S1 and S2 ions is initially sandwiched between zones of leading and trailing electrolytes (LE and TE, respectively). LE and TE are chosen such that their co-ions (having valence with same sign as that of analytes) have respectively higher and lower effective mobilities than those of analytes; co-ions of LE and TE are referred to as LE and TE ions, respectively. Usually, LE and TE have a common counter-ionic species. When electric field is applied, S1 and S2 migrate towards the electrode with opposite polarity and simultaneously redistribute themselves into contiguous zones, ordered by their electrophoretic mobilities (Figure 1.1b). Here we assume that mobility of S1 is everywhere greater than that of S2. Redistribution of analyte zones in ITP is accompanied by simultaneous increase in their local concentrations, and this maintains continuity of current while analyte ions displace LE ions. ITP is characterized by self-sharpening zone boundaries which result from a balance of electromigration and diffusive fluxes. These zone boundaries can be mathematically described as shock waves in ion-concentrations [7]. The self-sharpening nature of ITP zone boundaries prevent focused analyte zones from diffusing over time, and also make ITP robust to perturbations in bulk flow and turns in channel geometry. Depending on their initial amounts, analytes in ITP can focus in so called “plateau mode” or “peak mode” [39–41].

1.3.1 Plateau mode ITP

For sufficiently high initial analyte concentrations and sufficient focusing time, analytes rearrange themselves into “purified” plateau-like zones characterized by locally uniform concentrations and sharp zone boundaries. Figure 1.1b shows analyte S1 focused in plateau mode ITP. For the case of fully-ionized species, maximum plateau zone concentrations are governed by the time-invariant Kohlrausch regulating function [42] $K(x,t)$ defined as,

$$K(x,t)=\sum_i \frac{z_i c_i}{\mu_i}=K(x,0). \tag{1.3}$$

Here z_i, c_i, and μ_i respectively denote the valence, concentration and mobility (a signed quantity) of species i. Kohlrausch regulating function is a statement of conservation of charge and continuity of current, ignoring hydrodynamic flow and diffusive flux. Alternatively, Kohlrausch regulating function can be interpreted as the Riemann invariant corresponding to the zero eigenvalue of the set of hyperbolic partial differential equations governing species transport [7]. Similar regulating functions exist for weak electrolyte species, such as the Jovin and Alberty functions [43,44] for monovalent weak electrolyte species. Noting that the value of $K(x,0)$ in eq. (1.3) is set by the LE and assuming bulk electroneutrality $\left(\sum_i z_i c_i = 0\right)$ the concentration of analyte zone in plateau-mode is given by,

$$c_A = c_L \frac{z_L}{z_A} \frac{\mu_A}{\mu_L} \frac{\mu_L - \mu_C}{\mu_A - \mu_C}. \quad (1.4)$$

Here subscripts *L*, *A*, and *C* correspond to LE ion, analyte ion and background counter-ion, respectively. Note that the mobility of counter-ion (μ_C) has an opposite sign than the mobility of LE (μ_L) and analyte ions (μ_A). As suggested by eq. (1.4), analyte zone concentration in plateau-mode ITP is directly proportional to the concentration of LE ions, and the proportionally constant is typically $\mathcal{O}(1)$. Therefore, regardless of the initial analyte concentration, analyte zone concentrations in plateau-mode ITP are on order of LE ion concentration.

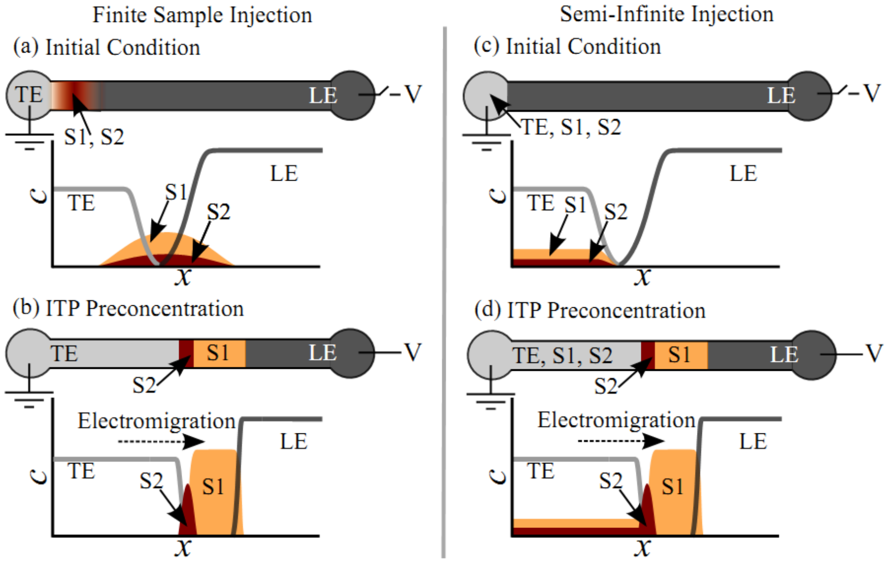
Finite Sample Injection
(a) Initial Condition
TE
LE
V
S1, S2
c
TE
S1
S2
LE
x
(b) ITP Preconcentration
TE
S1
LE
V
S2
Electromigration
LE
c
TE
S2
S1
x
Semi-Infinite Injection
(c) Initial Condition
LE
V
TE, S1, S2
LE
c
TE
S1
S2
x
(d) ITP Preconcentration
TE, S1, S2
S1
LE
V
S2
Electromigration
LE
c
TE
S2
S1
x

Figure 1.1: Schematics illustrating isotachophoretic focusing and separation of two analytes using finite and semi-infinite injection schemes. (a-b) ITP preconcentration and separation using finite sample injection. (a) Initially, a finite zone of analyte mixture consisting of S1 and S2 ions (electrophoretic mobilities, μ, such that $\mu_{S1} > \mu_{S2}$) is dispensed between LE and TE zones. Analytes are injected by filling the left reservoir with analyte mixture and then applying pressure or electric field. Following analyte injection, left well is emptied, rinsed, and filled with TE to obtain the necessary initial species distribution for ITP. (b) When electric field is applied, S1 and S2 focus between LE and TE zones, and analyte zones are ordered according to their mobilities. Here, S1 and S2 focus in "plateau mode" and "peak mode", respectively. These modes are associated with respectively high and low initial analyte concentrations. (c-d) Continuous ITP preconcentration and separation using semi-infinite injection. In the semi-infinite injection scheme, analytes are initially mixed with TE (and/or LE), and are allowed to focus continuously over time. In contrast to finite-injection, analyte zones in semi-infinite injection do not attain steady distributions; instead, the length of plateau zones and concentrations of peak-mode analytes respectively increase continuously over time.

Plateau-mode focusing allows use of ITP as an independent method for detection of analytes by simultaneously preconcentrating and separating them from complex mixtures. The plateau zones can be detected by directly measuring the local physicochemical properties of various zones, such as electrical conductivity [45], UV absorption [46], fluorescence intensity, and temperature [35]. Alternatively, plateau zones can be detected by indirect detection methods, such as the non-focusing tracer technique [47], which leverage differential migration velocities of one or more trace fluorescent species in ITP zones to yield zone specific fluorescent signal. Irrespective of the method of detection, typical isotachopherograms (signal measured in ITP) show series of distinct steps in the measured quantity. The width of these steps is proportional to the amount of focused analyte, and the difference in step heights determines the ability of plateau mode ITP to distinguish different analyte zones. Directly opposed to CZE, therefore, sensitivity in plateau mode ITP is determined by the zone thickness (*e.g.*, in time or space), and resolution by the relative signal values.

1.3.2 Peak mode ITP

In contrast to plateau mode ITP is the case of peak mode ITP where analytes are present in trace amounts. In peak mode ITP, concentration of analyte zones do not reach their corresponding plateau values, and instead analytes focus in the form of peaks within the interface (ion-concentration shock wave) of two neighboring zones. Although zone concentrations in peak mode ITP are considerably smaller than the corresponding plateau concentrations, they are typically significantly larger than initial analyte concentrations. Typically peak mode focusing is not preferred for indirect detection using ITP as focused analytes peaks are practically indistinguishable from their neighboring zones. Instead, peak mode focusing is more relevant, and often preferred over plateau mode, while coupling of ITP and CZE. The reason for this is that, disruption of plateau mode ITP while triggering CZE often results in fairly extensive dispersion of analytes during the ITP-to-CZE transition period. This severe, so-called electromigration dispersion [48] is because plateau-mode ITP analytes have concentrations comparable to those of LE and/or TE. In contrast, peak mode ITP prior to CZE separation does not lead to electromigration dispersion as analyte concentration are significantly smaller than those of LE and/or TE ions. Recently, peak mode ITP has also been demonstrated as method to accelerate a reaction between two species by simultaneously preconcentrating and mixing them into narrow overlapping zones [49].

1.3.3 Finite vs. semi-infinite injection

Sample mixtures can be injected in ITP by either finite or semi-infinite injection schemes. In the finite injection scheme, shown in Figure 1.1a and Figure 1.1b, a finite zone of sample is dispensed between the LE and TE zones, prior to application of electric field. This finite amount of analytes injected into the system results in steady spatial distributions of analytes and steady concentrations. Finite sample injection is often preferred for plateau mode ITP as it yields purified analyte zones during ITP focusing, and these zones can be detected based on specific physicochemical properties of analytes. Also, finite injection is more compatible with complex samples where total contribution of analytes and impurities to sample conductivity may be on the order of the conductivity of LE and TE zones. In this case (and unlike semi-finite injection), finite injection ensures that analytes are ultimately focused into a steady state distribution which is not a function of their initial concentrations. One drawback of finite injection is that very large injection volumes (*e.g.*, within a channel) may be required to ensure that trace analytes are detectable and/or achieve plateau mode.

One way of increasing the sensitivity of ITP is by loading the sample using semi-infinite injection of analytes, as shown schematically in Figure 1.1c and Figure 1.1d. In semi-infinite injection, sample mixture is initially mixed with TE (or LE, or both) and its constituent analytes are allowed to focus continuously over time. In the case of mixing analytes with a TE mixture at a reservoir, this injection scheme is alternatively referred to as electrokinetic injection or electrokinetic supercharging [50,51]. This injection can continue even until the point of detection to maximize sensitivity [40]. In contrast to finite-injection, analyte zones in semi-infinite injection do not attain steady distributions. Instead, the length of plateau zones and concentration of analytes focused in peak-mode increase continuously over time, enabling increase in the amount of analyte focused. Focusing rate in semi-infinite injection can be further enhanced by lowering the concentration of the TE as this increases the local electric field and electromigration speed of analytes in the TE reservoir itself [40]. Although semi-infinite injection increases sample accumulation in ITP, it is typically a good choice only when faced with relatively low conductivity samples. In such cases, TE zone properties (including conductivity, electric field, and pH) are determined only by TE (not by the sample), and this leads to predictable focusing conditions and ease of interpretation of measurements. Moreover, since focusing rate in semi-infinite injection depends on the conductivity of the mixture of TE and sample, variability in sample conductivities can affect quantification of target analytes.

1.3.4 Bidirectional ITP

Usually, ITP experiments are performed separately for focusing anions or cations in respectively anionic and cationic ITP. However, anionic and cationic ITP can also be performed simultaneously in a single channel [52,53]. The latter approach, called bidirectional ITP, is characterized by anionic and cationic ITP shock waves propagating in opposite directions. Depending on the initial conditions, shocks in bidirectional ITP can be made to propagate either towards or away from each other [53,54].

Kohlrausch [42,53] first proposed the basic idea of bidirectional ITP with diverging (i.e., moving apart) shocks, characterized by anionic and cationic ITP shocks moving apart. Since then, it has been used to simultaneously separate cationic and anionic components of samples [55,56]. Oshurkova and Ivanova [57] first demonstrated bidirectional ITP in so-called converging mode where cationic and anionic shocks approach each other. They used bidirectional ITP as a method of measuring the composition of a binary electrolyte solution. The anions and cations of this binary electrolyte solution formed the respective LE ions of the simultaneous anionic and cationic ITP processes [57]. Other than the Oshurkova and Ivanova study, we know of no further work on the study of converging ITP shocks. Prior to the current work, all of the bidirectional ITP studies with converging shocks were limited to the case where the system was analyzed prior to the interaction of anionic and cationic shock waves. For example, the Oshurkova and Ivanova quantified the concentration of the LE by analyzing the rate of convergence of the two shocks. No previous study presents or even discusses analysis of ion concentrations, shock propagation velocities, and/or pH after the interaction of cationic and anionic ITP shocks. To the best of our knowledge, our work is the first to explore the effect of shock interactions in ITP.

Later in Chapters 5-7, we show that shock interaction in bidirectional ITP can lead to fundamental modification of the electrophoretic conditions. For example, shock interaction can initiate changes in counter-ion species, concentration of co-ion species, local pH (*e.g.*, changing effective mobility), and species zone order. Such physicochemical changes associated with shock interactions in bidirectional ITP can be used to initiate either modified ITP modes or electrophoresis modes. Shock interaction can lead to two new ITP shocks (*e.g.*, in the case of fully ionized species), one shock and one rarefaction zone, or two rarefaction zones.

1.4 Scope of thesis

The objective of this dissertation is to improve the existing state of the art in modeling and simulations of nonlinear electrokinetic processes, and development of practical on-chip electrokinetic techniques for high-senstivity detection of chemical species. The dissertation makes the following major contributions:

1. Development of a generalized approach for modeling and simulations of quasi one-dimensional (1-D) nonlinear electrokinetic processes in channels with axially varying cross-sectional area, using cross-sectional area averaging of 3-D transport equations.
2. Development of two experimental methods for increasing sensitivity of ITP based detection of unlabeled analytes by: (i) leveraging variable cross-sectional area channels, and (ii) creating a gradient in concentration of leading electrolyte.
3. Development of a novel method for automated coupling of ITP and CZE in a single channel via interaction of anionic and cationic ITP shock waves in bidirectional ITP.
4. Demonstration of bidirectional ITP based coupled ITP-CZE for sequence-specific detection of multiple DNA fragments.

The dissertation is composed of six main chapters. In Chapter 2 we present development of a quasi 1-D model for multispecies electromigration-diffusion in channels with axially varying cross-sectional areas, and solve the resulting equations using a dissipative, non-oscillatory finite volume scheme. In Chapter 3 we present integration of models for ionic strength effects on electrophoretic mobility and ionic activity with numerical simulations, and present detailed validation with experiments. In Chapter 4 we present a theoretical and experimental study on increasing the sensitivity of ITP assays by varying channel cross-section. In Chapter 5 we present another method for increasing detection sensitivity of ITP, which leverages concentration cascade of leading electrolyte in bidirectional ITP. In Chapter 6 we present a technique for coupling ITP preconcentration and CZE separation using interaction of anionic and cationic ITP shock waves in bidirectional ITP. We demonstrate the application of our coupled ITP-CZE method for rapid DNA hybridization followed by separation of reaction of products in Chapter 7. We conclude by summarizing contributions of this work, and present recommendations for future research in Chapter 8.

2 Modeling and simulations of electrokinetic processes in variable cross-section channels

The contents of this chapter were previously published by S.S. Bahga, M. Bercovici and J.G. Santiago [58] in *Electrophoresis* journal and are reproduced here with minor modifications.

2.1 Introduction

Electrokinetic techniques such as capillary zone electrophoresis (CZE) and isotachophoresis (ITP) are widely used for separation and preconcentration of chemical and biological species in a variety of fields including genetics, food analysis and pharmacology [2,36]. With ever increasing demand of improving sensitivity and resolution of electrokinetic techniques, computer simulations can play a pivotal role in exploring optimal experimental parameters. While there has been significant progress in numerical simulations of electrokinetic techniques, many electrokinetic problems are still computationally challenging. These may be optimization problems which may require a large number of solutions. These also include individual solutions of nonlinear electrokinetic processes, such as ITP, electromigration dispersion in CZE, and isoelectric focusing (IEF), which can involve sharp gradients in ion-concentrations. Challenges in simulating such nonlinear processes have further increased with need of simulating electrokinetic techniques in miniaturized lab-on-a-chip systems, which can involve high electric fields, sharp concentration gradients, and complex geometries compared to those of standard benchtop systems.

As in the case of other physical phenomena, accurate simulations of electrokinetic processes require: (i) correct modeling of underlying physics including species transport and chemical reactions, and (ii) accurate numerical schemes for solving the governing equations. Over the past three decades, significant improvements have been made in modeling of electrokinetic processes, beginning with work of Bier et al. [59] and Saville and Palusinski [60]. Bier et al. provided a unified approach for simulating a variety of electrokinetic techniques by formulating generalized electromigration-diffusion equations for weak electrolyte species. Later, in a related publication, Saville and Palusinski [60] extended the model of Bier et al. to ampholytes (with univalent ionization states only). Thereafter, several improvements to models of electrokinetic flows have been proposed, such as model of protein mobility by Mosher et al. [61], and model for ionic-strength-dependent electroosmotic flow (EOF) by Thormann et al. [62]. More recently, Bercovici et al. [63] proposed a Taylor-Aris dispersion [64,65] type model to account for sample dispersion in presence of non-uniform EOF. Also, Hruska et al. [66] first proposed inclusion of ionic strength effects on species mobilities and ionic activity in electrophoresis simulations. They also added models of ionic strength effects in the SIMUL simulation tool. However, Hruska et al. did not report simulation results which accounted for ionic strength effects, and attributed this shortcoming to the high computational cost of such ionic strength corrections.

The second important issue associated with simulations of electrokinetic processes is the choice of numerical method, particularly the spatial discretization scheme. Several spatial discretization schemes have been proposed, and these can be roughly categorized as either non-dissipative or dissipative schemes. Most common of all schemes is the second-order central difference scheme implemented on a uniform grid. This is a non-dissipative approach and has been employed in well known simulation tools such as SIMUL [66] and GENTRANS [67]. However, the second-order central difference scheme which these tools implement requires grid spacing which strictly meets the requirement of a grid Peclet number, $Pe_{\Delta x} = u\Delta x / D < 2,$ to avoid unstable solutions [68]; here u denotes the electrophoretic velocity. For practical non-linear one-dimensional (1-D) electrokinetic problems this Peclet number requirement often translates to $\mathcal{O}\left(10^3\right)$ or more grid points. Simulations employing such large grids can take several hours to complete on current personal computers. To reduce the number of grid points and speed-up simulations, Bercovici et al. [69] presented a non-dissipative, sixth-order compact finite difference scheme coupled with an adaptive grid refinement algorithm. The grid adaptation scheme of Bercovici et al. automatically clusters grid points in regions with large concentration gradients, optimizing computational time for high accuracy. The numerical scheme of Bercovici et al. allows for resolution of high wave numbers with lesser number of grid points, thereby ensuring both good resolution and stability with only $\mathcal{O}\left(10^2\right)$ grid points. Similar to all non-dissipative schemes, the compact scheme (with or without adaptive grid refinement) does not guarantee monotonicity and may require judicious choice of grid size and adaptive grid parameters to ensure a non-oscillatory solution.

On the other hand, dissipative schemes result in more robust simulations by ensuring non-oscillatory solutions, but at the significant expense of higher numerical dissipation and lower accuracy (particularly in regions of high gradients). The most commonly used and easiest to implement dissipative scheme is the first-order upwind scheme [70]. Due to its lower accuracy, the upwind scheme when applied to electrokinetic problems with sharp gradients, such as ITP, results in low accuracy in the form of overly (artificially) diffused interfaces. This is true even with adaptive grid refinement [63]. Sounart and Baygents [71] improved the accuracy of dissipative schemes by using the flux corrected transport method [72], wherein numerical dissipation is added only to regions where solution needs to be stabilized. The numerical scheme of Sounart and Baygents, which they named PLPE1, results in second order accuracy in regions with smooth solution and automatically switches to first order accuracy in regions with local extrema in species concentrations, thereby insuring non-oscillatory solutions. However, the PLPE1 scheme is based on a uniform grid and the effects of numerical dissipation necessitate a number of grid points similar to that required by the second-order central scheme to obtain a converged solution. Recently Chou et al. [73] proposed a space-time conservation element solution element scheme with adaptive mesh refinement (AMR-CESE) for simulations of nonlinear electrokinetic processes at high electric fields. The AMR-CESE scheme also adds limited numerical dissipation to ensure non-oscillatory behavior and provides more accurate solutions than the upwind scheme. However, the simulations of Chou et al. showed that, even with their adaptive grid refinement, the AMR-CESE scheme was unable to capture sharp zone boundaries in ITP. Such comparisons of dissipative and non-dissipative schemes show that existing numerical schemes for electrophoresis simulations can either ensure high resolution or guaranteed stability, but not both.

We also note that the majority of simulation studies of electrokinetic techniques, including all of those mentioned above, are based on 1-D formulation of governing equations for species transport in uniform cross-section channels. Such simulations only predict streamwise variations in species concentrations and do not take into account spanwise variations in concentrations or channel cross-section. The natural way of studying multi-dimensional effects in electrokinetic processes is through two- or three-dimensional simulations. For example, Choi et al. [74] used two-dimensional simulations to demonstrate the effect of axially varying channel cross-sectional area on ITP focusing of proteins. Compared to 1-D simulations, multidimensional simulations suffer from much longer computational time due to large number of grid points required to resolve spanwise variations in species concentrations. This limits the use of multidimensional simulations to *ad hoc* studies of specific geometries, and cripples their ability to serve as rapid, routine optimization or design tools of electrokinetic assays. One approach of avoiding expensive 3-D simulations for electrokinetic processes is to solve quasi 1-D species transport equations based on area-averaging of the corresponding 3-D equations. Hruska et al. [75] employed a quasi 1-D approach in their SIMUL code and used it to simulate isoelectric trapping in compound channels made up of sections with different cross-sectional areas (each channel section having a uniform cross-sectional area). However, Hruska et al. did not provide details of their model or its numerical implementation. Later, Chou and Yang [76] presented an approximate analytical treatment describing electromigration and diffusion of species in variable cross-sectional area channels, and applied it to simulations of isoelectric focusing. However, the model of Chou and Yang incorrectly neglects diffusive current [63,77], and does not account for advection and dispersion of species due to non-uniform bulk flow.

2.1.1 Current work

In the current work, we address directly these deficiencies in state-of-the-art simulations of electrokinetic processes. Our goal is to produce simulations which are both accurate and fast; include effects of ionic strength on electrophoretic mobility and acid-base equilibria; and which apply to channels with variable cross-sectional area. The contributions of the current work are three-fold: (i) a generalized model of quasi 1-D electrokinetic processes in variable cross-sectional area channels, (ii) a high-resolution and unconditionally stable finite volume scheme for solving the quasi 1-D governing equations, and (iii) implementation and experimental validation of models for effects of ionic strength on species mobility and acid-base equilibria. In this chapter, we present a new quasi 1-D formulation of governing equations which takes into account the effect of non-uniform cross-sectional area on species concentrations. Our generalized approach includes multispecies transport, chemical equilibrium calculations (for multivalent weak electrolyte species), non-uniform electroosmotic flow, Taylor-Aris dispersion [64,65], and effects of ionic strength on mobility and acid-base equilibria. To solve the quasi 1-D governing equations we present a new approach based on a dissipative finite volume scheme which adds limited, localized numerical dissipation to guarantee non-oscillatory solutions. We also provide a novel grid refinement algorithm which improves the accuracy of our dissipative scheme by dynamically clustering grid points in regions with relatively high numerical dissipation. Coupled with adaptive grid refinement, our numerical scheme yields fast, stable and high resolution simulations using an order of magnitude less number of grid points compared to other dissipative schemes. As a demonstration, we present detailed simulations using our numerical method for various non-linear electrokinetic problems including electromigration dispersion in CZE, and ITP. For the more challenging ITP simulations, we consider both uniform and axially varying cross-section channels. For all simulations involving uniform cross-section channels we compare our results with the experimentally validated sixth-order compact scheme of Bercovici et al. [15,63,69]. We present a detailed numerical and experimental study of the effects of ionic strength of electrokinetic processes in Chapter 3. We also present detailed comparison and validation of simulations of ITP focusing in variable cross-section channels with experiments in Chapter 4. We have integrated the quasi 1-D formulation of species transport equations and the current numerical scheme in an existing electrokinetics solver SPRESSO [63,69]. The physical mechanisms addressed by the latest version of the code are summarized in Figure 2.1. The source code (and an executable version) can be downloaded for free from http://microfluidics.stanford.edu/spresso.

2.2 Mathematical Model

2.2.1 Quasi one-dimensional model for electrokinetics

Here we present a quasi one-dimensional model for electrokinetic transport of ionic species in channels with axially varying cross-sectional area. We begin with three-dimensional (3-D) advection-diffusion equations for concentration of each ionic state z within each species family i,

$$\frac{\partial c_{i,z}}{\partial t} + \nabla\cdot\left(\mathbf{u}c_{i,z} + \mu_{i,z}c_{i,z}\mathbf{E}\right) = \nabla\cdot\left(D_{i,z}\nabla c_{i,z}\right) + R_{i,z}, \quad i = 1,\ldots,N, \quad z = n_i,\ldots,p_i. \tag{2.1}$$

Here $c_{i,z}$ denotes the concentration, $\mu_{i,z}$ the electrophoretic mobility, $D_{i,z}$ the molecular diffusivity, and $R_{i,z}$ the rate of production (or consumption) of the corresponding species. The valence state, z, of species family i ranges between n_i and p_i, which are, respectively, the minimum and maximum valence states corresponding to that species family. Here “species family” refers to all ionization states of a species, so that, for example, i = arginine has four ionization states, z = -1, 0, +1, and +2 and hence $n_i = -1$ and $p_i = +2$. In eq. (2.1) vector fields $\mathbf{u} = u_x\hat{\mathbf{x}} + u_y\hat{\mathbf{y}} + u_z\hat{\mathbf{z}}$ and $\mathbf{E} = E_x\hat{\mathbf{x}} + E_y\hat{\mathbf{y}} + E_z\hat{\mathbf{z}}$ denote the velocity of bulk fluid and the electric field, respectively. Since the net production rate of species i is zero, summing eq. (2.1) over all its valence states and assuming each $D_{i,z}$ is spatially uniform (but distinct for different species and their valence states), yields a conservative set of equations in terms of the total (analytical) concentration of species, $c_i = \sum_z c_{i,z}$,

$$\frac{\partial c_i}{\partial t} + \nabla\cdot\left(\mathbf{u}c_i + \mu_i c_i\mathbf{E}\right) = \nabla^2\left(D_i c_i\right), \quad i = 1,\ldots,N. \tag{2.2}$$

Here μ_i and D_i denote the effective mobility and diffusivity of species family i, respectively, and are defined relative to its ionization states as,

$$\mu_i = \sum_{z=n_i}^{p_i} g_{i,z}\mu_{i,z}, \quad D_i = \sum_{z=n_i}^{p_i} g_{i,z}D_{i,z}, \quad g_{i,z} = \frac{c_{i,z}}{c_i}, \tag{2.3}$$

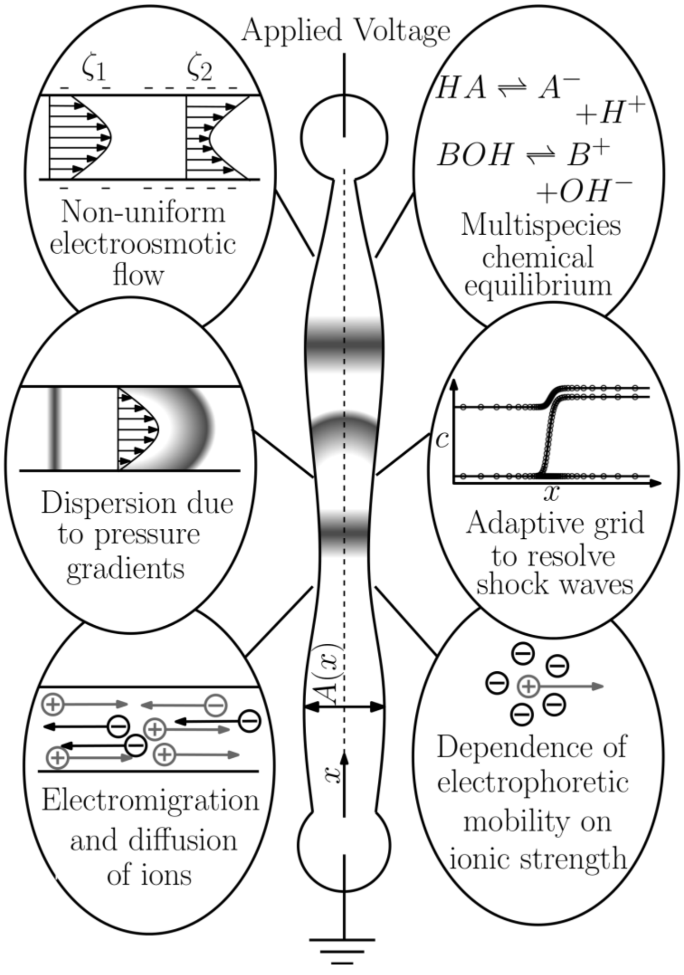
Applied Voltage
ζ_1
ζ_2
Non-uniform electroosmotic flow
$HA \rightleftharpoons A^- + H^+$
$BOH \rightleftharpoons B^+ + OH^-$
Multispecies chemical equilibrium
Dispersion due to pressure gradients
c
x
Adaptive grid to resolve shock waves
$A(x)$
x
Electromigration and diffusion of ions
Dependence of electrophoretic mobility on ionic strength

Figure 2.1: Schematic summarizing various physical features of the current simulation code. Our simulation code solves area-averaged electromigration-diffusion equations for non-linear electrophoresis problems and can handle slow axial variations in channel cross-section. The code uses a finite volume scheme with limited numerical dissipation, coupled with an adaptive grid refinement scheme to ensure accurate and non-oscillatory solutions. We have integrated the quasi 1-D formulation of species transport equations and the numerical scheme presented here into the open-source electrophoresis solver SPRESSO [63,69]. Other numerical schemes available in SPRESSO include a sixth-order compact scheme [63,69], a second-order central difference scheme, and a first-order upwind scheme. The code also includes physical modules for calculation of multispecies chemical equilibrium, correction of electrophoretic mobilities and acid-base equilibria for finite ionic strength [15], and estimation of effective dispersion coefficients using a model for Taylor-Aris type dispersion [64,65].

where $g_{i,z}$ denotes fraction of species *i*, ionized in valence state *z*. That is, the effective mobility and diffusivity of a particular species is the weighted mean of mobilities and molecular diffusivities of all its ionization states with weights $g_{i,z}$. As noted by Saville and Palusinksi [60], in typical electrophoresis experiments migration and diffusion of species occur at much longer time scales compared to the time scale of acid-base dissociation reactions. Therefore, knowing the total concentrations, c_i, the concentration of various ionization states, $c_{i,z}$, can be obtained by assuming local chemical equilibrium between different chemical species [63,69]. Later in Section 2.2.2 we discuss the chemical equilibrium calculations in more detail. We note that while deriving eq. (2.2) from eq. (2.1), we have neglected the effect of ionic strength on molecular diffusivity $(D_{i,z})$ since diffusivity is a weak function of the local ionic strength of electrolyte solution [14]. However, we do include relatively important effects of ionic strength on electrophoretic mobility, details of which are provided in Chapter 3.

To obtain quasi one-dimensional transport equations from the governing equations in three dimensions, we integrate eq. (2.2) over the channel cross-section. Noting that the flux of species into the channel walls is zero, the area-averaged equations can be represented as,

$$\frac{\partial}{\partial t}\left(A(x)\bar{c}_i\right)+\frac{\partial}{\partial x}\left(A(x)\overline{u_x c_i}+A(x)\overline{\mu_i c_i E_x}\right)=\frac{\partial}{\partial x}\left(A(x)\overline{\frac{\partial}{\partial x}(D_i c_i)}\right),\quad i=1,\ldots,N, \qquad (2.4)$$

where $A(x)$ denotes the cross-sectional area and the overbar symbol denotes area-averaged quantities. We note eq. (2.4) exactly describes the species transport in terms of the area-averaged quantities. However, to bring closure to these equations we use the following assumptions: (i) We assume that the fluid velocity and the electric field are locally axial (neglecting multidimensional effects in the slowly varying cross-section), (ii) we capture the order of magnitude of streamwise diffusive fluxes using the axial gradient of area-averaged species concentrations, $\bar{c}_i$, with diffusivity D_i. These assumptions are typical of lubrication theory [78] and hold well when the characteristic length scale in transverse direction, h, is much smaller than the characteristic length scale in streamwise direction, ℓ, i.e., $h/\ell \ll 1$. In the present case, h is the characteristic height (or diameter) of the channel and ℓ is the axial length scale over which gradient in species concentration persists. With the aforementioned assumptions, eq. (2.4) can be simplified to

$$\frac{\partial}{\partial t}\left(A(x)\bar{c}_i\right)+\frac{\partial}{\partial x}\left(A(x)\bar{u}_x\bar{c}_i+A(x)\mu_i\bar{c}_i\overline{E_x}\right)=\frac{\partial}{\partial x}\left(A(x)\frac{\partial}{\partial x}\left(D_i\bar{c}_i\right)\right),\quad i=1,\ldots,N. \qquad (2.5)$$

In Appendix A we show by rigorous asymptotic analysis that, in absence of bulk flow, for relatively narrow channel cross-sections $\left(\varepsilon=h/\ell<<1\right)$, dispersion due to non-axial electric field in axially varying cross-section is only $\mathcal{O}\left(\varepsilon^2\right)$. That is, in absence of non-uniform bulk flow, eq. (2.5) gives only $\mathcal{O}\left(\varepsilon^2\right)$ error in the description of species transport. Whereas in presence of both non-uniform bulk flow and electric field, eq. (2.5) captures only an order of magnitude approximation of diffusive fluxes. In Appendix A we also show that Taylor-Aris dispersion [64,65] due to non-uniformity in bulk flow can also be taken into account approximately by replacing D_i with a Taylor-Aris dispersion coefficient based on the local non-uniform bulk flow velocity. Besides dispersive effects of non-uniform bulk flow, the current model also accounts for dispersion due to axially non-uniform electric field in variable cross-sectional area channels. We note that our analysis and simulations do neglect secondary effects of temperature gradients and electrohydrodynamic flows which may arise and couple with electrokinetic processes associated with non-uniform cross-sectional area channels.

While the governing equations, eq. (2.5), correctly model species transport in variable cross-section channels when species concentrations vary over length scales longer than the characteristic channel thickness, they can also be used in situations where diffusion is limited to sharp concentration gradients. This situation is typical of ITP where analyte zones with locally uniform concentrations are separated by sharp zone boundaries. For such cases, eq. (2.5) can be used to accurately predict the concentrations, lengths, and migration velocities of various ITP zones, and approximately capture the features of diffusive zone boundaries in variable cross-section channels. We note that for uniform cross-section channels with no bulk flow, eq. (2.5) exactly describes the species transport, regardless of the length scales over which concentration gradients persist.

The governing equations, given by eq. (2.5), form a coupled set of N parabolic partial differential equations for total concentrations of species. The coupling between transport equations for different species comes from the local streamwise electric field, $\overline{E_x}$, which depends on the concentrations of all species via local electrical conductivity. The governing equation for electric field, $\overline{E_x}$, can be derived by invoking current conservation and assuming electroneutrality in the bulk fluid. The latter condition implies that we also neglect advection currents in current conservation. Accounting for only electromigration and diffusion currents in current conservation, the governing equation for electric field is given by

$$\frac{\partial}{\partial x}\left(A(x)\bar{\sigma}\overline{E_x}-A(x)\frac{\partial S}{\partial x}\right)=0, \tag{2.6}$$

where $\bar{\sigma}$ denotes the area-averaged conductivity and $\partial S/\partial x$ denotes the diffusive current density. Expressions of $\bar{\sigma}$ and S are given by,

$$\bar{\sigma}=\sum_{i=1}^{N}\sum_{z=n_i}^{p_i} z\bar{c}_{i,z}\mu_{i,z}F, \quad S=\sum_{i=1}^{N}\sum_{z=n_i}^{p_i} z\bar{c}_{i,z}D_{i,z}F, \tag{2.7}$$

where F is the Faraday's constant. By integrating eq. (2.6), streamwise electric field, $\overline{E_x}$, can be expressed in terms of applied current, $I(t)$, as

$$\overline{E_x}=\frac{1}{\bar{\sigma}}\left(\frac{I(t)}{A(x)}+\frac{\partial S}{\partial x}\right). \tag{2.8}$$

Note that the above relation for $\overline{E_x}$ holds irrespective of the means of applying external electric field (by current or voltage sourcing). For current sourcing, current $I(t)$ in eq. (2.8) is known *a priori*. Whereas, for problems where a known potential is applied across the channel (ΔV), $I(t)$ is obtained by simply integrating eq. (2.6) over the physical domain, x, and using the fact that $\int \overline{E_x}\mathrm{d}x=-\Delta V$. Note that, even though we assume bulk electroneutrality to derive eq. (2.6), the electric field can vary in the streamwise direction. See Hickman [79] for further discussion of the assumption of bulk electroneutrality. Briefly, electroneutrality in these systems holds in considering species conservation over regions with length scales significantly greater than the Debye screening length [11].

2.2.2 Chemical equilibrium and ionic strength effects

Analytes and background electrolytes in electrokinetic experiments are very often weak electrolytes. To model electromigration and diffusion of weak electrolyte species it is necessary to calculate the local pH of the electrolyte mixture using acid-base equilibrium theory. This is because effective mobility $\left(\mu_i\right)$ and effective diffusivity $\left(D_i\right)$ of a species family (as defined in eq. (2.3)) are strong functions of the ionization fractions, $g_{i,z}$, which themselves depend on the pH of solution. As noted by Saville and Palusinski [60], time scales at which species migrate and diffuse are much longer than the time scale at which chemical equilibrium is established. Therefore, concentrations of each of various ionic states can be obtained by solving algebraic chemical equilibrium equations, and these can be used to calculate effective mobilities and diffusivities using eq. (2.3).

Chemical equilibrium calculations for electrolyte solutions containing arbitrary number of ampholytes have been discussed in detail by Bercovici et al. [63,69]. Here we briefly outline the necessary algebraic equations for calculating the pH and the ionization fractions. Following Bercovici et al., the fraction of species i in valence state z, $g_{i,z}$, can be described in terms of hydronium ion concentration, c_H, and equilibrium constants, $K_{i,z}$ as

$$g_{i,z} = \frac{c_{i,z}}{c_i} = \frac{L_{i,z} c_H^z}{\sum_{z_i=n_i}^{p_i} L_{i,z} c_H^z}, \quad L_{i,z} = \begin{cases} \prod_{z'=z}^{-1} K_{i,z'} & z < 0, \\ 1 & z = 0, \\ \prod_{z'=0}^{z-1} K_{i,z'}^{-1} & z > 0. \end{cases} \tag{2.9}$$

The remaining equation required to obtain hydronium ion concentration, c_H, comes from the assumption of electroneutrality of the bulk solution,

$$\sum_{i=1}^{N}\sum_{z=n_i}^{p_i} z c_{i,z} + c_H - \frac{K_w}{c_H} = 0, \tag{2.10}$$

where K_w denotes the equilibrium constant for dissociation of water. Given the total concentrations of all species, $c_i, i = 1,\ldots, N,$ eqs. (2.9) and (2.10) can be solved iteratively to obtain the pH (or c_H), the ionization fractions, $g_{i,z}$. These calculations are performed at every time step of simulation to update the values of effective mobility and diffusivity of species using eq. (2.3).

In general, effective mobility also depends on the ionic strength of electrolyte solution, albeit weakly compared to its dependence on pH. Ion mobility decreases below its ideal value at infinite dilution as ionic strength increases, and this effect is more pronounced for multivalent species compared to univalent ions [15]. Variations in ionic strength can affect the relative magnitude of species mobility and cause changes of zone order in electrophoresis experiments [15]. To take into account the effect of ionic strength on effective mobility of species we correct the mobilities and the ionic activity for finite ionic strength using the extended Onsager-Fuoss model [80] and the extended Debye-Huckel theory [81], respectively. Details of numerical implementation, verification, and experimental validation of chemical equilibrium and ionic strength correction models in SPRESSO are presented in Chapter 3.

2.3 Numerical Method

We discretize the governing equations, given by eq. (2.5), using a finite volume method based on the Symmetric Limited Positive (SLIP) scheme of Jameson [82]. The SLIP scheme presented here is second order accurate in regions with smooth solution and automatically switches to first order accuracy in regions with a local extrema or oscillations. This is achieved by first constructing a stable, globally first-order scheme and then adding limited “anti-diffusion” terms in regions with smooth solution to recover second order accuracy. Thus, numerical dissipation associated with first order accuracy stabilizes the solution in the regions where it tends to become oscillatory and anti-diffusion improves the accuracy of numerical scheme to second order in regions where the solution is smooth. The spatial discretization in the SLIP scheme insures unconditional stability while maintaining relatively higher order (second order) accuracy at the majority of locations. This is in contrast to the non-dissipative schemes such as the second-order central scheme employed by Hruska [66] and the sixth-order compact scheme of Bercovici et al. [69], which do not guarantee non-oscillatory solutions on coarse grids. Another advantage of the current scheme over previous finite difference based schemes for simulations of electrokinetic processes is that, being a finite volume scheme, our approach explicitly conserves the mass of analytes irrespective of the grid density. The latter feature is especially useful in systems with varying cross-sectional area channels.

Many nonlinear electrokinetic processes such as ITP and electromigration dispersion in CZE involve sharp gradients in species concentrations. For such nonlinear electrokinetics problems, the current scheme adds numerical dissipation to regions with high gradients, resulting in artificially diffused interfaces. Therefore, to improve the accuracy of our scheme while using less grid points, we employ an adaptive grid algorithm which recruits grid points from regions with lower numerical dissipation (usually regions with smooth solution) and clusters them in regions with high numerical dissipation. Our finite volume scheme in conjunction with adaptive grid refinement yields high accuracy solutions with lower number of grid points while mathematically guaranteeing non-oscillatory solution. In Section 2.3.1 we present a conservative formulation of governing equations on a uniform computational grid using a nonlinear mapping between the physical and the computational domain. In Section 2.3.2 we present the spatial discretization scheme for the transformed governing equations in computational domain. In Section 2.3.3 we also discuss the grid adaptation procedure which determines the mapping between physical and computational space. In Section 2.3.4, we present a brief discussion of time integration scheme and the treatment of boundary conditions.

2.3.1 Governing equations in computational space

As is typical of simulations with dynamically adapting mesh, we transform the governing equations, eqs. (2.5) and (2.6), from an adapting physical grid to a uniform, stationary computational grid. After computing the solution on the computational grid we map the solution back on to the dynamically adapting physical grid. We define a smooth nonlinear mapping function, $x = H(\xi, t)$, that relates locations in physical space, x, to the corresponding locations in computational space, ξ, at any particular time, t. The Jacobian and the mesh velocity corresponding to this mapping are given by,

$$J = \frac{\partial x}{\partial \xi} = \frac{\partial H}{\partial \xi}, \quad V = \frac{\partial x}{\partial t} = \frac{\partial H}{\partial t}. \tag{2.11}$$

We then express the partial derivatives occurring in the governing equations, eqs. (2.5) and (2.6), using the chain rule. For example,

$$\begin{gathered} \left.\frac{\partial g}{\partial t}\right|_x = \left.\frac{\partial g}{\partial t}\right|_\xi - \frac{\partial g}{\partial \xi}\frac{\partial \xi}{\partial x}\frac{\partial x}{\partial t} = \left.\frac{\partial g}{\partial t}\right|_\xi - \frac{V}{J}\frac{\partial g}{\partial \xi}, \\ \frac{\partial g}{\partial x} = \frac{\partial g}{\partial \xi}\frac{\partial \xi}{\partial x} = \frac{1}{J}\frac{\partial g}{\partial \xi}, \end{gathered} \tag{2.12}$$

where g is a generic scalar field. Applying the transformations defined in eq. (2.12) to eq. (2.5) we obtain quasi 1-D advection-diffusion equations in the computational domain,

$$J\frac{\partial}{\partial t}\left(A\bar{c}_i\right) - V\frac{\partial}{\partial \xi}\left(A\bar{c}_i\right) + \frac{\partial}{\partial \xi}\left(A\bar{u}_x\bar{c}_i + A\mu_i\bar{c}_i\overline{E_x}\right) = \frac{\partial}{\partial \xi}\left(\frac{A}{J}\frac{\partial}{\partial \xi}\left(D_i\bar{c}_i\right)\right), \quad i = 1, \ldots, N. \tag{2.13}$$

In many cases the cross-sectional area, A, is not defined analytically and is known only at the grid points in physical space at the beginning of simulation. Therefore, as grid points adapt in physical space over time, it is necessary to evaluate cross-sectional area at newly adapted grid points. Noting that the channel walls are rigid and the cross-sectional area in physical domain is invariant with time, we solve

$$J\frac{\partial A}{\partial t} - V\frac{\partial A}{\partial \xi} = 0, \tag{2.14}$$

to evaluate cross-sectional area at new locations in physical space. In the physical domain, x, eq. (2.14) simply translates to $\partial A / \partial t = 0$.

In order to construct a conservative numerical scheme, we reformulate eqs (2.13) and (2.14) in a conservative form using the identity, $\partial J / \partial t = \partial V / \partial \xi \; (= \partial^2 x / \partial t \partial \xi,$

evident from eq. (2.11)). The conservative form of governing equations in computational domain is given by,

$$\frac{\partial}{\partial t}\left(JA\overline{c}_i\right)+\frac{\partial f_i}{\partial \xi}=0, \quad f_i=A\left(-V\overline{c}_i+\overline{u}_x\overline{c}_i+\mu_i\overline{c}_i\overline{E_x}-\frac{1}{J}\frac{\partial}{\partial \xi}\left(D_i\overline{c}_i\right)\right), \quad i=1,\ldots,N, \tag{2.15}$$

$$\frac{\partial}{\partial t}\left(JA\right)-\frac{\partial}{\partial \xi}\left(VA\right)=0. \tag{2.16}$$

Similarly, we transform the governing equation for electric field, eq. (2.6), from physical to computational domain to obtain,

$$\frac{\partial}{\partial \xi}\left(A\overline{\sigma}\overline{E_x}-\frac{A}{J}\frac{\partial S}{\partial \xi}\right)=0. \tag{2.17}$$

Equations (2.15)-(2.17) can now be discretized on a uniform stationary computational grid using any finite volume scheme. However, to close the system, it remains to determine the mapping between physical and computational domain, $x=H\left(\xi,t\right)$. In the current work we use an adaptive grid refinement scheme that minimizes numerical dissipation added by the spatial discretization scheme to stabilize the solution. Therefore, we first discuss the spatial discretization scheme in Section 2.3.2 and subsequently derive the necessary time evolution equation for the mapping function, $H\left(\xi,t\right)$, in Section 2.3.3.

2.3.2 Spatial discretization

We use the Symmetric Limited Positive (SLIP) scheme of Jameson [82] for spatial discretization of the transformed governing equations, eqs. (2.15)-(2.17). Construction of SLIP scheme involves addition of limited anti-diffusive terms to a low-order (first-order in the current work) scheme in a way that the anti-diffusive terms cancel out low-order numerical diffusion in regions with smooth solution. The resulting scheme yields second order accuracy in regions with smooth solution and reverts to first order accuracy in regions with local extrema or oscillations. Limited anti-diffusion is affected by a flux-limiter, which acts as a switch to turn off the anti-diffusive terms when solution shows a local extremum or spurious oscillations. As shown by Jameson [82] the

SLIP scheme mathematically guarantees monotonicity and so ensures non-oscillatory solutions. We note that, relatively lower accuracy of the current scheme at local extrema and sharp gradients in species concentrations can result in artificially diffused concentration peaks and interfaces. To circumvent this issue, in Section 2.3.3 we present an adaptive grid refinement scheme which improves the overall accuracy of our scheme by migrating grid points from regions with lower to higher numerical dissipation.

We discretize the computational domain of length L into n number of cells with thickness $\varDelta\xi = L/\left(n-1\right)$ and cell centers at $\xi_j = j\varDelta\xi,\ j = 1,\ldots,N.$ The governing equations for species concentration, eq. (2.15), spatially discretized using the SLIP scheme are given by,

$$\varDelta\xi\frac{\partial}{\partial t}\left(\left(JA\bar{c}_i\right)_j\right)+F_{i,j+1/2}-F_{i,j-1/2}=0,\quad j=2,\ldots,N-1. \tag{2.18}$$

where $F_{i,j+1/2}$ is the numerical flux of species i across the $\left(j+1/2\right)$-th cell edge, that separates cells j and $\left(j+1\right)$. The numerical flux $F_{i,j+1/2}$ is defined as,

$$F_{i,j+1/2}=\frac{1}{2}\left(f_{i,j}+f_{i,j+1}\right)-d_{i,j+1/2}, \tag{2.19}$$

where $f_{i,j}$ denotes the flux of species i (defined in eq. (2.15)) evaluated at cell center, j, and $d_{i,j+1/2}$ is the numerical dissipation flux added to stabilize the solution. The numerical dissipation flux, $d_{i,j+1/2}$, is defined as a combination of diffusive and anti-diffusive fluxes,

$$d_{i,j+1/2}=\alpha_{j+1/2}\left(\varDelta\bar{c}_{i,j+1/2}-L\left(\varDelta\bar{c}_{i,j+3/2},\varDelta\bar{c}_{i,j-1/2}\right)\right),\quad \varDelta\bar{c}_{i,j+1/2}=\bar{c}_{i,j+1}-\bar{c}_{i,j}, \tag{2.20}$$

where $L\left(\varDelta\bar{c}_{i,j+3/2},\varDelta\bar{c}_{i,j-1/2}\right)$ is the limited average of $\varDelta\bar{c}_{i,3+1/2}$ and $\varDelta\bar{c}_{i,j-1/2}$. Later, we discuss how limited average regulates the amount of anti-diffusion added to the solution based on the local smoothness of solution. In eq. (2.20) $\alpha_{j+1/2}$ is a scalar parameter that regulates the amount of numerical dissipation. Jameson [82] showed that the SLIP scheme guarantees non-oscillatory solutions when $\alpha_{j+1/2} > 0.5\max_i\left|\lambda_{i,j+1/2}\right|$, where λ denotes the characteristic waves speeds of the system of governing equations. In

Appendix B we discuss the choice of $\alpha_{j+1/2}$ in detail for electrokinetic systems. There we show that choosing $\alpha_{j+1/2} \geq 0.5 \max_i \left| A\bar{u}_x + \mu I_i \ \bar{\sigma}/ - VA \right|_{j+1/2}$ is sufficient to ensure non-oscillatory solutions for non-linear electrokinetics problems.

Similar to the spatial discretization of species transport equation, eq. (2.15), the equation for evaluating cross-sectional area at newly adapted grid points, eq. (2.16), can be discretized using the SLIP scheme as,

$$\Delta\xi \frac{\partial}{\partial t}\left((JA)_j \right) + F_{A,j+1/2} - F_{A,j-1/2} = 0. \tag{2.21}$$

Here $F_{A,j+1/2}$ is the numerical flux at $(j+1/2)$-th cell edge and is given by,

$$F_{A,j+1/2} = -\frac{1}{2}\left((VA)_{j+1} + (VA)_j \right) - \beta_{j+1/2}\left(\Delta A_{j+1/2} - L\left(\Delta A_{j+3/2}, \Delta A_{j-1/2} \right) \right). \tag{2.22}$$

In eq. (2.22) $\Delta A_{j+1/2} = A_{j+1} - A_j$, and $\beta_{j+1/2}$ is a factor analogous to $\alpha_{j+1/2}$ and chosen such that $\beta_{j+1/2} > 0.5\left| V_{j+1/2} \right|$ to avoid spurious oscillations.

It remains to define an appropriate limited average, L, in eqs. (2.20) and (2.22) which acts as a switch between first-order and second-order accurate schemes. Following Jameson [82], in the current work we use a family of limited averages (or flux limiter), defined by

$$L(v,w) = \frac{1}{2}(v+w)\left(1 - \left| \frac{v-w}{|v|+|w|} \right|^q \right), \tag{2.23}$$

where q is a positive integer. For $q = 1$ and 2, $L(v,w)$ reduces to the well-known minmod and Van Leer limiters [82], respectively. Further, as q increases the limited average defined in eq. (2.23) approaches the arithmetic mean of v and w. Note that $L(v,w) = 0$ if v and w have opposite signs; else $L(v,w) > 0$. All simulations shown here used a limited average defined by eq. (2.23) and with $q = 4$. The effect of limited anti-diffusion, $L\left(\Delta\bar{c}_{i,j+3/2}, \Delta\bar{c}_{i,j-1/2} \right)$, on the numerical dissipation flux, $d_{i,j+1/2}$, in eq. (2.20) can be interpreted as follows: In the regions where concentration profiles, $\bar{c}_i$, are smooth and have no local extrema $\Delta\bar{c}_{i,j+3/2}$ and $\Delta\bar{c}_{i,j-1/2}$ have same signs. In such a case, a limited anti-diffusion $L\left(\Delta\bar{c}_{i,j+3/2},\Delta\bar{c}_{i,j-1/2}\right)>0$ is applied and this cancels out the leading term of $\Delta\bar{c}_{i,j+1/2}$ in eq. (2.20) to provide $\mathcal{O}\left(\Delta\xi^3\right)$ numerical dissipation flux. This translates to $\mathcal{O}\left(\Delta\xi^2\right)$ discretization error in regions with smooth solution. On the contrary, if concentration, $\bar{c}_i$, attains a local extremum at *j*-th grid point, then $\Delta\bar{c}_{i,j+3/2}$ and $\Delta\bar{c}_{i,j-1/2}$ have opposite signs, which sets the anti-diffusive term $L\left(\Delta\bar{c}_{i,j+3/2},\Delta\bar{c}_{i,j-1/2}\right)=0.$ The absence of anti-diffusion in regions with local extrema results in $\mathcal{O}\left(\Delta\xi^2\right)$ numerical dissipation in eq. (2.18) and correspondingly first order accuracy of spatial discretization. Therefore, the current numerical scheme selectively adds higher numerical dissipation in regions with steep gradients and local extrema compared to regions with relatively smooth concentration profiles. This localized switching of accuracy insures stable solutions without adding excessive numerical dissipation to regions with smooth features.

2.3.3 Adaptive grid refinement

Adaptive grid refinement can be framed as a calculus of variations problem of minimizing a known cost functional. We follow the approach of Bercovici et al. [69] and define our cost functional as,

$$K(x)=\int_0^L w(\xi)J\mathrm{d}x=\int_0^L w(\xi)J^2\mathrm{d}\xi, \tag{2.24}$$

where J is the Jacobian defined in eq. (2.11) and $w(\xi)$ is a weighting function that regulates grid density at different locations in the physical domain. When the cost functional, K, is minimized, the grid density increases (and correspondingly J decreases) in regions where the weighting function acquires large values. As shown by Jameson and Vassberg [83], the cost functional in eq. (2.24) is minimized when the gradient, $G=0$, where G is defined as,

$$G \equiv 2\frac{\partial}{\partial \xi}\left(w(\xi)J\right) = 2\frac{\partial}{\partial \xi}\left(w(\xi)\frac{\partial x}{\partial \xi}\right). \tag{2.25}$$

Solving $G = 0$ requires solution of a boundary value problem for $x(\xi,t)$ at every time step, followed by interpolation of solution to the newly adapted grid points in physical space. To avoid this computationally expensive approach of computing an absolute minimum of the cost functional at every time step, we suffice with time-marching in the direction of minimum by solving,

$$\frac{\partial x}{\partial t} = -\kappa G. \tag{2.26}$$

Here κ is a positive scalar parameter that controls the migration speed of grid points in physical space. In practice the gradient, G, is smoothed before solving eq. (2.26). See Bercovici et al. [69], and Jameson and Vassberg [83] and for more details on smoothing the gradient and choosing appropriate value of κ.

Typically, the weighting function, $w(\xi)$, in eq. (2.25) is chosen as the local magnitude of concentration gradient so as to adapt the grid points in regions with large concentration gradients. For example, Bercovici et al. [69] used a weighting function based on concentration gradient to stabilize their non-dissipative compact scheme, which otherwise becomes unstable near sharp gradients for coarse grids. In contrast, the current scheme guarantees unconditional stability, but does so by adding lower-order numerical dissipation. Therefore, to improve the accuracy of our numerical scheme, we propose a new weighting function which forces the grid points to cluster in regions where the numerical scheme adds higher numerical dissipation to stabilize the solution. The current grid refinement scheme therefore not only clusters grid points at locations with steep gradients, but also does so at extrema of concentration peaks where our numerical scheme is first-order accurate. Note that adaptive grid scheme of Bercovici et al., in contrast, will not preferentially cluster grid points at peak extrema, where the gradient is zero but numerical dissipation is high. Furthermore, for problems with variable cross-sectional area, we augment the weighting function based on numerical dissipation to simultaneously aggregate grid points in regions with more rapid cross-sectional area variation. We define the weighting function at grid point j, $w_j\left(\xi\right)$, as

$$w_j\left(\xi\right)=\gamma_1\frac{\max\limits_{i}\left|\tilde{d}_{i,j+1/2}-\tilde{d}_{i,j-1/2}\right|}{\max\limits_{i,j}\left|\tilde{d}_{i,j+1/2}-\tilde{d}_{i,j-1/2}\right|}+\gamma_2\frac{\partial A/\partial\xi\big|_j}{\max\limits_{j}\partial A/\partial\xi\big|_j}+\frac{J_j}{\max\limits_{j}J_j}, \tag{2.27}$$
$$\tilde{d}_{i,j}=\Delta\bar{c}_{i,j+1/2}-L\left(\Delta\bar{c}_{i,j+3/2},\Delta\bar{c}_{i,j-1/2}\right).$$

Here $\tilde{d}_{i,j}$ is proportional to the numerical dissipation added to discretized transport equation for species *i* at grid point *j*. Here, the first two terms on the right hand side of eq. (2.27) tend to cluster grid points in regions with higher numerical dissipation and variation in cross-sectional area, respectively. Whereas, the third term in the definition of $w_j\left(\xi\right)$ in eq. (2.27) scales inversely with grid density and avoids excessive depletion of grid points from a particular region; it also prevents the weighting function from being zero in case of a constant solution in a uniform cross-section channel. The factors, γ_1 and γ_2 in eq. (2.27) are scalar constants that can be tuned to assign relative importance to the aforementioned criteria for clustering grid points. For example, when $\gamma_1 >> \gamma_2$ grid points will preferentially adapt in regions with higher numerical dissipation compared to the regions with non-uniform cross-sectional area. In Appendix C we use scaling analysis to derive simple guidelines for choosing factors γ_1 and γ_2. For general electrophoresis problems, we recommend values of order $\mathcal{O}\left(10^2-10^3\right)$ each for γ_1 and γ_2.

2.3.4 Boundary conditions and time integration

In electrokinetics simulations where species concentration profiles evolve far from the domain boundaries, it is often sufficient to use fixed concentration values (Dirichlet boundary conditions) at the boundaries. This approach has been used in the great majority of previous studies on electrophoresis simulations, including those by Palusinski et al. [84] and Dose and Guiochon [68]. However, simulations with fixed boundary conditions require a large computational domain so as to avoid interaction of propagating concentration waves with domain boundaries. Significant computational efficiency can be obtained by employing characteristic boundary conditions, which allow concentration waves to leave the domain without reflection from domain boundaries. Such boundary conditions allow use of smaller computational domain for simulating only the regions of interest. For example, in many ITP simulations it is computationally efficient to solve the governing equations in a frame of reference moving with analyte zones. In the current work we use characteristic boundary conditions for electrokinetics simulations as described by Bercovici et al. [69]. We refer interested readers to Section 3.4 of Bercovici et al. for details on formulation and implementation of these boundary conditions.

Nonlinear electrokinetic processes can exhibit complex phenomenon involving changes in characteristic speed of concentration waves over time. For simulations of such processes, it is difficult obtain *a priori* estimates of time steps to ensure stable time-integration. Furthermore, choosing a fixed conservative time step for simulating an electrokinetics problem with multiple temporal scales can lead to wastage of computational time. Therefore, we use an adaptive time stepping scheme to integrate spatially discretized governing equations, eqs. (2.18) and (2.21), along with the equation governing adaptive grid refinement, eq. (2.26). In the current work, we employ the third-order Runge-Kutta-Bogacki-Shampine (RK23) time-stepping scheme which uses an embedded second-order scheme to estimate the local truncation error and adapt the time step.

2.4 Results and discussion

We implemented the numerical algorithms discussed in Section 2.3 in Matlab and integrated them with our existing open-source electrokinetics solver, SPRESSO. We used the existing, experimentally validated modules for chemical equilibrium and ionic strength effects for calculation of pH, effective mobilities and diffusivities. The results presented here were obtained using Matlab release version 2007b running on 32 bit Windows XP operating system. An AMD 2.3 GHz Athlon 64 X2 4400+ with 2 GB RAM was used as the computing platform.

In this section, we first present simulations of CZE and ITP in uniform cross-section channels. We compare our simulation results with the upwind and sixth-order compact schemes; both previously implemented in SPRESSO. We then present simulations of ITP focusing and separation of analytes in converging cross-section channels and show the effect of non-uniform cross-sectional area on species concentration and analyte zone lengths. For all simulations presented in this chapter, we neglected the effect of ionic strength on the mobility and ionic activity of species. We present experimental validation of effects of ionic strength and variable cross-sectional area in Chapters 3 and 4, respectively.

2.4.1 Electromigration-dispersion in capillary zone electrophoresis

We first present simulations of a benchmark problem involving electromigration-dispersion in CZE using the SLIP scheme and compare the computed concentration profiles with results from the upwind and sixth-order compact schemes. This benchmark problem was originally proposed by Ermakov et al. [85] and subsequently adopted by Sounart and Baygents [71], and Bercovici et al. [63] to test the ability of their numerical schemes. This test case involves CZE separation of two high concentration analytes in a uniform cross-section channel. As high concentration analytes migrate along the channel, they perturb the local conductivity of the electrolyte solution which is otherwise governed by uniform background electrolyte in CZE. The non-uniformity in local electric field associated with variation in conductivity causes sharpening of analyte zone edge on one side and broadening on the other. Therefore, this model simulation serves as an example to demonstrate the ability of our numerical scheme to provide stable and high resolution solutions in presence of sharp gradients. For simulations using the SLIP scheme we used adaptive grid refinement based on minimizing numerical dissipation (see Section 2.3.3). On the other hand, for simulations using the upwind and compact sixth-order schemes, we used the existing implementation in SPRESSO with grid refinement procedure based on clustering grid points in regions with large concentration gradients.

We performed simulations using the SLIP, upwind and sixth-order compact schemes in a 200 mm long channel discretized with 400 grid points. The background electrolyte was 12 mM Tris (pK_a = 8.076 and $\mu = 29.5\times10^{-9}$ m^{2}V^{-1}s^{-1}) and 20 mM acetic acid (pK_a = 4.75 and $\mu = -42.4\times10^{-9}$ m^{2}V^{-1}s^{-1}). The weak base analytes aniline (pK_a = 4.8 and $\mu = 32.5\times10^{-9}$ m^{2}V^{-1}s^{-1}) and pyridine (pK_a = 5.16 and $\mu = 30\times10^{-9}$ m^{2}V^{-1}s^{-1}) were initially introduced in the channel at a distance of 30 mm from the left boundary, in form of Gaussian-shaped zones with 1 mM peak concentration. For each numerical scheme, we performed two sets of simulations corresponding to current densities of 2547 and 10190 A/m^2. We chose mesh adaptation parameters so as to ensure similar grid density for the SLIP and compact schemes. Minimum grid spacing used for simulations with current density of 2547 and 10190 A/m^2 was $\Delta x \approx 30\ \mu\text{m}$ and $\Delta x \approx 15\ \mu\text{m}$, respectively.

Figure 2.2a and Figure 2.2b show concentration profiles of fully separated analyte peaks at current density of 2547 and 10190 A/m^2, respectively, computed using the upwind, the SLIP (with parameter $q = 4$) and the sixth-order compact scheme. At lower current density, all three schemes yield non-oscillatory solution. Figure 2.2a shows that both SLIP and compact schemes accurately resolve the analyte peaks, including the sharp leading interfaces of analyte zones. In contrast, the upwind scheme yields overly diffused analyte peaks because of its lower (first order) accuracy throughout the domain. Figure 2.2b shows that at higher current density of 10190 A/m^2, the upwind and the SLIP scheme still produce non-oscillatory solution as they both ensure monotonicity. Again, the upwind scheme results in artificially diffused peaks due to high numerical dissipation associated with its first order accuracy. On other hand, for the simulation conditions used here, the sixth-order compact scheme of Bercovici et al. [69] yields spurious oscillations due to unresolved wave numbers. Unlike the compact scheme, the SLIP scheme yields stable solution at current density of 10190 A/m^2 with similar grid density. The SLIP scheme dampens unresolved wave numbers to ensure non-oscillatory solution. This dampening of unresolved wave numbers indeed affects the solution accuracy, but the resulting solution is still a better representation of the exact solution (with small error) compared to the non-physical oscillatory solution obtained from the higher-order compact scheme.

Figure 2.2 also shows preferential distribution of grid points at sharp interfaces due to adaptive grid refinement. We note that dynamically adapting grid employed here has significant advantages over fixed uniform grid as the former helps reduce the number of grid points to obtain a converged solution. As an illustration, for the case shown in

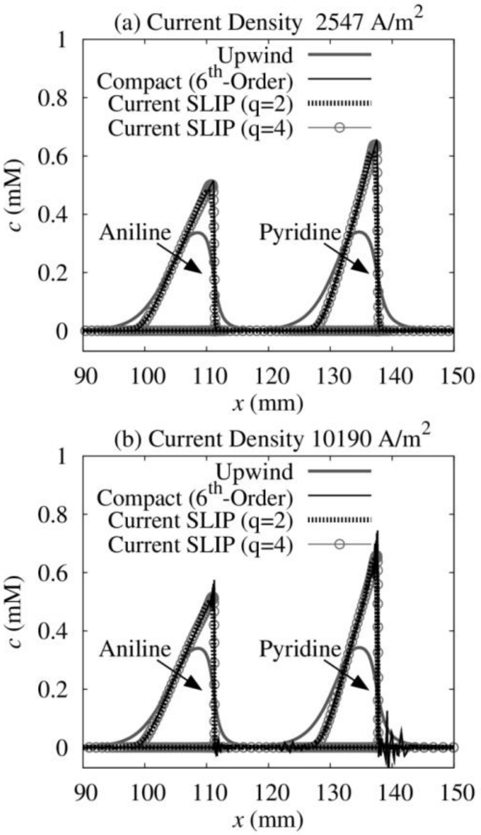

Figure 2.2: Simulations of electromigration dispersion in CZE using the upwind, sixth-order compact, and current SLIP spatial differencing schemes. Plots (a) and (b) show simulations of CZE separation of aniline and pyridine at current densities of 2547 and 10190 A/m^2, respectively. For both cases, the upwind and the current SLIP scheme yield non-oscillatory solutions as they both ensure monotonicity. (a) At relatively lower current density of 2547 A/m^2 the sixth-order compact scheme of Bercovici et al. [63] is stable and accurately resolves the sharp leading interfaces of analyte peaks. On the other hand, the upwind scheme is overly diffusive due to its first order accuracy throughout the domain. Concentration profiles computed using the SLIP scheme (for $q = 4$) compare well with the results using the more accurate sixth-order compact scheme. (b) At higher current density of 10190 A/m^2, the SLIP scheme still yields non-oscillatory and physically consistent solution. In comparison, for similar grid density, the compact scheme yields non-physical oscillations. For these simulations we used 200 mm long computational domain with 400 grid points. We chose mesh adaptation parameters so as to ensure similar grid density for the SLIP and compact schemes. The minimum grid spacing used for simulations shown in (a) and (b) are $\Delta x \approx 30\,\mu\text{m}$ and $\Delta x \approx 15\,\mu\text{m}$, respectively.

Figure 2.2a simulation using the PLPE1 scheme of Sounart and Baygents [71] required a uniform grid with 2000 grid points (Δx = 100 μm) for convergence. In comparison, for the same case we used only 400 grid points and yet obtained 3 times higher resolution

($\Delta x = 30$ μm). In other words, simulations using a numerical scheme with uniform grid would require 16 times more grid points in order to equal the spatial resolution of our current simulations.

2.4.2 Resolving sharp gradients in ITP

Next, we demonstrate the ability of our numerical scheme to accurately resolve sharp zone boundaries in ITP. In ITP, analytes focus and can separate between zones of high effective mobility leading electrolyte (LE) ions and low effective mobility trailing electrolyte (TE) ions. When present in sufficient amount, analytes in ITP focus into distinct, purified zones with locally uniform zone concentrations. This mode is termed as "plateau mode ITP" [40,41] and is characterized by sharp zone boundaries separating adjacent analyte zones with locally uniform concentrations. However, when analytes are present in small amounts, their zone concentrations do not reach the plateau values. Instead, the analytes focus into peaks with widths determined by the boundary thickness of neighboring zones. The latter mode is termed "peak mode ITP" [40,41].

To test our numerical scheme for simulating ITP problems, we consider the benchmark case of plateau mode ITP, originally proposed by Ermakov [85]. This test case involves cationic ITP focusing of two weak base analytes (aniline and pyridine). This test case is particularly interesting as it has been used previously to compare the performance of several numerical schemes, including those by Martens et al. [70], Sounart and Baygents [71], Yu et al. [86], Bercovici et al. [63], and Chou et al. [73].

We performed two sets of simulations, each using the SLIP, the upwind and the compact scheme, at current densities of 509 and 2260 A/m^2. For these simulations the LE was 18 mM sodium hydroxide (pK_a = 13.7, $\mu = 51.9 \times 10^{-9}$ m^{2}V^{-1}s^{-1}) and 20 mM acetic acid, and the TE was 40 mM β-alanine (pK_a = 3.3, $\mu = 36 \times 10^{-9}$ m^{2}V^{-1}s^{-1}) and 20 mM acetic acid. Figure 2.3 shows comparison of concentration profiles computed using the upwind, the SLIP and the sixth-order compact scheme at current density of 509 A/m^2. For this set of simulations we used a frame of reference moving with ITP zone to minimize the number of grid points. The computational domain was 15 mm long and we used 300 grid points for spatial discretization. Simulations using the upwind and the compact

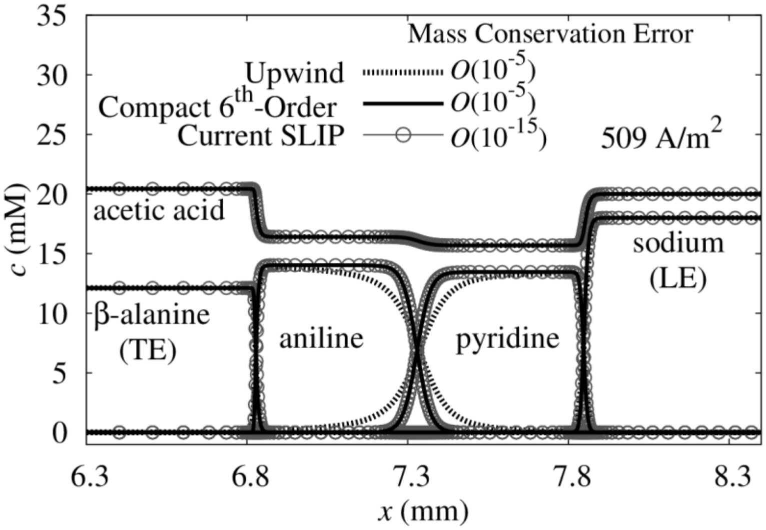

Figure 2.3: Simulation results of focusing and separation of aniline and pyridine in plateau mode ITP. The plot shows comparison of concentration profiles computed using the upwind, sixth-order compact, and the current SLIP differencing schemes. Simulations using the upwind and compact finite differencing used adaptive grid refinement based on clustering grid points in regions with large concentration gradients, as described by Bercovici et al. [63]. Whereas simulations with the current SLIP scheme used adaptive grid refinement procedure to minimize numerical dissipation as described in Section 2.3.3. Concentration profiles computed using the current SLIP scheme compare well with those obtained using more accurate sixth-order compact scheme. In particular, plateau concentrations and zone boundary thickness obtained using the current scheme agree well with the results from compact scheme. In comparison, the upwind scheme is more dissipative and so yields a non-converged solution due to artificial broadening of zone boundaries. Plot also shows how the grid refinement procedure adapts the grid points (shown in circles) from regions of uniform concentrations to sharp zone boundaries. Our finite volume scheme is based on conservative formulation of governing equations and conserves mass of focused analytes with $\mathcal{O}(10^{-15})$ accuracy. The simulations used 15 mm long domain with 300 grid points. We solved the equations in a frame of reference moving with ITP zones so as to reduce the number of grid points.

scheme used adaptive grid refinement scheme of Bercovici et al. [63] wherein grid points cluster in regions with large concentration gradients. For the current SLIP scheme, we used an adaptive grid refinement procedure to minimize numerical dissipation (see Section 2.3.3). As shown in Figure 2.3, concentration profiles computed using the SLIP scheme compare well with those obtained using the more accurate and previously verified sixth-order compact scheme. The current scheme is able to predict correctly the plateau concentrations and the thickness of diffusive zone boundaries. In comparison, the upwind scheme is only first-order accurate throughout the domain and yields a non-converged solution marred with artificial broadening of zone boundaries.

The distribution of grid points in Figure 2.3 illustrates how our adaptive grid algorithm preferentially clusters grid points at sharp interfaces. At these sharp interfaces, the SLIP scheme adds higher numerical diffusion to suppress spurious oscillations. The reduction in numerical dissipation due to adaptive grid refinement enables our dissipative SLIP scheme to predict thickness of sharp zone boundaries with a resolution comparable with the non-dissipative compact scheme. We note that besides the advantage of unconditional stability, the current scheme conserves mass significantly more precisely than the finite difference schemes (both compact and upwind) discussed by Bercovici et al. [63,69]. This is because our numerical scheme is based on a finite volume method for conservative formulation of governing equations, and hence conserves mass irrespective of the grid size. For example, for simulations shown in Figure 2.3 the current scheme conserves mass with $\mathcal{O}\left(10^{-15}\right)$ accuracy, while the upwind and the compact scheme (previously implemented in SPRESSO with non-conservative formulation of governing equations) conserve mass with relatively lower accuracy of $\mathcal{O}\left(10^{-5}\right)$. However, using the compact and the upwind finite differencing schemes for discretizing the conservative set of governing equations derived here will also yield accurate mass conservation.

In Figure 2.4 we show the zone boundary thickness predicted by our numerical scheme at current density of 2260 A/m^2 versus the number of grid points, and compare it with simulation results of Sounart and Baygents [71], Yu et al. [86], Bercovici et al. [63], and Chou et al. [73]. We used the same simulation conditions as those in the aforementioned numerical studies. Briefly, the analytes (aniline and pyridine) were injected as 1 mm plugs at a concentration of 10 mM in a 40 mm long capillary, and subsequently allowed to migrate for 42 s. As a fair comparison, we performed each of these simulations in a stationary frame of reference and varied the number of grid points from 200 to 4000. As shown in Figure 2.4, the compact scheme of Bercovici et al. provides a converged solution with grid independent zone boundary thickness when more than 400 grid points are used. Below 400 grid points, the compact scheme shows non-physical oscillations due to unresolved wave numbers [63]. Due to its non-dissipative nature and high accuracy, we here use predictions from the sixth-order compact scheme

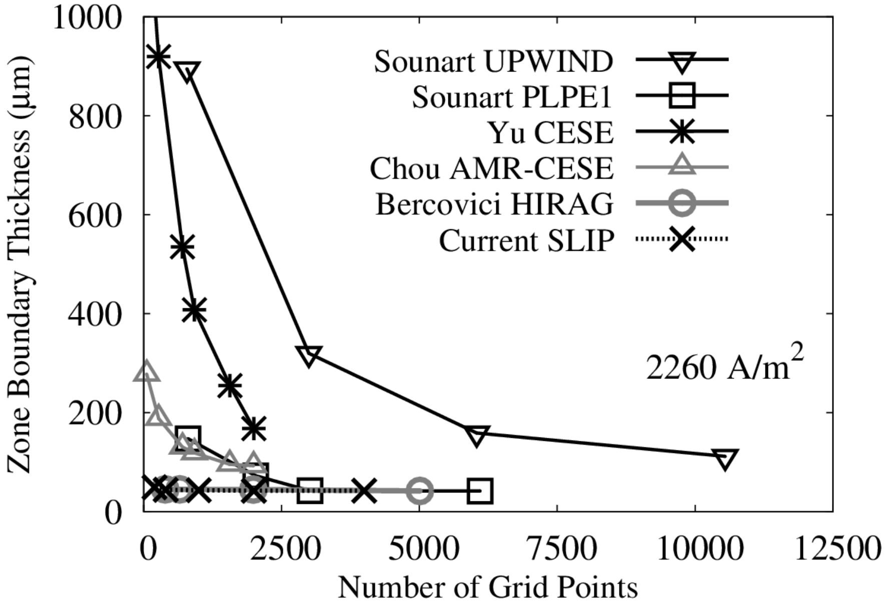

Figure 2.4: Comparison of six numerical schemes in predicting zone boundary thickness between aniline and pyridine zones in ITP. Here zone boundary thickness is defined as the length over which species concentration changes from 1% to 99% of its plateau value. Electrolyte chemistry and simulation parameters are the same as that for simulation shown in Figure 2.3, except for a higher current density of 2260 A/m^2 in this case. The UPWIND scheme is highly dissipative and does not show convergence of boundary thickness even when $\mathcal{O}\left(10^4\right)$ grid points are used. The CESE scheme of Yu et al. [86] and the PLPE1 scheme of Sounart and Baygents [71] are less dissipative than the UPWIND scheme. The CESE scheme with adaptive grid refinement (AMR-CESE scheme of Chou and Yang. [73]) shows improved accuracy compared to the CESE scheme and follows a convergence trend similar to the PLPE1 scheme. The HIRAG scheme of Bercovici et al. [63,69] is non-dissipative and coupled with adaptive grid shows convergence for all grids on which it produces a non-oscillatory solution. Note that the HIRAG scheme does not ensure monotonicity and results in oscillatory solutions for $\lesssim 400$ grid points. The current SLIP scheme, which preserves monotonicity and minimizes numerical dissipation using adaptive grid refinement, provides essentially grid independent prediction of interface thickness. Compared with other schemes, the SLIP scheme provides relatively accurate non-oscillatory solution with only 200 grid points. The data for the UPWIND and PLPE1 schemes was digitized from Sounart and Baygents et al. [71], and data for CESE and AMR-CESE schemes was digitized from Chou and Yang [73].

as baseline for comparison of other numerical schemes. Figure 2.4 shows that zone boundary thickness computed using dissipative schemes of Sounart and Baygents [71], Yu et al. [86], and Chou et al. [73] show strong dependence on grid size. For a higher number of grid points, the numerical dissipation in dissipative schemes decreases and improves the prediction of zone boundary thickness.

In comparison, the current numerical scheme is able to predict the interface thickness with reasonable accuracy. Compared to equivalent uniform grid schemes, such as PLPE1 of Sounart and Baygents [71] which takes ~2500 grid points to converge, the current scheme converges to the solution of the higher accuracy compact scheme in 400 grid points. The improved grid convergence behavior of our scheme compared to other dissipative schemes is due to the adaptive grid refinement procedure, which minimizes numerical dissipation. We note that, unlike the compact scheme of Bercovici et al. [63] which results in spurious oscillations below 400 grid points, our scheme yields stable solution with even 200 grid points. This stability with just 200 grid points is possible due to the numerical dissipation; however, it comes at a cost of ~15% error in computed interface thickness. Users of this scheme should, of course verify grid convergence of predicted solutions for simulations that require high accuracy.

2.4.3 Effect of variable channel cross-section on plateau mode ITP

In Section 2.4.2 we benchmarked our numerical scheme with the previously verified and experimentally validated sixth-order compact scheme of Bercovici et al. [15,63,69] for ITP problems in uniform cross-section channel. We now examine the effect of axially varying cross-sectional area on analyte focusing in ITP. Using variable cross-sectional area channels is a common and effective way of increasing sample loading and hence detection sensitivity in ITP [87,88]. In this technique, analytes are first allowed to focus in a large cross-section region and subsequently analytes are detected after they migrate into a narrow cross-section region. The large volume of the large cross-sectional area region increases the amount of analytes focused prior to their detection. Later, when the analyte zones transition from the large to small cross-section region, their zone lengths increase to conserve mass, providing higher detection sensitivity.

While ITP in variable cross-section channels has been used in several experimental studies for high sensitivity detection of ionic species, there has been limited work on simulations of this process. The majority of electrophoresis solvers, including SIMUL [66], GENTRANS [67] and older versions of SPRESSO [63], are based on 1-D formulation of advection-diffusion equations applicable in uniform cross-sectional area channels. Bahga et al. [88] presented a 1-D model for ITP in variable cross-sectional area channels based on the assumption of negligible diffusion. However, the diffusion-free model of Bahga et al. is well suited for predicting analyte zone concentrations and zone lengths only when analyte zones are significantly longer than diffusive zone boundaries. To the best of our knowledge simulations of ITP in variable cross-section geometry including both advective and diffusive fluxes have been limited to computationally expensive multidimensional numerical studies [74]. Here we present first-of-their-kind quasi 1-D simulations which account for advection and diffusion of species in ITP along with variation in channel cross-section.

We first examine the problem of plateau mode ITP focusing of two analytes in a channel with axially varying cross-section. The channel geometry, shown in Figure 2.5, consists of 5-fold reduction in cross-sectional area. The electrolyte chemistry was the same as that in ITP simulations shown in Figure 2.3 and Figure 2.4. Simulation results presented in Figure 2.5 show analyte zones at three locations as they migrate along the channel. Analytes first focus in the large cross-section region in the form of thin plateau zones (nearly overlapping as with peak mode ITP). As the analyte zones transition from large to small cross-section region, their zone lengths increase inversely with decreasing cross-sectional area, and the zone boundaries sharpen due to higher local electric field. After the analyte zones completely transition to the small cross-section region, their zone lengths attain steady values, which are about 5 times larger than the corresponding zone lengths in the large cross-sectional area region. However, variation in cross-sectional area does not affect the plateau concentration of analyte zones. This is because the maximum concentration of each analyte zone (the plateau concentration) is set by the regulating function established by the leading electrolyte mixture and does not depend on the channel cross-section. In the current case, the appropriate regulating functions are the

Jovin and Alberty functions [43,44], and we present detailed derivation of these regulating functions in Appendix D.

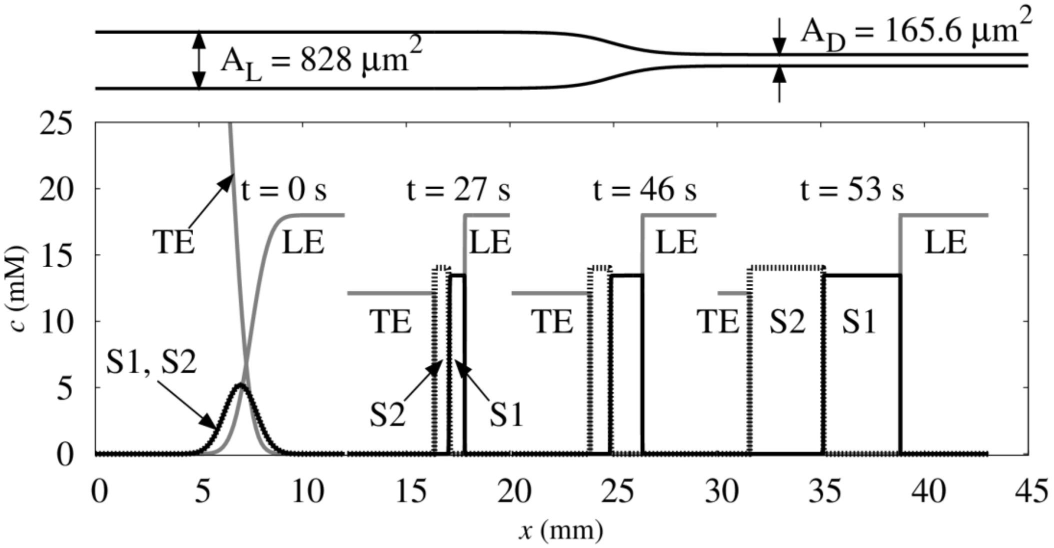

Figure 2.5: Simulation showing focusing and separation of pyridine and aniline in plateau mode ITP as it approaches and travels through a converging channel with 5-fold cross-sectional area reduction. Initially, at *t* = 0 s, pyridine (S1) and aniline (S2) are injected as overlapping, diffuse Gaussian peaks between the LE and TE zones. Upon application of an electric field, analytes (S1 and S2) focus between LE and TE zones (*t* = 27 s). Due to high initial amount of analytes and relatively high current densities, both S1 and S2 quickly form plateau-like zones in the large cross-section region. As the analyte zones transition from the large to small cross-section region (*t* = 46 s), their zone lengths increase inversely with decrease in cross-sectional area. Note that the plateau concentration of analytes does not depend on channel cross-section as this is simply set by the area-independent Jovin-Alberty regulating functions [43,44]. Later at *t* = 53 s, when analyte zones fully migrate into the narrow cross-section region, their zone lengths reach new steady values. Analyte zones elongate 5 times due to a 5-fold reduction in cross-sectional area. Electrolyte chemistry is the same as that for simulations in Figure 2.3. Simulations used a 60 mm long computational domain with 450 grid points and a constant applied current of 1 µA.

2.4.4 Effect of variable channel cross-section on peak mode ITP

Lastly, we present a simulation wherein analyze zones in peak mode ITP are migrated into a converging cross-section channel to transition them into plateau mode. In ITP, analytes focus in peak mode when the analytes zones do not reach their respective plateau concentrations. Peak mode ITP tends to occur when analytes are present in trace quantities or the zone boundaries are excessively diffused due to low electric field. Direct detection of analytes focused in peak mode ITP is typically limited by their peak concentrations relative to the signal noise and background. Bottenus et al. [89] experimentally demonstrated that the concentration of analytes peaks (and therefore detection sensitivity) in peak mode ITP can be increased using converging cross-sectional area channels. As analyte zones migrate from large to small cross-section region, both the local electric field and the amount of analytes focused per unit length of channel increase. Each of these effects promotes transition of peak mode focusing into plateau mode.

To illustrate the effect of variable cross-sectional area on peak mode ITP, we performed simulation of ITP focusing of two analytes (again, aniline and pyridine for ease of comparison) in a channel with 5-fold reduction in cross-sectional area. The channel geometry, analytes, and electrolyte chemistry were the same as those used for the (initially) plateau-mode ITP simulation shown in Figure 2.5 and discussed above. However, to ensure peak mode focusing of analytes, we here used 20-fold less initial amount of analytes and 10-fold lower current density compared to the plateau mode ITP simulation in Figure 2.5. Simulation results presented in Figure 6 show analyte zones at three locations along the converging cross-section channel. The lower initial analyte concentrations and lower current density results in analytes focusing in peak mode in the larger cross-section region. Peak mode results in overlapping peaks focused between the TE and LE zones. As the analyte zones transition to the smaller cross-section region, their peak concentrations increase (see Figure 2.6b). In this particular case, when analyte zones fully migrate into the small cross-section region (Figure 2.6c) the analyte zone concentrations reach their maximum possible values determined by the Jovin and Alberty regulating functions [43,44]. The constriction in channel cross-section therefore transforms peak mode ITP to plateau mode ITP.

We note that simulations of peak mode ITP can complement experimental observations as overlapping analyte peaks are hard to identify in experiments. Also, simulations of ITP in variable cross-sectional area channels can be used to optimize the channel geometry. For example, in such systems, for constant applied current, variation of the large-to-small-channel-area ratio results in a trade off between assay time and sensitivity of plateau mode detection (see Chapter 4). Fast, high accuracy simulations of such systems can significantly reduce design and optimization time and make prototyping efforts more efficient.

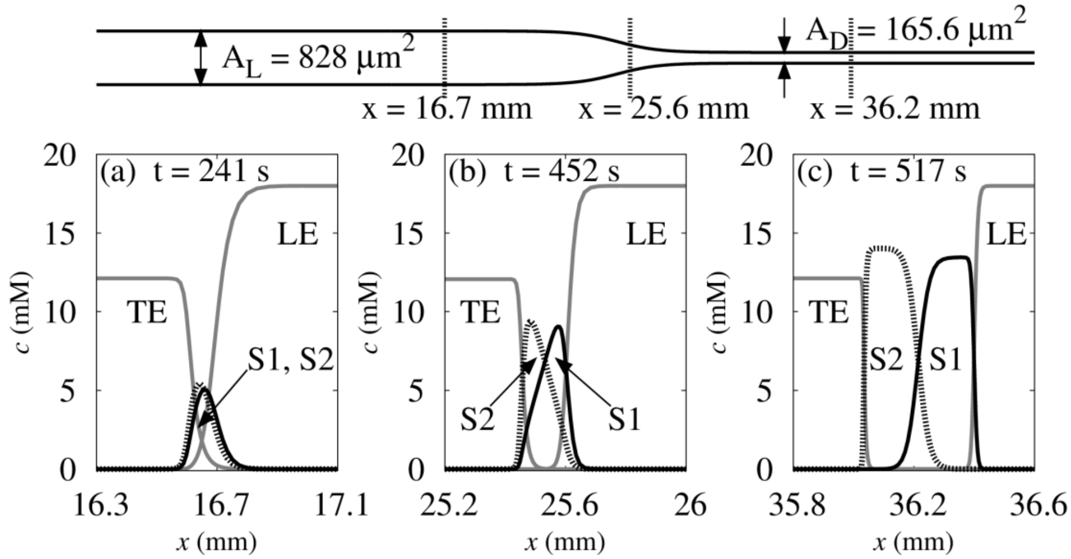

Figure 2.6: Simulation showing effect of variable channel cross-section on peak-mode ITP. Plots (a-c) show focusing of two analytes, pyridine (S1) and aniline (S2), at three locations along a converging channel with 5-fold reduction in cross-sectional area. (a) Due to their low initial concentrations, analytes S1 and S2 focus in peak mode in the large cross-section region. Peak mode focusing of analytes is characterized by largely overlapping analyte peaks with thickness comparable to the LE/TE zone boundary. (b) As the analyte zones transition from large to small cross-section region the analyte peak concentrations increase. This is in part due to relatively larger amount of sample focused per unit length of the channel, and to sharper zone boundaries associated with the higher local electric field. (c) In this particular case, when analyte zones fully migrate into the small cross-section region their zone concentrations nearly reach the plateau values determined by the Jovin and Alberty regulating functions [43,44]. Electrolyte chemistry and channel geometry used in this simulation are the same as that in Figure 2.5. Compared to the simulations shown in Figure 2.5, here we used 20-fold lower amount of analytes and 10-fold lower applied current (0.1 µA) to ensure peak mode focusing of analytes in the larger cross-section channel.

2.5 Summary

We have developed a generalized approach for modeling and simulation of quasi 1-D nonlinear electrokinetic processes in channels with axially varying cross-section.

Starting with 3-D advection-diffusion equations, we derived quasi 1-D equations for multispecies transport in terms of area-averaged quantities (species concentrations and axial electric field). Our formulation is based on typical assumptions of lubrication theory [78], including long, thin channels with slowly varying channel cross-sectional area. Our approach includes arbitrary variation in channel cross-section, chemical equilibrium calculations for multivalent weak electrolytes, ionic strength effects on species mobility [15] and acid-base equilibria, and Taylor-Aris dispersion [64,65] due to non-uniform bulk flow (due to either externally or internally generated pressure-driven flow components).

To solve the quasi 1-D governing equations, we have developed a dissipative finite volume scheme which selectively adds numerical dissipation at locations with sharp gradients and oscillations. This ensures unconditional stability of the scheme, regardless of the grid size. We have also provided a novel adaptive grid refinement algorithm which improves the accuracy of our scheme by migrating grid points from regions with low numerical dissipation to regions with higher numerical dissipation. We have benchmarked our numerical method with existing numerical schemes by simulating challenging electrokinetics problems (in uniform cross-section channels) involving sharp concentration gradients. These include simulations of ITP and electromigration-dispersion in CZE. Numerical experiments presented here show that the current approach yields robust and high resolution solutions using an order of magnitude less grid points compared to existing dissipative schemes [71,73,86]. Also, our simulation results show reasonable agreement with non-oscillatory solutions computed using non-dissipative schemes, such as the (experimentally validated) sixth-order compact scheme of Bercovici et al. [63,69]. Unlike non-dissipative schemes, the current numerical scheme is very robust as it is unconditionally stable. This feature makes our scheme advantageous for routine analysis and optimization of electrokinetic processes by researchers with little or no experience in computational methods. By comparison, non-dissipative schemes may be better suited for more detailed, fundamental electrokinetics studies where accuracy is preferred over computational efficiency.

We have also demonstrated first-of-their-kind quasi 1-D simulations of ITP in non-uniform cross-sectional area channels. In particular, we leveraged quasi 1-D simulations to predict the efficacy of converging cross-section channels in increasing detection sensitivity of both peak-mode and plateau-mode ITP. Until the current model, such studies have been limited to computationally expensive multidimensional simulations. The quasi 1-D approach presented here is computationally efficient and hence provides new possibilities for optimization of electrokinetic systems based on shape, chemistry, or electrical control schemes to achieve high detection sensitivity and rapid analysis. For example, simulations of ITP in converging cross-section channels can be used to determine the required amount of contraction in cross-sectional area so as to ensure complete transition from peak to plateau mode ITP. Such simulations can complement empirical designs of channel geometry and minimize trials involved in fabricating channels and performing experiments.

3 Ionic strength effects on electrophoretic focusing and separations

The contents of this chapter were previously published by S.S. Bahga, M. Bercovici and J.G. Santiago [15] in *Electrophoresis* journal and are reproduced here with minor modifications.

3.1 Introduction

Electrophoretic separation and preconcentration techniques such as capillary zone electrophoresis (CZE) and isotachophoresis (ITP) rely on differences in electrophoretic mobilities of analytes to separate them in the presence of an electric field. The analytes can be weak or strong acids and bases, or can be amphoteric and posses both anionic and cationic groups. The degree of dissociation of such analytes is typically a function of their dissociation constants (pK_a), local pH and local ionic strength. The degree of dissociation determines the degree of ionization (or effective charge) of the species and can be linked directly to its effective mobility. The dependence of effective ionic mobility on pH and pK_a is described in detail in [49,63,90–93]. There are several models with varying complexity [14,80,94–96] for predicting the fully-ionized mobility (actual ionic mobility) of ions (*e.g.*, a singly ionized weak acid at a pH a few units above the pK_a) at finite ionic strengths given their limiting mobility at zero ionic strength (i.e., the infinite dilution limit). Also, activity coefficients vary with ionic strength, leading to change in ionization and effective mobility [49]. In general, effective, observable ion mobility at finite ionic strength depends on the limiting fully-ionized mobility of the ion, the mobility of its counter- and co-ions, ionic charge (valence values), buffer composition, and ion dissociation constants (*e.g.*, pK_a values).

Several experimental studies have underlined the importance of ionic strength in separations and leveraged its understanding for improving the design of assays. For example, electrophoretic separations at high ionic strengths have been suggested to minimize peak distortion due to electromigration dispersion [97], and high ionic strength separations have also been used to reduce wall adsorption of cationic proteins [98] and increased analyte selectivity [99]. Other studies have reported on the adverse effects of high ionic strength, which may lead to zone reversal in CZE and ITP [35,100], and decreased focusing rate in isotachophoresis (ITP) [40].

These practical consequences underline the importance of the influence of ionic strength on ionic mobility in modeling electrophoretic focusing and separation. Numerical simulations can minimize the number of required experimental runs for choosing optimal conditions; can be used to design and perform at least preliminary optimizations of assays; and are a useful tool in evaluating experiments and elucidating underlying physicochemistry processes. Ionic strength models and calculations have been offered by and incorporated in the capillary electrophoresis solver Peakmaster [101], which solves for the chemical properties of a uniform buffer, as well as in the full electrophoresis simulation code SIMUL [66]. In [101] the authors provide a validation of Peakmaster by comparing computed results for several equilibrium buffer compositions with experimental measurements. However, significant (and sometimes prohibitive) computational costs associated with ionic strength-dependent calculations in numerical simulations have to date often limited their usefulness in electrophoretic separation research and practice. In [66], for example, the authors note that the simulations were conducted with the ionic strength model disabled in order reduce the computational time. The effect of ionic strength on simulation of separations and focusing were thus not studied in that work.

In this work, we present the implementation and experimental validation of an ionic strength model in a fast numerical solver for electrophoretic transport. We correct for ionic strength effects using the Onsager Fuoss model [80] and extended Debye-Huckel theory [81] for correction of ionic activity. We validate the ionic strength corrections with ionic mobility measurements of fluorescein in CZE. We also use simulations and experiments to demonstrate and analyze the influence of ionic strength on focusing and zone order in ITP. We also use our model to demonstrate a case of changes in selectivity and peak reversal in CZE (i.e., a change of the order of peaks in an electrophererogram), by varying ionic strength.

3.1.1 Mathematical Model for Fully-Ionized Mobility

We can define the "fully-ionized" mobilities (actual ionic mobility) of an ion in solution as the mobilities the ion would take on with integer values of its valence. For example, the ion A^- takes on its fully-ionized mobility for aqueous solutions of the singly ionized (single pK_a) acid HA at sufficiently high pH. A weak acid with two nearby pK_a values at charge -1 and -2 may never realize its fully-ionized mobility associated with the -1 charge state, but we can still define such fully-ionized mobility mathematically [49]. The presence of an ionic atmosphere around the ion in solution at finite ionic strength results in reduced actual mobility compared to mobility of an isolated ion (at zero ionic strength).

We here summarize the following models describing the effect of ionic strength on the fully-ionized mobility of ions: Kohlraush [14], Onsager [102,103], Onsager and Fuoss [80] and Pitts [94]. We discuss the differences between these models and present their associated mathematical relations, with the exception of Pitts model [94] whose formulation is fairly complex and does not provide additional insight in this discussion.

Onsager derived a theory for the dependence of conductivity of a strong electrolyte on concentration, based on the ionic atmosphere model of Debye-Huckel [81]. Onsager's theoretical model [102,103] is functionally equivalent to Kohlrausch's empirical [14] model for conductivity of an electrolyte at finite ionic strength. The latter is given by $\Lambda = \Lambda_0 - k\sqrt{c}$, where Λ is the molar conductivity, Λ_0 is its value at infinite dilution, c is the ion concentration, and k is an empirical constant. Onsager's model treats ions as point charges and is restricted to dilute electrolytes containing two fully ionized species of opposite charges. This original theory for conductivity at finite ionic strength can be expressed in terms of electrophoretic mobility μ as,

$$\mu_i = \mu_i^0 - (A_i\mu_i^0 + B_i)\sqrt{c}, \tag{3.1}$$

where μ_i^0 denotes the limiting ionic mobility of the species i at zero ionic strength (for a given integer value of valence), and c is the concentration of the solute. The reduction in mobility can be attributed primarily to two factors. First, an ion in solution attracts a cloud of counter-ions (ionic atmosphere) around itself, balancing local charge. Under an applied electric field, the ion and its counter-ionic cloud move in opposite direction and this causes a polarization (new counterions are recruited and old ions are rejected, but overall the ion and its ionic atmosphere polarize). This polarization has a finite relaxation time scale—equivalent to the time scale required for the ion cloud to again reach spherical symmetry for a rapidly deactivated electric field. This so-called relaxation effect is captured by the factor A_i in eq. (3.1). The second effect is associated with the drag force exerted by the moving ionic atmosphere on the central ion. This second effect is reflected by term B_i in eq. (3.1) and is termed as the electrophoretic effect. Detailed discussion on these effects can be found in [80,95,96]. Onsager's model is valid only for dilute, binary electrolytes and a more general theory is required for ITP and CZE, where multiple species co-exist in solution. In such a system, the mobility of any ion is dependent on the presence of all other ions in solution.

Onsager and Fuoss extended the model given by eq. (3.1) to account for an arbitrary mixture of ionic species as follows [80]:

$$\begin{aligned} \mu_i &= \mu_i^0 - (A\mu_i^0 + B)\sqrt{\mathit{\Gamma}}, \\ A_i &= z_i \frac{e^3}{12\pi}\left(\frac{N_{AV}}{(\varepsilon kT)^3}\right)^{1/2} \sum_{n=0}^{\infty} C_n R_i^n. \\ B_i &= |z_i| \frac{e^2}{6\pi\eta}\left(\frac{N_{AV}}{\varepsilon kT}\right)^{1/2}, \quad \mathit{\Gamma} = \sum_{i=1}^{s} \mathit{\Gamma}_i, \quad \mathit{\Gamma}_i = c_i z_i^{\,2}. \end{aligned} \tag{3.2}$$

Here s is the number of species, z_i is the charge number of the ith ionic species, ε is permittivity of solution, k is the Boltzmann constant, e is elementary charge, N_{AV} is the Avogadro constant, T is the temperature of the solution and $\mathit{\Gamma}$ is twice the ionic strength, $I = 0.5\sum_i c_i z_i^{\,2}$. The coefficients C_n and the vectors $\mathbf{R^n} = [R_1^n, R_2^n, \ldots, R_s^n]^T$ are given in [80]. However, similar to the Onsager model of eq. (3.1), the model described by eq. (3.2) again treats ions as point charges. The assumption of point charges is valid only for thick electrical double layers where the size of the ion can be considered negligible compared with its counter-ion atmosphere. This limits the validity of eqs. (3.1) and (3.2) to ionic strengths below order 1 mM.

At ionic strength higher than order 1 mM, finite ion size cannot be neglected. Pitts [94] provided a correction to the models of eqs. (3.1) and (3.2) which accounts for finite ion size. The Pitts model (the relation for which is not given here) is strictly applicable only for symmetric binary electrolytes. However, Li et al. [104], showed that the Pitts model is approximately equivalent to eq. (3.2), with an additional term in the denominator. This forms the basis of an extended Onsager-Fuoss model given by eq. (3.3), which we use in this work. We here adopt this simpler formulation which is an extended Onsager-Fuoss model given by [101]. This extended model takes into account the finite ionic radius and arbitrary mixtures of ions:

$$\mu_i = \mu_i^0 - (A_i \mu_i^0 + B_i)\frac{\sqrt{\Gamma}}{1+\frac{aD}{\sqrt{2}}\sqrt{\Gamma}}, \quad D = \left(\frac{2e^2 N_{AV}}{\varepsilon kT}\right)^{1/2}, \tag{3.3}$$

where a represents the mean distance of closest approach for the ions. In other words, a is the distance from center of the central ion to the start of the ionic atmosphere [101]. The value of $aD/\sqrt{2}$ lies between 1-2 mol$^{-1/2}$dm$^{3/2}$ [104]. Here (and for a wide variety of buffers) we choose a fixed value of aD as 1.5 mol$^{-1/2}$dm$^{3/2}$ as an approximation. Terms A_i and B_i in eq. (3.3) are the same as those in eq. (3.2). Appropriately, eq. (3.3) reduces to the Robinson Stokes equation for the case of binary electrolytes [96]. Equation (3.3) is applicable for ionic strengths up to 100 mM [14]. We use the Onsager-Fuoss extended model as it takes into account the relevant physics of a mixture of ions and captures, approximately, the effects of finite ion size. As examples, Figure 3.1 shows variations of the fully ionized mobility of a cation for four electrolytes composed of different anion:cation pairs. We see that the reduction of mobility of divalent ions is stronger than that of univalent ions at a finite ionic strength. Also, for the same ion, mobility reduction is higher if its counter ion bears higher charge (and thus more effectively shields the ion). The inset shows specifically the effect of finite ionic radii for a simple -1:1 electrolyte.

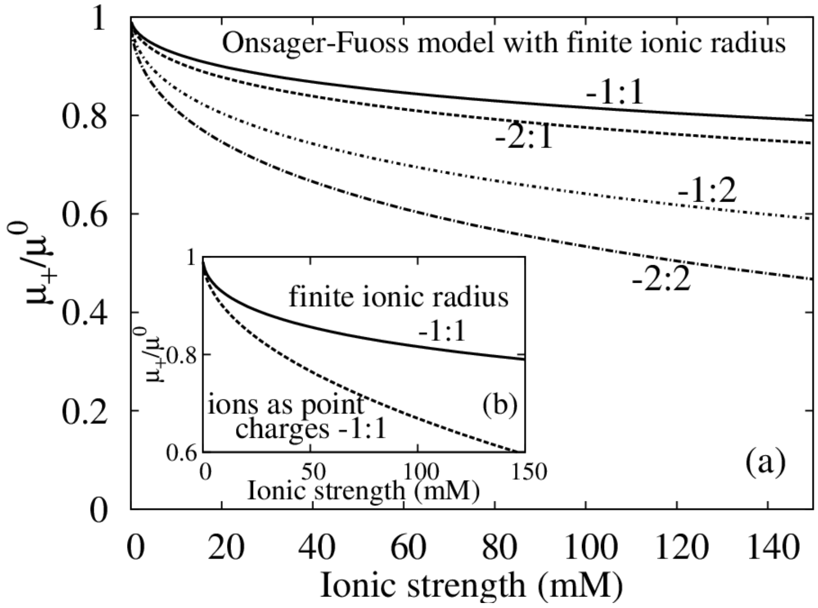

Figure 3.1: Mobility dependence of several binary electrolytes on ionic strength. Plot shows ionic mobility of a cation for binary electrolytes with various anion:cation valence values. (a) shows variation of electrophoretic mobility of cations with ionic strength using Onsager Fuoss model with finite ionic radius, eq. (3.3). Univalent cations have lesser reduction in mobility than divalent ions for increasing ionic strength. Thus cations in -1:1 and -2:1 electrolytes have lesser mobility, respectively, than cations in -1:2 and -2:2 electrolytes. Also, greater charge on counterions (anions) causes greater reduction in mobility. Thus cations in -2:1 and -1:2 electrolytes have lesser mobility, respectively, than cations in -1:1 and -2:2 electrolytes. (b) shows the effect of finite radius correction to Onsager-Fuoss model. Dotted line corresponds to Onsager Fuoss model assuming ions as point charges, eq. (3.2), and solid line corresponds to Onsager Fuoss model using finite ionic radius, eq. (3.3). Neglecting ionic radius overpredicts the reduction in mobility at finite ionic strengths. For these sample calculations, the mobilities of all ions is taken as $\mu^0 = 50\times10^{-9}$ $m^2V^{-1}s^{-1}$.

3.1.2 Mathematical Model for Activity Coefficient and Degree of Ionization

The observable ionic mobility of weak electrolytes (which we will call here the “effective mobility”) depends on the degree of ionization, which can be obtained by solving for equilibrium composition of ionic species. While finite kinetic rates of reaction are sometimes important [105,106], kinetic rates in most electrophoresis applications are faster than the characteristic times of advection and diffusion [60], and so each species can be assumed to be in chemical equilibrium at all times. Using the notation by Stĕdrý et al. [107], the total concentration of a general ampholyte i can be expressed as the sum of its constituent ionization states:

$$c_i = \sum_{z=n_i}^{p_i} c_{i,z}, \tag{3.4}$$

where $c_{i,z}$ is the concentration of an ionic state with valence z belonging to the species i, and n_i and p_i are the minimum and maximum valences of the species. The activities of two consecutive ionic states of species i, are related by the equilibrium constant $K_{i,z}$.

$$K_{i,z} = \frac{a_{i,z}a_H}{a_{i,z+1}} = \frac{\gamma_{i,z}\gamma_H}{\gamma_{i,z+1}}\frac{c_{i,z}c_H}{c_{i,z+1}}, \tag{3.5}$$

where c_H is the concentration of H^+ and $\gamma_{i,z}$ are the activity coefficients of zth ionic state of species i. For dilute solutions, concentrations can be used in place of chemical activities. However, at significant ionic strengths, activity coefficients are smaller than unity. Activity coefficients can be modeled by Debye Huckel theory [81] with an additional term depending on ionic strength as follows:

$$\log\gamma_{i,z} = -z^2 \frac{A_{DH}\sqrt{I}}{1+aD\sqrt{I}} + 0.1z^2 I, \quad I = \frac{1}{2}\sum_{i=1}^{s}\sum_{z=n_i}^{p_i} z^2 c_{i,z}. \tag{3.6}$$

The first term is the Debye-Huckel term which accounts for long range, non-specific, electrostatic interactions. The second term represents specific interaction occurring at high ionic strength, approximated by a linear correction term. Here A_{DH} is a temperature dependent term and I is ionic strength in $\mathrm{mol\,dm^{-3}}$. At room temperature A_{DH} is 0.5102 $\mathrm{dm^{1/2}mol^{-1/2}}$. Hence, in addition to reduction of (fully-ionized) mobility due to ionic shielding, high ionic strength also affects the equilibrium concentrations and so the effective mobility.

For convenience, we can relate the concentrations of species with an apparent equilibrium constant

$$\tilde{K}_{i,z} \equiv \frac{\gamma_{i,z+1}}{\gamma_{i,z}\gamma_H} K_{i,z} = \frac{c_{i,z}c_H}{c_{i,z+1}}. \tag{3.7}$$

These apparent equilibrium constants can then be readily used in the electroneutrality equation,

$$\sum_{i=1}^{s} c_i \sum_{z=n_i}^{p_i} z g_{i,z} + c_H - \frac{\tilde{K}_w}{c_H} = 0\,, \tag{3.8}$$

where $g_{i,z} = L_{i,z} c_H^z \,/ \sum_{z=n_i}^{p_i} L_{i,z} c_H^z$ is the dissociation level of the species i, c_i is the total concentration, and $\tilde{K}_w = K_w / \gamma_H \gamma_{OH}$ is the apparent dissociation constant of water. $L_{i,z}$ depends on the apparent dissociation constants and is given by,

$$L_{i,z} = \begin{cases} \prod_{z'=z}^{-1} \tilde{K}_{i,z'} & z < 0 \\ 1 & z = 0 \\ \prod_{z'=0}^{z-1} \tilde{K}_{i,z'}^{-1} & z > 0 \end{cases} \tag{3.9}$$

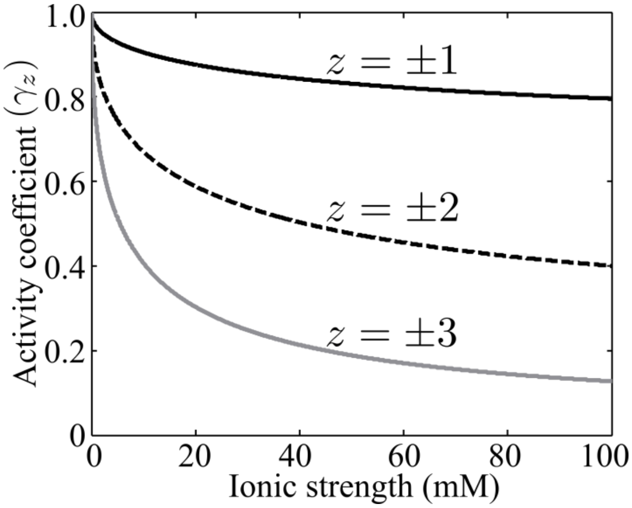

Figure 3.2: Effect of ionic strength on activity coefficient for varying ion valence. Plot shows variation of activity coefficient with ionic strength based on Debye Huckel theory [81] with an additional term to model specific interactions at high ionic strength (eq. (3.6)). Plot shows that multivalent ions have larger reduction in activity coefficient than univalent ions for increasing ionic strength.

If ionic strength effects are not considered, then $L_{i,z}$ and $\tilde{K}_w$ are constants in an electrophoresis simulation. However, when ionic strength effects are considered $L_{i,z}$ and $\tilde{K}_w$ vary in space and in time as a function of the local ionic strength. To solve this system, we perform the following process at every time step of simulation. We start by taking an initial guess on the value of c_H (at every grid point in the domain). At the first time step, this initial guess is simply the solution for eq. (3.8) with ionic strength effects neglected. For subsequent times, we use the previous solution as the new initial guess. This initial guess is used to calculate the ionic concentrations $c_{i,z}$ using $c_{i,z} = c_i g_{i,z}$ and the activity coefficients and equilibrium constants according to eqs. (3.6) and (3.7), respectively. Equation (3.8) is then solved by Newton iteration, and new species concentrations $c_{i,z}$ are obtained. We repeat this process until the solution c_H converges to within a predefined tolerance. After converging to a solution of chemical equilibrium, the obtained ionic strength is used to calculate the fully ionized mobility, $\mu_{i,z}$, of every ionic species, using extended Onsager-Fuoss model, given by eq. (3.3). This mobility is finally corrected to the effective mobility of species *i* by

$$\mu_i = \sum_{z=n_i}^{p_i} \mu_{i,z} g_{i,z} \ . \tag{3.10}$$

The equations evolving the dynamics of electrokinetic transport and (in the model used here) the adaptive grid formulation are then solved for each time steps (see Bercovici et al. [63,69]). All simulations shown in this chapter, were performed using the sixth-order compact scheme [63,69]. However, we note that same results can also be obtained using the SLIP scheme, as the SLIP and compact schemes yield nearly indistinguishable results (discussed in Chapter 2).

3.2 Materials and methods

We performed a series of experiments to validate our model and evaluate test cases. For the high ionic strength experiments, the LE consisted of 250 mM HCl and 400 mM Tris. For the low ionic strength experiments, the LE was of 10 mM HCl and

20 mM Tris. For both experiments the TE was 20 mM HEPES and 40 mM Tris and contained 5 mM of the analyte MOPS. All chemicals were obtained from Sigma Aldrich (St. Louis, MO) and diluted from 1 M stock solutions. We also added 1% polyvinylpyrrolidone (PVP) to both the LE and TE to suppress electroosmotic flow, and added 4 mM $Ba(OH)_2$ (100 mM stock solution) to the TE to precipitate dissolved carbon dioxide [108].

We obtained the fluorescent markers fluorescein and Oregon Green carboxylic acid (OGCA) from Invitrogen (Carlsbad, CA). We prepared 100 µM concentration stock solutions of these fluorescent analytes and diluted their final concentration in the TE. Their respective concentrations were 2 µM and 300 nM for the high ionic strength experiments, and 1 µM and 300 nM for the low ionic strength experiments. We also prepared 1 mM stock solution of the cationic dye rhodamine 6G (Acros Organics, Geel, Belgium), and used it to visualize the plateau zones of anionic ITP by mixing at a concentration of 100 µM in the LE (see description of this non-focusing tracer below). All solutions were prepared in UltraPure DNase/RNase free distilled water (GIBCO Invitrogen, Carlsbad, CA).

We obtained images using an inverted epifluorescent microscope (IX70, Olympus, Hauppauge, NY) equipped with a mercury lamp, U-MWIBA filter-cube from Olympus (460-490 nm excitation, 515 nm emission, and 505 nm cut off dichroic) and a 10X (NA = 0.4) UPlanApo objective. Images were captured using a 12 bit, 1300x1030 pixel array CCD camera (Micromax1300, Princeton Instruments, Trenton NJ). We controlled the camera using Winview32 (Princeton Instruments, Trenton NJ) and processed the images with MATLAB (R2007b, Mathworks, Natick, MA). We applied constant current (3 µA and 0.3 µA for the high and low ionic strength cases, respectively) using a high-voltage sourcemeter (model 2410, Keithley Instruments, Cleveland, OH).

We used off-the-shelf microfluidic borosilicate chips (model NS-95) from Caliper Life Sciences (Mountain View, CA) with channel dimensions 74 µm wide by 12 µm deep. We filled the North, South and West wells (reservoirs) of the chip with LE and applied vacuum to the East well until all channels were filled. We then rinsed the East well several times with distilled water and filled it with the TE, analyte and markers mixture. The electrodes were placed in the East and West wells and constant current was applied. We centered the field of view of the microscope at a fixed distance of 9 mm from the (East) TE well, and set the camera to take images continuously until manually stopped after we observed that an image of the zone was captured.

3.3 Results and Discussions

We integrated the ionic strength model discussed in Sections 3.1.1 and 3.1.2 into the existing electrophoresis solver SPRESSO [63,69]. The extended Onsager-Fuoss model used in our simulations is the same as that used in Peakmaster [93,101]. Our presentation here will center on the coupling this model to our adaptive-grid electrophoresis solver, and on detailed experimental validations of the related simulations. The ionic strength corrections to mobility and activity coefficients are applied in parallel to the transient simulations of electrokinetic transport equations. As we noted before, many of the physical processes in our code were first represented in SIMUL [66] (including multispecies electromigration transport of weak electrolytes, a coupling to a mobility and pK_a data base, and ionic strength effects). However, as noted in [66], ionic-strength-dependent calculations are typically computationally intensive as they are performed for every grid point in the domain, and require an additional set of iterations, compared to the zero ionic strength case. This results in significant (and sometimes prohibitive) computational times, limiting the usefulness of uniform grid solvers (such as SIMUL) in the design and optimization of electrophoretic separation assays.

The adaptive grid mechanism in SPRESSO allows for highly resolved calculations with significantly less grid points (*e.g.*, Bercovici et al. [63] demonstrated 50 fold decrease in required number of grid points for equivalent resolution at relatively high electric field simulations as compared to a uniform-grid simulation). The number of ionic strength calculations decreases accordingly, resulting in faster solutions. We here also further accelerate the simulations by computing ionic strength effects only when ionic strength at each grid point changes by a particular amount, typically 1%. Together, both features enable efficient computations with ionic strength corrections. This allows for easier comparison of numerical results with experiments, and short turnaround times in the design of electrophoretic assays for researchers and practitioners within the lab setting. In this section, we present several examples of the use of the code, and more importantly, provide validation of the code and ionic strength model with experimental results.

The results presented here were obtained using an un-compiled version of the code under Matlab release version R2007b on a 32 bit Windows XP operating system. An AMD Athlon 64 X2 4400+ with 2 GB RAM was used as the computing platform. The chemical properties for all analytes (except fluorescent dyes) were obtained from Hirokawa et al. [109,110]. A list of these chemical properties is built into the graphical user interface of SPRESSO. With ionic strength corrections, SPRESSO runs approximately 100 times faster than SIMUL. In particular, for the case presented in Figure 3.4, for 44 s of simulated time, SIMUL required 45,000 grid point to provide a non-oscillatory solution which resulted in a computational time of 63 h. For the same case and the same resolution, the combination of an adaptive grid and a moving frame of reference required only 100 grid points in SPRESSO, leading to a computation time of only 36 min. For the same case, but without ionic strength corrections, SPRESSO took 16 mins of computational time.

3.3.1 Effective Mobilities

We first benchmarked the calculations for ionic strength corrections for mobility by comparing our model results with Peakmaster [93,101]. We also validated our model by comparing predicted effective mobilities with experimental results. In Appendix D, we present a benchmark of our equilibrium calculations with similar calculations using Peakmaster. Jaros et al. [101] compared results from Peakmaster with experimental values of effective mobilities for several weak acids at different pH, for a small range of ionic strengths between 13 and 20 mM. Since ionic strengths of order 100 mM are common in CZE and ITP [104], we here examine electrophoretic mobility of fluorescein for two pH values of 7.15 and 9.35, and ionic strength varying from 30 mM to 90 mM. The mobility of fluorescein was measured using on-chip capillary electrophoresis. The experimental method and materials are explained in detail by Milanova et al. [111]. Figure 3.3, shows a comparison between experimental and computed values of effective mobility of fluorescein, as a function of ionic strength. As mentioned in Section 3.1.1, mobility reduces at higher ionic strengths. The model compares fairly well with experimental values. As expected, at all ionic strengths, the effective mobility at pH 9.35 is higher than that at pH 7.15, as fluorescein is a weak acid $(\mathrm{p}K_{a,-2} = 6.8)$ and thus more strongly disassociated at higher pH.

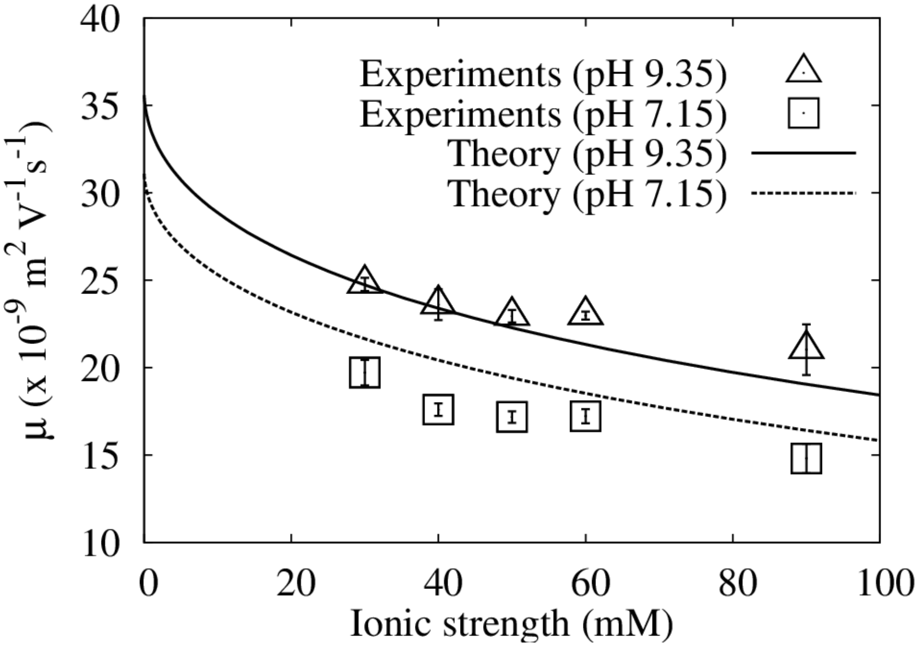

Figure 3.3: Effect of ionic strength on ionic mobility of Fluorescein at two pH values. Data points show the experimentally measured ionic mobility of fluorescein. Squares and triangles correspond to measurements obtained at pH 7.15 and pH 9.35, respectively. Measurements were made by capillary zone electrophoresis, using glycine-sodium hydroxide buffer at pH 9.35 and HEPES-sodium hydroxide buffer for pH 7.15. Plotted uncertainty bars correspond to 95% confidence in mean values, calculated using Student's-t distribution. The trends provided by numerical calculations (lines) agree fairly well with experimental observations of Milanova et al. [111]. Calculations were obtained using, $\mu_{-1}^{0} = -19\times10^{-9}$ $\mathrm{m^2V^{-1}s^{-1}}$, $pKa_{-1} = 4.4$ and $\mu_{-2}^{0} = -36\times10^{-9}$ $\mathrm{m^2V^{-1}s^{-1}}$, $pKa_{-1} = 6.8$.

3.3.2 Sample preconcentration in peak mode ITP

In isotachophoresis (ITP), sample ions focus between a leading (LE) and trailing electrolyte (TE) having typically higher and lower effective mobilities, respectively. "Peak mode" ITP refers to a focusing mode where analytes are initially at sufficiently low concentrations (and time of observation sufficiently short) that the analyte does not have enough time to form a plateau zone. In peak mode, analyte ions form a narrow concentrated peak whose width is determined by the diffuse boundaries of neighboring zones (*e.g.*, a diffuse boundary between the LE and TE zones). This type of focusing is common in biological applications such as immunoassays and DNA or RNA separations, where sample concentrations are inherently low [112,113].

In single-interface injections (that is, a "semi-infinite sample" configuration), the sample is mixed in the TE well (reservoir) and continuously overspeeds the TE ions to focus at the TE-LE interface. The TE and sample ions displace the LE ions and, in bulk liquid regions formerly occupied by LE ions, adjust to concentration levels dictated by the LE [40]. The sample concentration, $C_{S,te}$, in the new 'regulated' TE zone can be calculated from flux balance at the interface of TE well and regulated TE zone. $C_{S,te}$ is related to the initial sample concentration $C_{S,te\ well}$ as [40].

$$C_{S,te} = \frac{\mu_{S,te\ well}}{\mu_{S,te}} \frac{\mu_{T,te}}{\mu_{L,le}} \frac{\sigma_{le}}{\sigma_{te\ well}} C_{S,te\ well}, \tag{3.11}$$

where $\mu_{S,te\ well}$ and $\mu_{S,te}$ are the effective mobilities of the sample ions in the TE well and the regulated TE zone, and $\mu_{T,te}$ and $\mu_{L,le}$ are the effective mobilities of the TE ions in the regulated TE zone and LE ions in LE zone. σ_{le} and $\sigma_{te\ well}$ represent the conductivities of the LE zone and the TE well.

The amount of sample accumulated in peak mode, N_s, depends primarily on the ratio of the effective mobility of the analyte in the TE zone to that of the TE anion in the TE zone, the initial sample concentration, and the time elapsed between injection and detection. The rate of accumulation with respect to the distance traveled by the interface (neglecting electroosmotic flow) is given by [40].

$$\frac{dN_s}{dx} = \frac{dN_s}{dt}\frac{1}{dx/dt} = \frac{dN_s}{dt}\frac{1}{V_{ITP}} = \left(\frac{\mu_{S,te}}{\mu_{T,te}} - 1\right) C_{S,te} \tag{3.12}$$

where $V_{ITP} = \mu_{L,le} j / \sigma_{le}$ is the speed of ITP front. $\mu_{L,le}$ and σ_{le} are the effective mobility of LE ions, and conductivity of LE zone, respectively. At low ionic strengths, sample concentration in the TE zone increases proportionally with LE concentration (conductivity) as per eq. (3.11). As a result, from eq. (3.12), focusing rate of sample increases with increase in LE concentration. However, eqs. (3.11) and (3.12) show that a divalent ion experiences greater reduction in mobility than a univalent ion as ionic strength is increased. For univalent TE ions and divalent sample ions, the ratio $\mu_{S,te} / \mu_{T,te}$ in (3.12) therefore decreases with increasing ionic strength (as per eq. (3.3)). Thus the focusing rate of a divalent sample initially increases with increasing ionic strength in the low ionic strength regime (as per the $C_{S,te}$ factor in eq. (3.12)) but then decreases at higher ionic strengths as $\mu_{S,te} / \mu_{T,te}$ decreases. The net result is that for a divalent sample ion, the focusing rate increases with LE conductivity at low ionic strengths but then saturates and decreases with further increase of ionic strength.

Khurana and Santiago [40] experimentally observed reduction in focusing rate for divalent Alexa Fluor 488 (AF) ions in peak mode ITP. Their experimental data values are shown as circles in Figure 3.4. We here compare the predictions of sample accumulation in peak mode ITP obtained from time-dependent numerical simulations in SPRESSO with the experimental observations of Khurana and Santiago [40]. Figure 3.4a shows numerical predictions of accumulated moles of AF as a function of LE concentration for calculations performed with (solid line) and without (dashed line) ionic strength correction. As Khurana and Santiago point out, the sample concentration in the adjusted TE zone increases with increased LE concentration in accordance with eq. (3.11) . However, at sufficiently high ionic strength, the mobility of the divalent sample (AF) decreases more strongly than that of the univalent TE (3-phenylpropionic acid). This results in decreased accumulation of AF at higher ionic strengths, such that the accumulated moles reach maxima (at σ_{le} = 2 S/m) and decrease for higher LE conductivities.

In the inset of Figure 3.4, we plot the same AF accumulated amount data as the main plot but here as a function of LE concentration to further highlight the effect of neglecting ionic strength corrections in ITP simulations. The predictions obtained by considering ionic strength effects (solid curve) agree well with experimental observations (circles). However, the simulations that neglect ionic strength corrections (dotted curve in both inset and main plot) are clearly inaccurate above about 50 mM LE concentrations. These predictions do not take into account the reduced mobility of AF relative to TE ions at sufficiently high ionic strength and grossly overpredict the trend with increasing LE concentration.

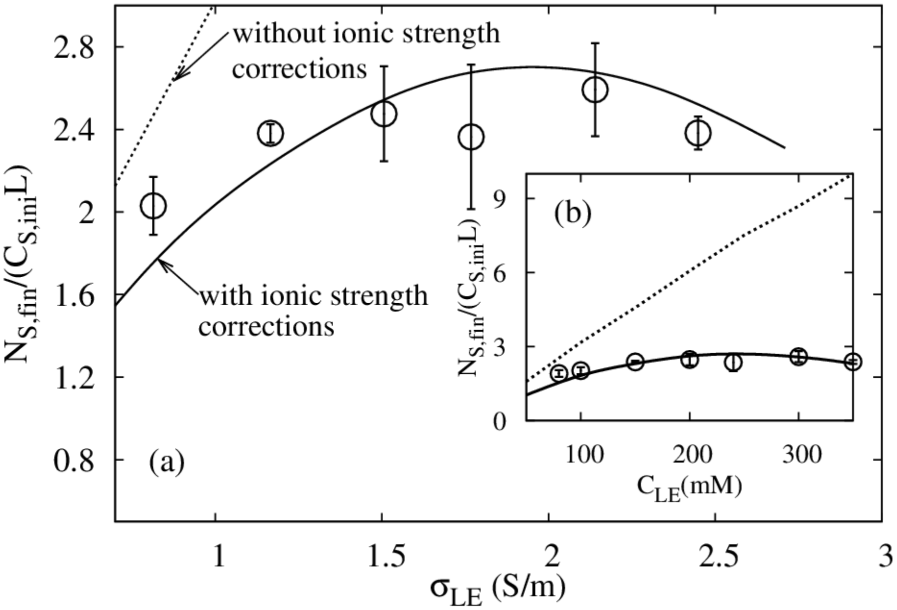

Figure 3.4: Influence of ionic strength dependence on a divalent analyte focusing in peak mode isotachophoresis (with univalent TE). (a) Experimental validation of the ionic-strength dependence model showing the moles of accumulated sample at an LE-TE interface versus the conductivity of the leading electrolyte. Circles show experimental data [40], while the solid line shows numerical which take into account the effect of ionic strength. The dotted line shows predicted sample accumulation when ionic strength effects are neglected. Inset (b) shows a comparison with the same data but now versus LE concentration. This highlights the discrepancy in simulated sample accumulation predicted with (solid line) and without (dotted line) ionic strength correction. The analyte is 10 nM Alexa Fluor 488 (AF) initially mixed with the TE. LE is histidine-HCl (500 mM stock solution, pH=4.3) and TE is 3-phenylpropionic acid (50 mM stock solution titarted with NaOH to pH=4.9). All of the computational results shown use identical conditions.

We note that the strong effect of ionic strength shown in Figure 3.4 is not expected for univalent sample ions with univalent TE co-ion. Our simulations show that, for a hypothetical univalent ion with a limiting mobility equal to that of AF, the accumulated moles in peak mode ITP follow the dotted curve in Figure 3.4b, irrespective of whether ionic strength effects are taken into account. This is because the effect of decreased mobility of univalent sample at high ionic strength is offset by the decrease in the mobility of univalent TE ions.

3.3.3 Simulation of mobility markers in ITP

Khurana and Santiago [41] proposed a technique for indirect detection of unlabeled non-fluorescent analytes using fluorescent markers in ITP. A set of fluorescent markers is initially mixed with the sample analytes. The markers are chosen to have specific mobilities so that they focus (typically in peak mode) at the interfaces between analytes zones. The unlabeled analytes are then detected as gaps in the fluorescence signal. The technique is effective provided the effective mobilities of the fluorescent markers bracket those of analytes of interest. The technique eliminates the need for labeling (and directly detecting) analyte ions. The choice of correct chemistry and fluorescent markers for a given analyte is crucial.

We here demonstrate the effect of ionic strength on the indirect detection of an analyte using the mobility markers technique. We examine the case of the detection of a single analyte, MOPS, using the fluorescent markers Oregon Green carboxylic acid (OGCA) and fluorescein. The LE and TE used in this example are Tris-HCl and Tris-HEPES respectively. The compositions of LE and TE for each case are given in Section 3.2 above. Each of the four plots in Figure 3.5 show both simulation (foreground curves) and experimental results (background). Figure 3.5a and Figure 3.5b show results for a high ionic strength (250 mM); while Figure 3.5c and Figure 3.5d show results for low ionic strength (10 mM). The experimental data in the two plots of the left column (Figure 3.5a and Figure 3.5c) shows results using the non-focusing tracer (NFT) technique [47]. The NFT used was 100 µM Rhodamine 6G (R6G), which was mixed with LE. R6G is a cation and does not focus. Instead its concentration (which is negligible and does not appreciably contribute to local conductivity) adapts according to local electric field in the various ITP zones. Figure 3.5a and Figure 3.5c also show simulations results which can be compared qualitatively with the NFT measurements. The experimental data in Figure 3.5b and Figure 3.5d (right column) are direct measurements of the fluorescence of analytes in peak mode. Shown with the latter are simulations of the concentration of these analytes.

The experimental data of Figure 3.5a and Figure 3.5c confirm the existence a MOPS zone. At both ionic strengths, the MOPS zone has significant width and is clearly made visible by the NFT as it migrates from LE to TE. The MOPS zone forms a “spacer” ion between the LE and TE, and the fluorescein mobility marker focuses either in front of or behind the MOPS, as dictated by the ionic strength of the LE.

Figure 3.5b shows the experimental and simulation data indicative of the concentration of the two mobility markers for the 250 mM ionic strength, fluorescein and OGCA here focus respectively behind and in front of the MOPS zone. The two mobility marker peaks thus indicate the presence of an analyte (MOPS) between them. Simulated signal peaks for both OGCA and fluorescein agree well with the experimental fluorescence signal, Figure 3.5d shows experimental and simulation results for the 10 mM case. In both cases, OGCA and fluorescein focus ahead of the MOPS zone (and behind the LE) and are so detected as a single peak in the experiment. Fluorescein is a divalent ion and so its mobility has a stronger dependence on ionic strength than the monovalent MOPS zone. Here, therefore, the mobility markers OGCA and Fluorescein focus in the same region and fail to detect the presence (via a gap) and concentration (via the zone width) of the MOPS zone. The simulations do well in predicting this effect and aid a user to design a successful mobility marker experiment.

We note that all of the experiments of Figure 3.5 were performed at a pH of about 8, at which all species are (to good approximation) fully ionized. Thus these results are indeed primarily indicative of mobility reduction due to ionic strength (*e.g.,* as per eq. (3.3)). Also, we note that we suspect the small zone between MOPS and LE in Figure 3.5c was carbonic acid, known to be present at substantial concentrations at the pH of the experiment [106] (despite our use of $Ba(OH)_2$ in the TE). This hypothesis was supported by experiments where we varied the amount of $Ba(OH)_2$ (increasing $Ba(OH)_2$ showed reductions in the reduction in zone width of this zone between MOPS and the LE).

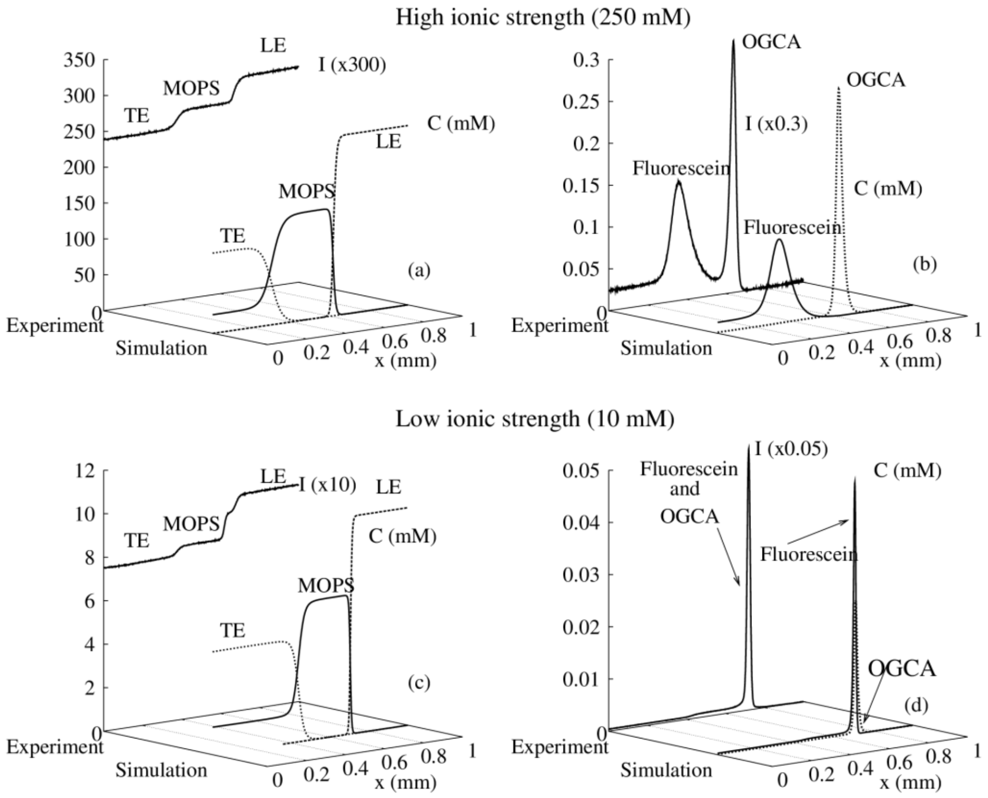

Figure 3.5: Comparison of numerical and experimental results of separation and detection of sample analytes, using NFT and fluorescent mobility markers at high (a-d) and low ionic strength (e-h). In (a) the analyte MOPS forms a plateau zone between the leading electrolyte and trailing terminating electrolyte. Simulated zones compare well with experimental NFT data. (b) shows the calculated concentration and measured intensity of the fluorescent markers fluorescein and OGCA at the two interfaces of the MOPS zone. The two distinct peaks show that fluorescein focuses behind MOPS, as predicted by numerical simulations. In (c), low ionic strength experiments and simulations show that the analyte MOPS also form a plateau zone between the LE and TE. (d) shows measured fluorescence intensity yielding a single peak, in agreement with the simulation. At 10 mM ionic strength the mobility of the divalent fluorescein is substantially higher and so both fluorescein and OGCA markers focus ahead of MOPS. These markers are thus unable to detect the MOPS plateau. For simulations, chemical properties of OGCA were taken to be $\mu_{-1}^{0} = -43\times10^{-9}$ $m^2V^{-1}s^{-1}$ and $pK_{a,-1} = 4.7$.

3.3.4 Selectivity changes in CZE at varying ionic strength

Ionic strength effects can also lead to fundamental changes in CZE electropherogram signals. Changes in peak shape and selectivity resulting from changes in ionic strength in CZE have been observed experimentally by, for example, [114]. Electrophoretic separations at varying ionic strength can also exhibit changes of peak order [115]. Harrold et al. [99] showed experimentally the effect ionic strength on selectivity of inorganic anions in capillary electrophoresis. We here present simulations based on experimental conditions of Harrold et al. [99]. To this end, we present two simulations of the electrophoretic separation of chloride, fluoride, sulfate and phosphate ions using sodium tetraborate buffer at pH 9.2, at 1 mM and 5 mM ionic strengths. The separations leveraged electroosmotic flow (EOF) with a mobility greater than and in direction opposite to the electrophoretic mobility of anions to achieve net migration toward the cathode. We incorporated into our simulations the EOF associated with these experiments (we determined the EOF mobility from a noticeable system peak in their measurements).

Figure 3.6 shows a plot of the experiments of Harrold et al. [99] along with our associated simulations. For this anionic CZE with dominant EOF, ions with highest electrophoretic mobility reach the detector last. At low ionic strength (1 mM), the experiments shows phosphate (HPO_4^{2-}) is barely resolved relative to fluoride (F^-). Also, sulfate (SO_4^{2-}) is not resolved relative to the chloride (Cl^-) ion. $\mathrm{F}^-$and Cl^- reach the detector before HPO_4^{2-} and SO_4^{2-}, respectively. The simulations capture well the shape of electropherogram including the poor resolution between the two ion pairs, and the reported order of elution.

Figure 3.6 (right side) also shows the experiment versus simulation comparisons for (the higher) ionic strength of 5 mM (again at pH = 9.2). At these conditions, the order of F^- and HPO_4^{2-} is reversed, as is the order of the $\mathrm{Cl}^-$and the SO_4^{2-} peaks. Further, the experiment shows that the Cl^- and SO_4^{2-} peaks changed order and are now well resolved. Again, the simulation well captures the electropherogram shape including the peak order reversal and improved resolution.

The electropherogram shape is determined by the relative mobility of these anions. At low ionic strength, the small electrophoretic mobility difference between Cl^- and SO_4^{2-} makes them difficult to resolve. However, the divalent SO_4^{2-} ion has a more strongly shielding ionic atmosphere than the univalent $\mathrm{Cl^-}$ ion, so $\mathrm{SO_4^{2-}}$ experiences greater decrease in mobility with increasing ionic strength. This yields good resolution of these ions at the higher ionic strength. This increased sensitivity of the divalent ion mobility (relative to monovalent) to ionic strength also explains the order reversal in each of the two ion pairs. Overall, our simulations well capture these effects and show very good qualitative agreement with the experimental observations of Harrold et al. [99]. We attribute small discrepancies between the data and simulations to the effects of EOF (which affects both placement and relative width of peaks).

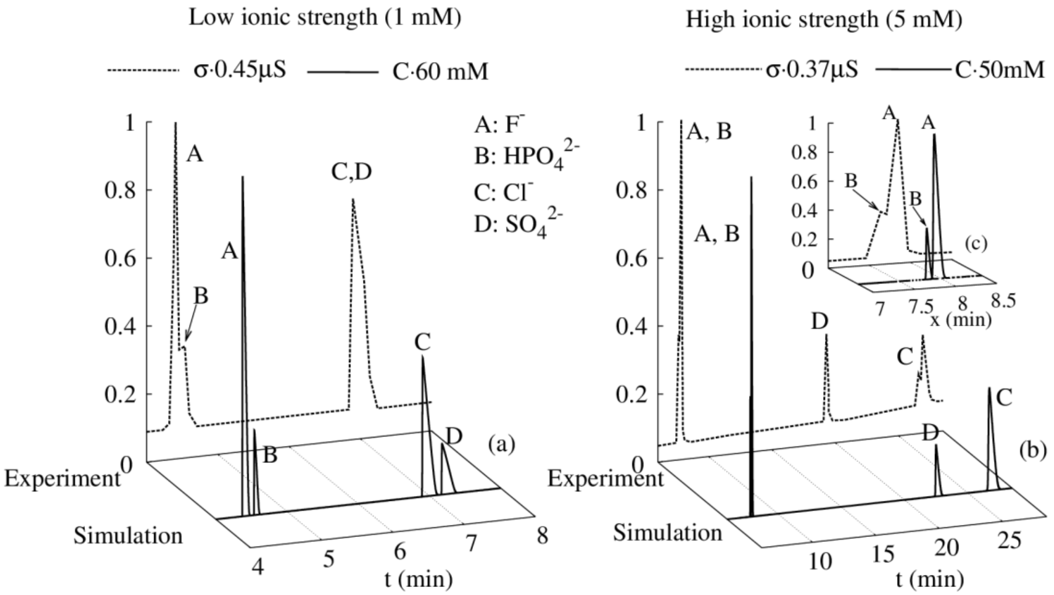

Figure 3.6: Experiments from Harrold et al. [99] and our respective simulations showing the effect of ionic strength dependence on electropherograms (from CZE) of four ions. (a) At 1 mM ionic strength, both experiments and simulations shows $\mathrm{Cl^-}$ is not well resolved from $\mathrm{SO_4^{2-}}$, and $\mathrm{HPO_4^{2-}}$ is not well resolved from $\mathrm{F^-}$. (b) At 5 mM ionic strength, the simulations capture the strong documented effect of ionic strength. Here we see the order of the $\mathrm{Cl^-}$ versus $\mathrm{SO_4^{2-}}$ and $\mathrm{HPO_4^{2-}}$ versus $\mathrm{F^-}$ are reversed. Further, the experiments and simulations show that the $\mathrm{Cl^-}$ is now very well resolved from $\mathrm{SO_4^{2-}}$. Inset (c) shows magnified view of the $\mathrm{F^-/HPO_4^{2-}}$ peak pair. The 1 mM and 5 mM cases were each sodium tetraborate at pH 9.2. For all simulations concentrations of anions were: 27 μM $\mathrm{Cl^-}$, 10 μM $\mathrm{SO_4^{2-}}$, 50 μM $\mathrm{F^-}$ and 10 μM $\mathrm{HPO_4^{2-}}$. In both cases, 60 cm long capillary with 75 μm inner diameter were used. Simulations and experiments used constant voltage of 24 kV.

3.4 Summary

We have developed and experimentally validated electrophoresis (open source) solver which includes the effects of ionic strength on both fully-ionized mobility of and activity coefficients for weak electrolytes. The solver provides fast, accurate solutions for separation and focusing assays including CZE and ITP. The simulations use Onsager Fuoss correction [80] for fully-ionized electrophoretic mobility and extended Debye Huckel theory [81] for correction of ionic activity. We use these models to understand and interpret experimental observations at low and high ionic strengths. Simulations show and experiments confirm reduced sample preconcentration for multivalent ions, in peak mode ITP, at high ionic strengths. This occurs because multivalent ions attract a stronger counter-ion atmosphere, which leads to greater shielding of applied electric field and ion-drag-induced reductions in electrophoretic mobility. Mobility of highly charged ions reduces faster compared to univalent ions, as ionic strength is increased. This can lead to fundamental changes in CZE and ITP peak/zone shape and order. We compared our simulations to experimental measurements to show that, they can predict qualitative changes such as zone order in ITP and CZE experiments.

Our solver uses faster numerical schemes and all cases were simulated with the same conditions as experiments. Such simulations can be employed for practical use in minimizing experimental trials and for determining the optimal choice of assay conditions including ionic strength, pH, and buffer types. Here we demonstrated the use of simulations for designing a successful a mobility marker assay [41] and in demonstrating a reversal in the order of sample peaks in CZE. Simulations which appropriately account for the effects of ionic strength can be important also in designing (*e.g.*, CZE or ITP) experiments using conductivity detection, where signal strength and shape itself is a strong function of ionic strength.

4 High-sensitivity detection using isotachophoresis with variable cross-section geometry

The contents of this chapter were previously published by S.S. Bahga, G.V. Kaigala, M. Bercovici and J.G. Santiago [88] in *Electrophoresis* journal and are reproduced here with minor modifications.

4.1 Introduction

Isotachophoresis (ITP) is widely applied to food analysis, pharmacology, and environmental monitoring [2,36,37] for simultaneous preconcentration and separation of analytes from complex mixtures. Separation of analytes based on their differential electrophoretic mobilities in ITP is possible only during plateau mode focusing, wherein analytes focus and segregate into distinct, contiguous zones with locally uniform (plateau-like) concentrations [116]. This is in contrast to peak mode ITP where analytes focus into peaks of width determined by the diffusive interface between neighboring zones [40]. Therefore, several adjacent analytes in peak mode ITP are practically indistinguishable from each other.

Plateau mode ITP is characterized by locally uniform zone concentrations whose values are governed by the LE buffer characteristics. At the zone boundaries, the analyte ions diffuse into adjacent zones. Assuming negligible advective dispersion [117], the thickness of boundaries is limited by molecular diffusion and decreases at higher electric fields. In ITP separations, plateau mode is often preferred over peak mode as analytes simultaneously preconcentrate and separate distinctly into purified zones. In the case of directly detectable analytes, plateaus can be detected by measuring, for example, electrical conductivity [45] or UV absorption [46]. The displacement physics of plateau mode ITP also enables indirect detection methods including the non-focusing tracer technique [47] and the fluorescent mobility markers technique [41,118]. Typical detected signals in plateau mode ITP are a series of distinct steps in the measured quantity (*e.g.,* as with conductivity [45] or fluorescence intensity [41,118]). The relative step heights in the signal yield information regarding the electrophoretic mobility of the analytes in respective zones [47]. The width of plateau zones is proportional to the amount of focused analyte, and ability to detect trace analytes is limited by the width of plateau zones relative to the width of interfaces. The sensitivity can therefore be expressed as signal-to-noise ratio (SNR) given by the length of the analyte plateau zone normalized by the characteristic length of diffused zone boundaries [41,118]. Directly opposed to common elution techniques like zone electrophoresis [119], therefore, ITP signals yield resolution information from signal values (and their fluctuations), and sensitivity information from measures of the independent parameter (*e.g.*, time or space).

Several methods have been published to improve the sensitivity of plateau mode ITP. These include (i) using long channels, (ii) application of hydrodynamic counter-flow [120], (iii) using a concentration cascade of LE [121] and (iv) cross-sectional area variation [87,122]. Techniques such as using longer channel and hydrodynamic counter-flow allow longer time for samples to accumulate prior to detection, thereby attaining larger analyte zone length. However, long (uniform) channels make low voltage operation difficult and counter-flow ITP requires additional off-chip instrumentation for precise control of adverse pressure gradient. Another way to improve sensitivity is, by using concentration cascade of ITP [121]; wherein a high concentration LE is used initially to obtain a large sample accumulation rate, and is followed by a low concentration LE to force longer analyte zones. We discuss this approach separately in Chapter 5.

An elegant approach to higher sensitivity via variation of the cross-sectional area of the ITP channel was first introduced by Everaerts et al. [122]. We depict the concept in Figure 4.1. Figure 4.1b shows a schematic of a channel with varying cross-section. Sample is focused in a large cross-section channel and subsequently detected in a smaller cross section (high electric field region) channel. Since the mass flux of analyte in ITP is proportional to local cross-section area and system current, large amounts of sample are accumulated in the large cross-section channel. As the analyte zone enters the smaller cross-section channel, the zone elongates to conserve the mass, resulting in improved sensitivity (in comparison to a uniform cross-section channel depicted in Figure 4.1a). This technique is also known as column coupling [122] or volume coupling in ITP [87], and is particularly interesting as standard chemistries can be used without pressure-driven flow control. For example, Dolnik et al. [87] used column coupling and a potential gradient (conductivity) detector to detect 1 μM concentrations of β-alanine, γ-aminobutyric acid and creatinine as model analytes. Also, Bodor et al. [123] demonstrated on-chip integration of this technique and showed conductivity-based detection of 20 μM concentrations of several anions, such as chloride, sulfate, nitrate and phosphate ions. Bodor et al. [123] also demonstrated the use of cross-sectional area variation as a pre-separation step for on-chip coupled ITP-capillary zone electrophoresis (ITP-CZE) (where ITP is disrupted to initiate CZE). However, despite its use in such applications, there has been no systematic theoretical and experimental study of the effects of cross-sectional area variation on sensitivity in ITP.

4.1.1 Current work

Here, we develop a methodology for designing ITP channels with variable cross-sectional area to achieve plateau mode and improve sensitivity to detect trace analytes. We consider constraints on geometry, detection time and applied voltage (or current). Understanding the tradeoffs between various figures of merit and developing appropriate design tools is especially important for on-chip systems with either limited chip area or limited voltage, such as portable isotachophoresis systems [124]. We begin by presenting a new formulation for ITP dynamics which leverages a diffusion-free model for fast calculations and which is particularly useful in plateau mode ITP problems in variable cross-section channels. We present comparisons of the model with more comprehensive numerical predictions. More importantly, we present extensive validation of the model using a series of controlled experiments on a set of microfluidic chips with varying geometries. We then leverage our model to derive a set of algebraic relations for the dependence of zone length and assay time on channel geometry. In particular, the model elucidates the advantage of using variable cross-section geometries, to reduce assay time (compared to the assay time in uniform cross-section channels) for a given SNR. Finally, using a channel with a cross-section are ratio of 16, we demonstrate indirect fluorescence detection with a sensitivity of 100 nM. To the best of our knowledge this is the most sensitive demonstration of indirect detection on chip.

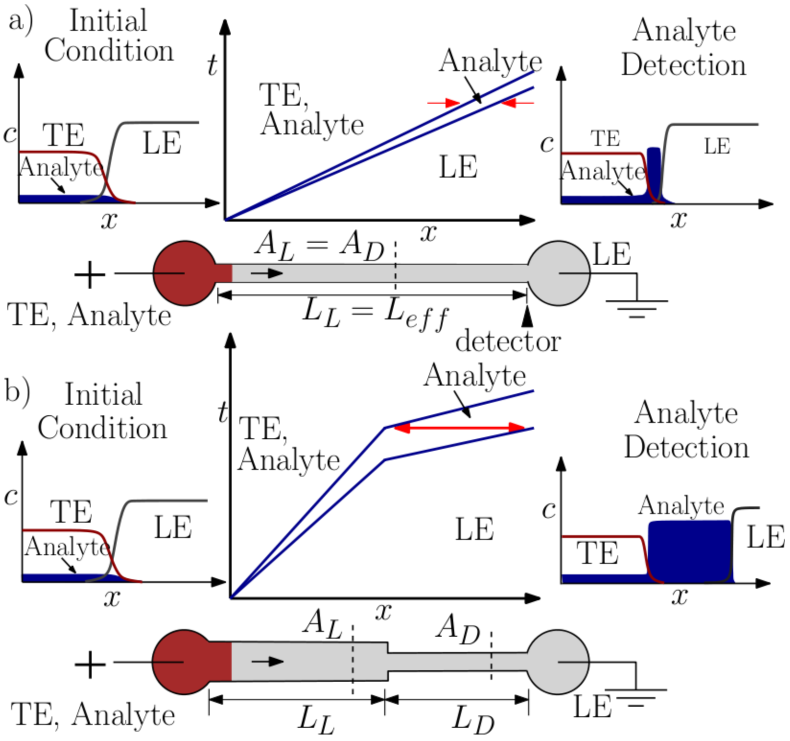
a)
Initial Condition
c
TE
Analyte
LE
x
t
TE, Analyte
Analyte
LE
x
Analyte Detection
c
TE
Analyte
LE
x
$A_L = A_D$
+
TE, Analyte
$L_L = L_{eff}$
LE
detector
b)
Initial Condition
c
TE
Analyte
LE
x
t
TE, Analyte
Analyte
LE
x
Analyte Detection
c
Analyte
TE
LE
x
A_L
A_D
+
TE, Analyte
L_L
L_D
LE

Figure 4.1: Schematic illustrating the effect of varying channel cross-section on sensitivity of isotachophoretic separation and detection. In the channel schematic, the reservoir on the right and the channel are initially filled with LE, and a mixture of TE and analyte is present in the reservoir on the left. Upon application of current, the analyte focuses between the LE and TE zone. (a) For a uniform cross-section channel and constant current, the analyte-to-LE and TE-to-analyte interfaces propagate at constant speeds. The speed of the former is slightly larger than the latter due to the accumulation rate of sample. In the characteristic (space-time) diagram, the propagating interfaces appear as straight lines at different angles to the *x*-axis. (b) shows ITP separation in a channel with variable cross-section areas. The concentration shocks propagate slower in the large cross-section region and faster in the smaller cross-section due to respectively low and high electric fields in these sections. For a finite time, the leading interface of the analyte zone (in the thinner channel) migrates faster than the trailing interface (in the thick section). The varying shock velocities thus result in a rapid expansion of the analyte zone, which proceeds until the trailing electrolyte interface also enters the thinner section.

4.2 Theory

Several models exist with varying degrees of complexity which approximate the physics of isotachophoresis (ITP). Most basic analytical models of ITP are based on describing purified (i.e., a single co-ionic species within each zone) plateau-mode properties at steady state. Under these conditions, and for finite amounts of sample, all interfaces in ITP travel at equal velocities. For fully-ionized species, the statement of conservation of charge and continuity of current describing these problems is Kohlraush's law [42]. Conservation principles based on electroneutrality and current continuity for weak electrolytes are the Jovin and Alberty's relations [43,44]. The Kohlrausch function is applicable for strong, multivalent electrolyte systems, and the Jovin and Alberty functions apply to weak, univalent electrolyte systems. However, none of these simple models describe unsteady dynamics of ITP (*e.g.*, startup, development phase). We also note that latter two functions do not strictly apply to the case where sample analytes are mixed uniformly with the TE (semi-infinite injection), or when hydronium and hydroxide ion concentrations are comparable to electrolyte concentrations. In the latter case where the TE-analyte mixture yields a steady supply of analytes, true steady state is never obtained and sample zones grow slowly in time as ITP progresses and so interfaces move at different velocities. Thus unsteady models are required for such processes.

One approach for unsteady ITP problems is full numerical simulations of quasi 1-D area averaged advection-diffusion transport equations [58] discussed in Chapter 2. As shown in Section 2.4.3, such simulations can accurately predict transient variations in the length and concentration of analyte zones during plateau mode ITP in variable cross-sectional area channels. However, for plateau mode ITP problems where diffusion is primarily limited to narrow zone boundaries, a faster diffusion-free approach may suffice for prediction of concentration and length of various analyte zones. Further, semi-analytical, diffusion-free approaches such as that described here offer physical insights into problems and can point out key parameters and figures of merit.

The assumption of negligible diffusion often holds well for plateau mode ITP, as diffusion effects are often limited to interface regions which are typically small compared to zone lengths. For example, Zhukov [7] developed a detailed unsteady diffusion-free model for ITP. A key limitation to Zhukov's model is the assumption of analytes to be fully ionized or very weakly ionized (negligible degree of ionization). Zusková et al. [125] presented a diffusion-free formulation for modeling unsteady ITP in the presence of a single a common component (admixture) in LE and TE. The latter model applies to both strong and weak electrolytes. However the models by Zhukov [7] and Zusková et al. [125] apply only to channels with uniform cross-sections.

Below we present a model which focuses on unsteady ITP separation dynamics in variable cross-section channels. The model is well suited for unsteady and steady state plateau-mode ITP problems and can handle both an arbitrary number of weak or strong electrolytes and varying-cross sectional area channels.

4.2.1 Diffusion-free model

We start with electromigration-diffusion transport equation,

$$\frac{\partial c_i}{\partial t} = \nabla \cdot \left(\mu_i c_i \nabla \phi + \nabla \left(D_i c_i \right) \right), \quad i = 1, \ldots, N, \tag{4.1}$$

where c_i, μ_i, D_i denote the concentration, effective mobility and molecular diffusivity of species i, and $\nabla \phi$ is the electric field. We here define mobility as a signed quantity $\mu_i = u_i / E$ where μ_i is species drift velocity and E is local electric field. Evaluating eq. (4.1) in one dimension, integrating over the cross-section, neglecting diffusion, and using $\nabla \phi = -J / \left(A(x) \sigma \right)$ we obtain,

$$\frac{\partial c_i}{\partial t} + \frac{J}{A(x)} \frac{\partial}{\partial x} \left(\frac{\mu_i c_i}{\sigma} \right) = 0, \tag{4.2}$$

where σ is the electrical conductivity (defined by eq. (2.7)) and J is current through the separation channel. $A(x)$ is the cross-sectional area of the channel allowed to vary over the axial channel dimension x. Equation (4.2) can be further simplified by transforming the spatial coordinate x to a volume coordinate η,

$$\frac{\partial c_i}{\partial t} + J \frac{\partial}{\partial \eta} \left(\frac{\mu_i c_i}{\sigma} \right) = 0, \quad \eta = \int_0^x A(\xi) \mathrm{d}\xi. \tag{4.3}$$

The above equation is similar to one-dimensional (1-D) transport equation without diffusion, except it is now based on a new (volume) coordinate η, instead of x.

Integrating eq. (4.3) over a small element $(\eta,\eta+d\eta)\times(t,t+dt)$ around a shock we obtain the Hugoniot jump conditions [126] across that shock.

$$\int_t^{t+dt}\int_\eta^{t+d\eta}\left(\frac{\partial c_i}{\partial t}+J\frac{\partial}{\partial\eta}\left(\frac{\mu_i c_i}{\sigma}\right)\right)\mathrm{d}\eta\mathrm{d}t=0,\quad \frac{dx}{dt}(c_i^+-c_i^-)=\frac{J}{A(x)}\left(\frac{\mu_i^+c_i^+}{\sigma^+}-\frac{\mu_i^-c_i^-}{\sigma^-}\right),\qquad(4.4)$$

where $-$ and $+$ denote the evaluation of a property behind and in front of a shock, respectively. Solving for these jump conditions across each shock and for each species, we obtain the concentrations and shock speeds (dx/dt). We present a more detailed formulation of this problem in Appendix E. In a system consisting of simply a leading electrolyte (LE) ions, terminating electrolyte (TE) ions, and analyte and background counter-ion; two propagating shocks form. These correspond to the adjusted-TE-to-analyte interface and the analyte-to-LE interface, as shown in Figure 4.1. The adjusted TE-to-analyte interface propagates at speed, $\mu_{t,T}J/(\sigma_T A)$, while the speed of analyte-to-LE interface is given by $\mu_{l,L}J/(\sigma_L A)$. Here $\mu_{t,T}$ and $\mu_{l,L}$ are the effective mobilities [108] of TE ions in the adjusted TE zone and LE ions in the LE zone, respectively, while σ_T and σ_L denote the conductivity of adjusted TE and LE zones. (In our notation, the first small-case subscript identifies the ion, and the second capitalized subscript identifies the zone of interest.)

Let $x(t),\ y(t),\ z(t)$ denote the coordinates of the analyte-to-LE, adjusted TE-to-analyte, and the TE well-adjusted TE interfaces, respectively. We can account for possible electroosmotic flow (EOF) in the channel by subtracting the local bulk velocity of $\bar{Q}_{EOF}/A(x)$ to the velocity of the interfaces in the channel. Thus, the time evolution of these interfaces can be written in form of a set of ordinary differential equations,

$$\begin{aligned}\text{analyte-to-LE: }&\frac{dx}{dt}=\frac{\mu_{l,L}J}{\sigma_L A(x)}+\frac{\bar{Q}_{EOF}}{A(x)},\quad x(0)=0,\\ \text{adjusted TE-to-analyte: }&\frac{dy}{dt}=\frac{\mu_{t,T}J}{\sigma_T A(y)}+\frac{\bar{Q}_{EOF}}{A(y)},\quad y(0)=0,\qquad(4.5)\\ \text{TE well-to-adjusted TE: }&\frac{dz}{dt}=\frac{\bar{Q}_{EOF}}{A(z)},\quad z(0)=0,\end{aligned}$$

where $\bar{Q}_{EOF}$ is the mean flow rate due to the product of electric field and EOF mobility averaged over the length of the channel. See Ghosal [127], and Bhardwaj and Santiago [128] for similar treatments of electroosmotic flow in area-averaged channels. Each zone has an associated local electric field which couples with local EOF mobility to contribute to overall bulk flow. Also, for a constant applied voltage across the channel, the current, J depends on location of all interfaces, as the channel resistance changes with time.

The zone length, Δ_P, of focused analyte is given by the difference between positions of analyte-to-LE interface and the adjusted TE-to-analyte interface, $\Delta_P(t) = x(t) - y(t)$. Solution to eq. (4.5) is obtained by numerical integration. Figure 4.2 shows a comparison of our model with a full 1-D simulation using SPRESSO [63,69] for the case of buffering (weak electrolyte) counter-ion, a strong electrolyte LE, a weak acid analyte, and a weak acid TE (see figure caption for details). The comparison with the full SPRESSO simulation (which includes diffusion) shows excellent agreement in zone concentrations and zone length. As shown in the figure, the effects of diffusion are limited to zone boundaries in this plateau mode ITP problem. We emphasize that even the final time solution shown cannot be obtained using steady state models (*e.g.*, similar to that of Everaerts et al. [35]) as such models apply conservation laws assuming that all shocks are propagating at equal speeds. We also note that, even in the case where diffusion length scales are significant relative to (or larger than theoretical) zone lengths, the current diffusion-free model will yield the correct amount of sample accumulated in each analyte zone. For example, if the sample is physically accumulated in peak mode, the current model will yield a short theoretical plateau zone which contains the correct amount of accumulated analyte.

4.2.2 Analytical relations and scaling arguments

We use the model presented in Section 4.2.1 to derive analytical relations for the dependence of plateau zone length and detection time on channel geometry and buffer chemistry. Consider the separation channel in Figure 4.1b, consisting of a large cross-section region with area A_L, followed by a smaller cross-section region with area A_D. In ITP with semi-infinite injection, the analyte primarily accumulates in the large cross-section channel, which we refer to as the "loading section". This accumulation is often in peak mode. The analyte zone then reaches the small cross-section channel and expands axially along the channel, resulting in a newly created plateau or plateau with larger zone length. To achieve higher sensitivity, the analyte is detected in this smaller cross-section channel, which we will refer to as the "detection section." The zone length, Δ_P, is obtained by solving eq. (4.5). Assuming negligible EOF, eq. (4.5) can be written as,

$$\frac{dy}{dx} = \frac{\mu_{t,T}\sigma_L}{\mu_{l,L}\sigma_T}\frac{A(x)}{A(y)}, \tag{4.6}$$

which describes the relative motion of the trailing interface to the leading interface. For a varying cross-section channel with large cross-section followed by small cross-section region (each section with uniform area) as in Figure 4.1b, eq. (4.6) can be solved to obtain,

$$\begin{aligned} \int_0^{L_L} A(y)\mathrm{d}y &= \frac{\mu_{t,T}\sigma_L}{\mu_{l,L}\sigma_T}\int_0^{L_L+\Delta_P} A(x)\mathrm{d}x, \\ A_L L_L &= \frac{\mu_{t,T}\sigma_L}{\mu_{l,L}\sigma_T}(A_L L_L + A_D\Delta_P). \end{aligned} \tag{4.7}$$

Rearranging this expression, we obtain an expression for zone length, Δ_P, in terms of channel geometry and electrolyte chemistry,

$$\Delta_P = \left(\frac{\mu_{l,L}}{\sigma_L} - \frac{\mu_{t,T}}{\sigma_T}\right)\left(\frac{A_L L_L}{A_D}\right)\frac{\sigma_T}{\mu_{t,T}}. \tag{4.8}$$

Next, we apply the jump conditions (eq. (4.4)) across the TE-to-analyte interface and define $V_{ITP} = \mu_{a,A}J/\sigma_A = \mu_{l,L}J/\sigma_L$, where V_{ITP} is the velocity of the LE-to-analyte interface. Thus, the parenthetic mobility term on the right-hand-side of eq. (4.8) can be written explicitly in terms of analyte concentrations as

$$\left(\frac{\mu_{l,L}}{\sigma_L} - \frac{\mu_{t,T}}{\sigma_T}\right) = \left(\mu_{a,T} - \mu_{t,T}\right)\frac{c_{a,T}}{\sigma_T c_{a,A}}. \tag{4.9}$$

The concentration of analyte in the adjusted TE zone, $c_{a,T}$, can then be related to its concentration in the well using the jump conditions across the stationary interface of TE well and adjusted TE,

$$\frac{\mu_a^0}{\sigma^0} c_a^0 = \frac{\mu_{a,T}}{\sigma_T} c_{a,T}. \tag{4.10}$$

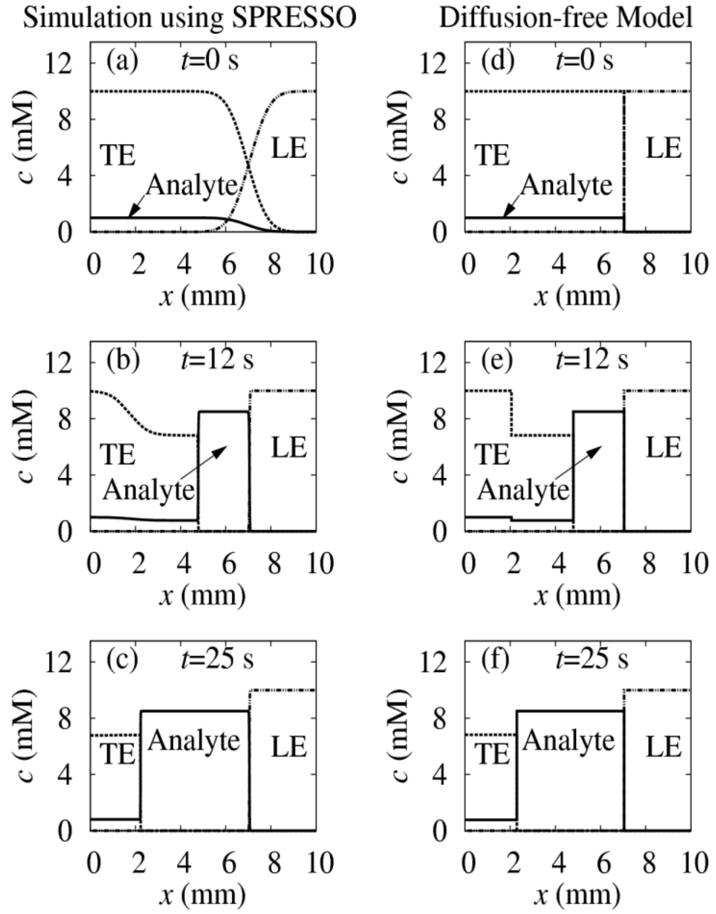

Figure 4.2: Comparison of our diffusion free model (d-f) with a full numerical simulation (a-c), for the case of plateau mode ITP with semi-infinite injection of analyte (i.e., analyte mixed homogenously with TE). Simulations for detailed electromigration-diffusion model were performed using our open source code SPRESSO. The numerical calculations were performed in a frame of reference moving with the LE-analyte interface. The diffusion free model predicts plateau zone lengths correctly as diffusion effects are limited to zone boundaries. LE is 10 mM HCl and 20 mM bistris; TE is 10 mM Tricine and 20 mM bistris; and the model analyte is 1 mM acetic acid. Calculations were performed for a constant current of 1 µA, applied through a circular channel with uniform cross section of diameter 50 µm.

where the superscript describes a property evaluated at the well. Combining expressions (4.8)(4.9), and (4.10) we obtain an explicit dependence of zone length on the concentration of the analyte in the TE well and on channel geometry,

$$\varDelta_P = \left(1 - \frac{\mu_{t,T}}{\mu_{a,T}}\right) \frac{\mu_a^0}{\mu_{t,T}} \frac{\sigma_T}{\sigma^0} \left(\frac{A_L L_L}{A_D}\right) \frac{c_a^0}{c_{a,A}}. \tag{4.11}$$

This shows that the plateau zone length of an analyte, $\varDelta_P$, is proportional to both the concentration of the analyte in the well, c_a^0, and to the geometric parameter $A_L L_L / A_D$. This geometric parameter is equivalent to the total length of a uniform cross-section channel (irrespective of cross-sectional area or applied current) which would have been required to obtain the same zone length. We therefore refer to $A_L L_L / A_D$ as the "effective length" of the variable-area channel, and denote it by L_{eff}. For a given chemistry, the zone length, $\varDelta_P$, therefore scales as,

$$\varDelta_P \propto L_{eff} c_a^0, \quad L_{eff} = \frac{A_L L_L}{A_D}. \tag{4.12}$$

Resource limits on applied voltage and/or applied current influence the dynamics since they directly affect the detection time. For example, the miniaturized ITP device of [118] had a voltage limited to 200 V (currently, this device has a limit of 350 V). To derive an appropriate scaling for the detection time in such systems, we here neglect EOF, and solve for the location of the front interface with eq. (4.5),

$$\frac{dt}{dx} = \frac{\sigma_L A(x)}{\mu_{l,L}} \frac{\varDelta V}{R(x)}. \tag{4.13}$$

Here R denotes the electrical resistance of the channel. The resistance of the channel increases during ITP, as high conductivity LE is replaced by a lower conductivity TE. Since the analyte zone is typically much smaller than the overall channel length, we here neglect its contribution to the channel resistance. With this assumption we show in Appendix F that the detection time, T, can be approximated as

$$T \approx \frac{L_L L_D}{\mu_{l,L} \Delta V}\left(\frac{A_L}{A_D}+\frac{1}{2}\left(1+\frac{\sigma_L}{\sigma_T}\right)\frac{L_L}{L_D}\right). \qquad (4.14)$$

The two analytical expressions (4.12) and (4.14) enable simple evaluation of the advantages of using variable cross-section channels over uniform cross-section channels. For example, if we take $A_L / A_D = 10,\ L_L = L_D = L,\ \sigma_L / \sigma_T = 10,$ then from eq. (4.12) the effective length is $L_{eff} = 10L$. This means that in order to obtain same zone length, a uniform cross-section channel would require a 10 fold longer channel. Furthermore, using eq. (4.14), one can show that the detection time using the variable cross-section geometry is 35-fold shorter than that of an longer channel with uniform cross-section and actual length equal to L_{eff} $(L_L = L_{eff},\ L_D = 0).$ This example shows that variable cross-section channels not only results in higher sensitivity compared to fixed cross-section channels, but also in significantly shorter detection times for fixed plateau widths.

Theoretical plateau widths are directly relevant to sensitivity of the assay. For example, a good working definition for the sensitivity limit is when the theoretical plateau width is significantly larger (say twice or more) than the interface width caused by diffusion and advective dispersion (see Khurana and Santiago [40] for further discussion). Plateau zone lengths are independent of applied voltage or current (see eq. (4.11)). However, in absence of advective dispersion [39], interface thickness is inversely proportional to the electric field in the channel [60]. Thus the interface thickness (and SNR) show different dependence on channel geometry for constant voltage and constant current operation.

The trade-offs of assay time, SNR, channel area ratio, applied voltage, and applied current are discussed in detail in Appendix F, and summarized here. For fixed voltage operation, increasing cross-section ratio results in larger zone length, higher electric field and sharper interfaces. Therefore, SNR improves significantly by increasing the cross-section ratio. Whereas, increasing length of the loading section increases the zone length but leads to lower electric field and thicker interfaces. Thus, SNR does not improve significantly by increasing the length of loading section. For a fixed voltage and channel length, SNR can be increased by increasing the cross-sectional area ratio, but at the expense of longer assay time.

In contrast, for fixed current operation, electric field and interface thickness in the detection section do not depend on the dimensions of the loading section. Therefore, significant improvements in SNR can be obtained by increasing both cross-section ratio and loading length, which give larger zones and sharper zone boundaries. For both fixed current and channel length, SNR can be increased by decreasing the area of detection section (A_D), without increasing the assay time.

4.3 Materials and methods

We performed a series of experiments with varying channel geometries and analyte concentrations to validate our model. We performed cationic ITP experiments to avoid interference of bicarbonate ions (from reaction of dissolved carbon dioxide with water) which can focus and create spurious analyte zones [106,110]. For these cationic ITP validation experiments, the LE ion was the sodium ion from 10 mM NaOH, TE ion was 10 mM pyridine, and 20 mM HEPES was used as the counter-ion. To study the effect of analyte concentration we varied the model analyte (bistris) concentration from 1 to 4 µM. We also prepared 1 mM stock solution of the Alexa Fluor 488 dye (Invitrogen, Carlsbad, CA), and used it to visualize the plateau zones of cationic ITP as a non-focusing tracer ion [47] by mixing at a concentration of 70 µM in the LE. For the experiments demonstrating 100 nM sensitivity, we used the same buffer ions but reduced TE concentration to 3 mM pyridine with 6 mM HEPES to increase electric field and focusing rate.

For the experiments demonstrating the principle of the variable cross-section technique (see Figure 4.3) we used 50 mM NaOH and 100 mM HEPES as LE buffer; 10 mM pyridine and 20 mM HEPES as TE buffer. We used 10 µM bistris as the model focusing analyte, initially mixed with TE.

For all experiments presented in this paper, we added respectively 1% and 0.5% polyvinylpyrrolidone (PVP) to LE and the TE to suppress EOF. All chemicals were obtained from Sigma Aldrich (St. Louis, MO) and diluted from 1 M stock solutions. All solutions were prepared in UltraPure DNase/RNase free distilled water (GIBCO Invitrogen, Carlsbad, CA). We captured images using an inverted epifluorescent microscope (IX70, Olympus, Hauppauge, NY) equipped with a LED lamp (LEDC1, Thor

Labs, Newton, NJ), U-MWIBA filter-cube from Olympus (460-490 nm excitation, 515 nm emission, and 505 nm cut off dichroic) and a 10X (NA = 0.4) UPlanApo objective (Olympus, Hauppauge, NY). Images were captured using a 12 bit, 1300x1030 pixel array CCD camera (Micromax1300, Princeton Instruments, Trenton NJ). We controlled the camera using Winview32 (Princeton Instruments, Trenton NJ) and processed the images with MATLAB (R2007b, Mathworks, Natick, MA). We conducted the experiments by applying constant voltage across the microchannels using a sourcemeter (model 2410, Keithley Instruments, Cleveland, OH).

All experiments were performed on custom-made, wet-etched, borosilicate glass microfluidic chips fabricated using standard lithographic processes. Figure 4.3a shows a schematic of the microfluidic chips, consisting of a single channel with end-channel reservoirs (2 mm holes diamond drilled into cover glass of chip). The channels consisted of sections with relatively large (1400 to 2230 μm^2) cross-sectional areas followed by section with a 90 to 1400 μm^2 cross-section. The geometric parameters of all channels used in this study are listed in Table 4.1.

Table 4.1: Geometric parameters of the five microchannel geometries used in this study. The effective length is defined as $L_{eff} = A_L L_L / A_D$.

Chip No.	Thicker Loading Section		Thinner Detection Section		Effective Length L_{eff} (mm)
	Area A_L (μm^2)	Length L_L (mm)	Area A_D (μm^2)	Length L_D (mm)	
1	1400	10	1400	7.5	10
2	2000	5	90	7.5	111
3	1500	10	90	7.5	167
4	2230	10	90	7.5	241
5	1450	22	90	8.0	354

All experiments used a semi-infinite injection scheme wherein the analyte was initially mixed with TE. We visualize ITP zones by indirect fluorescence detection using a non-focusing tracer (NFT) technique [47] (see Section 4.4). Figure 4.3b shows the ITP assay protocol for our ITP experiments. We filled the East well of the chip with a mixture of LE and NFT and applied vacuum to the West well until the channel was filled. We then rinsed the West well several times with deionized water and filled it with the mixture of TE and analyte. The electrodes were placed in the East and West wells and constant voltage was applied. We centered the field of view of the microscope at a fixed distance of 1 mm to the right of the junction of the large and small area channel sections, and set the camera to obtain images continuously until manually stopped after capturing images of ITP zones.

4.4 Experiments

We performed experiments to validate the diffusion-free, variable area ITP dynamics model and study the effects of area-variation on analyte detection sensitivity via ITP.

4.4.1 Parametric variations and zone visualizations

To validate the model presented in Section 4.2.1, we conducted a detailed parametric study in which we varied analyte concentrations in the range 1-4 µM, and varied chip geometries to vary effective lengths from 10 to 241 mm (see Table 4.1). We implemented NFT using an anionic fluorescent species mixed with LE. In cationic ITP, fluorescent anions do not focus, but their concentration adjusts to the local electric fields in different zones. Using mass flux balance across the analyte-to-LE interface, Chambers and Santiago [47] showed that the concentration of non-focusing tracer in analyte zone is given by,

$$\frac{c_{NFT,A}}{c_{NFT,L}} = \frac{\mu_{a,A}}{\mu_{l,L}}\left(\frac{\mu_{NFT,L}-\mu_{l,L}}{\mu_{NFT,A}-\mu_{a,A}}\right), \tag{4.15}$$

where μ_{NFT} denotes the effective mobility of (here, anionic) NFT. The step change in concentration of NFT is observed as a step change in fluorescence signal. Figure 4.3c shows NFT visualization of analyte zone along a variable cross-section channel. The inverted intensity images (high intensity implies high NFT concentration and low local electric field) in Figure 4.3c show the analyte zone slowly increasing in length in the loading (larger cross-section) section. As the analyte zone enters the detection section, it spreads out, the zone length increases and the zone boundaries sharpen due to higher local electric field.

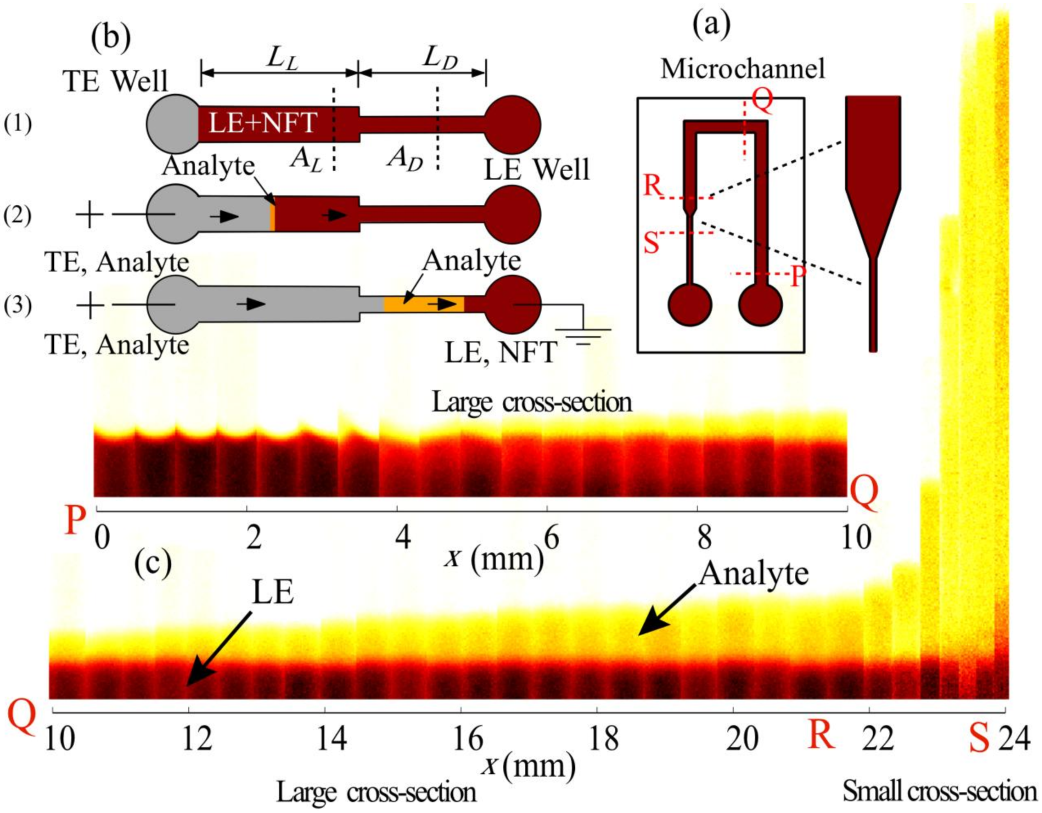

Figure 4.3: ITP injection protocol and variation of analyte zone length along the separation channel. (a) Glass microchips consisted of a large cross-sectional area loading section (sections P, Q, and R) of length L_L and then a smaller cross section detection section (detector at S) of length L_D (see Table 4.1). (b) Channel schematic showing ITP with semi-infinite analyte injection: (1) We filled the LE well with a mixture of LE and NFT and applied vacuum on TE well. We then emptied the TE well, rinsed, and filled it with a mixture of analyte and TE, and (2) applied potential between the TE and LE reservoirs. The NFT concentration adjusted to the local electric field and we imaged the steps in fluorescent intensity. (3) the analyte zone expanded in the small cross-section. (c) shows 49 raw inverted-fluorescent intensity images of the analyte zone as a function of axial position along the channel, x. The analyte zone length grows slowly while in the large cross-section region, and then rapidly elongates as it enters the small cross-section region ($x > 22$ mm). For the images, we used a constant applied potential of 700 V on a chip with large and small cross sections of 1450 and 90 μm^2, respectively. We here subtracted the mean value of intensity in TE zone for clarity of presentation.

4.4.2 Effect of initial analyte concentration on zone length

We performed experiments to validate the dependence of zone length on initial concentration as given by eq. (4.12). For this effect, we varied analyte concentration while keeping the channel geometry fixed. We used Channel 4 (see Table 4.1) and varied the concentration of the analyte from 1 to 4 µM. Figure 4.4 shows the variation of measured and theoretical zone lengths, as a function of the concentration of the analyte in the well. We observed a proportional increase in zone length with analyte concentration. This is expected as the flux of analyte into the analyte zone is proportional to the concentration of analyte in the TE well (i.e., the concentration in the unadjusted TE).

Although we suppressed EOF using PVP, we observed residual EOF in our experiments. We accounted for EOF as follows. As ITP progresses, the lower conductivity analyte and TE mixture replaces higher conductivity LE in the channel, resulting in increased resistance and lower overall current. We observed only gradual decrease in current with time while the TE was in the loading section, as expected. When the TE zone entered the detection section, resistance increased rapidly and we observed a sudden drop in current. We accounted for EOF by tuning a (uniform) EOF mobility in our model so as to match the observed time at which the TE enters the detection section. This yielded an estimate EOF mobility of $2\times10^{-9}\ \mathrm{m^2V^{-1}s^{-1}}$. The model uses this simple empirical estimate of residual EOF to estimate zone length as a function of position as shown in Figure 4.4a.

Figure 4.4a shows measurements of zone length as a function of analyte concentration for Chip 4 of Table 4.1, as well as corresponding image data (flat-field corrected, raw images) for these experiments. As shown, the model agrees very well with measurements of analyte zone length versus initial analyte concentrations.

4.4.3 Effect of channel geometry on zone length

We also experimentally established the effect of channel geometry on zone length. We performed ITP experiments on four chip geometries with effective lengths, L_{eff}, ranging from 10 to 241 mm, and using an identical analyte concentration of 2 µM and applied voltage of 350 V. As shown in Table 4.1, the changes in effective length were obtained by changing both the cross-sectional area ratios and the lengths of the loading zone. Figure 4.4c shows the dependence of measured zone length on effective length of the channel. The experiments show the zone length to be directly proportional to the effective length, as predicted by our theoretical model.

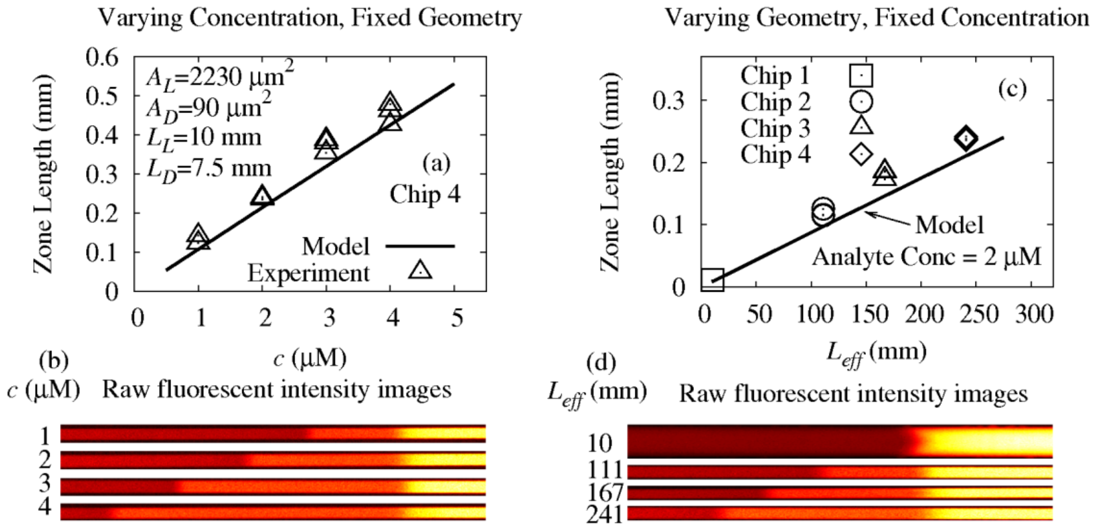

Figure 4.4: Effect of analyte concentration and channel geometry on zone length. (a) shows the variation of measured and theoretical zone length as a function of analyte concentration in the chip TE well and for a fixed chip geometry (Chip #4 of Table 4.1). Theoretical predictions are in good agreement with experimental observations. (b) shows corresponding example images for four concentrations. (c) shows measured and predicted values of analyte zone length for as a function of effective channel lengths, $L_{eff} = A_L L_L / A_D$, (representing four channel geometries) and a fixed analyte concentration of 2 μM. (d) shows the corresponding experimental images. The top image in (d) shows the case for the uniform area channel, $L_L = L_{eff} = 10$ mm, where no analyte plateau was observed as analyte is in peak mode. However, the images below that show that the same analyte concentration and applied voltage yields significant increase in sensitivity (plateau zone length) for increased effective lengths associated with the area ratios of Chips 1-4 of Table 4.1. All data here are for 350 V applied voltage, and the NFT is 70 μM Alexa Fluor 488. EOF mobility is 2x10^{-9} m^{2}V^{-1}s^{-1}.

We note that for a uniform cross-section channel with $L_{eff} = L_L = 10$ mm (top image in Figure 4.4d) we do not observe a plateau, as the analyte is in peak mode. However, the same concentration of analyte and same applied voltage of 350 V yield increasing analyte plateau lengths for chip geometries with longer effective lengths. This illustrates the efficacy of variable cross-section geometries in increasing detection sensitivity of ITP. We also emphasize this improvement in sensitivity using variable cross-section geometry compared to uniform cross-section geometry does involve longer detection time. However, as noted in Section 4.2.2, for the same sensitivity, the detection time using variable cross-section geometry is shorter than the detection time in a uniform cross-section channel.

In Figure 4.5 we plot all of the experimental results shown in Figure 4.4a and Figure 4.4c in a single plot of dimensional zone thickness versus the product $L_{eff} c_a^0$. L_{eff} is the effective length across all chip geometries of the data (Chips 1-4 of Table 4.1). c_a^0 is the analyte concentration in TE well set by the initial condition (i.e., the analyte level established by a particular application). As predicted by the theory, the analyte plateau

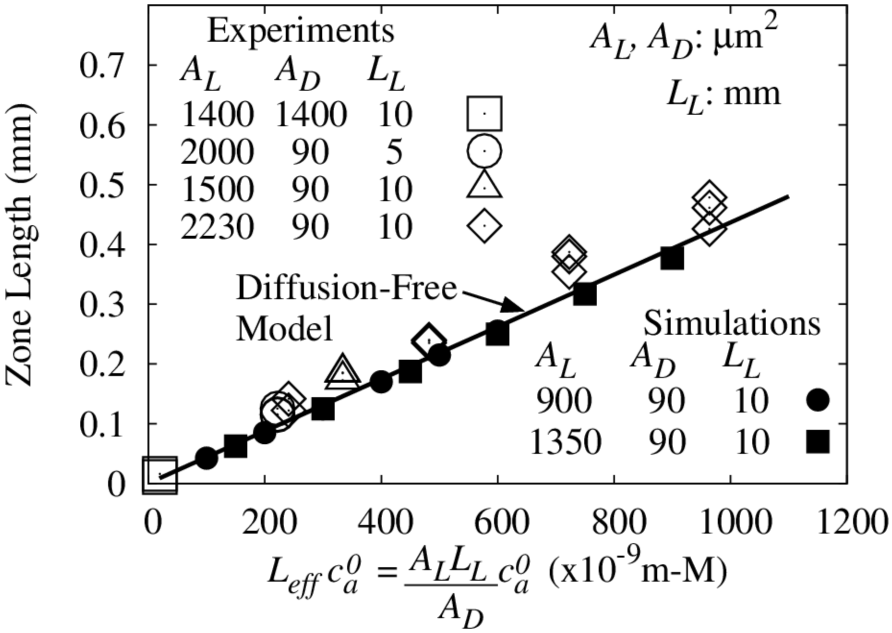

Figure 4.5: Comparison of experimentally observed analyte zone length in ITP in variable cross-section channels with predictions using a diffusion-free model and the current quasi 1-D model. Open data points and solid line, respectively, show experimental data and results from the diffusion-free model; solid data points show zone length predictions using the quasi 1-D simulations using SPRESSO [58]. The plot shows analyte zone length plotted against the theoretical scaling of $L_{eff} c_a^0$ (equal to $A_L L_L c_a^0 / A_D$). The analyte is focused in plateau mode after the convergence in the channel, so the predictions using diffusion-free model are in fairly good agreement with the quasi 1-D model. Further, analyte zone lengths computed using the quasi 1-D model agree very well with experimentally observed linear variation of analyte zone length with $L_{eff} c_a^0$. The experimental conditions are similar to those for experiments presented in Figure 4.4. To account for EOF in the semi-analytical model and quasi 1-D simulations we used experimentally an estimated EOF mobility of 2×10^{-9} m^{2}V^{-1}s^{-1}.

length is directly proportional $L_{eff} c_a^0$ and all experimental data points collapse on a single line. Figure 4.5 also shows analyte zone thickness predicted by the quasi 1-D simulations, discussed in Chapter 2. The quasi 1-D simulations were performed for two different channel geometries with $L_{eff} = 100$ and 150 mm, each with six different initial analyte concentrations (c_a^0) ranging from 1 to 6 µM. Analyte zone lengths obtained from the quasi 1-D simulations show good agreement with experimental data and the zone length predictions of the diffusion-free model.

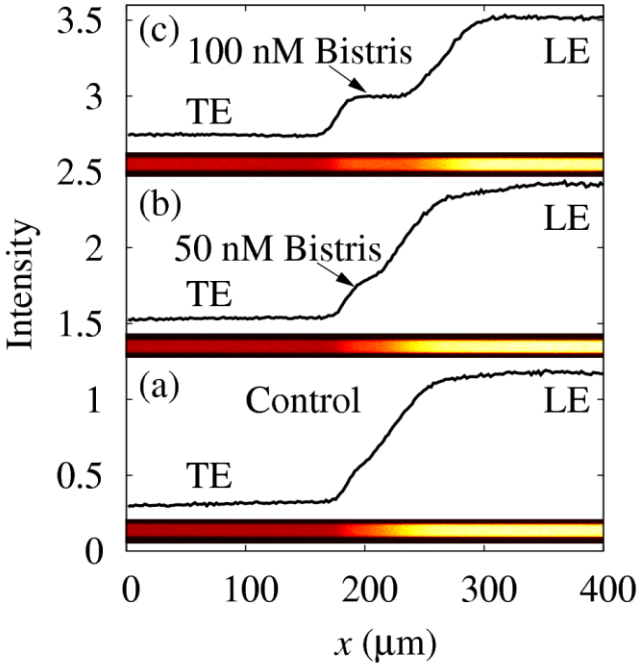

Figure 4.6: Indirect fluorescence detection of 100 nM bistris using non-focusing tracer technique with variable area geometry channel. (a) shows a single step in fluorescent intensity, corresponding to the LE and TE zones. (c) shows a distinct step in NFT signal when 100 nM bistris is mixed with TE. This step corresponds to bistris focused in plateau mode. (b) shows detection of 50 nM bistris, initially mixed with TE. For 50 nM concentration, bistris zone is not distinct enough in comparison with the control signal. This lower SNR at 50 nM bistris is due to diffusion length scale comparable to the analyte zone thickness. The non-focusing tracer is 70 µM Alexa Fluor 488, mixed initially with LE. For these experiments we used a constant potential of 350 V on a chip with effective length of 354 mm, and large and small cross-sections of 1450 and 90 µm^2, respectively.

4.4.4 Demonstration of high sensitivity ITP indirect detection

Lastly, we used a variable cross-section geometry to demonstrate improvement on the sensitivity of an ITP detection with fixed physical length and constant applied voltage. We note that increasing analyte theoretical plateau length, and therefore sensitivity, using variable cross-section channels is independent of the detection technique, direct or indirect. For these experiments we used Chip 5 of Table 4.1 with effective length of 354 mm but an actual length channel of 30 mm. We were successfully able to detect 100 nM bistris in 5 min using the NFT technique. Figure 4.6 shows the fluorescent intensity signals corresponding to the control experiment (without analyte), and for 100 and 50 nM bistris concentrations (for our purposes we here use bistris model analyte with well known properties for these controlled experiments). At 100 nM concentration, the bistris zone is sufficiently resolved. At 50 nM concentration, the bistris zone plateau length is approximately equal to the length scale of the adjusted TE-to-LE interface, rendering it practically indistinguishable from the control signal.

4.5 Summary

We have developed a methodology for designing channels with variable cross-sectional area to maximize sensitivity while reducing or minimizing assay time. Our analysis is based on a diffusion-free model of unsteady dynamics of ITP in channels with axially varying cross-section. The model incorporates multi-species electromigration physics. We benchmarked our model with numerical simulations based on an experimentally-validated, detailed model of ITP. To verify accuracy in predicting zone lengths, we performed a series of experiments on channels with variable cross-section. Our model predicts and experiments confirm that ITP in initially large and then small cross-sectional area channels leads to higher sensitivity than equal total length channels with uniform cross section. The large channel cross-section (area A_L, where L is for loading) focuses large amounts of sample, and then analyte zones elongate and zone boundaries sharpen in the small cross-section, detection section region (area A_D) where electric field is high. For a given buffer chemistry, zone length in the small cross-section channel is directly proportional to initial analyte concentration and an effective length

L_{eff} of the channel equal to $L_{eff} = A_L L_L / A_D$, where L_L is the length of the loading section.

We used the diffusion-free model to derive analytical relations for the dependence of zone length and assay time on channel geometry. Based on these relations, we showed that short channels with variable cross-section geometry yield sensitivity comparable to that achieved in much longer channels with uniform cross-section. For fixed voltage and SNR of plateaus, variable cross-section channels reduce both overall channel length and assay time compared to uniform cross-section channels. Further, for fixed voltage and channel length, larger cross-section ratio channels yield better SNR, but at the expense of longer assay time. In contrast, for fixed current operation, SNR can be increased by reducing cross-section of detection section and without increasing the assay time. We presented detailed comparisons of the galvanostatic versus potentiostatic cases in Appendix F.

Variation of ITP channel cross-sectional area represents a method of increasing sensitivity in a wide variety of ITP assays, and the approach is relatively independent of the detection method (*e.g.*, applicable to both direct and indirect analyte detection strategies). Our model can be applied for practical use in designing optimal channels, with constraints on SNR, geometry, voltage and detection time. This is particularly important in the context of portable, on-chip systems, with limited voltage supply and chip area. To demonstrate this, we here presented on-chip, indirect fluorescence detection with 100 nM sensitivity using a variable cross-section geometry. The latter is to our knowledge the highest ever reported sensitivity for ITP in indirect detection mode.

5 Concentration cascade of leading electrolyte using bidirectional isotachophoresis

The contents of this chapter were previously published by S.S. Bahga and J.G. Santiago [129] in *Electrophoresis* journal and are reproduced here with minor modifications.

5.1 Introduction

In Chapter 4 we demonstrated the use to plateau mode ITP for indirect detection of analytes by simultaneous preconcentration and separation of analytes into distinct plateau-like zones with locally uniform concentrations. Plateau mode ITP is characterized by relatively long zones with locally uniform concentrations separated by thinner zone boundaries [40,41]. For trace quantities, analyte species may not develop into such plateaus. Instead, multiple trace analyte species bounded by TE and LE focus into nearly completely overlapping peaks whose widths are governed by the diffuse TE-to-LE interface. This regime, termed peak mode ITP [39,40], is not preferable for indirect detection of analytes as adjacent analyte zones are practically indistinguishable from each other. Of course, a system with multiple analytes with a wide range of concentrations can form a “mixed mode” ITP condition. In mixed mode, depending upon their amounts, some analytes form peaks while others form plateaus (see, for example, Figure 1c of Bercovici et al. [118]).

Plateau mode ITP allows separation and detection of multiple analytes. Typical isotachopherograms obtained in plateau mode ITP, with direct [45,46] or indirect detection methods [47], consist of steps in the measured quantity (*e.g.*, conductivity or fluorescence) corresponding to different ITP zones. The width of these steps is proportional to the amount of focused analytes, and the ability to detect trace amount of analytes is limited by the step width relative to the thickness of diffused boundaries. The sensitivity of plateau mode ITP detection is improved by increasing plateau zone width relative to the diffusive length of interfaces. As described by Garcia-Schwarz et al. [114], interface widths scale inversely with electric field and can be affected by advective dispersion and the mobility difference between co-ions in neighboring ITP zones.

In Section 4.1 we reviewed several methods which can be used to increase the zone lengths in plateau mode ITP, including use of longer separation channels, the application of hydrodynamic counter-flow [120], varying channel cross-sectional area [87,88,122], and using concentration cascade of the LE in the so-called "cascade ITP" technique [121]. All these techniques favor a longer sample accumulation time prior to the detection, and thereby increase plateau zone lengths. Longer analysis time also increases the separation capacity [122] of the system as analytes in the initial mixture have longer time to separate into purified zones [34,121]. All or some of these techniques can be coupled to increase detection sensitivity, largely without affecting their individual performance. Therefore, these techniques can be studied and optimized independently before their integration.

In ITP, the concentrations of plateau zones scale proportionally to the concentration of the LE ions. Analytes can be said to "adjust" to a concentration established by that of the LE and an order unity (typically < 1.0) multiplier associated with the system's ion mobilities [42,44]. Cascade ITP [34] leverages this feature by focusing analytes sequentially using two LE zones. Analytes are first focused using a high concentration LE which increases sample loading and separation capacity; subsequently, analytes are detected using a low concentration LE. Analyte zones migrate from regions formerly occupied by the first LE into regions formerly occupied by the second LE and, as they do so, their concentration adjusts to a lower value set by the low concentration LE. This adjustment is accompanied by a corresponding increase in analyte zone lengths, in accordance to the mass conservation of species. Cascade ITP was first introduced by Bocek et al. [121], who used two LEs with a concentration ratio of 5:1 to enhance the separation of orthophosphate and pyrophosphate ions. Later, Kaniansky et al. [130] demonstrated on-chip integration of this technique and showed conductivity based detection of several anions, including nitrate, chloride and fluoride ions. To our knowledge, all previous work on cascade ITP required pre-set, physical separations between zones of high and low concentration LE. This separation has been accomplished using a column coupling arrangement (basically a T-junction) [130] and often controlled with valves [34]. These requirements complicate the application of cascade ITP and have excluded the integration of cascade ITP into a simple, single channel architecture. These requirements also require an actuation step (of electrodes and/or valves) mid-way into the assay.

5.1.1 Current Work

We here present a novel method of creating a concentration cascade of LE. Our method requires no actuation and can be achieved in a single, straight channel system. We effectively "chemically" transition from one LE to another by using bidirectional isotachophoresis. Bidirectional isotachophoresis involves simultaneous anionic and cationic ITP in a single channel, and is characterized by anionic and cationic ITP shocks propagating either towards or away from each other [53,54]. In the current work, we use a bidirectional ITP mode where the anionic and cationic shock waves approach each other and interact to modify the electrophoresis conditions [131]. Prior to shock wave interaction, analytes are subjected to a relatively high concentration LE. Shock wave interaction then causes a sudden decrease of the LE ion concentration in the region ahead of the focused analytes. The technique can be used with either anionic or cationic ITP, removes the requirement of physical separation of LEs, and can be "programmed" into a cascade ITP process in a single, straight channel by setting the initial electrolyte chemistry.

We begin the chapter by describing our method of creating a concentration cascade of LE using bidirectional ITP. We then present an analytical model to predict the increase in zone length due to shock interaction and to help in selection of electrolyte chemistry for maximum detection sensitivity. We also present detailed numerical simulations to illustrate our technique. We confirm these simulations using experimental visualization of cascade ITP process in bidirectional ITP. We then present a series of controlled bidirectional ITP experiments with various electrolytes which show maximized detection sensitivity. Lastly, we employ our technique for the high-sensitivity, indirect-fluorescence-based detection of 2,4,6-trichlorophenol, a carcinogenic pollutant [132].

5.2 Theory

5.2.1 Concept of creating concentration cascade of leading electrolyte using bidirectional ITP

Bidirectional ITP involves simultaneous anionic and cationic ITP and is characterized by anionic and cationic ITP shock waves which propagate in opposite directions. Bidirectional ITP experiments require two oppositely charged pairs of LE and TE ions, which we here term as LE+, TE+, LE-, and TE-. LE and TE again denote the leading and trailing electrolyte ions, respectively, and + and – correspond to cations and anions, respectively. Depending on the initial conditions, shocks in bidirectional ITP can be made to propagate either towards or away from each other. In the former mode, anionic and cationic ITP shocks eventually interact and result in the formation of new ITP zones. Electrophoretic conditions in these newly created zones can differ markedly from those prior to the shock interaction. For example, shock interaction can change the identity of the counterion species, the concentration of co-ion species, local ionic strength, and pH; and this can quickly establish new focusing or separation conditions for analytes.

In the current work, we use shock interaction in bidirectional ITP to initiate a decrease in concentration of LE- ions and thereby elongate the zones of focused anionic analytes (consistent with cascade ITP). That is, prior to the shock interaction we focus anions with a high concentration LE- and then have shock interaction suddenly decrease the concentration of LE- ahead of the focused anions. Under these modified ITP conditions, the focused analyte zones are forced to readjust to lower concentrations. This decrease in the concentration of analyte zones is accompanied by a corresponding increase in the zone lengths. Although we here explore anionic ITP, in general our technique is equally applicable for increasing the sensitivity of cationic ITP by effecting a change in LE+ concentration.

Figure 5.1 shows a schematic of our technique. We first fill a straight channel with a mixture of LE+ and LE-, as shown in Figure 5.1a. We empty and then fill the reservoir on the left with a mixture of TE- and LE+. Similarly, we empty and then fill the reservoir on the right with a mixture of TE+ and LE-. LE- and LE+ serve as the leading electrolyte ions for anionic and cationic ITP, respectively. Whereas, TE- and TE+ serve as trailing electrolyte ions for anionic and cationic ITP, respectively. We inject the analyte ions, S-, between the LE- and TE- zones.

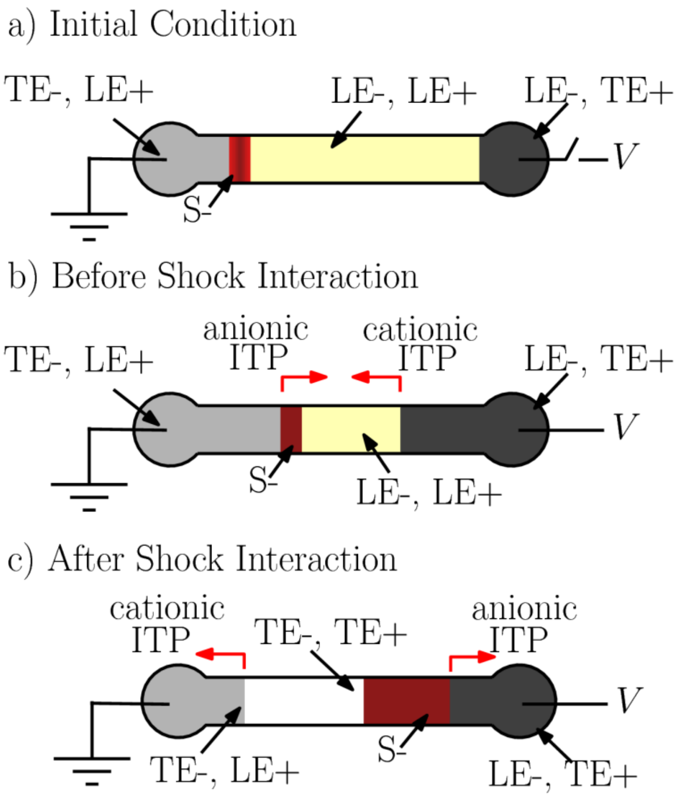

Figure 5.1: Schematic illustrating increase in analyte zone length upon shock interaction in bidirectional ITP. (a) The channel is initially filled with a mixture of LE+ and LE-. The reservoir on the left is filled with TE-/LE+ mixture, and the reservoir on the right is filled with LE-/TE+ mixture. Sample ions S- can be injected between the LE- and TE- zones. Buffers are chosen such that LE+ and TE+ are cations of weak bases and have respectively high and low absolute mobility. LE- and TE- are anions with effective mobility higher and lower than that of S-, respectively. b) When voltage is applied, the anionic analyte (S-) focuses between LE- and TE- and the analyte zone propagates towards the right. Simultaneously, a leftward-propagating cationic ITP shock forms between LE+ and TE+. Behind the cationic ITP shock, the total concentration of TE+ (a weak base) becomes on the order of LE+ concentration. Whereas, the concentration of fully-ionized LE- drops across the cationic ITP shock. Therefore, TE+ is only partially ionized behind the cationic ITP shock. (c) When the cationic ITP shock interacts with the analyte zone, the LE zone transitions from LE-/LE+ to LE-/TE+. Electrolytes are chosen such that LE- concentration is significantly lower in LE-/TE+ zone than in LE-/LE+ zone. The ITP focusing physics therefore dictates that analyte concentration drops (to balance electromigration flux and maintain electroneutrality). This decrease in the S- concentration is accompanied by a strong increase in sample zone length, significantly increasing the detection sensitivity.

As shown in Figure 5.1b, when voltage is applied along the channel, S- ions focus between the LE- and TE- ions and migrate rightwards. Simultaneously, a cationic ITP shock (LE+/TE+ interface) forms near the right reservoir and migrates leftwards. To create a concentration cascade in LE-, we choose our electrolytes such that the concentration of LE-, the counterion for cationic ITP, drops significantly behind the cationic ITP shock (in the LE-/TE+ zone). Subsequently, when the cationic ITP shock meets the focused anionic analyte zone, LE-/TE+ zone replaces the LE-/LE+ zone as the leading electrolyte for anionic ITP. The low concentration of LE- in the LE-/TE+ zone compared to the LE-/LE+ zone causes the analyte zone to readjust to lower concentration. Consequently, the analyte zone length increases significantly (Figure 5.1c). Note that the maximum analyte zone elongation is limited by the minimum possible concentration of LE- in the LE-/TE+ zone without compromising buffering capacity (typically order 5 mM). Therefore, starting with order 250 mM concentration of LE- in the LE-/LE+ zone, the current method cannot yield more than 50-fold elongation in analyte zone length. Later in Section 5.2.3 we discuss and quantify the choices of electrolyte chemistries which control and help maximize the zone length after the shock interaction.

In our technique, the cationic ITP does not affect the initial focusing of analyte ions in anionic ITP. The purpose of cationic ITP is to automatically trigger a change from high to low LE- concentration via shock interaction. In this way, our technique differs significantly from traditional cascade ITP wherein two unidirectional anionic ITP processes with different LE- concentration are coupled physically via valves [121] or a column coupling arrangement [130]. In other words, in traditional cascade ITP, the gradient in LE- concentration is realized by using bulk flow to establish two distinct regions in space which have different values of the regulating function (Kohlrausch [42] for strong electrolyte systems, and Jovin-Alberty [43,44] for weak monovalent electrolyte systems), as determined by two, independent chemical mixtures. In contrast, our technique uses interaction with a cationic ITP interface to effect a temporal change of the LE- concentration, while keeping the regulating function constant (and equal to the value set initially by the LE-/LE+ mixture in the channel).

We note our technique also differs markedly from previous applications of bidirectional ITP with approaching shock waves. Bidirectional ITP with approaching shock waves was introduced by Oshurkova and Ivanaova [57], who used it to measure the conductivity of a binary electrolyte consisting of LE- and LE+ ions. However, their analysis was limited to states of the system prior to shock interaction (namely the analysis of rate at which the shock waves approach). We know of no study, other than that by Bahga et al. [131], where shock interaction in bidirectional ITP has been used to couple two electrophoretic processes. Bahga et al. used the changes in ITP focusing conditions associated with shock interaction to couple ITP preconcentration with capillary electrophoresis (CE) (see Chapter 6). Here we present a new use of shock interaction in bidirectional ITP for effecting cascade ITP.

We also note our scheme is compatible with both "finite" and "semi-infinite" injection schemes, discussed earlier in Sections 1.3.3. In Figure 5.1, we show a finite sample injection scheme wherein sample ions are initially sandwiched between LE-/LE+ and TE-/LE+ zones. Alternatively, to increase sensitivity and minimize complexity, sample ions can be mixed with the TE-/LE+ mixture and allowed to focus continuously over time. In both cases, ITP focusing with high LE- concentration allows for greater sample loading prior to detection in the region formerly occupied by the low LE- concentration. We emphasize that an increase in lengths of anionic ITP zones occurs primarily due to the decrease in LE- concentration across the cationic ITP shock. Therefore, the injection method has no effect on the increase in zone length due to shock interaction. To illustrate these injection methods, we will here use both finite and semi-infinite injection schemes for our experiments (see Section 5.4).

5.2.2 Theory of cascade ITP

In ITP, analytes focus between LE and TE zones under applied electric field only if their electrophoretic mobilities are less than that of LE ions in the LE zone and greater than TE ions in the TE zone. When present in large quantities, analytes in ITP focus and segregate into plateau-like zones, whose concentrations are directly proportional to the LE ion concentration [42,44]. Thus, for a fixed amount of focused analyte, zone length $(\mathit{\Delta})$ is inversely proportional to the LE ion concentration (c_L). Furthermore, irrespective of the injection scheme, the maximum amount of sample which can be focused (load capacity, N_a) is proportional to the LE ion concentration [40,133]. For maximum attainable zone length in ITP, the effects of LE ion concentration on load capacity and the analyte zone concentration therefore cancel since

$$N_a \propto c_L, \quad \Delta \propto \frac{N_a}{c_L}. \tag{5.1}$$

Therefore in ITP with uniform LE concentration, the maximum achievable zone length does not change with LE concentration. However, in cascade ITP, this limitation does not exist since load capacity is determined by the high concentration LE, while analyte zone concentration during detection is governed by the low concentration LE.

In conventional cascade ITP, analytes first focus behind high concentration LE which allows for higher sample loading $(N_a \propto c_{L,high})$. The analyte zones are subsequently detected in a region with a lower concentration of the same LE, where the analyte zone concentrations are proportional to the lower LE concentration $(c_{L,low})$. The maximum zone length of focused analytes in cascade ITP, therefore, scales with the ratio of high to low LE concentrations,

$$N_a \propto c_{L,high}, \quad \Delta \propto \frac{N_a}{c_{L,low}}, \quad \Delta \propto \frac{c_{L,high}}{c_{L,low}}. \tag{5.2}$$

Further, in cascade ITP, for a fixed amount of analyte focused between the LE and TE zones, the ratio of analyte zone length in the high and low concentration LE is given by, $\Delta_{after} / \Delta_{before} = c_{L,high} / c_{L,low}$. Here subscripts *before* and *after* denote the state of analyte zones in regions formerly occupied by high and low LE concentrations, respectively. Thus, the increase in zone length due to the transition of analyte zone is set simply by the concentrations of the two LEs.

5.2.3 Prediction of increase in zone length in bidirectional ITP

Unlike conventional cascade ITP, the gradient in LE concentration in our technique (shown in Figure 5.1) is generated in situ. Therefore, the increase in zone length in our technique is not known directly from the initial conditions. To study the effect of shock interaction on analyte zone lengths, we here develop a simplified model for bidirectional ITP with interacting shocks. Knowing the composition of initial LE-/LE+ mixture and the species mobilities, our model predicts the concentrations of analyte zones before and after the shock interaction. The change in analyte zone concentration due to shock interaction can then be related to the change in the zone lengths.

We begin by considering an electrolyte system consisting of N chemical species. We assume safe pH conditions (5<pH<9, [134]) at which hydronium and hydroxyl ions do not contribution significantly to the local electrical conductivity, and that all species are monovalent acids or bases. We note these conditions are satisfied by the experiments presented in (see Section 5.4). For simplicity, we neglect the effect of ionic strength on electrophoretic mobilities of species (later in Section 5.2.4, we show detailed numerical simulations where we include the effects of ionic strength on species mobilities). We also neglect hydrodynamic flow as it only affects the shock propagation velocity and not the zone concentrations. Under these assumptions, we can use the conservation functions derived by Jovin [43] and Alberty [44] (also known as regulating functions, see Appendix D) to relate species concentrations in different bidirectional ITP zones to the initial concentrations of LE- and LE+. For N species, the Jovin function, $J\left(x,t\right)$, and the Alberty function, $A\left(x,t\right)$, for weak monovalent electrolytes can be written as,

$$J(x,t)=\sum_{i=1}^{N} z_i c_i(x,t)=J(x,0), \quad A(x,t)=\sum_{i=1}^{N}\frac{z_i c_i(x,t)}{\mu_i^0}=A(x,0). \tag{5.3}$$

Here $z_i=\{\pm 1\}$, c_i and μ_i^0 respectively denote the valence, total (analytical) concentration, and absolute mobility of weak monovalent species i. Throughout, we use c_i to denote the total concentration (analytical concentration) of species i, defined as the sum total of concentrations of all ionization states belonging to species i [108]. Mobility is here defined the ratio of actual drift velocity to local electric field, a signed quantity. The superscript 0 in mobility refers to the absolute mobility, defined as the species mobility when fully ionized at zero ionic strength [14]. Eliminating the concentration of Nth species from the Jovin and Alberty functions defined in eq. (5.3), we define a "combined Jovin-Alberty conservation function",

$$F(x,t)=\sum_{i=1}^{N-1}\left(\frac{1}{\mu_i^0}-\frac{1}{\mu_N^0}\right)z_i c_i(x,t)=F(x,0). \tag{5.4}$$

We now use this conservation function, $F(x,t)$, to determine concentrations of analyte zones before and after the shock interaction.

As shown in Figure 5.1a, initially the channel is filled with the LE-/LE+ mixture, which alone sets the value of combined Jovin-Alberty function throughout the channel. When electric field is applied, S- ions displace LE- ions and their concentration adjusts to the value of $F(x,t)$ set by the LE-/LE+ mixture (Figure 5.1b). Using LE+ as the Nth species in eq. (5.4), we obtain the concentration of focused analyte before the shock interaction $\left(c_{S-,before}\right)$ in terms of the initial LE- concentration $\left(c_{L-,init}\right)$,

$$\left(\frac{1}{\mu_{S-}^0}-\frac{1}{\mu_{L+}^0}\right)c_{S-,before}=\left(\frac{1}{\mu_{L-}^0}-\frac{1}{\mu_{L+}^0}\right)c_{L-,init}. \tag{5.5}$$

Here, subscripts $S-$, $L-$ and $L+$ denote analyte, LE- and LE+ ions, respectively. The second subscript *init* denotes the value set by the initial conditions. When the anionic and cationic ITP shocks interact, TE+ replaces LE+ as the counter-ion for anionic ITP (see Figure 5.1c). To obtain the concentration of analyte after the shock interaction, $c_{S-,after}$, we choose TE+ (denoted by $T+$) as the Nth species in eq. (5.4),

$$\left(\frac{1}{\mu_{S-}^0}-\frac{1}{\mu_{T+}^0}\right)c_{S-,after}=\left(\frac{1}{\mu_{L-}^0}-\frac{1}{\mu_{T+}^0}\right)c_{L-,init}-\left(\frac{1}{\mu_{L+}^0}-\frac{1}{\mu_{T+}^0}\right)c_{L+,init}^0. \tag{5.6}$$

Equations (5.5) and (5.6) give the expressions for analyte zone concentrations before and after the shock interaction in terms of the species mobilities and the initial concentrations of LE+ $(c_{L+,init})$, and LE- $(c_{L-,init})$. For a fixed amount of accumulated sample, the gain in zone length due to shock interaction is, therefore, given by,

$$\frac{\Delta_{after}}{\Delta_{before}}=\frac{c_{S-,before}}{c_{S-,after}}=\left(\frac{1-\mu_{L+}^0/\mu_{L-}^0}{1-\mu_{L+}^0/\mu_{S-}^0}\right)\left(\frac{1-\mu_{T+}^0/\mu_{S-}^0}{1-\mu_{T+}^0/\mu_{L-}^0}\right)\left[1-\frac{c_{L+,init}}{c_{L-,init}}\left(\frac{1-\mu_{T+}^0/\mu_{L+}^0}{1-\mu_{T+}^0/\mu_{L-}^0}\right)\right]^{-1}. \tag{5.7}$$

The three parenthetic expressions in this relation for $\Delta_{after} / \Delta_{before}$ are the ratios $c_{S-,before} / c_{L-,init}$, $c_{L-,after} / c_{S-,after}$, and $c_{L-,init} / c_{L-,after}$, respectively. In typical ITP experiments, the ratio of LE concentration to the corresponding analyte zone concentration is order unity. Therefore, the first two terms in eq. (5.7) do not contribute, significantly, to the increase in zone length; and the expression for $\Delta_{after} / \Delta_{before}$ in eq. (5.7) can be approximated as

$$\frac{\Delta_{after}}{\Delta_{before}} \approx \left[1 - \frac{c_{L+,init}}{c_{L-,init}} \left(\frac{1 - \mu^0_{T+} / \mu^0_{L+}}{1 - \mu^0_{T+} / \mu^0_{L-}} \right) \right]^{-1}. \tag{5.8}$$

In other words, the change in zone length is primarily due to the ratio of LE-concentrations across the cationic ITP shock, and to a lesser extent due to the change in counter-ion from LE+ to TE+ upon shock interaction. Moreover, the change in analyte zone length, given by eq. (5.8), does not depend on the acid dissociation constants of species, provided safe pH conditions (5<pH<9, [134]) hold. This is a consequence of the fact that Jovin and Alberty regulating functions for weak monovalent electrolytes do not depend on the acid dissociation constants of species.

Equation (5.8) is useful to quickly and approximately evaluate the effectiveness of electrolyte chemistry in increasing the detection sensitivity via shock interaction. For example, choosing $c_{L+,init} / c_{L-,init} = 3$, $\mu^0_{T+} / \mu^0_{L+} = 2/5$, and $\mu^0_{T+} / \mu^0_{L-} = -1$, by eq. (5.8) yields up to 10 fold increase in the zone length due to shock interaction. Note that, eq. (5.8), yields a singularity which suggests non-physical, infinite elongation of analyte zone upon shock interaction. Infinite elongation of analyte zones corresponds the case of vanishing LE- concentration across the cationic ITP shock. This non-physical conclusion stems from the fact that eq. (5.8) neglects the contribution of hydronium and hydroxyl ions to local conductivity. Therefore, eq. (5.8) is invalid for electrolyte systems having species concentrations less than order 0.1 mM, and cannot be employed to conclude infinite zone elongation due to vanishing LE- concentration after the shock interaction.

The analytical expression for increase in zone length given by eq. (5.8) allows us to derive qualitative guidelines for choosing electrolyte chemistry to maximize the detection sensitivity. These guidelines based on an approximate analytical model are also supported by detailed numerical simulations, presented in Section 5.4.2. For an anionic analyte focused behind the zone of fully-ionized LE- ion, the gain in zone length increases by increasing the proportion of weakly-ionized LE+ in the initial LE-/LE+ mixture, i.e., higher $c_{L+,init} / c_{L-,init}$ ratio. Secondly, choosing TE+ as a weak base with a very low absolute mobility compared to that of LE+ (lower μ^0_{T+} / μ^0_{L+} ratio) favors longer analyte zones after the shock interaction. When these two conditions are satisfied, the higher value of the total LE+ concentration in the LE-/LE+ mixture causes TE+ to adjust to a high total concentration relative to the approximately fully ionized LE- concentration. Note that, TE+ being a weak base can have significantly higher total concentration compared with that of fully-ionized LE-, while satisfying electroneutrality in the TE+ zone. That is, TE+ is then a weak base which is only partially ionized behind the LE+/TE+ interface at these conditions. As a result, the conductivity of TE+ zone drops significantly and the local electric field correspondingly jumps to a significantly higher value behind the LE+/TE+ interface. Choosing TE+ with very low absolute mobility also promotes this by further lowering local conductivity behind the cationic ITP shock. The high local electric field in the LE-/TE+ zone is consistent with a strong decrease of LE- concentration, in accordance with the continuity of electromigration flux across the cationic ITP shock. As the shocks interact, the LE-/TE+ mixture with low LE- concentration replaces the initial LE-/LE+ mixture as the leading electrolyte for anionic ITP. This causes anionic ITP zones to readjust to lower LE- concentrations and longer lengths. This achieves cascade ITP automatically and robustly with absolutely no actuation (such as voltage changes, electric switches, or valves).

We here provide some examples of viable electrolyte chemistries for our technique. These can be used to increase the sensitivity of anionic ITP by just modifying the initial electrolyte chemistries. The key requirements are that LE+ concentration should be high compared to LE- concentration and TE+ ions should have very low absolute mobility compared to LE+ ions. Since the required concentrations of LE+ and TE+ in our method are higher than those of anionic species, we choose LE+ and TE+ as weak bases so as to keep the ITP zones well buffered. Several choices exist for high and low mobility weak bases applicable as LE+ and TE+, respectively. Table 5.1 shows three practical choices each for LE+ and TE+, combination of which yield nine unique cationic

ITP chemistries. Since the gain in analyte zone length is not a strong function of LE- and TE- mobilities, there are no specific constraints on LE- and TE- except the usual requirements on species mobilities for focusing anions in anionic ITP. For example, chloride, sulfate, MES, and MOPS can be used as LE-; and HEPES, tricine, taurine, and serine can be used as TE-.

Table 5.1: Possible cationic ITP buffer systems which are compatible with bidirectional, cascade ITP. These buffers effect large increase in zone lengths of anionic analytes upon shock interaction in bidirectional ITP. Listed are absolute mobilities of the cations and their acid dissociation constant.

Cationic LE (LE+)	μ_{+1}^{0} $(\times 10^{-9}$ $m^2V^{-1}s^{-1})$	$pK_{a,+1}$
Imidazole	52	7.15
2-methyl pyridine	40.1	6.2
4-methyl pyridine	40.1	6.1
Cationic TE (TE+)	μ_{+1}^{0} $(\times 10^{-9}$ $m^2V^{-1}s^{-1})$	$pK_{a,+1}$
Bistris	26	6.4
Pyridine	30	5.18
Tris	29.5	8.07

To obtain the analytical expression for increase in zone length (eq. (5.7)) we have neglected the effect of ionic strength on species mobilities. However, ITP experiments are generally performed at higher ionic strengths (10-100 mM range) to achieve significant buffering capacity. Therefore the analytical model presented above is strictly valid only in the limit of zero ionic strength, and should be used only for qualitative electrolyte selections and rough predictions of the effect of electrolyte chemistry on the zone length. For more quantitative estimates of zone length, it is necessary to couple a model of ionic strength effects on species mobility with ITP dynamics.

In the current work, we use the SPRESSO simulation tool [58,63] with SLIP scheme (discussed in Chapter 2) to solve one-dimensional species transport equations coupled with Onsager-Fuoss [80] and Debye-Huckel [81] models for ionic strength dependence on mobilities and ionic activities, respectively. Time dependent simulations using SPRESSO are particularly useful for predicting transient behavior, such as analyte focusing during the startup and the transients of zone elongation due the shock interaction. However, for quicker estimates of increase in zone length in bidirectional

ITP, we have also developed and used a steady state solver based on a diffusion-free model of ITP [88]. The solver computes species concentrations in all bidirectional ITP zones by solving the moving boundary equations [34] (Hugoniot conditions across ITP shocks [88]) coupled with models for ionic strength effect on mobilities and acid dissociation constants [15]. We used both SPRESSO and this steady state solver to design and analyze the processes described here. Unless otherwise stated, all simulations presented below are from SPRESSO. In Appendix G, we provide an outline of the steady state solver and benchmark it against transient simulations using SPRESSO.

5.2.4 Simulation of cascade ITP process in bidirectional ITP

We performed simulations of the bidirectional, cascade ITP process for focusing and separation of two model analytes using the SPRESSO simulation tool. For our simulations, we used 100 mM MOPS as LE-, 20 mM taurine as TE-, 280 mM imidazole as LE+, 100 mM bistris as TE+, and HEPES (S1-) and tricine (S2-) as the model analytes. To illustrate the technique, we used a finite injection scheme for our simulations where S1- and S2- were initially present between the LE- and TE- zones. Further, we chose our initial conditions such that the analytes focused completely in plateau mode prior to shock interaction. This allowed us to quantify precisely the increase in zone length due to shock interaction. All simulations shown here take into an account the effect of ionic strength on both mobilities and dissociation constants.

Figure 5.2a and Figure 5.2b show the initial conditions of the simulation. Analytes, S1- and S2-, are placed between LE- and TE- zones. When electric field is applied, S1- and S2- focus and separate into distinct zones between LE- and TE-, as shown in Figure 5.2c and Figure 5.2d. Simultaneously, a cationic ITP shock (LE+/TE+ interface) interface forms between the LE+ and TE+ zones and propagates leftward. Behind the LE+/TE+ interface, the concentration of LE- drops significantly compared to its initial concentration (Figure 5.2c). At the time LE+/TE+ interface meets the focused analytes, the high concentration LE- is completely replaced by the low concentration LE-. Because the analyte zone concentrations in ITP are proportional to the LE concentration, the interaction of cationic and anionic ITP shocks results in a decrease in zone concentrations of S1- and S2-. This readjustment of analyte zone concentrations is accompanied by simultaneous increase in their zone lengths. Figure 5.2e and Figure 5.2f, show this transition from high to low concentration LE-, where the S1- zone has partially readjusted to the lower concentration and S2- is still focused at high concentration. Figure 5.2g and Figure 5.2h show the final state where both S1- and S2- are fully adjusted to new concentrations, and their zone lengths have increased (5-fold in this case) compared to those before the shock interaction. Also, the cationic ITP shock remains intact after the shock interaction and continues propagating leftwards.

The simulation of cascade ITP process in bidirectional ITP shown in Figure 5.2 itself highlights several advantages of our technique over conventional cascade ITP. As shown in Figure 5.2c, the gradient in LE- concentration forms inside the channel by simply applying an electric field. Our technique, therefore, eliminates integration of two or more channels containing different concentrations of LE- via valves or column coupling arrangements, as done in conventional cascade ITP. This in situ generation of cascade in LE ion concentration makes it possible to perform cascade ITP in a single channel, so it is easily accomplished in on- or off- chip systems. Further, in the current technique, the gradient in LE concentration remains sharp over time as it sweeps across the focused analyte zones. This well controlled, sharp gradient in LE ion concentration, which typically occurs over a distance of about 10 µm, provides us with a fast transition from focusing at high concentration LE to low concentration LE. This feature of our assay minimizes required channel lengths and assay time. These qualities are in contrast to conventional cascade ITP where the interface between high and low concentration LE diffuses over time and is susceptible to dispersive effects of non-uniform electroosmotic flow and hydrodynamic flow. Hence, a complete readjustment of analyte zones to lower concentration LE is not achieved in conventional cascade ITP until the analyte zones completely migrate out of the dispersed region between the high and low concentration LE.

We also performed a simulation at conditions which allow experimental visualization of all bidirectional ITP zones. The results are shown in Figure 5.3a. We used electrolyte chemistry similar to that used in Figure 5.2, except here we added a fluorescent non-focusing tracer (NFT) in trace concentration (25 µM) into the initial TE-/TE+ mixture. The NFT effective mobility was higher than all other anions.

Initial Condition (t = 0 s)

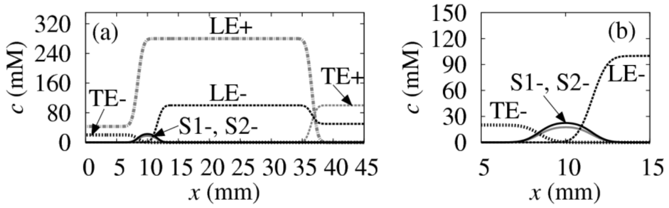

Focusing Before Shock Interaction (t = 260 s)

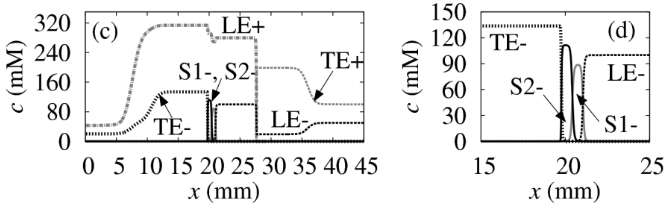

Transition (t = 358 s)

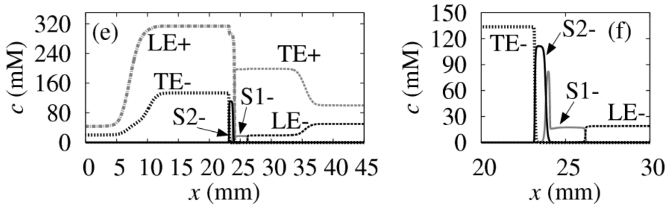

Zone Elongation After Shock Interaction (t = 374 s)

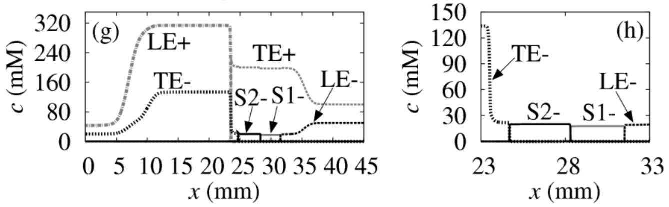

Figure 5.2: Simulation showing increase in zone length of anionic analytes using concentration cascade of LE- in bidirectional ITP. Plots in the second column are magnified views of species distributions shown in the first column. (a-b) show the initial distribution of chemical species, prior to activating current. (c-d) show the anionic and cationic ITP shocks shortly after application of electric field. (c) shows anionic ITP shocks (x = 20 mm) propagating rightward and a cationic ITP shock (x = 27 mm) propagating leftward. (d) shows anionic analytes S1- and S2- completely focused between LE- and TE- in narrow plateau zones. (e-f) show the transition from high concentration LE- to low concentration LE- upon shock interaction. When the LE-/TE+ zone meets the focused analyte zones, it sets a new focusing condition for sample ions corresponding to a low LE- concentration. This forces S1- and S2- zones to readjust to lower concentrations, and this is accompanied by elongation of analyte zones (in accordance with conservation of species). (f) shows S1- zone readjusting to a lower concentration after interacting with the LE+/TE+ interface, while S2- zone is still at the previously adjusted higher concentration. (g-h) show the final state, in which analyte zones are fully adjusted to lower concentrations. (h) shows the fully elongated analyte zones which are 5 times longer than those prior to the shock interaction. Chemistry is described in text. We assumed a constant current of 2 µA, and a D-shaped, wet-etched channel 90 µm wide and 20 µm deep.

The NFT does not focus or disturb zone concentrations in bidirectional ITP, but its concentration quickly adapts to local electric fields in all zones. The NFT fluorescent intensity distribution therefore clearly delineates the various bidirectional ITP zones. In Section 5.4.1 we present corresponding experimental validation of this simulation (Figure 5.3b) and discuss the NFT visualization technique in more detail.

Shown in Figure 5.3a is a simulated spatiotemporal plot of fluorescent intensity of NFT during bidirectional cascade ITP. Here, the abscissa is the distance along the channel, the ordinate is time, and the scalar plotted is the fluorescent intensity of the NFT. To obtain the spatiotemporal plot from simulation, we neglect the effects of photobleaching and assumed a proportional relationship between the fluorescent intensity and the NFT concentration. Figure 5.3a shows zones of focused S1- and S2- ions propagating rightward, and a cationic ITP shock (LE+/TE+) shock propagating leftward. Since the NFT and LE- are both counter-ions for cationic ITP, their concentrations across the LE+/TE+ interface are in proportion to each other. The low fluorescent intensity in the LE-/TE+ zone compared to the LE-/LE+ zone, therefore, indirectly quantifies the manifold decrease in LE- concentration across the LE+/TE+ interface. When the anionic and cationic ITP shocks interact ($25\text{ s} < t < 45\text{ s}$), the analyte zones readjust to lower concentrations (shown by the decrease in NFT intensity in the analyte zones) and achieve longer zone lengths. After the LE+/TE+ interface completely passes over the analyte zones ($t > 45\text{ s}$), the zone lengths reach steady state values that are much greater than those before the shock interaction. For example, compare the width of the S2- at $t = 25$ s (0.65 mm) with its width at 45 s (3.6 mm). See also Figure 5.5b for comparison with eq. (5.7). Also, note the cationic ITP interface remains intact after its interaction with the analytes and continues propagating toward the left. To take into an account the effect of electroomostic flow on the wave speeds in our simulations, we used the following approximate electroosmotic mobility dependence on conductivity (as suggested by the data of Bharadwaj et al. [128]): $\mu = \mu_r \left(\sigma_r / \sigma\right)^{1/3}$, where $\mu_r = 3\times10^{-10}$ $V^{-1}.m^{2}.s^{-1}$ and $\sigma_r = 0.5$ $S.m^{-1}$. The product $\mu_r \sigma_r^{1/3}$ is therefore the only fitting parameter used to match all experimentally measured shock speeds. (See Section 5.4.1 on experimental visualization of cascade ITP process in bidirectional ITP.)

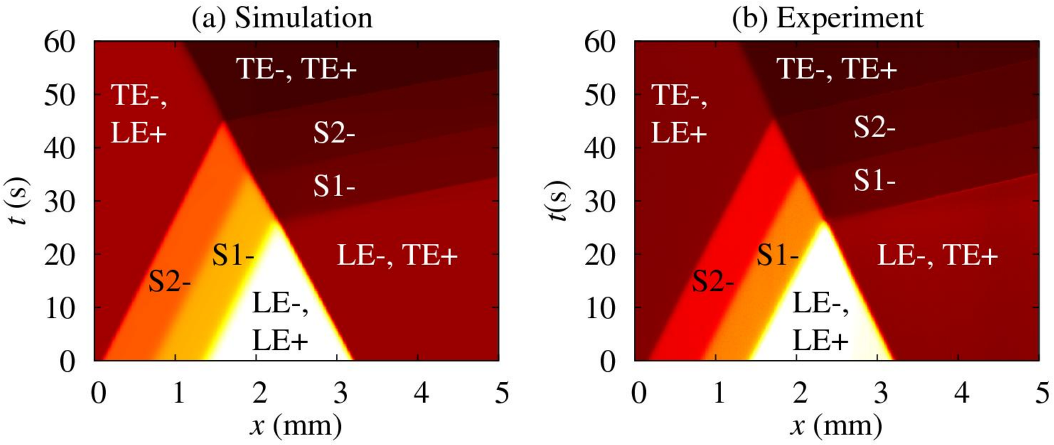

Figure 5.3: Numerical simulation and experimental visualization of increase in analyte zone length due to interaction of anionic and cationic ITP shocks. (a) shows numerical simulation of propagating zones of anionic analytes (S1- and S2-) and a cationic ITP shock in bidirectional ITP. The spatiotemporal plot shows the intensity of a fluorescent non-focusing tracer (NFT) versus the distance along the channel axis, x, and time, t. The NFT fluorescent intensity is inversely proportional to local electric field in each zone. (b) shows experimental visualization of the same process using the fluorescent NFT technique [47]. Both (a) and (b) show anionic analyte zones and LE+/TE+ interface (cationic ITP shock) propagating towards the right and left, respectively. The LE+/TE+ interface meets the focused analyte zones near $x = 2.3$ mm and $t = 25$ s. Thereafter, analyte zones elongate by a factor of 5 and the LE+/TE+ interface continues migrating leftward (for $t > 25$ s). The elongation of analyte zones around $t = 25$ s is accompanied by increase in their migration speed (visible as decrease in slope of anionic ITP shocks). The electrolyte chemistry and electroosmotic mobility are the same as that in the simulation shown in Figure 5.2, except we here mixed 25 µM Alexa Fluor 488 (NFT) in TE- to visualize ITP zones. Both simulations and experiments used a constant current of 2 µA, and a 53 mm long D-shaped, wet-etched channel 90 µm wide and 20 µm deep.

5.3 Materials and Methods

We performed experiments to visualize and quantify the increase in analyte zone lengths due to concentration cascade of LE in bidirectional ITP. We used the fluorescent non-focusing tracer (NFT) technique [47] for simultaneous visualization of all bidirectional ITP zones. For these visualization experiments, LE- was 100 mM MOPS, TE- was 20 mM taurine, LE+ was 280 mM imidazole, and TE+ was 100 mM bistris. We used HEPES and tricine as model anionic analytes. We used a similar protocol as shown schematically in Figure 5.1. To inject finite amounts of analytes, we first added HEPES and tricine to the TE-/LE+ mixture at a concentration of 0.5 mM and 1 mM, respectively. We then allowed these analytes to focus until the analyte zones moved 5 mm from the TE- well. Subsequently, we replaced the mixture of analytes and TE-/LE+ with pure TE-/LE+, to effect a finite injection. We describe the injection protocol in more detail in Figure 5.4. We used a similar electrolyte chemistry and injection protocol for experiments demonstrating the effect of electrolyte composition on analyte zone length (Section 5.4.2). There, we adjusted the composition of LE-/LE+ mixture by fixing the concentration of LE- at 100 mM and changing LE+ concentration from 200 to 320 mM.

For the experiments demonstrating focusing and detection of 2,4,6-trichlorophenol (TCP), we used 150 mM MES as LE-, 20 mM HEPES as TE-, 470 mM imidazole as LE+ and 300 mM bistris as TE+. To increase the sample loading by continuously focusing the sample, we mixed TCP with TE-/LE+ mixture (diluted from 1 mM stock).

To visualize zones in all experiments, we prepared 1 mM stock solution of the Alexa Fluor 488 dye (Invitrogen, Carlsbad, CA) and used it as a fluorescent NFT by mixing at a concentration of 25 µM in the TE-/LE+ mixtures. We prepared 1 M stock solutions of MOPS, MES, tricine, HEPES, imidazole, bistris and 200 mM solution of taurine before diluting them to the desired concentrations in different solutions. We added 1% w/w polyvinylpyrrolidone (PVP) to all solutions to suppress EOF. All chemicals were obtained by Sigma Aldrich (St. Louis, MO) and were prepared in UltraPure DNase/RNase-free distilled water (GIBCO Invitrogen, Carlsbad, CA).

We captured images using an inverted epifluorescent microscope (IX70, Olympus, Hauppauge, NY) equipped with a LED lamp (LEDC1, Thor Labs, Newton, NJ), U-MWIBA filter-cube from Olympus (460–490 nm excitation, 515 nm emission, and 505 nm cut off dichroic), and 2x (NA = 0.08) and 10x (NA = 0.3) objectives (Olympus). Images were captured using a 12 bit, 1300×1030 pixel array CCD camera (Micromax1300, Princeton Instruments, Trenton, NJ). We controlled the camera using Winview32 (Princeton Instruments) and processed the images with MATLAB (R2007b, Mathworks, Natick, MA). We conducted the experiments by applying either constant voltage or current using a sourcemeter (model 2410, Keithley Instruments, Cleveland, OH).

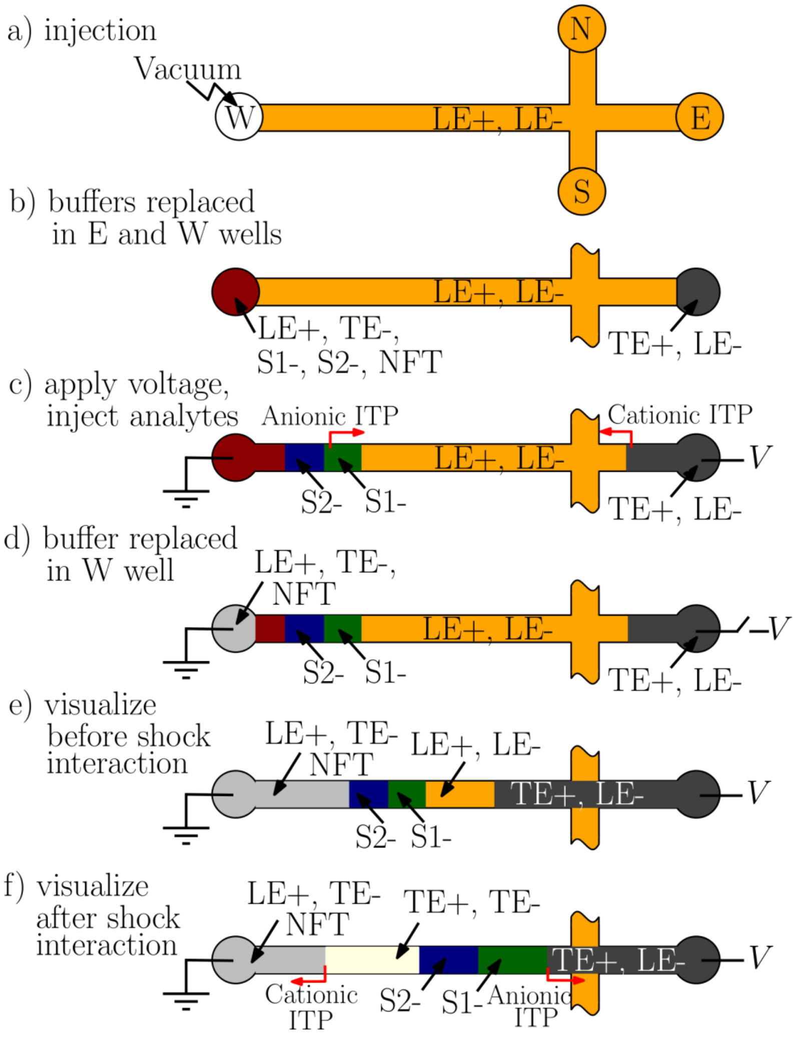
a) injection
Vacuum
W
N
E
S
LE+, LE-
b) buffers replaced in E and W wells
LE+, LE-
LE+, TE-, S1-, S2-, NFT
TE+, LE-
c) apply voltage, inject analytes
Anionic ITP
Cationic ITP
LE+, LE-
V
S2-
S1-
TE+, LE-
d) buffer replaced in W well
LE+, TE-, NFT
LE+, LE-
V
S2-
S1-
TE+, LE-
e) visualize before shock interaction
LE+, TE- NFT
LE+, LE-
TE+, LE-
V
S2-
S1-
f) visualize after shock interaction
LE+, TE- NFT
TE+, TE-
TE+, LE-
V
Cationic ITP
S2-
S1-
Anionic ITP

Figure 5.4: Protocol for visualizing increase in analyte zone lengths due to shock interaction in bidirectional ITP. For visualization experiments on Caliper NS 12A chips: (a) we injected LE+/LE- mixture by applying vacuum on W well. We then emptied the E and W wells and (b) filled the E well with TE+/LE- mixture, and the W well with a mixture of LE+, TE-, analytes (S1-, S2-) and non-focusing tracer (NFT). (c) We then electrokinetically injected S1- and S2- ions by applying voltage between E and W wells. (d) Next, we turned off the voltage, emptied the W well and filled it with a mixture of LE+, TE- and NFT. This step ensured injection of finite amounts of S1- and S2- ions in the channel. (e) We then applied voltage between E and W wells and imaged the focused analyte zones, prior to the shock interaction. (f) We again imaged the focused analyte zones after the interaction of cationic and anionic shock waves.

All experiments were performed on off-the-shelf Caliper NS 12A borosilicate glass microchips from Caliper Life Sciences (Mountain View, CA). These microchips have channels wet etched to a depth of 20 µm with a mask width of 50 µm. In Figure 5.4 we show a schematic of the microchip and injection protocol. Although the chip consisted of four channels in a cross-geometry, we applied electric field only along one channel (53 mm long) for our experiments. We filled the North, South and East reservoirs of the chip with LE-/LE+ mixture and applied vacuum to the West reservoirs until all channels were filled. We then rinsed the East and the West reservoirs with distilled water and filled them with cationic and anionic TE solutions, respectively.

5.4 Results and discussion

5.4.1 Experimental visualization of increase in analyte zone length in bidirectional ITP

We performed visualization experiments to study and quantify the dynamics of the cascade ITP process in bidirectional ITP. For these experiments, we used finite injections of analytes in anionic ITP and visualized the effect on their zone lengths before, during, and after interaction with cationic ITP shock. We visualized the increase in zone lengths of focused analytes due to shock interaction in bidirectional ITP using the NFT technique [47]. In the NFT technique, fluorescent species which do not obey the ITP focusing conditions [135] are mixed with one or more of the ITP buffers in trace quantities. These fluorescent species do not focus in ITP, but their concentrations adapt to the local electric field and conductivity in different ITP zones. The fluorescent intensity of NFT, therefore, indicates the gradients in local conductivity across the ITP interfaces. For our experiments, we used 25 µM Alexa Fluor 488 (AF, an anionic dye) in the TE-/LE+ mixture as the NFT. In our experiments, AF is faster than all other anions and so does not focus. Further, anionic species cannot focus in the cationic ITP process. Hence, we visualized both anionic and cationic ITP zones in bidirectional ITP using AF as the lone NFT.

Figure 5.3b shows an experimentally measured spatiotemporal plot of the fluorescent intensity of NFT in bidirectional ITP with a concentration cascade of LE-.

Like the simulated spatiotemporal plot (Figure 5.3a), Figure 5.3b shows a measured spatiotemporal plot showing the dynamics of the zones of focused analytes (S1- and S2-) before (t <25 s), during (25 s < t < 45 s), and after (t > 45 s) the shock interaction. The scalar quantity plotted (versus distance along channel axis and time) is the fluorescence intensity (from CCD images) in the channel averaged along the spanwise width of the channel. Our experimental visualizations compare well with the numerical simulations shown in Figure 5.3a. First we capture qualitatively the dynamics of the entire process including propagation velocities of four shocks, their interactions and the fluorescent intensity ratios across the shocks. We see clearly the rightward propagation of the focused sample zones S1- and S2- and the effect of interaction with the cationic shock. Compare the axial width of zones S1- and S2- prior to shock interaction (*e.g.*, at t = 20 s) to their width after shock interaction (t > 45 s). Quantitatively, our simulations predict ratios of the final to initial analyte zone lengths of 5.0 and 5.5 for S1- and S2-, respectively. Experimentally we observe gains in zone length of 4.8 and 5.3 for S1- and S2-, respectively. Further, our simulations predict initial to final fluorescence intensity ratios of 7.0 and 8.4 for S1- and S2- zones respectively, versus the observed values of 7.2 and 8.1. Importantly, these two parameters are independent of EOF mobility, and so each is predicted from first principles. By using a conductivity-dependent electroosmotic mobility as a single fitting parameter, we also accurately predict the time and the location of shock interactions and the eight observable shock speeds.

5.4.2 Effect of electrolyte chemistry on increase in zone length

We performed experiments to validate the dependence of analyte zone lengths on the electrolyte chemistry as given by the analytical model in Section 5.2.3 and by the diffusion-free model discussed earlier. According to the analytical model, for a given electrolyte chemistry, the ratio of the final to initial analyte zone lengths depends primarily on the ratio of LE+ to LE- concentrations in the initial LE-/LE+ mixture. For our experiments, we therefore kept the same LE-/LE+ chemistry but used seven ratios of LE+ to LE- concentrations $(c_{L+,init} / c_{L-,init})$ ranging from 2.0 to 3.2. The changes in composition of LE-/LE+ mixture were obtained by fixing the concentration of LE- at 100 mM and varying LE+ concentration from 200 to 320 mM. Figure 5.5a and Figure

5.5c show the relative increase in zone length $(\Delta_{after} / \Delta_{before})$ of two analytes (HEPES and tricine) due to shock interaction, for different proportions of LE+ in the LE-/LE+ mixture. The insets (Figure 5.5b and Figure 5.5d) show the same data, but here the ordinate is the inverse of the gain in zone length, i.e. $\Delta_{before} / \Delta_{after}$.

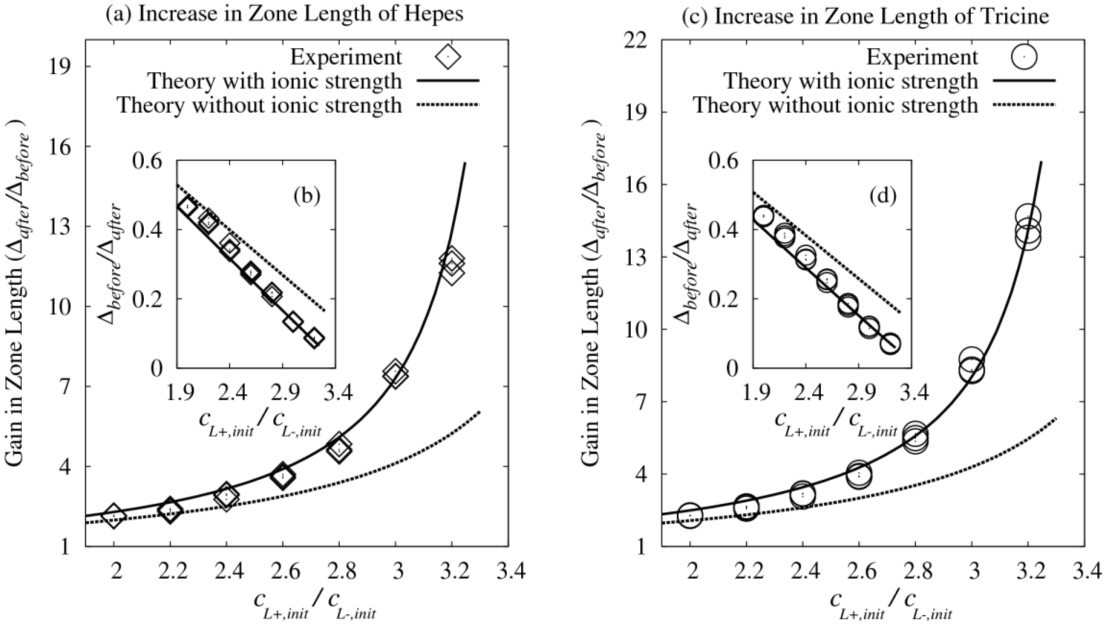

Figure 5.5: Effect of the leading electrolyte composition on gain in analyte zone lengths due to shock interaction. (a) and (c) show the variation of measured and theoretical gain in zone length $(\Delta_{after} / \Delta_{before})$ of two analytes (HEPES and tricine) versus the ratio of LE+ to LE- concentration in the initial LE+/LE- mixture $(c_{L+,init} / c_{L-,init})$. The gain in analyte zone length increases non-linearly with increase in $c_{L+,init} / c_{L-,init}$. Both (a) and (c) show theoretical predictions with and without ionic strength correction for species mobility. Theoretical predictions which take into an account the effect of ionic strength on mobilities are in good agreement with experimental observations. Theoretical predictions from the analytical model (without ionic strength corrections) capture trends but underpredict gains in zone length. Insets (b) and (d) show the comparison with same data, but now the ordinate is the inverse of the gain in zone length $(\Delta_{before} / \Delta_{after})$. The simple analytical solution is useful for assay design and correctly predicts the linear variation of $\Delta_{before} / \Delta_{after}$ with $c_{L+,init} / c_{L-,init}$. LE- is MOPS, LE+ is imidazole, TE- is 20 mM taurine and TE+ is 100 mM bistris. To vary the ratio $c_{L+,init} / c_{L-,init}$ we fixed the concentration of LE- at 100 mM and varied the concentration of LE+ from 200 mM to 320 mM. We visualized different ITP zones using Alexa Fluor 488 as a fluorescent NFT. All theoretical results use the same conditions.

As predicted by the analytical model (eq. (5.7)), both experiments and calculations using the diffusion-free model show a linear decrease in $\Delta_{before} / \Delta_{after}$ with increasing $c_{L+,init} / c_{L-,init}$. Correspondingly, the ratio of final to initial analyte zone lengths increases non-linearly with increase in ratio of initial LE+ to LE- concentrations. As shown in Figure 5.5a and Figure 5.5c, the predictions of gain in zone length from the diffusion-free model agree well with the experimental observations. The predictions from analytical model agree qualitatively with experimental observations, but show significant differences in magnitude to the experimentally measured gain in zone length. As shown in Figure 5.5a and Figure 5.5c, the error in analytical predictions increases for larger gain in zone lengths (higher $c_{L+,init} / c_{L-,init}$). This error is a result of our assumption of negligible dependence of ionic strength on species mobilities in our analytical model. This conclusion is supported by fact that the analytical model compares well with the diffusion-free model if ionic strength effects are neglected in the latter (see Appendix G). At high ionic strengths (around 100 mM), effective mobilities decrease considerably from the corresponding absolute mobility values (see Chapter 2). This change in mobilities strongly affects gains in zone length as predicted by eq. (5.7).

Here we used the diffusion-free model along with ionic strength corrections for species mobilities to predict correctly the increase in zone lengths over wide range of LE-/LE+ compositions. We note that simulations using SPRESSO can alternatively be used for the same purpose, albeit at the expense of longer computational time (typically an order of magnitude longer than the diffusion-free model). In Figure 5.5, we omit the results from SPRESSO simulations, as the differences between the predicted gain in zone lengths using the diffusion-free model and SPRESSO are negligible. However, we show their comparison in Appendix G, where we benchmark the diffusion-free model against SPRESSO simulations.

5.4.3 Demonstration of high sensitivity detection using bidirectional ITP

Lastly, we used bidirectional ITP with concentration cascade of LE- for high sensitivity detection of TCP, a carcinogenic pollutant [132]. For these experiments we used 150 mM MES as LE-, 20 mM HEPES as TE-, 470 mM imidazole as LE+ and 300 mM bistris as TE+. Our simulations predict ~20 fold increase in zone length due to shock interaction with this electrolyte chemistry. To increase the sample loading, we performed semi-infinite injection of TCP by mixing it with anionic TE (TE-/LE+ mixture).

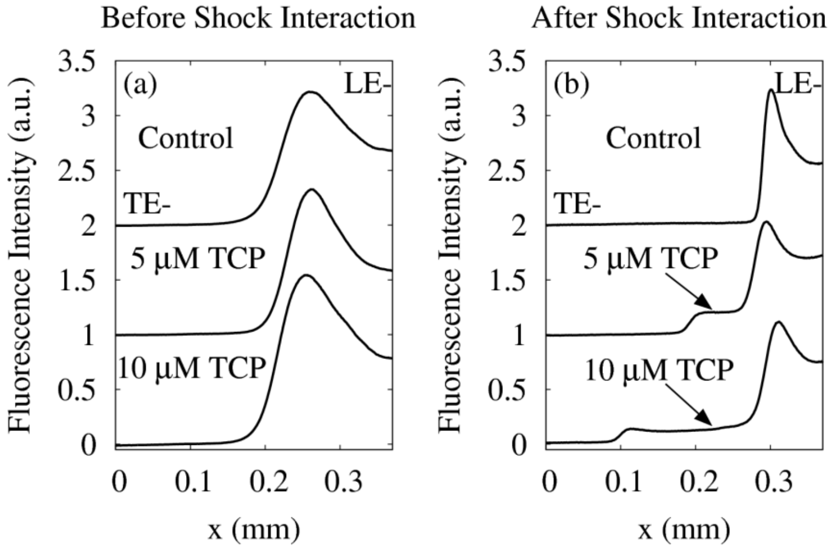

Figure 5.6: Indirect fluorescence detection of 5 µM 2,4,6-trichlorophenol (TCP) using the NFT technique with concentration cascade of LE-. (a) shows the fluorescent intensity of NFT (Alexa Fluor 488) prior to the interaction of the cationic and anionic ITP shock waves. Before shock interaction, the control experiment in the absence of TCP shows a single upward step in the fluorescent intensity from TE- to LE-. When TCP is mixed with TE- at concentrations of 5 and 10 µM, the fluorescence signal before the shock interaction does not change appreciably. At these conditions, TCP is focused in peak mode and so has negligible effect on the background electric field. (b) shows the fluorescence intensity of NFT after the shock interaction. For the cases where 5 and 10 µM TCP are present in TE-, we observe a distinct step in NFT signal after the shock interaction. Thus TCP which focuses in peak mode before the shock interaction, transitions to plateau mode after the interaction of anionic and cationic ITP shock waves. We observed a signal overshoot at the boundary of the LE- zone (see text). For these experiments, we used a constant potential of 500 V across a 53 mm long, D-shaped, wet-etched channel 90 µm wide and 20 µm deep.

Figure 5.6a and Figure 5.6b show measured isotachopherograms obtained before and after the shock interaction. For the control experiment, where no TCP was present in the TE-/LE+ mixture, we observe a single step in the NFT signal corresponding to the LE-/TE- interface. When TCP is spiked in anionic TE at concentrations of 5 µM and 10 µM, the signal prior to shock interaction is unchanged. At these low concentrations, TCP is focused in peak mode and so its zone length is on the order of LE-/TE- interface thickness. However, in the same experiments, the TCP zone length increases upon its interaction with the cationic ITP shock. Figure 5.6b shows well resolved plateau zones of TCP after the shock interaction. As expected, the TCP zone lengths are proportional to the initial amount of TCP in the anionic TE. We note that we observed in these experiments a signal overshoot at the boundary of LE- zone. Similar overshoots have been observed in other ITP systems [135,136], including those with the NFT technique [47]. However, we note this signal overshoot does not here affect our ability to detect and quantify the length of the TCP zone. The detection sensitivity of our technique is currently in the µM range. We estimate that the sensitivity can be further increased by at least a factor of ~50 by using other techniques in concert with our bidirectional cascade ITP method, including variation of channel cross-section [88,122] and hydrodynamic counterflow [120].

5.5 Summary

We developed a new method to create concentration cascade of LE in ITP by leveraging interaction of anionic and cationic shock waves in bidirectional ITP. We described how bidirectional ITP with approaching and interacting shock waves can be used to focus analytes and simultaneously create a gradient in LE ion concentration across a counter-ionic ITP shock wave. We used this feature of bidirectional ITP to initially focus analytes using a high concentration of LE ions. Shock interaction then causes a decrease in the LE ion concentration ahead of focused analytes. The high LE ion concentration prior to the shock interaction increases the sample loading capacity. The subsequent, lower concentration of LE ions established by the shock interaction increases the detection sensitivity by enforcing longer analyte zones. To the best of our knowledge, this is the first time where cascade ITP has been performed by generating in situ gradient in LE concentration using only the initial condition of the chemistry.

We presented an analytical model to predict the gain in analyte zone length due to shock interaction. Based on the analytical model we discussed practical choices of electrolyte chemistries for maximizing the detection sensitivity. To illustrate the dynamics of analyte zone elongation, we performed detailed numerical simulations of one-dimensional electromigration diffusion equations. We validated the simulations using visualizations based on indirect fluorescence of bidirectional ITP zones. Our simulations predict accurately (and from first principles) the local zone concentrations and the gain in analyte zone length due to shock interaction. By further incorporating a single fitting parameter for electroosmotic mobility, the simulations also correctly predict the dynamics of shock wave propagation in bidirectional ITP before, after, and during the shock wave interaction. We performed a series of controlled bidirectional ITP experiments to demonstrate the effect of varying proportion of cationic to anionic LE concentrations on the gain in zone length of anionic analytes. Our experiments show that the gain in zone length of anionic analytes due to shock interaction increases with increase in ratio of cationic to anionic LE concentrations. Similar behavior is predicted qualitatively by our analytical model and more precisely by numerical simulations. Based on these results, we designed a bidirectional ITP chemistry to demonstrate a factor of 20 increase in detection sensitivity of 2,4,6-trichlorophenol.

Bidirectional ITP with interacting shock waves is an elegant way of triggering a wide range of modifications to ITP processes. Here we demonstrated cascade ITP for high sensitivity detection using bidirectional ITP. Our process, eliminates the requirement of physical separation of high and low concentration LEs using valves or a column coupling arrangements. Unlike conventional implementations of cascade ITP, the LE concentration gradient in our technique is generated in situ, and this allows its integration in a single channel such as in standard CE equipments. Furthermore, the technique can be easily applied in concert with hydrodynamic counter-flow and/or converging channel cross-sections to further enhance detection sensitivity.

6 Coupled isotachophoretic preconcentration and electrophoretic separation using bidirectional isotachophoresis

The contents of this chapter were published previously by S.S. Bahga, R.D. Chambers and J.G. Santiago [131] in *Analytical Chemistry*, and partly (Section 6.1) based on a review article by S.S. Bahga and J.G. Santiago [1] in *Analyst*. The contents from these publications and are reproduced here with minor modifications.

6.1 Introduction

Isotachophoresis (ITP) and capillary zone electrophoresis (CZE) are extensively used as standalone analytical methods of separation and detection of ionic species for a wide range of sample mixtures. This is because ITP and CZE have respectively highest sensitivity and highest resolution among all electrophoresis techniques. However low separation resolution of ITP and low sensitivity of CZE often limit their applicability for analysis of trace species. Isotachophoretic analysis of trace analytes typically results in peak mode focusing, wherein overlapping peaks of focused analytes render them indistinguishable for each other. On the other hand, CZE can separate the same analytes into distinct zones, but dispersion of analyte zones during separation results in low signal-to-noise ratio [22].

These limitations of ITP and CZE for analysis of trace species can be addressed by coupling ITP and CZE, which integrates high preconcentration ability of ITP and high resolution capacity of CZE. Besides having the highest preconcentration ability among all electrophoretic preconcentration techniques, ITP has several unique advantages which makes it particularly suited for online-preconcentration in CZE [137,138]. Firstly, the ultimate preconcentration ability of ITP is independent of the sample conductivity [139]. This is contrast to other electrophoretic preconcentration techniques in which high conductivity samples can interfere with preconcentration mechanisms and cause significant dispersion of stacked analytes. Further, ITP can be used to selectively focus target analytes while eliminating unwanted impurities. Selective focusing in ITP can be achieved by correctly choosing LE and TE ions whose mobilities bracket only those of the target analytes and not of other contaminant species. Even if excess amounts of impurities are present in the sample, ITP tends to normalize their concentrations to the level of LE ion concentration. That is, concentrations of trace species and excess impurities tend toward similar concentrations as ITP progresses, decreasing the impurity-to-trace species concentration ratio. Lastly, ITP preconcentration provides an ideal method for sample injection prior to CZE as ITP focusing of trace analytes yields a narrow zone of overlapping analyte peaks (typically order 10-50 µm wide peaks), and this improves separation resolution [140]. Since coupling of ITP and CZE involves an initial, temporary ITP focusing of analytes, these methods are usually referred to as transient ITP-CZE (tITP-CZE).

Several methods exist for coupling ITP and CZE, and all leverage the fact that disruption of ITP focusing results in electrophoretic separation of analytes. Since ITP involves focusing of analyte ions between zones of relatively high mobility LE ions and low mobility TE co-ions, CZE can be triggered by either: (1) *disrupting zone order*, such that LE and TE zones no longer (spatially) sandwich analyte zones, or (2) *changing mobility order of species*, such that the mobility value of analytes is no longer bound by those of LE and TE ions. Here, we present a brief review of these principles of coupling ITP and CZE. We present a comprehensive review and comparison of these methodologies elsewhere [1].

6.1.1 Triggering CZE by disrupting zone order in ITP

One approach to trigger electrophoretic separation is to disrupt the spatial, front-to-back, LE-sample-TE zone order of ITP such that analytes are no longer led by LE and trailed by TE. The simplest way to do this is to reverse the direction of applied electric field during ITP, causing complete and immediate reversal of LE, analyte, and TE zone orders. However, this approach does not yield meaningful electrophoretic separations as the associated, prolonged conductivity gradients induced by the long-time mixing of LE and TE co-ions into each other results in excessive electromigration dispersion of analyte zones. This mixing causes conductivity and electric field gradients which act to “stretch” and mix analyte zones in a way that is highly detrimental to separation.

The highest resolution CZE separation following ITP preconcentration is achieved by effecting a process which transitions quickly from the discontinuous LE-sample-TE co-ion system of ITP to a condition approaching a locally uniform BGE for the analytes. Uniform BGE ensures that analyte ions can freely overtake or lag behind co-ions of BGE without the electromigration-dispersion of analyte zones associated with gradients in electric field caused by BGE conductivity gradients. That is, efficient transition from ITP to CZE can be ensured by replacing the LE-sample-TE zone order of ITP by condition which locally approximates a homogenous BGE and sample mixture. In practice, to simplify the disruption of ITP zone order, either LE or TE is chosen as the BGE for CZE. Transitions from ITP to CZE are therefore most often achieved by replacing the TE zone with LE, or vice versa [138,141]. For example, when LE ions are introduced behind the TE zone, LE ions overtake the TE zone, and migrate into and through the focused analyte zones. This eventually exposes focused analyte ions to a region whose electric field is dominated by LE ions, forcing analyte ions to defocus and separate.

tITP-CZE methods based on disruption of LE-sample-TE zone order of ITP are applicable to a wide range of ionic species and do not require specialized electrolyte chemistry. However, transition from ITP to CZE in these methods is gradual and depends strongly on the mobility of analytes and electrolyte chemistry [142]. As a result methods based on disruption of ITP zone order have typically low separation resolution, and migration time of analyte zones cannot be used easily for peak assignments [142]. Several methods exist which can potentially address these limitations by ensuring faster ITP-to-CZE transition during disruption of ITP zone order [1]. However, all those methods require specialized hardware, such as column-coupled channels [137,138,140,141] or accurate external pressure controllers for applying hydrodynamic counter-flow [143–146].

6.1.2 Triggering CZE from ITP by changing mobility order of species

Another approach to couple ITP and CZE involves sudden change in electrophoretic mobility(ies) of species such that analyte mobilities are no longer bracketed by those of LE and TE ions. Consequently, analytes fall out of ITP focusing mode and separate based on their electrophoretic mobilities. There are two primary ways of changing order of species mobilities in ITP to trigger CZE. The first method is mostly applicable to tITP-CZE of macromolecular analytes, such as nucleic acids and proteins, whose mobilities are strong functions of the local concentration of a sieving medium. In this approach, a sharp, spatial gradient in sieving matrix concentration is employed to shift the mobility of focused macromolecules below the mobility of TE ions, thereby initiating CZE. tITP-CZE induced by sieving matrix gradients yields high resolution and repeatable separations. However, these methods may require significant experimental preparation, for example, to prepare in situ polymerized sieving gels and also involve difficulties in replacing and reusing those gels [18].

Coupling of ITP and CZE can alternatively be realized through pH induced variations in mobility of weak electrolyte species. In this approach, a spatial pH gradient is imposed on ITP to change the relative magnitudes of effective mobilities of analyte, TE, and/or LE ions, such that analytes cease to focus in ITP and start to separate in CZE. pH gradients have been used successfully in conjunction with a gradient in sieving matrix concentration to change the relative mobility order of species in ITP and trigger CZE [147,148]. Despite their applicability, pH gradients have not yet been employed as a standalone means of coupling ITP and CZE.

6.1.3 Current work

In the current work we leverage bidirectional ITP to focus analytes via one ITP interface and simultaneously generate a strong pH gradient across a second, counter-migrating ITP interface. These counter-migrating anionic and cationic ITP shock waves subsequently interact and trigger a transformation from ITP preconcentration to electrophoretic separation. Traditional ITP buffer systems use only two co-ionic species (leading and trailing) and a single counter-ionic species. Here, our bidirectional experiments require four species (i.e., two oppositely-charged pairs of leading and trailing ions) which we term LE+, LE-, TE+, and TE-. Here, LE and TE again denote the leading and the trailing electrolyte ions, respectively, and + and – correspond to cations and anions, respectively. We explore the case of anionic analytes initially focused between TE- and LE-. Before the anionic and cationic ITP shocks meet, the counter-ion of the focused analyte zones is LE+. After these shocks meet, TE+ replaces LE+ as the counter-ion for analyte zones. This changes the pH such that ITP focusing conditions for analyte ions no longer hold and consequently analytes begin to separate electrophoretically. The method negates the need for deactivating power during the experiment or manual buffer exchanges as in typical tITP-CZE experiments based on disruption of ITP zone order [140,149,150].

We begin by describing the principle of coupling ITP preconcentration and electrophoretic separation using bidirectional ITP with converging anionic and cationic ITP shock waves. We discuss choices of electrolyte chemistries appropriate for coupling ITP focusing and electrophoretic separation. We then present simulations to illustrate the technique and verify our choice of electrolyte chemistry. We confirm these simulations by experimental visualization of interacting anionic and cationic ITP shocks. Using simulations, we then compare the separation resolution of bidirectional ITP and unidirectional tITP-CZE based on disruption of ITP zone order. Lastly, using our technique we experimentally demonstrate coupled ITP preconcentration and high resolution separation of a 1 kbp dsDNA ladder.

6.2 Theory

6.2.1 Concept of initiating electrophoresis *via* ITP shock interaction

In ITP, analyte ions focus only if their charge has the same sign as respective LE and TE ions. Two other requirements for focusing analyte ions are that analyte ions should have higher effective mobility (μ) than TE ions in both TE and analyte zones,

$$\left|\mu_{a,T}\right| > \left|\mu_{te,T}\right|, \quad \left|\mu_{a,A}\right| > \left|\mu_{te,A}\right|, \tag{6.1}$$

and that the effective mobility of analyte ions should be smaller than that of LE ions in both LE and analyte zones [135],

$$\left|\mu_{a,L}\right| < \left|\mu_{le,L}\right|, \quad \left|\mu_{a,A}\right| < \left|\mu_{le,A}\right|. \tag{6.2}$$

In our notation, the first (small case) subscript indicates the chemical species and the second (capital) subscript indicates the zone of interest. Subscripts *a*, *te*, *le* therefore denote analyte, TE and LE ions, respectively, while subscripts *A*, *T*, *L* denote analyte, TE and LE zones.

Whether and when the ITP focusing conditions given by eqs. (6.1) and (6.2) are valid depends strongly on local conditions, as effective mobility is a strong function of pH [108] and a weaker function of ionic strength [15]. For example, the effective mobility of a weak acid analyte increases monotonically with increasing pH, and saturates at the lowest (negative) valence. Conversely, the effective mobility of a weak base decreases with increasing pH may saturate at the highest valence. In this work, we will consider only singly ionized ions so that the aforementioned saturation values are the fully-ionized mobilities of the +1 cation and -1 anion, respectively. See Persat et al. [108] for a review of the interplay between electromigration and buffer chemistry, particularly effective mobility versus pH.

In this work we use bidirectional ITP with converging shocks to quickly and precisely alter the pH of migrating ITP zones so that analytes isotachophoretically focus before the shock interaction, and electrophoretically separate thereafter. Figure 6.1 shows a schematic of our technique. We fill a simple, straight channel with a mixture of LE+, LE- and anionic analytes (S1- and S2-) as shown in Figure 6.1a. LE+ and LE- serve as leading electrolyte ions for cationic and anionic ITP, respectively. We fill the reservoir on the left with a mixture of TE- and LE+ (LE+ acts as the counter-ion). Similarly we fill the reservoir on the right with TE+ and LE-. For anionic ITP we choose LE-, TE- and background counter-ion (LE+) such that ITP focusing conditions, eqs. (6.1) and (6.2), hold for analytes S1- and S2- prior to the shock interaction. As shown in Figure 6.1b, when voltage is applied across the channel, S1- and S2- focus between the LE- and the TE- zones. The anionic ITP (LE-/TE- interface) shock propagates towards the right and the cationic ITP shock (LE+/TE+ interface) propagates towards the left. Subsequently, the shocks meet and interact. The LE+/TE+ shock sweeps over the focused anionic analytes, replacing the local LE+ counter-ions with TE+ ions. In this newly created region where TE+ ions replaced the LE+ ions, the pH and effective mobilities of the buffer and analyte ions change. To initiate electrophoretic separation, we choose the conditions such that the effective mobility of TE- in the newly created zone is larger than the effective mobilities of S1- and S2-. This causes TE- ions to overtake and pass the analyte zones. Thereafter, S1- and S2- separate, as in capillary zone electrophoresis (Figure 6.1c). In Chapter 7, we describe an alternate electrolyte system wherein shock interaction causes the mobility of LE- ions to decrease below the mobility of analytes. This causes analyte ions to overtake LE- ions after the shock interaction and separate in bidirectional ITP.

In our bidirectional ITP experiments, the cationic ITP interface plays no role in the initial ITP focusing of analytes at the anionic ITP interface. The purpose of cationic ITP is to initiate electrophoretic separation of these analytes upon interaction of the anionic and cationic ITP shocks. We note that our technique, therefore, differs markedly from unidirectional tITP-CZE [140,149,150] wherein LE ions are injected behind focused anionic samples to initiate separation.

There are several choices to be made in designing ITP shock interactions which initiate electrophoretic separation. We here focus our discussion on choosing electrolytes (LE+, LE-, TE+, and TE-) to preconcentrate and separate strongly ionized analytes, such as nucleic acids. However, we note that our technique is also applicable to a wide variety of cases including that of weak electrolyte species. In Appendix H, we describe a strategy of choosing electrolytes for the case of weakly acidic species, and present an example simulation of preconcentration and separation of two amino acids using bidirectional ITP. For the case of strongly ionized analytes, we choose a high fully ionized mobility (absolute mobility) weak base for the LE+, and stronger base with low mobility for TE+. This creates a pH gradient across the initial LE+/TE+ shock, with a higher pH on the cationic TE+ side. For the anionic ITP component, we choose from relatively strong acids for LE-. We then choose a weaker acid for TE-, but one which has a high fully-ionized mobility. The latter is the key choice as we will use bidirectional ITP to effect a titration of the TE- (weak acid) to create TE- ions which overtake analyte ions after the shock interaction.

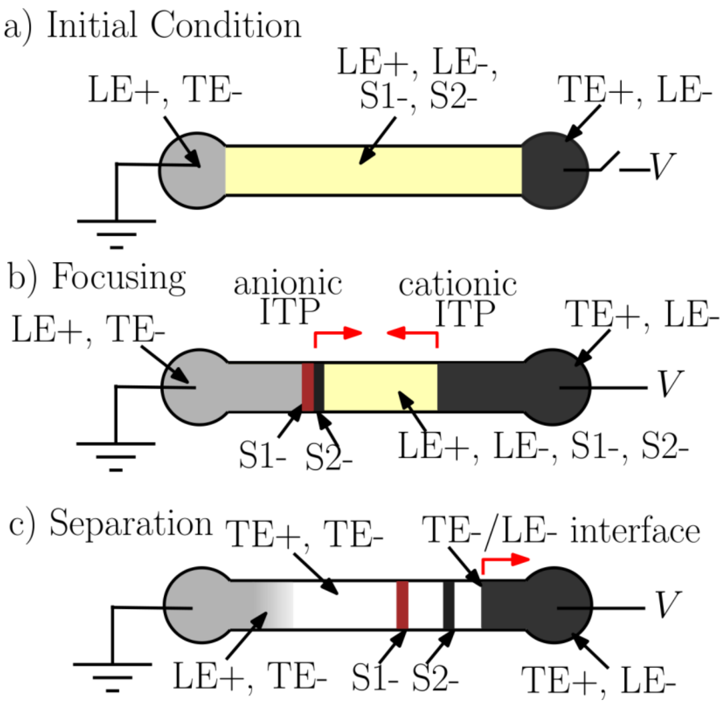

Figure 6.1: Schematic illustrating focusing and separation of analytes using bidirectional ITP. (a) The channel is initially filled with a mixture of LE+, LE- and analytes S1- and S2-. The reservoir on the left is filled with LE+/ TE- mixture, while the reservoir on the right is filled with TE+/LE- mixture. Buffers are chosen such that, LE+ is a cation of a weak base with high mobility and TE+ is a cation of a strong base with low mobility. Furthermore, LE- is an anion of a strong acid with high mobility and TE- is an anion of weak acid with low mobility. b) When voltage is applied, the anionic analytes focus between LE- and TE-. The focused analyte zones propagate towards the right. Simultaneously, a leftward-propagating cationic ITP shock forms between LE+ and TE+ zones. Because TE+ is a stronger base than LE+, TE+ raises the pH behind the LE+/TE+ shock. (c) When the LE+/TE+ shock washes over the focused anionic analytes, it similarly raises the pH of anionic ITP zones. The increase in pH of anionic ITP zones increases the local value of the effective mobility of TE- (an anion of a weak acid). Thereafter, TE- ions overtake the focused analyte ions, breaking the ITP focusing conditions for S1- and S2-. Consequently, the anionic analytes S1- and S2- cease focusing and commence electrophoretic separation.

After the shock interaction, TE+ (cation of strong base) replaces LE+ (cation of weak base) as the counter-ion for anionic ITP. This increases the local pH of anionic ITP zones and therefore raises the raises the local value of effective mobility of TE- ions. In contrast, the effective mobilities of LE- ions and the anionic analytes do not change appreciably after the shock interaction as they are anions of relatively stronger acids. If we make these choices correctly, the shock interaction causes the effective mobility of

TE- to increase to a value larger than that of analyte ions. This then violates the ITP focusing condition given by eq. (6.1) and initiates electrophoretic separation. This transition from focusing to separation is analogous in function to unidirectional tITP-CZE based on disruption of ITP zone order [140,149,150].

However, in unidirectional tITP-CZE LE ions are injected behind the focused analytes (typically by deactivating applied current and effecting a buffer exchange at the TE reservoir [150]) to initiate electrophoretic separation. Here we use the titration caused by the interaction between cationic and anionic ITP shocks to effect a change in the mobility of TE ions, such that they themselves overtake the focused analytes. Our method therefore features an initial condition which governs both focusing and separation dynamics, and the transition from ITP to separation can be initiated automatically with no buffer exchange or intermediate injections. As we show below, our method also achieves this transition with much less dispersion of the focused analytes compared to that in unidirectional tITP-CZE.

We here provide specific examples of viable electrolyte chemistries for our method. Note that a key requirement is that the LE+ should be a cation of a weak base with high fully-ionized mobility, while TE+ should be a cation of a strong base with low fully-ionized mobility. For strong base, fast cations we can use Na^+ and K^+. However, several choices exist for high fully-ionized mobility cations of weak bases and low fully-ionized mobility cations of strong bases. Table 6.1 shows three choices each for cationic LE and TE (nine usable combinations of LE+ and TE+) which satisfy our requirements. Another requirement is that the effective mobility of TE- ions should be less than that of analyte ions when the buffering counter-ion is LE+ and otherwise when the counter-ion is TE+. In order to effect a substantial increase in effective mobility of TE- after the shock interaction, TE- should therefore be a weak acid such that $pK_{a,LE+} < pK_{a,TE-} < pK_{a,TE+}$. For example, in our experiments we used tricine ($pK_{a,TE-} = 8.15$) as TE- along with imidazole ($pK_{a,LE+} = 7.15$) as LE+ and arginine ($pK_{a,TE+} = 8.92$) as TE+. On the other hand, there are no specific constraints on LE-, which can be any fast ion such as Cl^- and SO_4^{2-}.

We note that our bidirectional ITP experiments are compatible with both "semi-infinite" and "finite" sample injection schemes. For example, in Figure 6.1a we show a semi-infinite sample injection scheme, wherein sample ions are initially mixed in the LE-/LE+ mixture. Such an injection scheme both increases sensitivity (by continuously focusing sample until the shock interaction), and minimizes the complexity of the injection protocol. Alternatively, semi-infinite sample injection can be performed by mixing the sample ions in the TE-/LE+ reservoir. As a third alternative, sample ions can be injected using a more traditional finite injection protocol, wherein a finite amount of analyte mixture is initially sandwiched between pure LE-/LE+ and TE-/LE+ zones. However, we emphasize that the choice of sample injection scheme does not have a significant effect on the transition from ITP to CZE mode or the quality of CZE separation.

Table 6.1: Possible cationic buffer systems for coupled preconcentration and separation of anions using bidirectional ITP. Note that arginine has two other ionization states corresponding to $\mathrm{p}K_{a,-1} = 12.48$ and $\mathrm{p}K_{a,+2} = 1.78$. However, arginine is primarily disassociated in its +1 state under safe pH conditions of 5 < pH < 9.

cationic LE (LE+)	μ_{+1} ($\times 10^{-9}$ m^{2}V^{-1}s^{-1})	p$K_{a,+1}$
Imidazole	52	7.15
3-methyl pyridine	40.1	5.5
4-methyl pyridine	40.1	6.1
cationic TE (TE+)	μ_{+1} ($\times 10^{-9}$ m^{2}V^{-1}s^{-1})	p$K_{a,+1}$
Arginine	26.9	8.92
Tris	29.5	8.08
Amediol	33.5	8.78

6.2.2 Simulations of bidirectional ITP for focusing and separation of analytes

We performed simulations of coupled ITP focusing and electrophoretic separation of two model analytes in bidirectional ITP using the SPRESSO simulation tool [58,63] with SLIP scheme (discussed in Chapter 2). For our simulations we used 75 mM HCl as LE-, 20 mM tricine as TE-, 150 mM imidazole as LE+ and 30 mM arginine as TE+. To illustrate the technique we used two model anionic analytes S1- and S2- for the simulation with mobilities -20×10^{-9} $m^2V^{-1}s^{-1}$ and -12×10^{-9} $m^2V^{-1}s^{-1}$, respectively. These analytes were assumed to be fully ionized under the conditions of simulation. Figure 6.2a and Figure 6.2b show the initial conditions of the simulation. Analytes S1- and S2- were initially mixed in the LE-/LE+ mixture at a concentration of 15 µM and 10 µM, respectively. When electric field is applied, LE-/TE- and LE+/TE+ shocks propagate towards the right and the left, respectively. Prior to shock interaction, analytes S1- and S2- focus between the LE- and TE- ions, as shown in Figure 6.2d. For this particular buffer chemistry, LE+ and TE+ form a shared cationic ITP zone as shown in Figure 6.2c. (We see a shared zone since the effective mobility of LE+ ions in the TE+ zone is smaller than that of TE+ ions, but the effective mobility of LE+ ions in the LE+ zone is greater than that of TE+ ions.) When the LE+/TE+ and LE-/TE- shocks interact the effective mobility of TE- increases and it overtakes the focused analytes S1- and S2-. This initiates electrophoretic separation of S1- and S2-. Figure 6.2g and Figure 6.2h show the final state where both analyte ions, S1- and S2-, are fully separated. We note that, for electrophoretic separation to occur it is necessary for TE- ions to overtake the focused analytes. However, TE- ions need not overtake LE- ions and the LE-/TE- shock may persist, as shown in Figure 6.2g and Figure 6.2h. In contrast, the shock interaction interrupts the LE+/TE+ interface and this interface mixes (via electromigration dispersion) thereafter. That is, after the shock interaction, TE- replaces LE- as the counter-ion for cationic ITP. Since the conjugate acid of TE- is weaker than the conjugate acid of LE-, the pH of cationic ITP zones increases after the shock interaction. As a result, the effective mobility of LE+ (cation of a weak base) decreases considerably compared to TE+ (cation of a strong base), causing disruption of the cationic ITP interface.

Simulation results, shown in Figure 6.2 highlight the advantages of focusing and separation using bidirectional ITP over unidirectional tITP-CZE. As shown in Figure 6.2e and Figure 6.2f, TE- ions begin overtaking focused analyte ions (S1- and S2-) as soon as the LE+/TE+ shock wave washes over the focused analyte ions. Thus, the transition from focusing to separation occurs quickly after shock interaction. This is in contrast with unidirectional tITP-CZE, in which LE ions injected behind the TE zone must first overtake the entire TE zone before disrupting the ITP focusing [140,149,151].

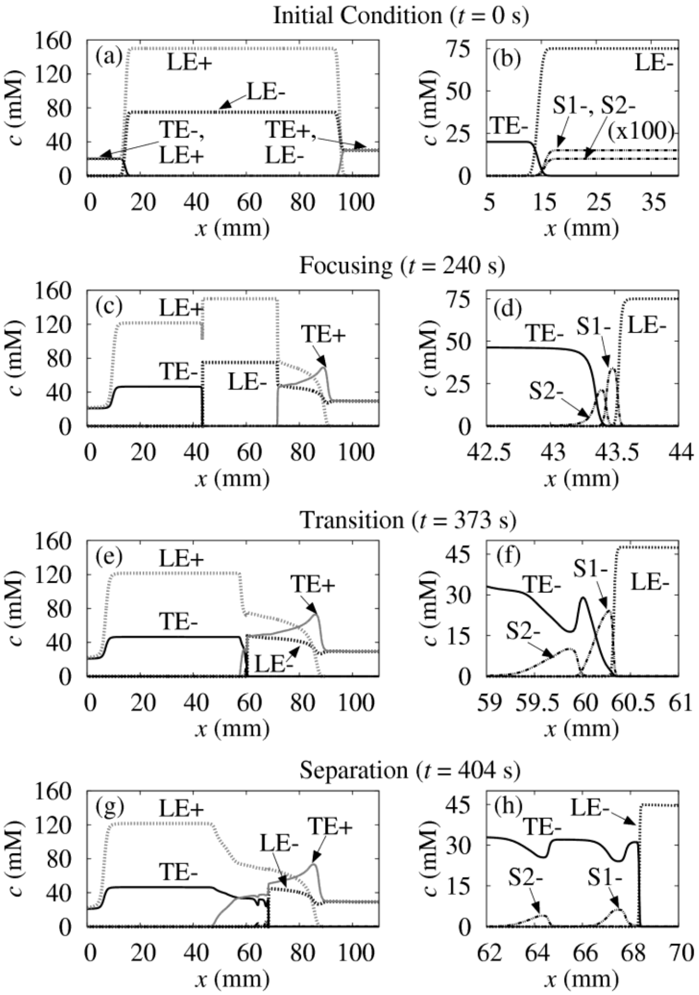

Figure 6.2: Simulation showing focusing and separation of species using bidirectional ITP. Plots in second column are detailed views of the distributions in the first column. (a-b) show the initial distribution of chemical species in the separation channel, prior to activating current. (c-d) show LE-/TE- and LE+/TE+ shocks after the electric field is applied. (c) shows an LE-/TE- shock (*x* = 43 mm) propagating rightward and a LE+/TE+ shock (*x* = 70 mm) propagating leftward. (d) shows anionic analytes S1- and S2- focused between LE- and TE-. (e-f) show the transition from focusing to separation upon the interaction of LE-/TE- and LE+/TE+ ITP shocks. The high pH TE+ zone washes over the focused anionic analytes, increasing the effective mobility of TE- ions, while only negligibly affecting the mobility of S1- and S2- which are stronger acids. Here, the effective mobility of TE- increases above those of S1- and S2-, thereby initiating separation. (f) shows TE- overtaking focused S1- and S2-, thus initiating electrophoretic separation. (g-h) show the final state, in which analytes S1- and S2- are fully separated. (h) shows fully separated peaks of S1- and S2-, but an intact ITP interface between LE- and TE-. Chemistry is described in text. We assumed a constant current of 1.4 µA, and a D-shaped, wet-etched channel 74 µm wide and 12 µm deep. We approximately account for electroosmotic flow using a constant and uniform electroosmotic mobility of 2×10^{-9} $m^2V^{-1}s^{-1}$.

More importantly, in unidirectional tITP-CZE, LE ions injected behind the TE zone first tail into analyte zones and effect a longer, more gradual disruption of ITP focusing [141,150]. The latter can lead to significant electromigration dispersion of the analyte zones prior to separation. Here, we observe a rapid change of local electromigration conditions (from ITP to zone electrophoresis separation) during which we observe negligible dispersion. (In Section 6.2.3 we compare the separation resolution of bidirectional ITP and unidirectional tITP-CZE using numerical simulations.) Rapid transition from ITP to CE in our technique is especially important for on-chip systems where channel lengths may be limited. Finally, the transition from focusing to separation in bidirectional ITP is fully automated and does not require buffer replacement or switching electric field between column-coupled channels as in traditional tITP-CZE [141]. Thus the current technique can be easily adapted for on- or off-chip single channel systems, including commercial CE systems.

We also performed a simulation at conditions where we can directly compare numerical predictions with experimental visualization of interacting shocks waves. For this, we used the same ITP chemistry and the initial conditions as in the previous simulation (Figure 6.2), but instead of analytes S1- and S2-, we used a fluorescent non-focusing tracer (NFT). The NFT does not disturb or change the ITP or focus during ITP, but its concentration adapts to the local electric fields in each ITP zone (see Figure 6.3a). Thus the regions of varying fluorescence intensity highlight and denote different ITP zones (more on NFT visualization technique [47] in Section 6.4.1).

Figure 6.3a shows a simulated spatiotemporal plot of the fluorescence intensity of the fluorescent NFT in the channel during bidirectional ITP. The scalar quantity plotted here is the fluorescence intensity of NFT (averaged along the channel width) as a function of distance along the axis of the channel (abscissa) and time (ordinate). Our simulation neglects the effects of photobleaching and we assume a linear relationship between fluorescence intensity and the NFT concentration. The plot shows an anionic ITP (LE-/TE-) shock and a cationic ITP (LE+/TE+) shock propagating towards the right and the left, respectively. After these shock waves meet, the rightward traveling LE-/TE- shock remains intact as LE- ions (Cl^-) have higher effective mobility than TE- ions (tricine) even after the shock interaction. On the other hand, shock interaction disrupts the leftward propagating LE+/TE+ shock, creating a rarefaction wave (the zones gradually mix via electromigration dispersion). In this simulation we used a constant electroosmotic mobility of 2×10^{-9} $m^2V^{-1}s^{-1}$ as our only fitting parameter to match all experimentally measured wave speeds (see Section 6.4.1).

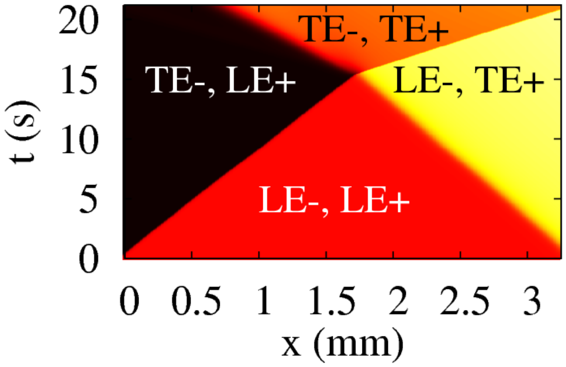
(a) Simulation

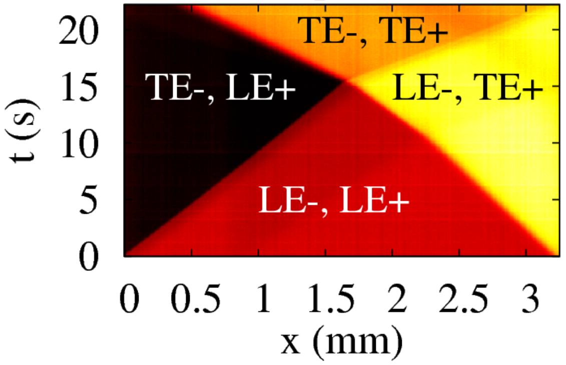
(b) Experiment

Figure 6.3: Numerical simulation and experimental visualization of interacting anionic and cationic ITP shocks. (a) shows numerical simulation of propagating LE-/TE- and LE+/TE+ shocks. The spatiotemporal plot shows the intensity of a fluorescent non-focusing tracer (NFT) [47] versus distance along the channel axis, x, and time, t. The NFT does not focus via ITP, but its concentration adapts to the local electric field in each zone. Regions of different fluorescence intensity mark ITP zones. (b) shows experimental visualization of the same process using the fluorescent non-focusing tracer (NFT) technique [47]. Both (a) and (b) show LE-/TE- and LE+/TE+ shocks propagating towards the right and left, respectively. These shocks meet near $x = 1.6$ mm. The rightward traveling LE-/TE- shock remains intact (positive slope to the right of $x = 1.6$ mm). In contrast, the LE+/TE+ interface is disrupted and the interface starts to mix (barely noticeable in this field of view). To account for electroosmotic flow in our simulation, we used a constant electroosmotic mobility of 2×10^{-9} $m^2V^{-1}s^{-1}$. We used Rhodamine 6G as the NFT. We applied 1.4 μA current across a D-shaped, wet-etched 74 μm wide and 12 μm deep channel.

6.2.3 Comparison of bidirectional ITP and unidirectional tITP-CZE

We here compare traditional unidirectional tITP-CZE and bidirectional ITP using numerical simulations. Figure 6.4a and Figure 6.4b respectively show simulated spatiotemporal plots of these two cases. In both cases, we consider the same anionic analytes (S1- and S2-) as in Figure 6.2 but, to aid in visualization of various ITP zones, we also consider addition of a NFT which is initially mixed with LE-/LE+ buffer. The background fluorescence intensity values in Figure 6.4a and Figure 6.4b therefore correspond to the concentration of NFT in the various ITP zones, while the brighter zones correspond to the analyte peaks.

For the unidirectional anionic tITP-CZE simulations, we used the anionic ITP chemistry (with LE+ as the counter-ion), channel geometry and applied current of the simulation of Figure 6.2. Traditional unidirectional anionic tITP-CZE does not involve cationic ITP, so we did not use TE+ in the unidirectional tITP-CZE simulations. We first performed simulation of ITP focusing of analyte ions, S1- and S2-, between zones of LE- and TE- ions. We then stopped the simulation and replaced TE- ions in the TE-/LE+ reservoir (near the leftmost boundary) with LE- ions; this initiated the process of disrupting ITP. Figure 6.4a shows S1- and S2- ions initially focused in a narrow ITP zone which propagates rightwards at a constant speed (the constant slope line for $t < 25$). Around $t = 25$ s and $x = 4$ mm, LE- ions begin overtaking the focused analytes and initiate electrophoretic separation of S1- and S2-. Figure 6.4a shows the separation phase of unidirectional tITP-CZE for $t > 25$ s, during which the distance between the analyte peaks increases over time, while the peaks themselves broaden due to diffusion and electromigration dispersion. Interestingly, during the transition from ITP focusing to CE separation, the speed of analyte zones decreases considerably. This deceleration of analyte zones is apparent in Figure 6.4a, where the analyte peak locations vary nonlinearly with time after $t = 25$ s. Similar deceleration of analyte zones in unidirectional tITP-CZE has been observed experimentally by Chambers and Santiago [47]. The transition phase in unidirectional tITP-CZE is slow, analytes zones disperse, and the distance between the analyte peaks does not exceed their characteristic widths until about $t = 90$ s.

For the bidirectional ITP simulation (Figure 6.4b) we used the same conditions as those of Figure 6.2, including the electrolyte chemistry, applied current and the channel geometry; the only difference being the presence of NFT in Figure 6.4b. We note that the results shown in Figure 6.2 and Figure 6.4b are quite similar, as the presence of the NFT in trace amounts (100 µM initial concentration) has a negligible effect on local electric fields, and focusing and separation of S1- and S2-. Figure 6.4b shows the LE-/TE- shock wave propagating towards the right and the LE+/TE+ shock wave propagating towards the left (for $t < 25$ s). Analytes S1- and S2- initially focus at the LE-/TE- interface. When the LE-/TE- and LE+/TE+ shock waves interact around $x = 4$ mm and $t = 25$ s, ITP focusing of S1- and S2- very quickly transitions to CE separation. Thereafter (for $t > 25$ s), the relative distance between S1- and S2- peaks keeps increasing, while the peaks gradually diffuse over time.

Comparison of Figure 6.4a and Figure 6.4b shows that the analyte peaks in bidirectional ITP are much better resolved than in unidirectional tITP-CZE. That is, for the same distance between the two peaks, the peaks in bidirectional ITP are much less dispersed than in unidirectional tITP-CZE. Bidirectional ITP yields higher resolution separations since the ITP-to-CE transition in bidirectional ITP occurs quickly after the anionic and cationic ITP shocks interact. Thus analytes are exposed to local conductivity gradients (which cause electromigration dispersion) for much shorter distance and time. In contrast, in unidirectional tITP-CZE, LE- ions injected behind the TE- zone tail significantly into the focused analyte zones and only gradually and slowly disrupt ITP preconcentration [141,150], yielding significant and prolonged electromigration dispersion. In addition to better resolution, the faster ITP-to-CE transition offered by bidirectional ITP results in reduced separation time and increased signal-to-noise ratio for a given resolution. Compare for example the resolution obtained by bidirectional ITP in Figure 6.4b at $t = 45$ s. Such resolution is not observed in the unidirectional tITP-CZE case (Figure 6.4a) even at $t = 150$ s.

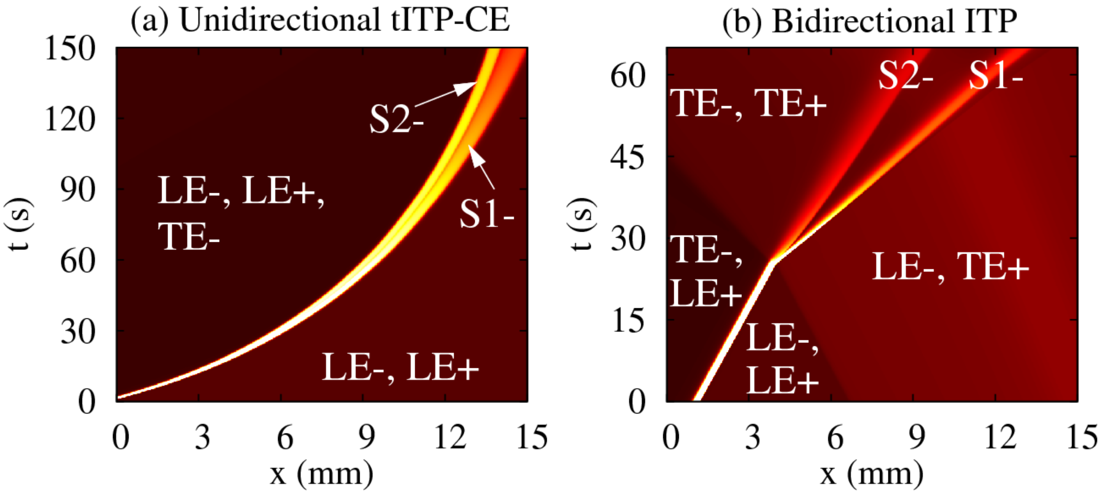

Figure 6.4: Simulations comparing unidirectional transient ITP-CZE (tITP-CZE) and bidirectional ITP. (a) and (b) respectively show simulated spatiotemporal diagrams of focusing and separation of two anionic species (S1- and S2-) in unidirectional tITP-CZE and bidirectional ITP. Both plots show fluorescence intensity of S1-, S2- and a non-focusing tracer (NFT) [47] versus distance along the channel axis, *x*, and time, *t*. Background fluorescence values correspond to NFT concentration in various ITP zones. The brighter zones correspond to the analyte peaks. (a) shows unidirectional tITP-CZE process where S1- and S2- are initially ($t < 25$ s) focused in a narrow zone. This focused ITP zone propagates towards the right, until it is disrupted by the overtaking LE- ions. Around $t = 25$ s, ITP focusing is disrupted and S1- and S2- zone start separating. This transition is gradual and yields significant electromigration dispersion . (b) shows S1- and S2- ions initially ($t < 25$ s) focused at the LE-/TE- interface of bidirectional ITP. The LE-/TE- shock propagates rightward (positive slope for $t < 25$ s), while the LE+/TE+ shock propagates leftward. These shocks interact near $x = 4$ mm at $t = 25$ s, and very quickly initiate electrophoretic separation of S1- and S2-. This fast ITP-to-CE transition results in much less electromigration dispersion, higher separation resolution, and smaller analysis time. Chemistry used here described in the text. The channel dimensions, applied current, and EOF mobility were the same as those used for Figure 6.2.

6.3 Materials and Methods

We performed experiments to visualize interacting cationic and anionic ITP shock waves in bidirectional ITP using the fluorescent non-focusing tracer (NFT) technique [47] (c.f. Section 6.4.1). For these visualization experiments, LE- was the chloride ion from 75 mM HCl, TE- was 20 mM tricine, LE+ was 150 mM imidazole and TE+ was

30 mM arginine. We prepared 10 mM stock solution of the Rhodamine 6G dye (Invitrogen, Carlsbad, CA) and used it as an NFT by mixing at a concentration of 100 µM in the LE+/LE- mixture.

For the experiments demonstrating coupled ITP preconcentration and separation of DNA fragments (Section 6.4.2) we used chloride ion from 150 mM HCl as LE-, 20 mM tricine as TE-, 300 mM imidazole as LE+ and 30 mM arginine as TE+. We added a 1kbp DNA ladder from New England BioLabs (Ipswich, MA) to the mixture of LE+ and LE-, with final concentration of 50 ng/ml. We used 0.75% w/w hydroxyl ethyl cellulose (HEC) as a sieving matrix (mixed with LE-) to achieve a size-dependence on the mobility of fragments, as the free solution mobility of dsDNA fragments greater than ~400 bp is effectively independent of molecular weight [152]. To visualize the DNA fragments, we used the fluorescent intercalating dye SYBR Green I (Invitrogen, Carlsbad, CA). (We note that intercalating dyes, such as SYBR Green I, should be handled carefully due to their potential mutagenic properties [153].)

We prepared 1 M stock solutions of HCl, tricine and imidazole, and 300 mM stock solution of arginine hydrochloride before diluting them to desirable concentrations in different solutions. We added 1% w/w polyvinylpyrrolidone (PVP) to all solutions in order to suppress electroosmotic flow. All chemicals were obtained from Sigma Aldrich (St. Louis, MO) and were prepared in UltraPure DNase/RNase free distilled water (GIBCO Invitrogen, Carlsbad, CA). We captured images using an inverted epifluorescent microscope (IX70, Olympus, Hauppauge, NY) equipped with a LED lamp (LEDC1, Thor Labs, Newton, NJ), U-MWIBA filter-cube from Olympus (460-490 nm excitation, 515 nm emission, and 505 nm cut off dichroic) and a 10X (NA = 0.3) UPlanApo objective (Olympus, Hauppauge, NY). Images were captured using a 12 bit, 1300x1030 pixel array CCD camera (Micromax1300, Princeton Instruments, Trenton NJ). We controlled the camera using Winview32 (Princeton Instruments, Trenton NJ) and processed the images with MATLAB (R2007b, Mathworks, Natwick, MA). We conducted the experiments by applying either constant voltage or current using a sourcemeter (model 2410, Keithley Instruments, Cleveland, OH).

For all our experiments, we used off-the-shelf Caliper NS-95 borosilicate glass micro-chips from Caliper Life Sciences (Mountain View, CA). Figure 6.4a shows a schematic of the channels with cross-geometry. The channels consist of a wider loading section (50 µm mask width) and a narrower separation section (10 µm mask width). All channels are wet etched to a depth of 12 µm. The variable cross-section geometry allows us to achieve higher sensitivity in ITP by focusing a large amount of sample in the loading section prior to entering the separation channel [87,88].

6.4 Experiments

We first performed on-chip bidirectional ITP experiments to visualize interacting cationic and anionic ITP shock waves. For these experiments, we did not focus analytes, but instead visualized the interaction of cationic and anionic LE/TE interfaces. We used these visualization experiments to optimize our injection protocol to precisely control the location of shock interaction. We then performed bidirectional ITP experiments to demonstrate coupled preconcentration and high resolution separation of DNA fragments from 1 kbp dsDNA ladder.

6.4.1 Visualization of interacting shocks in bidirectional ITP

We visualized interacting anionic and cationic ITP shocks in bidirectional ITP using the NFT technique [47]. In the NFT technique, fluorescent, co-ionic species which do not obey the ITP focusing conditions given by eqs. (6.1) and (6.2) are mixed with the ITP buffers. These fluorescent species do not focus, but their concentration adapts to local electric field in different ITP zones in order to maintain the continuity of electromigration flux. For our experiments, we used 100 µM concentration of Rhodamine 6G (R6G, a cationic dye) in the LE+/LE- mixture as the NFT. In our experiments R6G is slower than the cationic TE ions and so does not focus. Hence, we visualized propagating anionic and cationic ITP shock waves simultaneously using a single non-focusing fluorescent species (Rhodamine 6G). The experimental protocol for these experiments is similar to that shown in Figure 6.1. We performed experiments in Caliper NS-95 chip shown schematically in Figure 6.5 with a cross-geometry. However, we applied electric field only across the longer channel, and visualized shock interaction in the large cross-sectional area region connecting West reservoir (see Figure 6.5).

Figure 6.3b shows an experimentally measured spatiotemporal plot of fluorescence intensity in a bidirectional ITP experiment with converging shock waves. To obtain this spatiotemporal plot, we captured CCD camera images of fluorescence intensity in a 3.25 mm long section of the channel at a rate of 10 frames per second. We then width-averaged the fluorescent intensity for 210 images and plotted this axial intensity distribution for each point (in time) along the ordinate. In Figure 6.3b, the abscissa is axial distance along the channel, the ordinate is time, and the intensity of plotted scalar is the measured fluorescence intensity. The slopes of features in such spatiotemporal plots are therefore inversely proportional to the velocities of ITP zone interfaces. Figure 6.3b show that, prior to the shock interaction ($t < 15$ s), the LE-/TE- shock propagates towards the right and the LE+/TE+ shock towards the left. After the LE-/TE- and LE+/TE+ shocks interact (at $x = 1.6$ mm and $t = 15$ s), the LE+/TE+ interface is disrupted and a rarefaction wave ensues. This is because the effective mobility of TE+ becomes higher than LE+ after the shock interaction. However after the shock interaction ($t > 15$s), the LE-/TE- interface remains intact as the mobility of fully-ionized chloride ion (LE-) remains higher than the effective mobility of tricine (TE-) throughout the experiment. Our experimental visualization results compare well with the simulated spatiotemporal diagram shown in Figure 6.3a. Our simulations correctly predict the persistence of LE-/TE- interface and the disruption of LE+/TE+ interface after the shock interaction. We use an electroosmotic mobility value of 2×10^{-9} $\mathrm{m^2V^{-1}s^{-1}}$ as the only fitting parameter, and yet the simulations correctly predict the time and the location of shock interaction and the four observable propagation velocities.

We note that experimental visualization and simulations of interacting shocks in bidirectional ITP are particularly helpful in tuning the initial conditions to precisely select the location of shock interaction and transition from ITP focusing to electrophoretic separation. For our experiments on DNA separations (Section 6.4.2) we used a NFT [47] to tune our injection protocol to initiate electrophoretic separation as soon as the focused analytes entered the narrow separation channel. This allowed us to obtain higher resolution by using the entirety of the separation channel for the CE mode.

6.4.2 Coupled preconcentration and separation of DNA fragments

We performed experiments to demonstrate coupled ITP preconcentration and electrophoretic separation of DNA fragments using bidirectional ITP. The injection protocol for these experiments is shown in Figure 6.5. Briefly, we first filled all channels with a mixture of LE+, LE- and DNA fragments. We then emptied the East and the West well and filled them with TE+/LE- mixture and LE+/TE- mixture, respectively. We then moved the LE+/TE+ interface up to the junction by applying voltage across East and South wells. This optional step ensured that the LE+/TE+ shock interacted with focused anions earlier in the narrow separation channel. We then applied voltage across the East and the West wells and visualized separated DNA fragments at the end of separation channel. (We note that precaution should be taken and the high voltage supply should be turned off while manually switching electrodes as shown in Figure 6.5.)

As shown in Figure 6.5d, prior to the shock interaction, the 1kbp dsDNA ladder is focused between the LE- and the TE- zones. When the LE+/TE+ shock washes over the focused DNA fragments, both the pH of the TE- zone and the effective mobility of TE- ions increase. However, under the conditions of our experiments (pH > 7), DNA fragments are fully ionized and any increase in pH has no significant effect on the effective mobility of DNA fragments. TE- ions, therefore, overtake focused DNA after the shock interaction, initiating electrophoretic separation in the HEC sieving matrix (shown schematically in Figure 6.5e). In our experiments, we used a semi-infinite injection scheme by mixing DNA fragments with the LE- and LE+ mixture in order to increase the sensitivity by continuously focusing DNA fragments until the shock interaction. We note that the DNA fragments can also be initially mixed with LE+/TE- mixture.

Figure 6.6 shows the results of DNA preconcentration and separation using bidirectional ITP. Initially, all DNA fragments are focused in a thin zone between the LE- and TE- zones (Figure 6.6a). Later, the shock interaction initiates CE separation of focused DNA fragments. The initial phase of CE separation is shown in Figure 6.6b. Figure 6.6c shows an electropherogram measured at the end of separation channel showing a fully resolved DNA ladder consisting of distinct peaks 1 to 11 corresponding to the 10, 8, 6, 5, 4, 3, 2, 1.5, 1, 0.517, and 0.500 kbp fragments. The electropherogram from our experiments is in qualitative agreement with slab-gel separations of the same DNA ladder (provided by the vendor, New England BioLabs, Ipswich, MA).

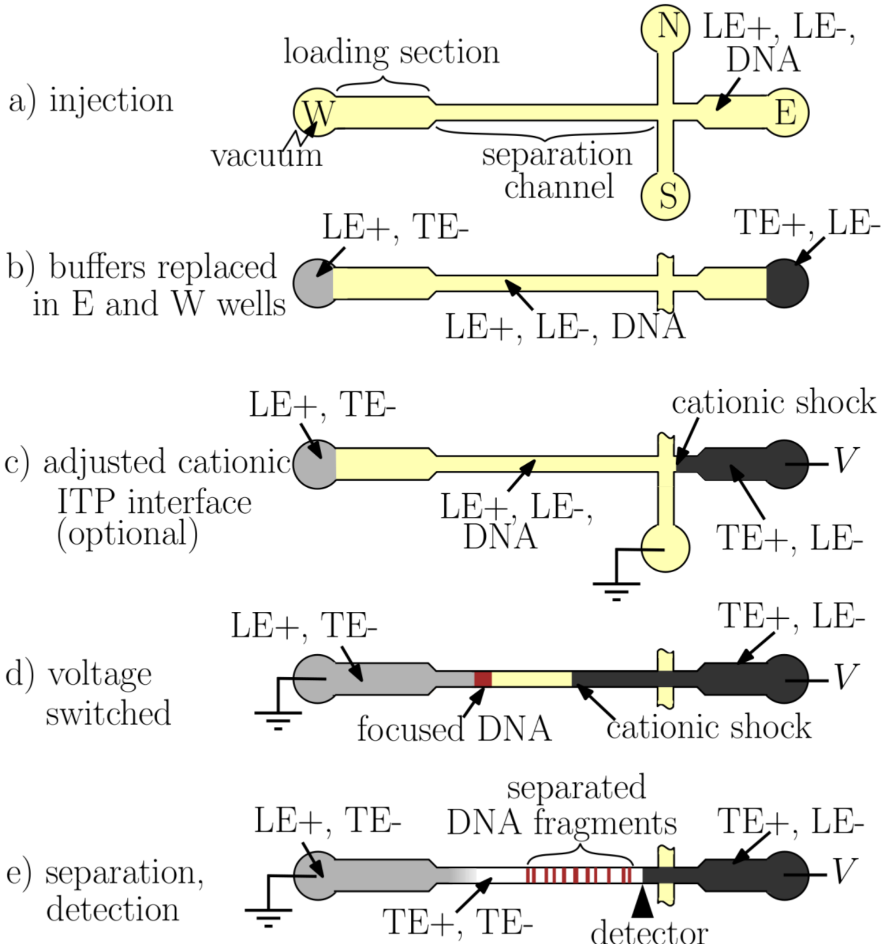
a) injection
loading section
N
LE+, LE-, DNA
W
E
vacuum
separation channel
S
b) buffers replaced in E and W wells
LE+, TE-
TE+, LE-
LE+, LE-, DNA
c) adjusted cationic ITP interface (optional)
LE+, TE-
cationic shock
V
LE+, LE-, DNA
TE+, LE-
d) voltage switched
LE+, TE-
TE+, LE-
V
focused DNA
cationic shock
e) separation, detection
LE+, TE-
separated DNA fragments
TE+, LE-
V
TE+, TE-
detector

Figure 6.5: Protocol for DNA separations using bidirectional ITP leveraging channel cross-sectional area reduction for increased sensitivity. For separation experiments with finite sample loading: (a) we injected the mixture of LE+, LE- and DNA fragments by applying vacuum on W well. We then emptied E and W wells and (b) filled E and W wells with TE+/LE- mixture and LE+/ TE- mixture, respectively. (c) We then moved the LE+/TE+ interface up to the junction by applying voltage between E and S wells. We performed this optional step to ensure that the LE-/TE- and LE+/TE+ shocks interacted precisely near the entrance of the separation channel (the smaller cross-section channel). (d) We then switched the electrodes between E and W wells. The LE+/TE+ shock meets the focused DNA fragments and initiates electrophoretic separation. (e) We imaged the separated DNA fragments at the end of the separation channel. Injection protocol for semi-infinite injection of samples is similar, except that the analytes of interest (here DNA fragments) are initially mixed with LE+/TE- mixture in the W well. No manual buffer exchanges are needed once voltage is applied, and we stress that the voltage switching used here is optional.

We note that peaks 10a and 10b (corresponding to 500 and 517 bp) are clearly resolved by our technique (see Figure 6.6c) but not resolved in agarose-gel electrophoresis (*e.g.*, Figure 6.5d). These distinct peaks corresponding to 500 and 517 bp have also been observed for this ladder in higher resolution separations on polyacrylamide gels [154]. For these experiments, we diluted the DNA to 50 ng/ml concentration in the LE+/LE- mixture with only 1 pg DNA initially injected into the separation channel.

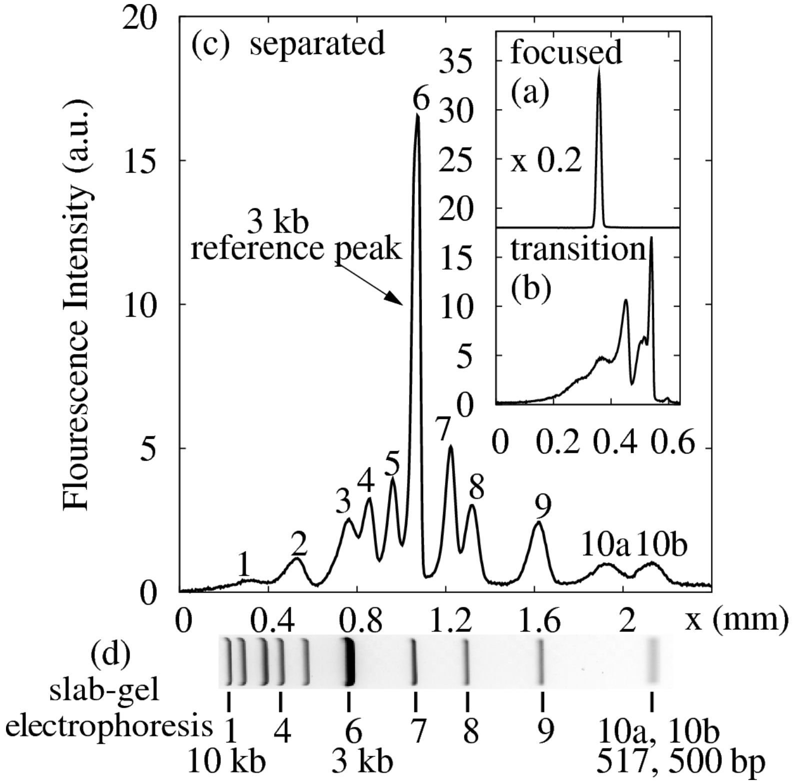

Figure 6.6: Experimental preconcentration and separation of 1 kbp dsDNA ladder using bidirectional ITP. (a) shows initially focused DNA fragments in anionic ITP. (b) shows the transition from focusing to separation after the cationic ITP interface washes over the focused DNA fragments. (c) shows fully resolved DNA ladder with 11 peaks at the end of separation channel. (d) shows visualization (inverted) of agarose gel electrophoresis separation (provided by the vendor, New England BioLabs, Ipswich, MA). Note that the agarose gel does not resolve peaks 10a and 10b corresponding to 517 and 500 bp fragments. The electropherogram at (c) is measured 15 mm to the right of the point where the shocks interact. For this experiment we used a semi-infinite injection of DNA sample to increase the detection sensitivity and minimize the injection complexity.

6.5 Summary

We have developed a new technique to automatically couple isotachophoretic preconcentration and electrophoretic separation via shock interaction in bidirectional ITP. We have described how interaction of cationic and anionic ITP shocks in converging bidirectional ITP can lead to fundamental changes in focusing behavior of analytes. We leveraged shock interaction in bidirectional ITP to precisely change the pH of migrating zones, so that initially focused analytes initiate electrophoretic separation upon shock interaction. To the best of our knowledge, this is the first time that shock interaction in bidirectional ITP has been leveraged to couple different electrophoresis modes.

We discussed practical choices of electrolyte chemistries for bidirectional ITP which give electrophoretic separation after the interaction of cationic and anionic ITP shocks. To illustrate the technique and verify our choice of buffer chemistry we performed numerical simulations using 1-D area averaged electromigration-diffusion transport equations. Based on these simulations, we showed that the transition from focusing to separation in bidirectional ITP is fast and results in negligible electromigration dispersion of electrophoretic zones. We confirmed the simulation results with indirect fluorescence visualization experiments of bidirectional ITP zones. Using a single fitting parameter (electroosmotic mobility) we showed that our simulations capture accurately the observed dynamics of shock interaction, including shock velocities and disruption of ITP interfaces after shock interaction. We then used simulations to compare separation resolution of bidirectional ITP and unidirectional tITP-CZE. Our simulations show that bidirectional ITP yields separations with significantly higher resolution and shorter analysis time compared to unidirectional tITP-CZE. Finally, as an example application we used bidirectional ITP to couple ITP preconcentration and high resolution electrophoretic separation of DNA fragments of a 1 kbp DNA ladder. We fully resolve the ladder in 7 min (only 3 min after shock interaction) starting from a 30 µl sample dispensed into chip reservoir at 50 ng/ml concentration (after which ~1 pg of DNA injected into the channel) and using no manual steps.

Shock interaction in bidirectional ITP is an elegant way to couple ITP preconcentration and electrophoretic separation. The method eliminates the need for intermediate steps such as buffer exchange and deactivation and re-activation of a power supply. Unlike unidirectional tITP-CZE, transition from focusing to separation in bidirectional ITP occurs over a relatively small distance (here order 100 µm) allowing optimal use of channel length for the ITP focusing and electrophoretic separation phases. This aspect is particularly important for on-chip systems which have constraints on maximum channel length. The technique can also be applied to conventional single channel CE systems (*e.g.*, using fused silica capillaries), and eliminates the need of column-coupled channels for buffer replacement.

7 Integration of rapid DNA hybridization and capillary zone electrophoresis using bidirectional isotachophoresis

The contents of this chapter are based on an article by S.S. Bahga, C.M. Han and J.G. Santiago [155] in *Analyst*. S.S. Bahga and C.M. Han contributed equally to this work. S.S. Bahga developed the bidirectional ITP based methodology to couple ITP and CZE, and C.M. Han developed the methodology for accelerating DNA hybridization using ITP. The details presented here deal with contribution of S.S. Bahga to the above manuscript, and are reproduced here with minor modifications.

7.1 Introduction

DNA hybridization is essential to a wide range of diagnostics and biological sample processing steps. For example, DNA hybridization is deployed in methods for genetic profiling [156] and many nucleic acid based pathogen detection assays [157]. However, slow, second-order hybridization kinetics at low concentrations of DNA samples often results in long analysis times [158], limiting assay speed and applicability.

We here present a novel combination of two recently-demonstrated methods for DNA analysis. The first is the use of isotachophoresis (ITP) to achieve rapid, sequence-specific DNA hybridization [159]. The second is bidirectional ITP which uses a strong counter-migrating pH gradient across a cationic ITP interface to disrupt ITP preconcentration and trigger capillary zone electrophoresis separation (CZE) [131], as discussed in Chapter 6. This combination is unique and relevant as it integrates the rapid hybridization enabled by ITP with high resolution separation of reaction products by CZE. ITP can rapidly mix and preconcentrate single-stranded DNA (ssDNA) fragments within a small (order 10 pL) reaction zone, thus accelerate the rate of hybridization. The method was first demonstrated experimentally by Persat et al. [160], who applied it to the profiling of micro-RNA. Bercovici et al. [161] applied ITP based hybridization to the extraction and detection of 16S ribosomal RNA (rRNA) of *E. coli* in human urine samples. Recently, Bercovici et al. [159] presented a detailed study of the physicochemical processes which govern DNA hybridization under ITP focusing. The latter study used molecular beacons [162] (MBs) to quantify reaction rates, and demonstrated 14,000-fold reduction in hybridization time.

MBs provide a sequence-specific fluorescence signal increase upon hybridization [162], but also limit sensitivity and dynamic range of assay due to the background signal from unreacted MBs [163]. We here present a method that directly addresses the issue of relatively high background signal in ITP based hybridization assays by effecting CZE separation to separate unreacted labelled probes from target-probe hybrids. Further, CZE separation of DNA reaction products provides a simple way to extend the functionality of ITP based hybridization assays for multiplexed, sequence-specific detection of nucleic acids. We trigger CZE separation using bidirectional ITP which uses the interaction of anionic and cationic ITP fronts to effect strong changes in the physicochemical environment of the focused analyte zone (see Chapter 6). Here, the interaction of these fronts disrupts ITP focusing of analytes (products of DNA hybridization reaction) and initiates CZE.

Analysis of DNA hybridization reaction products using CZE was originally demonstrated by Chen et al. [164] as a method for removal of background signal from the products of hybridization reaction between a synthetic oligonucleotide and a fluorescently labelled probe. Later, Bianchi et al. [165] applied hybridization and CZE on polymerase chain reaction (PCR) products, to detect HIV-1 genomic sequences. However, these and other previous studies performed a slow, off-line DNA hybridization followed by manual transfer and loading of the hybridization products into an electrophoresis setup. Our combination integrates rapid ITP-hybridization and CZE separation in a single, integrated process where no manual steps are required after initiating ITP. Further, our method allows rapid detection of multiple-length ssDNA targets having a common portion in their sequences.

7.2 Coupling rapid ITP based DNA hybridization and CZE

In ITP, analytes focus between zones of high effective mobility leading electrolyte (LE) ions and low effective mobility trailing electrolyte (TE) ions. ITP is characterized by self-sharpening and electromigrating interfaces (or ion-concentration shock waves [7,134]) between adjacent zones, which prevent focused analytes from diffusing over time. Our assay uses bidirectional ITP, which involves simultaneous anionic and cationic ITP processes in a single microchannel or capillary, as discussed in Chapter 6. Our experiments therefore require two oppositely charged pairs of LE and TE ions. Here we term these ions LE+, TE+, LE-, and TE-. LE and TE denote the leading and trailing electrolyte ions, respectively, and + and – correspond to cations and anions, respectively.

Figure 7.1 shows schematic of our technique. We fill the separation channel with a mixture of LE- and LE+ ions. We fill the right (anodic) reservoir with the TE+/LE- mixture, and similarly the left (cathodic) reservoir with a mixture of LE+, TE-, ssDNA target, and the molecular beacon probe. When electric field is applied along the channel (Figure 7.1b), the target and the probe preconcentrate, mix, and react at the interface of LE- and TE- zones while propagating rightwards. Simultaneously, a cationic ITP shock forms between LE+ and TE+ zones near the right reservoir, and propagates leftwards. Anionic ITP preconcentration of target and molecular beacon probe results in rapid hybridization and corresponding increase in fluorescence signal. Later, when the anionic and the cationic ITP shocks interact (Figure 7.1c), LE+ is replaced with TE+ as the counter-ion for anionic ITP. This counter-ion exchange decreases the local pH of anionic ITP zones to a value at which effective mobility of LE- becomes significantly lower than the mobilities of all DNA fragments. Thus, shock wave interaction causes target, probe, and target-probe hybrid to migrate into the LE zone, triggering electrophoretic separation of the products of hybridization and unreacted species (see Bahga and Santiago [1] for an exhaustive review of methods to integrate ITP and CZE). The electropherogram signal shows peaks corresponding to the target-probe hybrid and the unreacted probe (the unreacted target has no attached fluorophore). The separation of products removes background signal associated with unreacted MB probes, and enables simultaneous identification of multiple length targets.

Here, we chose the following electrolyte chemistry: 150 mM sodium bicarbonate for LE+/LE- mixture; 10 mM sodium hydroxide and 34 mM HEPES for the LE+/ TE- mixture; and 100 mM pyridine and 50 mM hydrochloric acid for the TE+/LE- mixture (cationic TE). Note that the cationic TE mixture is titrated with hydrochloric acid instead of carbonic acid. However this does not affect our bidirectional ITP experiments as chloride ion remains in the anodic reservoir and does not enter the separation channel.

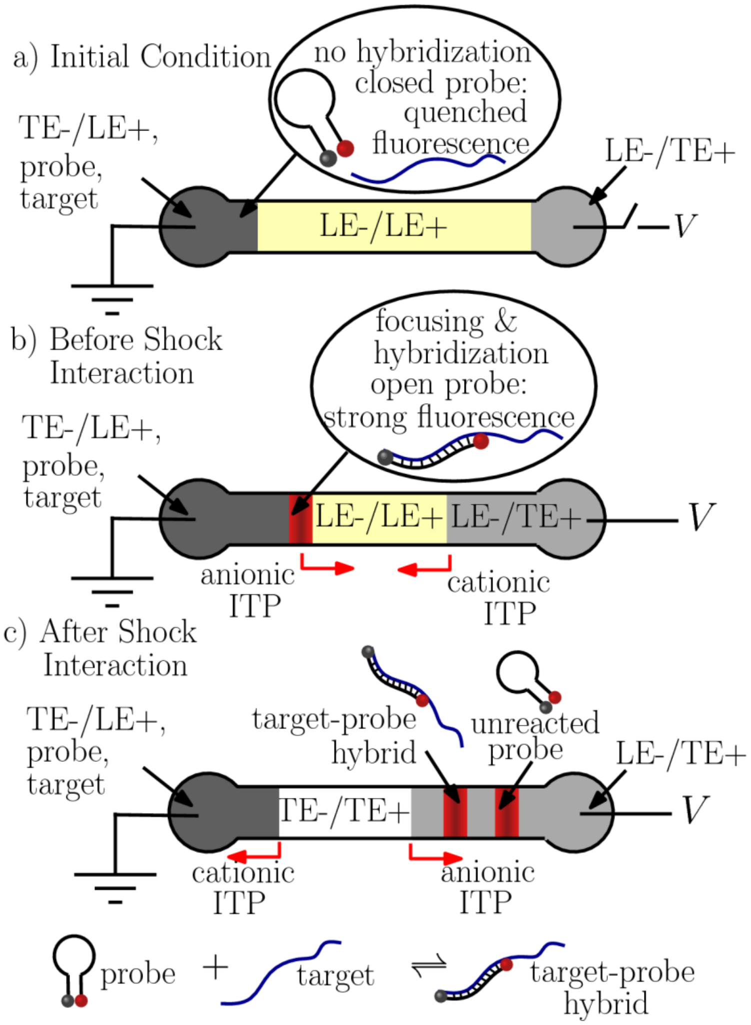
a) Initial Condition
no hybridization
closed probe:
quenched
fluorescence
TE-/LE+,
probe,
target
LE-/TE+
LE-/LE+
V
b) Before Shock
Interaction
focusing &
hybridization
open probe:
strong fluorescence
TE-/LE+,
probe,
target
LE-/LE+
LE-/TE+
V
anionic
ITP
cationic
ITP
c) After Shock
Interaction
TE-/LE+,
probe,
target
target-probe
hybrid
unreacted
probe
LE-/TE+
TE-/TE+
V
cationic
ITP
anionic
ITP
probe
+
target
⇌
target-probe
hybrid

Figure 7.1: Schematic of preconcentration and hybridization of nucleic acids followed by electrophoretic separation of reaction products using bidirectional ITP. (a) The channel is initially filled with LE+/LE- mixture. The left (cathodic) reservoir is filled with a mixture of TE-, LE+, ssDNA target and probe (molecular beacon). The right (anodic) reservoir is filled with the TE+/LE- mixture. (b) When voltage is applied, the target and the probe focus at the anionic ITP interface and propagate rightwards. Simultaneously, a cationic ITP interface forms near the right reservoir and propagates leftwards. Anionic ITP preconcentration dramatically accelerates hybridization between the target and probe. (c) At a later time, the cationic ITP interface interacts with focused hybridization products, and triggers CZE separation. The resulting electropherogram shows peaks corresponding to the fluorescent unreacted probe and the target-probe hybrid.

Prior to shock interaction, pH of anionic ITP zones is around 8.1. At this pH, effective mobilities of LE- and TE- ions bracket the mobility of DNA fragments. Therefore, DNA fragments focus in anionic ITP. After shock interaction, pyridine (TE+, $pK_{a,+1} = 5.2$) replaces sodium (LE+, $pK_{a,+1} = 13.7$) as the counter-ion for anionic ITP. Pyridine is a weaker base than sodium hydroxide and so lowers the pH of anionic ITP zones to a value of ~5.7, which is lower than the $pK_{a,-1}$ of carbonic acid ($pK_{a,-1} = 6.4$, $pK_{a,-2} = 10.3$). Therefore, the effective mobility of LE- becomes significantly smaller than the mobility of DNA fragments (which is fairly constant over pH > 5). Thus, shock interaction in our bidirectional ITP experiments causes DNA fragments to overtake the LE-/TE- interface and separate as in CE. Alternate choices of electrolyte chemistry for coupling ITP with CE using bidirectional ITP exist, and they are discussed in Chapter 6.

7.3 Materials and Methods

We performed bidirectional ITP experiments involving hybridization between MB probe and two synthetic ssDNA targets (39 and 90 nt) to demonstrate rapid DNA hybridization and separation. The 5’ and 3’ terminals of the MB probe were labeled with Cy5 and Black Hole Quencher 2 (BHQ2), respectively: 5’-/Cy5/CCG AGC [CAT CGT TTA CGG CGT GGA CTA CCA GGG] GCT CGG/BHQ2/-3’. Here, 27 bases within the brackets indicate a probe sequence complementary to a part of the 16S rRNA of *E. coli* bacteria [161]. The 39 and 90 nt ssDNA targets have a common 27 nt long portion of sequence which is perfectly complementary to the bracketed probe sequence. The 39 nt target sequence is TAG ATA [CCC TGG TAG TCC ACG CCG TAA ACG ATG] TCG AC; and 90 nt target sequence is GGA CGA AGA CTG ACG CTC AGG TGC GAA AGC GTG GGG AGC AAA CAG GAT TAG ATA [CCC TGG TAG TCC ACG CCG TAA ACG ATG] TCG ACT TGG. The target and probe DNA were obtained from Integrated DNA Technologies (IDT, Coralville, Iowa), and 10 µM probe and 100 µM target stock solutions were stored at -20°C.

For all experiments, we used the following respective initial concentrations: 150 mM sodium bicarbonate for LE+/LE- mixture; 10 mM sodium hydroxide and 34 mM HEPES for the LE+/ TE- mixture; and 100 mM pyridine and 50 mM hydrochloric acid for the TE+/LE- mixture (cationic TE). To the LE+/LE- mixture, we added 1% w/w of hydroxyl ethyl cellulose (HEC) to serve as a sieving matrix for DNA separations. We also added 1% w/w polyvinylpyrrolidone (PVP; MW 1.3 MDa; ACROS Organics, NJ) to all electrolyte solutions to suppress electroosmotic flow. All chemicals, except PVP, were obtained from Sigma Aldrich (St. Louis, MO). All solutions, including electrolytes, PVP and HEC, were prepared in UltraPure DNase/RNase-free deionized water (GIBCO Invitrogen, Carlsbad, CA).

We performed all experiments on an inverted epifluorescent microscope (IX70, Olympus, Hauppauge, NY) equipped with a Cy5 filter-cube (Cy5-4040A, Semrock, Rochester, NY). To capture spatiotemporal data (Figure 7.3) we used a 627 nm LED lamp (LEDC25, ThorLabs, Newton, NJ); a 4× (NA = 0.16) UPlanApo objective (Olympus, Hauppauge, NY); a CCD camera (Micromax1300, Princeton Instruments, Trenton NJ) triggered at a frame rate of 4.6 Hz. For ITP-CZE experiments for multiplexed detection (Figure 7.4) we used a custom point-wise confocal setup coupled to the microscope, described in detail by Bercovici et al. [162]. We applied constant current of 3 µA for the experiments shown in Figure 7.3, and constant voltage of 1 kV for the experiments shown in Figure 7.4. In both cases, we used a sourcemeter (model 2410, Keithley Instruments, Cleveland, OH, USA).

7.3.1 Microchip and experimental protocol

We used off-the-shelf Caliper NS12A crown glass microchips from Caliper Life Sciences (Mountain View, CA) for all our experiments. These microchips have four wet-etched channels (depth 20 µm and mask width 50 µm) laid in a cross-channel layout; we used the longest (45 mm) of the four channels for CZE experiments. Figure 7.2 shows a schematic of the microchip and the injection protocol. We first filled the North (N), South (S), and East (E) reservoirs of the chip with LE+/LE- mixture and applied vacuum to the West (W) reservoir until all four channels were filled with LE+/LE- mixture (Figure 7.2a). We then rinsed the E and W reservoirs with distilled water and filled them with cationic and anionic TE solutions, respectively (Figure 7.2b). To increase the amount of sample processed, we used continuous electrokinetic injection of the probe and the ssDNA targets by mixing them into the LE+/TE- mixture.

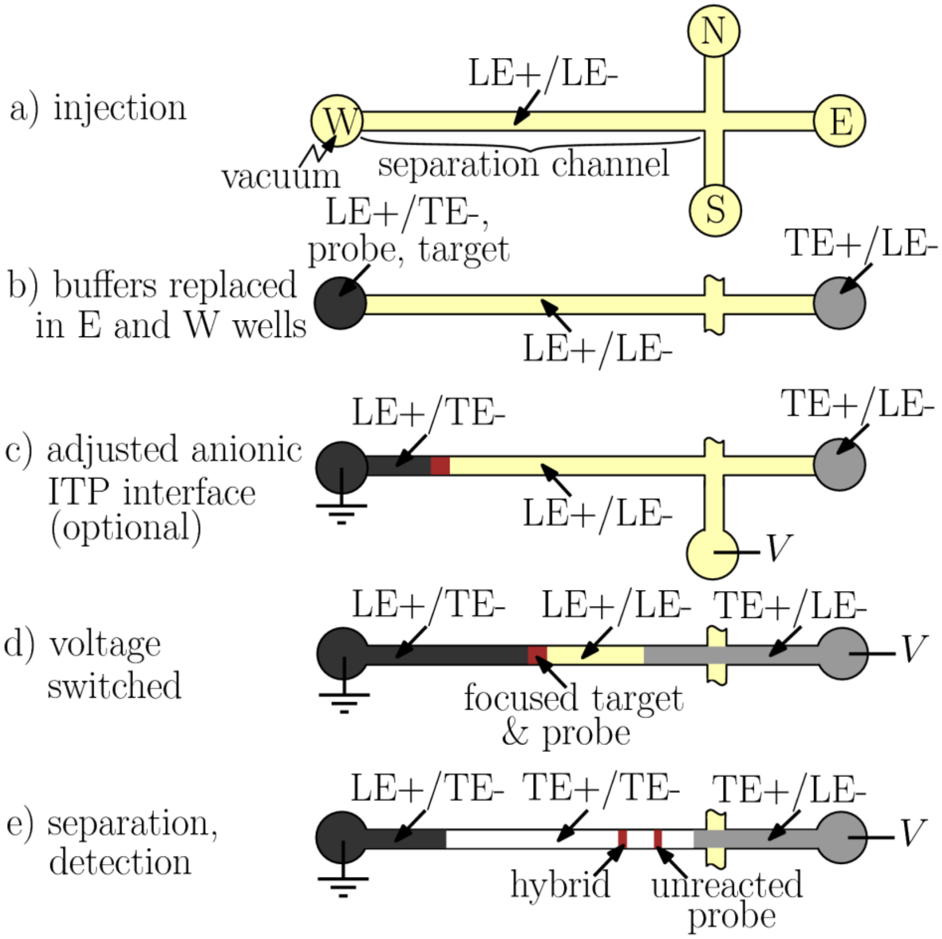
a) injection
LE+/LE-
N
W
E
vacuum
separation channel
S
LE+/TE-,
probe, target
TE+/LE-
b) buffers replaced
in E and W wells
LE+/LE-
LE+/TE-
TE+/LE-
c) adjusted anionic
ITP interface
(optional)
LE+/LE-
V
LE+/TE-
LE+/LE-
TE+/LE-
d) voltage
switched
V
focused target
& probe
LE+/TE-
TE+/TE-
TE+/LE-
e) separation,
detection
V
hybrid
unreacted
probe

Figure 7.2: Protocol for performing coupled ITP-based hybridization and CZE separation using bidirectional ITP. For bidirectional ITP experiments on Caliper NS 12A chips: (a) we injected LE+/LE- mixture by filling the N, S, and E wells, then applying vacuum to the W well. (b) We then emptied the E and W wells and filled them with TE+/LE- and LE+/TE- mixtures, respectively. The DNA target and probe were initially mixed with anionic TE (LE+/TE- mixture). (c) As an optional step, we preconcentrated target and probe DNA fragments in anionic ITP by applying voltage between W and S wells. This step is ensures that target and probe have longer time to hybridize. (d) We then switched voltage across E and W wells. This step initiates bidirectional ITP, and is therefore characterized by anionic and cationic ITP fronts approaching each other. (e) After shock interaction, unreacted probe and target-probe hybrid separate electrophoretically. We imaged the separated DNA fragments close to the cross-junction. We stress that, bidirectional ITP can be set up with simpler protocols without any voltage switching steps, such as that shown in Figure 7.1.

Also, to allow for longer hybridization time, we first focused target and probe DNA in unidirectional anionic ITP by applying 1 kV from the S to E reservoirs for 40 s (Figure 7.2c). This step is optional and can be eliminated if the microchannel or capillary is sufficiently long to allow for enough hybridization time. We then switched the 1 kV from the E to W reservoirs to initiate bidirectional ITP, and recorded the fluorescent intensity at a distance of 44 mm from the W reservoir (Figure 7.2d and Figure 7.2e).

7.4 Results and discussion

7.4.1 Experimental visualization of DNA hybridization and separation

We first performed bidirectional ITP experiments to visualize and demonstrate ITP hybridization followed by CZE separation of the reaction products. For these visualizations, we used relatively high concentrations of a 90 nt ssDNA target (20 nM) and 39 nt MB probe (500 nM) so as to capture full field images using a CCD camera. Figure 7.3 shows representative spatiotemporal plots of the experimentally measured fluorescence intensity in the channel (scalar) *versus* distance along the channel (abscissa) and time (ordinate). Figure 7.3a shows that, prior to the interaction of anionic and cationic ITP shocks ($t < 10$ s), the ssDNA target and MB probe mix, focus, and hybridize in a narrow anionic ITP zone. The focused analyte zone in anionic ITP shows a strong signal and migrates rightwards at constant velocity (i.e., a positive slope for $t < 10$ s in Figure 7.3a). The strong fluorescence signal during ITP is a result of preconcentration as well as hybridization-induced increase in fluorescence signal from the MB probe. At about $t = 10$ s, focused ssDNA target and MB probe interact with a counter-migrating cationic ITP front, and within less than 1 s previously focused analytes begin to separate in CZE mode. Initiation of separation is indicated by the sudden change in the migration speed (inverse of the slope in t *vs.* x plot) of the fluorescent zone around $t = 10$ s. Figure 7.3b and Figure 7.3c show separation of the unreacted probe and the target-probe hybrid at later times. As is usual with CZE, the analyte zones diffuse as they gradually separate over time. Note that excess, unreacted MB probe and inefficiencies in its fluorescence quenching yield peak fluorescent intensity comparable to that of the target-probe hybrid peak. Quantifying fluorescence from the target-probe hybrid in such a case is extremely difficult without removal of background signal from the unreacted probe.

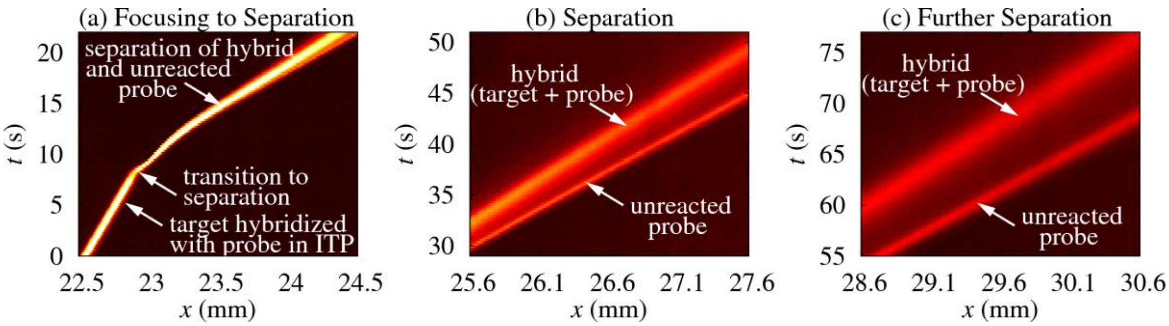

Figure 7.3: Experimental visualization of preconcentration and hybridization of nucleic acids followed by electrophoretic separation using bidirectional ITP. Spatiotemporal plots (a-c) show the intensity of fluorescent probe in channel versus the distance along the channel axis, x, and time, t. (a) Initially ($t < 10$ s), ssDNA target and MB probe mix, focus, and hybridize in anionic ITP. At $x = 23$ mm and $t = 10$ s, a counter migrating cationic ITP interface interacts with the focused analyte zones, initiating CZE separation. (b-c) show resolved peaks of fluorescent hybrid and unreacted probe in the CZE mode. Electrolyte chemistry and other experimental parameters are presented in Section 7.3.

7.4.2 Demonstration of multiplexed detection

We also performed experiments to demonstrate the feasibility of our assay for multiplexed detection of multiple-length ssDNA targets by simultaneously detecting 39 and 90 nt targets. The total assay time for these experiments was less than 3 min, including 40 s of hybridization time in unidirectional ITP. Figure 7.4 shows electropherograms for varying concentrations of 39 and 90 nt targets (order 100 pM concentrations) and a fixed concentration of MB probe (1 nM). We observed three well-resolved peaks corresponding to unreacted probe, and target-probe hybrids for 39 and 90 nt targets. For the control experiment where no targets were added to the system, electropherogram shows a single peak corresponding to unreacted probe. We identified the target-probe hybrid peaks by noting the relative change in peak intensities when the concentrations of 39 and 90 nt targets were individually varied in the initial sample (see Figure 7.4c and Figure 7.4d).

The electropherograms shown in Figure 7.4c and Figure 7.4d also highlight the high resolving power of this integrated ITP-CZE separation; here we separate and resolve single-stranded 39 nt probe from its double-stranded hybrid of the same length within about 50 s of separation time. Our method is significantly more sensitive and faster than existing electrophoretic separation based DNA hybridization assays such as Southern blotting [166] (order 10-100 µM sensitivity and 24 h assay time) and its capillary electrophoresis based alternatives (10-100 nM sensitivity and 1.5 h assay time) [164,165]..

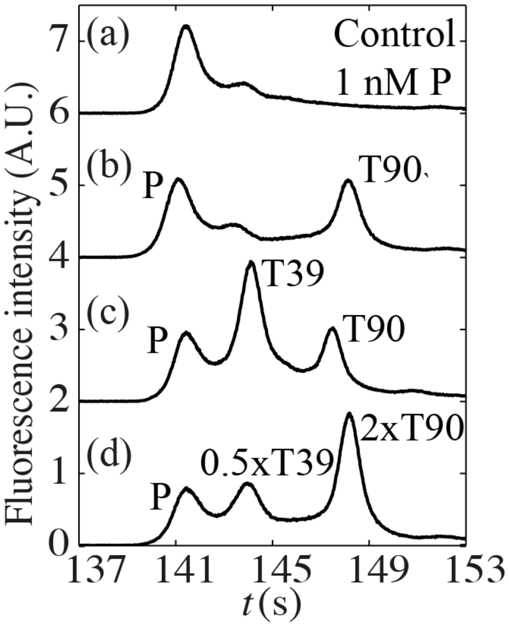

Figure 7.4: Multiplexed sequence-specific detection of two target oligonucleotides (39 and 90 nt) including the same 27 bases complementary to the molecular beacon probe. Plot shows fluorescent intensity of unreacted probe (P) and target-probe hybrids (T39 and T90) after hybridization and separation. (a) The control case, where no target was present, shows one dominant peak corresponding to the 1 nM probe. (b) When 200 pM of 90 nt target is added with the probe, a second peak corresponding to the hybrid of 90 nt target and probe (T90) appears. The separation between two peaks indicates the effective removal of excess probe from the hybrids. (c) Addition of 39 and 90 nt targets, respectively at 100 and 200 pM, to the probe yields three peaks respectively corresponding to P, T39, and T90. (d) We identified these peaks by noting the relative change in peak intensity upon varying the initial concentrations of 39 and 90 nt targets to 50 and 400 pM, respectively. For these data, we performed anionic ITP focusing for 40 s to enable longer hybridization time and then initiated bidirectional ITP. The abscissa shows the total analysis time, including anionic and bidirectional ITP (during hybridization stage). Electrolyte chemistry and channel geometry are the same as that in Figure 7.3.

One limitation of our assay is the limited choices of electrolyte systems that can ensure coupling of ITP and CZE via shock interaction in bidirectional ITP. Detailed guidelines to select electrolytes for coupling ITP and CZE using bidirectional ITP can be found in Chapter 6 along with several practical examples. We note that, besides bidirectional ITP, several other coupled ITP-CE methods exist [1], that can potentially be applied to this problem

7.5 Summary

We have demonstrated integration of ITP-based DNA hybridization and CZE separation of reaction products using bidirectional ITP, and applied it to sequence-specific detection of two ssDNA targets with a fluorescently-labeled DNA probe. Our method combines high preconcentration ability of ITP to accelerate slow DNA hybridization kinetics, and high resolving power of CZE to separate and identify reaction products. CZE separation of products of DNA hybridization reaction removes background signal associated with unreacted probes. This allows quantification of fluorescence from target-probe hybrid even when the signal from unbound MB well exceeds the hybridization signal. CZE separation of reaction products also provides a way of extending functionality of ITP-based hybridization to detect multiple-length DNA targets. Potential extensions of our method include multiplexed detection of a larger number of DNA targets and application to the identification of sequence variations in restriction fragments.

8 Conclusions and recommendations

In this chapter we summarize the contributions and conclusions of the work presented in this dissertation. We also present recommendations for future research directions based on this work.

8.1 Major Contributions

Here we highlight major contributions of the current work in improving state-of-the-art of electrokinetic simulations and developing ITP based methods for high-senstivity and high-resolution detection.

8.1.1 Modeling and simulation of nonlinear electrokinetic processes

8.1.1.1 Generalized model for quasi 1-D electrokinetic transport

1. We developed a generalized quasi 1-D model for multispecies electromigration-advection-diffusion transport in variable cross-sectional area channels, using area averaging of 3-D species transport equations. The model accounts for arbitrary, axial variation in channel cross-section, multispecies acid-base equilibrium, ionic strength effects on electrophoretic mobility and ionic activity, and Taylor-Aris [64,65] type dispersion due to non-uniform bulk flow.
2. We performed a detailed asymptotic analysis on 3-D electromigration-advection-diffusion equations to derive quasi 1-D governing equations in terms of area-averaged quantities. Our analysis is based on typical assumptions of lubrication theory, including long, thin channels with slowly varying channel cross-sectional area.
3. We showed using asymptotic analysis that, in absence of bulk flow, slow variations in channel cross-section yield small transverse variations in electric field and correspondingly minimal dispersion of concentration boundaries.
4. We showed that dispersion of concentration boundaries in electrolyte solutions due to non-uniform bulk flow differs from that of usual Taylor-Aris dispersion of a neutral solute advecting in bulk flow. Unlike Taylor-Aris dispersion of a neutral

solute, dispersion of ionic species is affected by the presence of other ionic species so as to maintain electroneutrality of bulk solution.

8.1.1.2 Simulations of quasi 1-D electrokinetic processes

1. We developed a conservative formulation of quasi 1-D governing equations for electrokinetic transport on a dynamically adapting grid, using a mapping function between the adapting physical domain and a stationary, uniform computational domain. This formulation allows construction of conservative finite volume schemes to ensure accurate mass conservation, along with dynamically adapting grid to simulate sharp concentration gradients.
2. We leveraged the Symmetric Limited Positive (SLIP) scheme to solve the quasi 1-D species transport equations and obtain unconditionally stable simulations of ITP and nonlinear CZE. The SLIP scheme selectively adds numerical diffusion at locations with sharp gradients and oscillations to ensure grid independent stability.
3. We developed a new adaptive grid refinement algorithm which improves the accuracy of otherwise dissipative SLIP scheme by migrating grid points from regions with low numerical diffusion to regions with higher numerical diffusion. Consequently, our numerical scheme requires an order of magnitude less grid points compared to existing dissipative schemes.
4. We verified our numerical method with simulations using sixth-order compact scheme for various nonlinear electrokinetics problems, including ITP and electromigration-dispersion in CZE. The current numerical scheme is more robust than non-dissipative schemes, such as the compact scheme, and yields stable simulations for the cases where the latter scheme results in oscillatory solutions.
5. We demonstrated the applicability of quasi 1-D simulations to predict increase in detection sensitivity of plateau mode and peak mode ITP in converging cross-sectional area channels.

8.1.1.3 Ionic strength effects on electrophoretic focusing and separation

1. We integrated models for ionic strength effects on electrophoretic mobility and ionic activity with our numerical solver. Our simulations use Onsager-Fuoss

model [80] to correct fully-ionized electrophoretic mobility and extended Debye Huckel theory [81] to correct ionic activity for finite ionic strength of electrolyte solutions.

2. We demonstrated the use of simulations with ionic strength effects in predicting qualitative and quantitative variations in ITP and CZE experiments at low and high ionic strengths. In particular, our simulations are able to capture experimentally observed decrease in focusing rate of multivalent ions in peak mode ITP at high ionic strengths, and reversal of peak locations in CZE at low and high ionic strengths.
3. We used simulations with ionic strength corrections to design a successful mobility marker assay for detection of an unlabeled analyte in ITP.

8.1.2 Methods for increasing detection sensitivity of ITP

8.1.2.1 ITP in converging cross-sectional area channels

1. We developed a methodology for designing microfluidic channels with converging cross-sectional area geometry to increase detection sensitivity of plateau mode ITP, while simultaneously reducing assay time.
2. We developed a diffusion-free model to simulate unsteady dynamics of plateau mode ITP in axially varying cross-sectional area channels. We benchmarked our diffusion-free model with comprehensive simulations of electromigration-diffusion equations. We then used the diffusion-free model to derive algebraic scaling relations for dependence of analyte zone length and assay time on geometric parameters.
3. We showed that for voltage limited systems, converging cross-sectional area geometry allows use of shorter channels to yield SNR comparable to that achieved by uniform cross-section channels. In addition, shorter channels with variable cross-sectional area yield significantly faster detection compared to uniform cross-section channels.
4. We validated our diffusion-free model with controlled plateau mode ITP experiments on a set of microfluidic channels with a wide range of cross-sectional area reductions, and with varying concentrations of a model analyte.

5. We demonstrated indirect fluorescence based detection of 100 nM model analyte in 5 min using ITP in a microfluidic chip with initially large and then small cross-sectional area channels.

8.1.2.2 Creating concentration cascade of leading electrolyte in bidirectional ITP

1. We developed a method for creating sharp, in situ gradients in LE concentration in single channel systems to enforce longer analyte zones in plateau mode ITP.
2. We demonstrated use of simultaneous anionic and cationic ITP processes in bidirectional ITP to focus analytes and create a concentration cascade of LE across the counter-migrating ITP shock wave. We demonstrated that shock wave interaction in bidirectional ITP can be used to effect sudden decrease in concentration of LE ions ahead of focused analytes, and thereby trigger elongation of analyte zones.
3. We developed an analytical model to predict the gain in analyte zone length due to shock wave interaction in bidirectional ITP. Using the analytical model we provided practical guidelines for choosing electrolyte chemistries to maximize detection sensitivity.
4. We presented 1-D simulations of analyte zone elongation due to shock wave interaction in bidirectional ITP, and validated them with simultaneous experimental visualizations of all bidirectional ITP zones.
5. Using simulations and a series of controlled experiments with varying proportion of cationic to anionic LE concentrations, we showed that gain in zone length of anionic analytes upon shock interaction increases with increase in ratio of cationic to anionic LE concentrations.
6. Based on simulation and experimental results, we designed an electrolyte chemistry for bidirectional ITP to demonstrate 20-fold increase in detection sensitivity of 2,4,6-trichlorophenol, a carcinogenic pollutant.

8.1.3 Coupling ITP and CZE for high-resolution detection

8.1.3.1 Method for coupling ITP and CZE using bidirectional ITP

1. We developed a technique to automatically couple isotachophoretic (ITP) preconcentration and electrophoretic separation in a single channel using interaction of anionic and cationic ITP shock waves in bidirectional ITP.
2. We described a methodology for effecting a sudden and large change in local pH of anionic ITP zones via shock interaction, such that initially focused analytes begin to separate electrophoretically after the shock interaction.
3. We discussed practical choices of bidirectional ITP chemistries that can be leveraged to couple ITP and CZE via shock interaction for analysis of both strong and weak electrolyte species.
4. We verified the choice of bidirectional ITP chemistry for coupling ITP and CZE by performing detailed numerical simulations. Based on simulations, we showed that bidirectional ITP based tITP-CZE yields significantly higher separation resolution and shorter assay time compared with traditional unidirectional tITP-CZE. We also showed that transition from ITP to CZE in bidirectional ITP occurs over a small distance (usually 100 µm) allowing optimal use of channel length for preconcentration and separation.
5. We validated our simulations results for shock wave interaction in bidirectional ITP with simultaneous experimental visualization of all bidirectional ITP zones. We showed that our simulations capture the dynamics of shock interaction including shock velocities and formation of new nonlinear waves after the shock interaction, using electroosmotic mobility as the only fitting parameter.
6. We demonstrated application of our bidirectional ITP based tITP-CZE method for preconcentration and high-resolution separation of 11 DNA fragments of a 1 kbp DNA ladder, with fragment sizes ranging from 0.5 to 10 kbp. Our experiments required only ~1 pg of DNA sample and 7 min assay time.

8.1.3.2 Application of coupled ITP and CZE for high-senstivity sequence-specific detection of DNA fragments

1. We demonstrated integration of rapid ITP-based DNA hybridization and CZE separation of reaction products using bidirectional ITP, and applied it to sequence-specific detection of DNA fragments.
2. We showed that CZE separation of reaction products can improve detection sensitivity of ITP-based DNA hybridization by separating target-probe hybrids from unreacted labeled probes, thus removing background signal associated with unreacted probes. We demonstrated successful detection of target-probe hybrid in cases where unreacted probe and target-probe hybrid have comparable fluorescent intensities; detection in such cases in otherwise impossible in ITP as background signal interferes with hybridization signal.
3. We demonstrated speed and sensitivity of our method by detecting order 100 pM, ssDNA target within 3 min, using a molecular beacon probe.
4. We demonstrated that CZE separation of DNA hybridization products can be used to extend functionality of ITP-based hybridization to detect multiple-length DNA fragments. We presented simultaneous detection of 39 and 90 nt ssDNA fragments, each having a portion of sequence complementary to that of the probe sequence.

8.2 Conclusions

8.2.1 Modeling and simulation of nonlinear electrokinetic processes

1. The quasi 1-D governing equations derived from the detailed asymptotic analysis of 3-D species transport equations accurately capture advection-diffusion of species in long, thin channels with slowly varying channel cross-sectional area.
2. The Symmetric Limited Positive (SLIP) scheme coupled with the new adaptive grid refinement algorithm yields unconditionally stable solutions to the quasi 1-D species transport equations. Compared with non-dissipative schemes, the current dissipative scheme yields robust and high-resolution simulations using an order of magnitude less number of grid points.

3. Robustness and stability of the current simulation approach makes it better suited for routine design and optimization of electrokinetic assays by researchers with little or no experience in computational methods. In contrast, non-dissipative schemes are better suited for fundamental studies of electrokinetic flows where numerical accuracy is preferred over simulation speed.
4. Coupling of ionic strength effects on fully-ionized electrophoretic mobility and ionic activity with electrokinetic simulations is essential to obtain qualitative and quantitative agreement of simulations with experiments. Ionic strength effects on electrophoretic mobility are more pronounced for multivalent species compared with univalent ions, and neglecting these effects can yield pronounced inaccuracies in simulation results, such as incorrect peak orders in CZE and focusing rate in ITP.
5. We demonstrated that by using Onsager-Fuoss model [80] and extended Debye Huckel theory [81] to correct fully-ionized electrophoretic mobility and ionic activity, respectively, electrokinetic simulations are able to predict qualitative and quantitative variations in ITP and CZE experiments at low and high ionic strengths.

8.2.2 Methods for increasing detection sensitivity of ITP

1. Variation in channel cross-sectional area represents a method for increasing detection sensitivity of peak and plateau mode ITP, and the approach is relatively independent of the signal transduction method. In particular, converging cross-sectional area geometry yields large increase in sensitivity by allowing larger amount of sample accumulation prior to detection. Moreover, for fixed dectection sensitivity, converging cross-section geometry allows shorter channel lengths compared with uniform cross-section geoemtry, resulting in significant reduction in assay time.
2. The dynamics of plateau mode ITP in variable cross-sectional area channels can be conveniently studied with the diffusion-free model, which neglects diffusive fluxes and solves for area-averaged species concentrations. The diffusion-free

model can be used for quick optimization of channel geometry, while taking into account the constraints on SNR, applied voltage and assay time.

3. Shape optimization of converging cross-sectional area channels for higher detection sensitivity is particularly important for portable, on-chip ITP systems due to constraints on applied voltage and channel length. We demonstrated the efficacy converging cross-section geometry by indirectly detecting 100 nM model analyte in 5 min using ITP. To the best of our knowledge, this the most sensitive indirect ITP based detection ever demonstrated.
4. Detection sensitivity of plateau mode ITP can alternatively be increased by creating a concentration cascade of LE, such that analytes initially focus behind high concentration LE and subsequently transition to a region with low concentration LE. High concentration LE increases the sample loading capacity, whereas low concentration LE enforces longer analyte zones, increasing sensitivity.
5. We demonstrated shock wave interaction in bidirectional ITP as an elegant way of transitioning from high to low-concentration LE. Shock interaction eliminates the requirement of physical separation of high and low concentration LEs using valves or column coupling arrangement, which are otherwise required for cascade ITP.
6. Our analytical models and simulations suggest, and experiments confirm that gain in analyte zone length upon shock interaction can be precisely controlled by varying the ratio of cationic to anionic LE concentrations. Furthermore, the gain in analyte zone length in this method is independent of other methods of increasing detection sensitivity of ITP. Consequently, the technique can be applied in converging cross-sectional area channels and/or with hydrodynamic counter-flow to further enhance sensitivity.

8.2.3 Coupling ITP and CZE for high-resolution detection

1. Analysis of trace species using ITP and CZE is often limited by low separation resolution of ITP and low sensitivity of CZE. These limitations of ITP and CZE

can be addressed by coupling ITP and CZE, which integrates high preconcentration ability of ITP and high resolution capacity of CZE.

2. Interaction of anionic and cationic ITP shock waves in bidirectional ITP is an elegant method for triggering CZE separation from ITP preconcentration. Shock interaction can be made to create sudden changes in physicochemical conditions, such as pH and ionic strength, of ITP zones such that analytes focused in ITP cease to focus after the shock interaction and begin to separate in CZE.
3. Shock interaction yields automated transition from ITP to CZE without the need for intermediate steps such as buffer exchange and switching electric fields. Moreover, transition from ITP to CZE in bidirectional ITP is significantly faster than in unidirectional tITP-CZE, yielding higher separation resolution. This feature makes bidirectional ITP based tITP-CZE particularly interesting for on-chip systems which have constraints on maximum channel length.
4. The method also enables higher detection sensitivity of ITP based DNA hybridization by removing background signal associated with unreacted labeled-probes via CZE separation. Furthermore, bidirectional ITP based tITP-CZE extends the functionality of ITP based hybridization assays to detect multiple-length DNA fragments sharing a common portion in their sequences.

8.3 Recommendations for future work

8.3.1 Modeling and simulation of nonlinear electrokinetic processes

1. The current model for electrokinetic transport of species with acid-base equilibria can be extended to include complexation reactions. Similar to acid-base equilibrium reactions, complex-formation reactions occur at significantly shorter time scales compared with electromigration and diffusion time scales [167]. Therefore, existing conservative formulation of governing equations can be extended to include local complex-forming equilibria. This would enable simulations of important electrokinetic processes, including affinity electrophoresis and ITP separation of metal-ligand complexes.

2. Current model and numerical scheme can be extended to incorporate chemical reactions that occur over time scales comparable to those of electromigration and diffusion. This would enable simulations of relatively slow nucleic acid hybridization reactions in electrokinetic techniques. Such simulations could potentially be applied to estimate DNA hybridization rates, given time-resolved data from affinity electrophoresis experiments.
3. Our fast 1-D electrokinetics simulation code can be used to create a large data set of ITP simulations with a wide range of electrolyte chemistries and analytes. This pre-computed data can then be applied, along with statistical learning techniques, for automated design of ITP electrolyte chemistries. A fast optimization tool based on this approach would be of great interest to the electrophoresis community as time-consuming, empirical selection of electrolytes often limits applicability of ITP over other electrophoresis techniques.
4. Our simulation code can be extended to include effects of temperature on electrophoretic mobility of species. This would enable simulation of the temperature gradient focusing technique [168], wherein gradients in electrophoretic mobility induced by temperature gradients are used to stack ionic species. Further, simulating temperature effects in electrophoresis would help design electrokinetics experiments, such as DNA separations at denaturing conditions, that are performed at temperatures higher than ambient conditions.
5. There is an interesting possibility to integrate effects of external electromagnetic fields on species mobilities with our simulation tool. These effects can be important for simulations of DNA electrophoresis as mobilities of long DNA fragments can vary appreciably with electric field [169]. Also, in particular cases, effects of external electromagnetic radiation on analyte mobilities can be leveraged to generate solitary waves in electrophoresis [8].

8.3.2 Methods for increasing detection sensitivity of ITP

1. Strongly converging channels should be used along with concentration cascade of LE to achieve higher detection sensitivities in ITP. Since principles of zone elongation due variation in channel cross-section and gradient in LE concentration

are independent of each other, coupling these methods would yield multiplied gains in analyte zone length. For example, integrating 50-fold reduction in channel cross-section with 20-fold decrease in LE concentration across a counter-migrating shock wave in bidirectional ITP would yield 1000-fold increase in detection sensitivity, and may enable indirect detection of order 1 nM analytes.

2. High-sensitivity detection using cascade ITP in converging channels should be used for analysis of practically relevant analytes in complex samples. Potential applications for high-sensitivity detection of analytes using plateau mode ITP include, determination of organic acids in foodstuffs, and inorganic and organic species in pharmaceuticals.
3. In the current work, we demonstrated use of bidirectional ITP to create concentration cascade of only anionic LE ions. However, bidirectional ITP can be used analogously to increase detection sensitivity of cationic ITP by creating a gradient in concentration of cationic LE ions.
4. Precisely controlled EOF can be used to counter electromigration of analyte zones in ITP, and thereby allow longer time for analytes to focus and separate between LE and TE zones. By appropriately choosing LE, TE and pH of electrolytes, EOF can also be used to attain stationary analyte zones in ITP. Coupled with semi-infinite injection of analytes, stationary analyte zones in ITP can be used to focus extremely low concentrations of analytes in plateau mode ITP.

8.3.3 Coupling ITP and CZE for high-resolution detection

1. Sensitivity and resolution of our tITP-CZE assay can be improved by further optimization of chip geometry. An ideal microfluidic chip for tITP-CZE experiments should consist of a large cross-sectional area channel coupled with a relatively long channel with small cross-sectional area. Reduction in channel cross-section would help increase concentration of analytes focused in peak mode ITP prior to separation, and longer channel would lead to higher resolution during electrophoretic separation.
2. Rapid DNA hybridization and CZE separation using bidirectional ITP can be used for practical applications where detection of multiple-length DNA fragments

having a common portion in their sequences is required. Relevant applications include, restriction fragment length polymorphism (RFLP) analysis [170] and mutation detection [171].

3. Coupling ITP and CZE using bidirectional ITP could be extended for analysis of weak electrolyte species, such as amino acids and proteins. However, for protein separations, care must be taken to avoid charge reversal or decrease in solubility due to large variations in pH in bidirectional ITP based tITP-CZE.
4. Our bidirectional ITP based hybridization and separation assay can be extended to perform rapid immunoreactions and separation of reaction products. In this case, an unlabeled antigen and a fluorescently-labeled antibody can be preconcentrated in peak mode ITP prior to shock interaction, to speed up the immunoreaction. Subsequent separation of reaction products after the shock interaction would enable determination of antigen-antibody complex.
5. Shock wave interaction in bidirectional ITP could potentially be applied to couple rapid ITP based reactions with selective focusing of reaction products. In this approach, reacting species can be preconcentrated in ITP to accelerate second-order hybridization reactions, prior to shock interaction. Subsequently, shock interaction can be used to change the electrophoresis conditions such that only the desired reaction product focuses in ITP, while the remaining species defocus. Selective ITP focusing of a particular reaction product would enable efficient removal of background signal associated with unreacted species while retaining high detection sensitivity of ITP.

Bibliography

[1] Bahga, S. S., and Santiago, J. G., 2013, “Coupling isotachophoresis and capillary electrophoresis: A review and comparison of methods,” Analyst, **138**, pp. 735–754.

[2] Auroux P. A., Iossifidis D., Reyes D. R., and Manz A., 2002, “Micro Total Analysis Systems. 2. Analytical standard operations and applications,” Anal. Chem., **74**(12), pp. 2637–2652.

[3] Squires T. M., and Quake S. R., 2005, “Microfluidics: Fluid physics at the nanoliter scale,” Rev. Mod. Phys., **77**(3), pp. 977–1026.

[4] Hassan I., Phutthavong P., and Abdelgawad M., 2004, “Microchannel Heat Sinks: An Overview of the State-of-the-Art,” Microscale Therm. Eng., **8**(3), pp. 183–205.

[5] Kjeang E., Djilali N., and Sinton D., 2009, “Microfluidic fuel cells: A review,” J. Power Sources, **186**(2), pp. 353–369.

[6] Psaltis D., Quake S. R., and Yang C., 2006, “Developing optofluidic technology through the fusion of microfluidics and optics,” Nature, **442**(7101), pp. 381–386.

[7] Zhukov M. Y., 1984, “A non-stationary model of isotachophoresis,” USSR Comput. Math. Math. Phys., **24**(2), pp. 138–149.

[8] Kist T. B. L., 1995, “Solitary waves of molecular distributions in liquids generated by electrophoresis and optical fields,” Phys. Rev. Lett., **75**(6), pp. 1210–1213.

[9] Jorgenson J. W., and Lukacs K. D., 1983, “Capillary zone electrophoresis,” Science, **222**(4621), pp. 266–272.

[10] Hunter R. J., 1981, Zeta potential in colloid science, Academic Press, London.

[11] Lyklema J., 1995, Fundamentals of interface and colloid science, Academic Press, London.

[12] Probstein R. F., 1994, Physicochemical hydrodynamics, Wiley, New York.

[13] Bruus H., 2008, Theoretical microfluidics, Oxford University Press, New York.

[14] Porras S. P., Riekkola M. L., and Kenndler E., 2003, “The principles of migration and dispersion in capillary zone electrophoresis in nonaqueous solvents,” Electrophoresis, **24**(10), pp. 1485–1498.

[15] Bahga S. S., Bercovici M., and Santiago J. G., 2010, “Ionic strength effects on electrophoretic focusing and separations,” Electrophoresis, **31**(5), pp. 910–919.

[16] Landers J. P., ed., 1997, Handbook of Capillary Electrophoresis, CRC Press, Boca Raton.

[17] Frazier R. A., Ames J. M., and Nursten H. E., 1999, “The development and application of capillary electrophoresis methods for food analysis,” Electrophoresis, **20**(15-16), pp. 3156–3180.

[18] Kleparnik K., and Bocek P., 2007, “DNA diagnostics by capillary electrophoresis,” Chem. Rev., **107**(11), pp. 5279–5317.

[19] Dabek-Zlotorzynska E., 1997, “Capillary electrophoresis in the determination of pollutants,” Electrophoresis, **18**(12-13), pp. 2453–2464.

[20] Desai M. J., and Armstrong D. W., 2003, “Separation, identification, and characterization of microorganisms by capillary electrophoresis,” Microbiol. Mol. Biol. Rev., **67**(1), pp. 38–51.

[21] Giddings J. C., 1969, “Generation of variance, theoretical plates, resolution, and peak capacity in electrophoresis and sedimentation,” Separ. Sci., **4**(3), pp. 181–189.

[22] Bharadwaj R., Santiago J. G., and Mohammadi B., 2002, “Design and optimization of on-chip capillary electrophoresis,” Electrophoresis, **23**(16), pp. 2729–2744.

[23] Baba Y., Tsuhako M., Enomoto S., Chin A. M., and Dubrow R. S., 1991, “High performance separations of nucleic acids using capillary electrophoresis and high-performance liquid chromatography,” J. High Res. Chromatog., **14**(3), pp. 204–206.

[24] Cohen A. S., Vilenchik M., Dudley J. L., Gemborys M. W., and Bourque A. J., 1993, “High-performance liquid chromatography and capillary gel electrophoresis as applied to antisense DNA,” J. Chromatogr. A, **638**(2), pp. 293–301.

[25] Kubáň P., and Hauser P. C., 2008, “A review of the recent achievements in capacitively coupled contactless conductivity detection,” Anal. Chim. Acta., **607**(1), pp. 15–29.

[26] Swinney K., and Bornhop D. J., 2000, “Detection in capillary electrophoresis,” Electrophoresis, **21**(7), pp. 1239–1250.

[27] Jung B., Zhu Y., and Santiago J. G., 2007, “Detection of 100 aM fluorophores using a high-sensitivity on-chip CE system and transient isotachophoresis,” Anal. Chem., **79**(1), pp. 345–349.

[28] van den Beld C. M. B., Tjaden U. R., Reinhoud N. J., Stegehuis D. S., and van der Greef J., 1990, “Determination of some β-endorphin fragments in human plasma by high-performance liquid chromatography with laser induced fluorescence detection,” J. Control. Release, **13**(2–3), pp. 129–139.

[29] Albin M., Weinberger R., Sapp E., and Moring S., 1991, “Fluorescence detection in capillary electrophoresis: evaluation of derivatizing reagents and techniques,” Anal. Chem., **63**(5), pp. 417–422.

[30] Chien R. L., and Burgi D. S., 1991, “Field amplified sample injection in high-performance capillary electrophoresis,” J. Chromatogr. A, **559**(1–2), pp. 141–152.

[31] Jacobson S. C., and Ramsey J. M., 1995, “Microchip electrophoresis with sample stacking,” Electrophoresis, **16**(1), pp. 481–486.

[32] Aebersold R., and Morrison H. D., 1990, “Analysis of dilute peptide samples by capillary zone electrophoresis,” J. Chromatogr. A, **516**(1), pp. 79–88.

[33] Britz-McKibbin P., and Chen D. D. Y., 2000, “Selective focusing of catecholamines and weakly acidic compounds by capillary electrophoresis using a dynamic pH junction,” Anal. Chem., **72**(6), pp. 1242–1252.

[34] Bocek P., 1981, “Analytical isotachophoresis,” Analytical Problems, Springer Berlin/Heidelberg, pp. 131–177.

[35] Everaerts F. M., Beckers J. L., and Verheggen T. P. E. M., 1976, Isotachophoresis–theory, instrumentation and applications, Elsevier, Amsterdam.

[36] Chen L., Prest J. E., Fielden P. R., Goddard N. J., Manz A., and Day P. J. R., 2006, “Miniaturised isotachophoresis analysis,” Lab. Chip, **6**(4), pp. 474–487.

[37] Gebauer P., and Bocek P., 2002, “Recent progress in capillary isotachophoresis,” Electrophoresis, **23**(22-23), pp. 3858–3864.

[38] Jung B., Bharadwaj R., and Santiago J. G., 2006, “On-chip millionfold sample stacking using transient isotachophoresis,” Anal. Chem., **78**(7), pp. 2319–2327.

[39] Chen S., Graves S. W., and Lee M. L., 1999, “Zone shape and concentration in isotachophoresis–capillary electrophoresis,” J. Microcolumn Sep., **11**(5), pp. 341–345.

[40] Khurana T. K., and Santiago J. G., 2008, “Sample zone dynamics in peak mode isotachophoresis,” Anal. Chem., **80**(16), pp. 6300–6307.

[41] Khurana T. K., and Santiago J. G., 2008, “Preconcentration, separation, and indirect detection of nonfluorescent analytes using fluorescent mobility markers,” Anal. Chem., **80**(1), pp. 279–286.

[42] Kohlrausch F., 1897, “Ueber Concentrations-Verschiebungen durch Electrolyse im Inneren von Lösungen und Lösungsgemischen,” Annalen der Physik, **298**(10), pp. 209–239.

[43] Jovin T. M., 1973, “Multiphasic zone electrophoresis. I. Steady-state moving-boundary systems formed by different electrolyte combinations,” Biochemistry, **12**(5), pp. 871–879.

[44] Alberty R. A., 1950, “Moving boundary systems formed by weak electrolytes. Theory of simple systems formed by weak acids and bases,” J. Am. Chem. Soc., **72**(6), pp. 2361–2367.

[45] Zemann A. J., Schnell E., Volgger D., and Bonn G. K., 1998, “Contactless conductivity detection for capillary electrophoresis,” Anal. Chem., **70**(3), pp. 563–567.

[46] Ludwig M., Kohler F., and Belder D., 2003, “High-speed chiral separations on a microchip with UV detection,” Electrophoresis, **24**(18), pp. 3233–3238.

[47] Chambers R. D., and Santiago J. G., 2009, “Imaging and quantification of isotachophoresis zones using nonfocusing fluorescent tracers,” Anal. Chem., **81**(8), pp. 3022–3028.

[48] Gaš B., and Kenndler E., 2000, “Dispersive phenomena in electromigration separation methods,” Electrophoresis, **21**(18), pp. 3888–3897.

[49] Persat A., Suss M. E., and Santiago J. G., 2009, “Basic principles of electrolyte chemistry for microfluidic electrokinetics. Part II: Coupling between ion mobility, electrolysis, and acid–base equilibria,” Lab. Chip, **9**(17), pp. 2454–2469.

[50] Hirokawa T., Okamoto H., and Gaš B., 2003, “High-sensitive capillary zone electrophoresis analysis by electrokinetic injection with transient isotachophoretic preconcentration: Electrokinetic supercharging,” Electrophoresis, **24**(3), pp. 498–504.

[51] Xu Z. Q., Hirokawa T., Nishine T., and Arai A., 2003, “High-sensitivity capillary gel electrophoretic analysis of DNA fragments on an electrophoresis microchip using electrokinetic injection with transient isotachophoretic preconcentration,” J. Chromatogr. A, **990**(1–2), pp. 53–61.

[52] Thormann W., Arn D., and Schumacher E., 1985, “Bidirectional analytical isotachophoresis: Simultaneous determination of anionic and cationic boundaries,” Electrophoresis, **6**(1), pp. 10–18.

[53] O.V. Oshurkova, and A.I. Gorshkov, 1993, “New trends in capillary isotachophoresis,” Russ. Chem. Rev., **62**(8), pp. 729–742.

[54] Oshurkova O. V., Gorshkov A. I., and Nesterov V. P., 2004, “Use of counterflow in bidirectional capillary isotachophoresis,” Russ. J. Electrochem., **40**(5), pp. 516–520.

[55] Hirokawa T., Watanabe K., Yokota Y., and Kiso Y., 1993, “Bidirectional isotachophoresis: I. Verification of bidirectional isotachophoresis and simultaneous determination of anionic and cationic components,” J. Chromatogr. A, **633**(1–2), pp. 251–259.

[56] Prest J. E., Baldock S. J., Fielden P. R., Goddard N. J., and Brown B. J. T., 2002, “Bidirectional isotachophoresis on a planar chip with integrated conductivity detection,” Analyst, **127**(11), pp. 1413–1419.

[57] Oshurkova O. V., and Ivanova I. A., 1976, “Coulophoretic titration,” Dokl. Akad. Nauk SSSR, **227**, pp. 1371–1374.

[58] Bahga S. S., Bercovici M., and Santiago J. G., 2012, “Robust and high-resolution simulations of nonlinear electrokinetic processes in variable cross-section channels,” Electrophoresis, **33**, pp. 3036–3051.

[59] Bier M., Palusinski O. A., Mosher R. A., and Saville D. A., 1983, “Electrophoresis: mathematical modeling and computer simulation,” Science, **219**(4590), pp. 1281–1287.

[60] Saville D. A., and Palusinski O. A., 1986, “Theory of electrophoretic separations. Part I: Formulation of a mathematical model,” AIChE J., **32**(2), pp. 207–214.

[61] Mosher R. A., Dewey D., Thormann W., Saville D. A., and Bier M., 1989, “Computer simulation and experimental validation of the electrophoretic behavior of proteins,” Anal. Chem., **61**(4), pp. 362–366.

[62] Thormann W., Zhang C. X., Caslavska J., Gebauer P., and Mosher R. A., 1998, “Modeling of the impact of ionic strength on the electroosmotic flow in capillary electrophoresis with uniform and discontinuous buffer systems,” Anal. Chem., **70**(3), pp. 549–562.

[63] Bercovici M., Lele S. K., and Santiago J. G., 2009, “Open source simulation tool for electrophoretic stacking, focusing, and separation,” J. Chromatogr. A, **1216**(6), pp. 1008–1018.

[64] Taylor G., 1953, “Dispersion of soluble matter in solvent flowing slowly through a tube,” Proc. R. Soc. Lond. A, **219**(1137), pp. 186–203.

[65] Aris R., 1956, “On the dispersion of a solute in a fluid flowing through a tube,” Proc. R. Soc. Lond. A, **235**(1200), pp. 67–77.

[66] Hruška V., Jaroš M., and Gaš B., 2006, “Simul 5 – Free dynamic simulator of electrophoresis,” Electrophoresis, **27**(5-6), pp. 984–991.

[67] Thormann W., Caslavska J., Breadmore M. C., and Mosher R. A., 2009, “Dynamic computer simulations of electrophoresis: Three decades of active research,” Electrophoresis, **30**(S1), pp. S16–S26.

[68] Dose E. V., and Guiochon G. A., 1991, “High-resolution modeling of capillary zone electrophoresis and isotachophoresis,” Anal. Chem., **63**(11), pp. 1063–1072.

[69] Bercovici M., Lele S. K., and Santiago J. G., 2010, “Compact adaptive-grid scheme for high numerical resolution simulations of isotachophoresis,” J. Chromatogr. A, **1217**(4), pp. 588–599.

[70] Martens J. H. P. A., Reijenga J. C., ten Thije Boonkkamp J. H. M., Mattheij R. M. M., and Everaerts F. M., 1997, “Transient modelling of capillary electrophoresis: Isotachophoresis,” J. Chromatogr. A, **772**(1–2), pp. 49–62.

[71] Sounart T. L., and Baygents J. C., 2000, “Simulation of electrophoretic separations by the flux-corrected transport method,” J. Chromatogr. A, **890**(2), pp. 321–336.

[72] Boris J. P., and Book D. L., 1973, “Flux-corrected transport. I. SHASTA, a fluid transport algorithm that works,” J. Comput. Phys., **11**(1), pp. 38–69.

[73] Chou Y., and Yang R. J., 2010, “Numerical solutions for isoelectric focusing and isotachophoresis problems,” J. Chromatogr. A, **1217**(3), pp. 394–404.

[74] Choi H., Jeon Y., Cho M., Lee D., and Shim J., 2010, “Effects of cross-sectional change on the isotachphoresis process for protein-separation chip design,” Microsyst. Technol., **16**(11), pp. 1931–1938.

[75] Hruška V., Gaš B., and Vigh G., 2009, "Simulation of desalting that occurs during isoelectric trapping separations," Electrophoresis, **30**(3), pp. 433–443.

[76] Chou Y., and Yang R. J., 2009, "Simulations of IEF in microchannel with variable cross-sectional area," Electrophoresis, **30**(5), pp. 819–830.

[77] Munson M. S., Cabrera C. R., and Yager P., 2002, "Passive electrophoresis in microchannels using liquid junction potentials," Electrophoresis, **23**(16), pp. 2642–2652.

[78] Howison S., 2005, Practical Applied Mathematics, Cambridge University Press, Cambridge, UK.

[79] Hickman H. J., 1970, "The liquid junction potential — the free diffusion junction," Chem. Eng. Sci., **25**(3), pp. 381–398.

[80] Onsager L., and Fuoss R. M., 1932, "Irreversible processes in electrolytes. Diffusion, conductance and viscous flow in arbitrary mixtures of strong electrolytes," J. Phys. Chem., **36**(11), pp. 2689–2778.

[81] Debye P., and Hückel E., 1923, "Zur Theorie der Elektrolyte. I. Gefrierpunktserniedrigung und verwandte Erscheinungen," Phys. Z., **24**, pp. 185–206.

[82] Jameson A., 1995, "Analysis and design of numerical schemes for gas dynamics, 1: Artificial diffusion, upwind biasing, limiters and their effect on accuracy and multigrid convergence," Int. J. Comput. Fluid D., **4**(3-4), pp. 171–218.

[83] Jameson A., and Vassberg J. C., 2000, "Studies of alternative numerical optimization methods applied to the brachistochrone problem," Comput. Fluid Dyn. J., **9**(3), pp. 281–296.

[84] Palusinski O. A., Graham A., Mosher R. A., Bier M., and Saville D. A., 1986, "Theory of electrophoretic separations. Part II: Construction of a numerical simulation scheme and its applications," AIChE J., **32**(2), pp. 215–223.

[85] Ermakov S. V., Bello M. S., and Giorgio Righetti P., 1994, "Numerical algorithms for capillary electrophoresis," J. Chromatogr. A, **661**(1–2), pp. 265–278.

[86] Yu J. W., Chou Y., and Yang R. J., 2008, "High-resolution modeling of isotachophoresis and zone electrophoresis," Electrophoresis, **29**(5), pp. 1048–1057.

[87] Dolník V., Deml M., and Bocek P., 1985, "Large sample volume preseparation for trace analysis in isotachophoresis," J. Chromatogr. A, **320**(1), pp. 89–97.

[88] Bahga S. S., Kaigala G. V., Bercovici M., and Santiago J. G., 2011, “High-sensitivity detection using isotachophoresis with variable cross-section geometry,” Electrophoresis, **32**(5), pp. 563–572.

[89] Bottenus D., Jubery T. Z., Ouyang Y., Dong W. J., Dutta P., and Ivory C. F., 2011, “10 000-fold concentration increase of the biomarker cardiac troponin I in a reducing union microfluidic chip using cationic isotachophoresis,” Lab. Chip, **11**(5), pp. 890–898.

[90] Beckers J. L., Everaerts F. M., and Ackermans M. T., 1991, “Determination of absolute mobilities, pK values and separation numbers by capillary zone electrophoresis : Effective mobility as a parameter for screening,” J. Chromatogr. A, **537**, pp. 407–428.

[91] Friedl W., and Kenndler E., 1993, “Resolution as a function of the pH of the buffer based on the analyte charge number for multivalent ions in capillary zone electrophoresis without electroosmotic flow: Theoretical prediction and experimental evaluation,” Anal. Chem., **65**(15), pp. 2003–2009.

[92] Gluck S. J., and Cleveland Jr. J. A., 1994, “Investigation of experimental approaches to the determination of pKa values by capillary electrophoresis,” J. Chromatogr. A, **680**(1), pp. 49–56.

[93] Gaš B., Coufal P., Jaroš M., Muzikář J., and Jelínek I., 2001, “Optimization of background electrolytes for capillary electrophoresis: I. Mathematical and computational model,” J. Chromatogr. A, **905**(1–2), pp. 269–279.

[94] Pitts E., 1953, “An extension of the theory of the conductivity and viscosity of electrolyte solutions,” Proc. R. Soc. Lond. A, **217**(1128), pp. 43–70.

[95] Bockris J. O., and Reddy A. K. N., 1998, Modern electrochemistry 1: Ionics, 2nd edition, Plenum Press, New York.

[96] Robinson R. A., and Stokes R. H., 2002, Electrolyte solutions, 2nd revised edition, Dover Publications, New York.

[97] Šustáček V., Foret F., and Bocek P., 1991, “Selection of the background electrolyte composition with respect to electromigration dispersion and detection of weakly absorbing substances in capillary zone electrophoresis,” J. Chromatogr. A, **545**(2), pp. 239–248.

[98] Bushey M. M., and Jorgenson J. W., 1989, “Capillary electrophoresis of proteins in buffers containing high concentrations of zwitterionic salts,” J. Chromatogr. A, **480**, pp. 301–310.

[99] Harrold M., Stillian J., Bao L., Rocklin R., and Avdalovic N., 1995, “Capillary electrophoresis of inorganic anions and organic acids using suppressed conductivity detection strategies for selectivity control,” Journal of Chromatography A, **717**(1–2), pp. 371–383.

[100] Friedl W., Reijenga J. C., and Kenndler E., 1995, “Ionic strength and charge number correction for mobilities of multivalent organic anions in capillary electrophoresis,” J. Chromatogr. A, **709**(1), pp. 163–170.

[101] Jaroš M., Včeláková K., Zusková I., and Gaš B., 2002, “Optimization of background electrolytes for capillary electrophoresis: II. Computer simulation and comparison with experiments,” Electrophoresis, **23**(16), pp. 2667–2677.

[102] Onsager, L., 1926, “Zur Theorie der Elektrolyte I,” Phys. Z., **27**, pp. 388–392.

[103] Onsager, L., 1927, “Zur Theorie der Elektrolyte II,” Phys. Z., **28**, pp. 277–298.

[104] Li D., Fu S., and Lucy C. A., 1999, “Prediction of electrophoretic mobilities. 3. Effect of ionic strength in capillary zone electrophoresis,” Anal. Chem., **71**(3), pp. 687–699.

[105] Gebauer P., and Bocek P., 1984, “Chemical kinetics in isotachophoresis : Effects of non-instantaneously reversible complexing equilibria on the stability of zones,” J. Chromatogr. A, **299**, pp. 321–330.

[106] Khurana T. K., and Santiago J. G., 2009, “Effects of carbon dioxide on peak mode isotachophoresis: Simultaneous preconcentration and separation,” Lab. Chip, **9**(10), pp. 1377–1384.

[107] Štědrý M., Jaroš M., Hruška V., and Gaš B., 2004, “Eigenmobilities in background electrolytes for capillary zone electrophoresis: III. Linear theory of electromigration,” Electrophoresis, **25**(18-19), pp. 3071–3079.

[108] Persat A., Chambers R. D., and Santiago J. G., 2009, “Basic principles of electrolyte chemistry for microfluidic electrokinetics. Part I: Acid–base equilibria and pH buffers,” Lab. Chip, **9**(17), pp. 2437–2453.

[109] Hirokawa T., Nishino M., and Kiso Y., 1982, “Isotachophoretic determination of mobility and pKa by means of computer simulation : II. Evaluation of m0 and pKa of 65 anions,” J. Chromatogr. A, **252**, pp. 49–65.

[110] Hirokawa T., Nishino M., Aoki N., Kiso Y., Sawamoto Y., Yagi T., and Akiyama J. I., 1983, “Table of isotachophoretic indices : I. Simulated qualitative and quantitative indices of 287 anionic substances in the range ph 3–10,” J. Chromatogr. A, **271**(2), pp. D1–D106.

[111] Milanova D., Chambers R. D., Bahga S. S., and Santiago J. G., 2011, “Electrophoretic mobility measurements of fluorescent dyes using on-chip capillary electrophoresis,” Electrophoresis, **32**(22), pp. 3286–3294.

[112] Schoch R. B., Ronaghi M., and Santiago J. G., 2009, “Rapid and selective extraction, isolation, preconcentration, and quantitation of small RNAs from cell lysate using on-chip isotachophoresis,” Lab. Chip, **9**(15), pp. 2145–2152.

[113] Lin C. C., Hsu B. K., and Chen S. H., 2008, “Integrated isotachophoretic stacking and gel electrophoresis on a plastic substrate and variations in detection dynamic range,” Electrophoresis, **29**(6), pp. 1228–1236.

[114] Mechref Y., Ostrander G. K., and El Rassi Z., 1997, “Capillary electrophoresis of carboxylated carbohydrates: IV. Adjusting the separation selectivity of derivatized carboxylated carbohydrates by controlling the electrolyte ionic strength at subambient temperature and in the absence of electroosmotic flow,” J. Chromatogr. A, **792**(1–2), pp. 75–82.

[115] Reijenga J. C., Verheggen T. P. E. M., Martens J. H. P. A., and Everaerts F. M., 1996, “Buffer capacity, ionic strength and heat dissipation in capillary electrophoresis,” J. Chromatogr. A, **744**(1–2), pp. 147–153.

[116] Martin A. J. P., and Everaerts F. M., 1967, “Displacement electrophoresis,” Anal. Chim. Acta, **38**, pp. 233–237.

[117] Garcia-Schwarz G., Bercovici M., Marshall L. A., and Santiago J. G., 2011, “Sample dispersion in isotachophoresis,” J. Fluid Mech., **679**, pp. 455–475.

[118] Bercovici M., Kaigala G. V., Backhouse C. J., and Santiago J. G., 2010, “Fluorescent carrier ampholytes assay for portable, label-free detection of chemical toxins in tap water,” Anal. Chem., **82**(5), pp. 1858–1866.

[119] Jorgenson J. W., 1984, "Zone electrophoresis in open-tubular capillaries," TrAC-Trend Anal. Chem., **3**(2), pp. 51–54.

[120] Everaerts F. M., Vacik J., Verheggen T. P. E. M., and Zuska J., 1971, "Isotachophoresis: Experiments with electrolyte counterflow," J. Chromatogr. A, **60**, pp. 397–405.

[121] Bocek P., Deml M., and Janák J., 1978, "Effect of a concentration cascade of the leading electrolyte on the seperation capacity in isotachophoresis," J. Chromatogr. A, **156**(2), pp. 323–326.

[122] Everaerts F. M., Verheggen T. P. E. M., and Mikkers F. E. P., 1979, "Determination of substances at low concentrations in complex mixtures by isotachophoresis with column coupling," J. Chromatogr. A, **169**, pp. 21–38.

[123] Bodor R., Madajová V., Kaniansky D., Masár M., Jöhnck M., and Stanislawski B., 2001, "Isotachophoresis and isotachophoresis — zone electrophoresis separations of inorganic anions present in water samples on a planar chip with column-coupling separation channels and conductivity detection," J. Chromatogr. A, **916**(1–2), pp. 155–165.

[124] Kaigala, G. V., Benham, M., Bliss, C., Khorasani, M., Ho, S., McMullin, J. N., Elliot, D. G., and Backhouse, C. J., 2009, "Inexpensive, universal serial bus-powered and fully portable lab-on-a-chip-based capillary electrophoresis instrument," IET Nanobiotechnol., **3**(1), pp. 1–7.

[125] Zusková I., Gaš B., and Vacík J., 1993, "Electromigration in systems with additives in background electrolytes: II. Ionic admixture," J. Chromatogr. A, **648**(1), pp. 233–244.

[126] LeVeque, R. L., 2002, Finite Volume Methods for Hyperbolic Problems, Cambridge University Press, Cambridge, UK.

[127] Ghosal S., 2006, "Electrokinetic Flow and Dispersion in Capillary Electrophoresis," Annu. Rev. Fluid Mech., **38**(1), pp. 309–338.

[128] Bharadwaj R., and Santiago J. G., 2005, "Dynamics of field-amplified sample stacking," J. Fluid Mech., **543**, pp. 57–92.

[129] Bahga S. S., and Santiago J. G., 2012, “Concentration cascade of leading electrolyte using bidirectional isotachophoresis,” ELECTROPHORESIS, **33**(6), pp. 1048–1059.

[130] Kaniansky D., Masár M., Bielčiková J., Iványi F., Eisenbeiss F., Stanislawski B., Grass B., Neyer A., and Jöhnck M., 2000, “Capillary electrophoresis separations on a planar chip with the column-coupling configuration of the separation channels,” Anal. Chem., **72**(15), pp. 3596–3604.

[131] Bahga S. S., Chambers R. D., and Santiago J. G., 2011, “Coupled isotachophoretic preconcentration and electrophoretic separation using bidirectional isotachophoresis,” Anal. Chem., **83**(16), pp. 6154–6162.

[132] Gowda H. T., Lock J., and Kurtz R., 1985, “A comprehensive study of risk assessment for a hazardous compound of public health concern,” Water Air Soil Poll., **24**(2), pp. 189–206.

[133] Mikkers F. E. P., Everaerts E. M., and Peek J. A. F., 1979, “Isotachophoresis: The concepts of resolution, load capacity and separation efficiency I. Theory,” J. Chromatogr. A, **168**(2), pp. 293–315.

[134] Ermakov S. V., Zhukov M. Y., Capelli L., and Righetti P. G., 1998, “Isotachophoresis at pH extremes: Theory and experimental validation,” Electrophoresis, **19**(2), pp. 192–205.

[135] Gebauer P., and Bocek P., 1983, “Zone order in isotachophoresis : The concept of the zone existence diagram and its use in cationic systems,” J. Chromatogr. A, **267**, pp. 49–65.

[136] Bočker P., Gebauer P., and Deml M., 1981, “Migration behaviour of the hydrogen ion and its role in isotachophoresis of cations,” J. Chromatogr. A, **217**, pp. 209–224.

[137] Kaniansky D., and Marak J., 1990, “On-line coupling of capillary isotachophoresis with capillary zone electrophoresis,” J. Chromatogr. A, **498**, pp. 191–204.

[138] Křivánková L., and Bocek P., 1997, “Synergism of capillary isotachophoresis and capillary zone electrophoresis,” J. Chromatogr. B, **689**(1), pp. 13–34.

[139] Timerbaev A. R., and Hirokawa T., 2006, “Recent advances of transient isotachophoresis-capillary electrophoresis in the analysis of small ions from high-conductivity matrices,” Electrophoresis, **27**(1), pp. 323–340.

[140] Foret F., Szoko E., and Karger B. L., 1992, “On-column transient and coupled column isotachophoretic preconcentration of protein samples in capillary zone electrophoresis,” J. Chromatogr. A, **608**(1–2), pp. 3–12.

[141] Křivánková L., Gebauer P., and Bocek P., 1995, “Some practical aspects of utilizing the on-line combination of isotachophoresis and capillary zone electrophoresis,” J. Chromatogr. A, **716**(1–2), pp. 35–48.

[142] Křivánková L., Gebauer P., Thormann W., Mosher R. A., and Bocek P., 1993, “Options in electrolyte systems for on-line combined capillary isotachophoresis and capillary zone electrophoresis,” J. Chromatogr. A, **638**(2), pp. 119–135.

[143] Reinhoud N. J., Tjaden U. R., and van der Greef J., 1993, “Automated isotachophoretic analyte focusing for capillary zone electrophoresis in a single capillary using hydrodynamic back-pressure programming,” J. Chromatogr. A, **641**(1), pp. 155–162.

[144] Reinhoud N. J., Tjaden U. R., and van der Greef J., 1993, “Strategy for setting up single-capillary isotachophoresis—zone electrophoresis,” J. Chromatogr. A, **653**(2), pp. 303–312.

[145] Urbánek M., Varenne A., Gebauer P., Křivánková L., and Gareil P., 2006, “Determination of trace cationic impurities in butylmethylimidazolium-based ionic liquids: From transient to comprehensive single-capillary counterflow isotachophoresis-zone electrophoresis,” Electrophoresis, **27**(23), pp. 4859–4871.

[146] Davis N. I., Mamunooru M., Vyas C. A., and Shackman J. G., 2009, “Capillary and microfluidic gradient elution isotachophoresis coupled to capillary zone electrophoresis for femtomolar amino acid detection limits,” Anal. Chem., **81**(13), pp. 5452–5459.

[147] Ornstein L., 1964, “Disc electrophoresis-I Background and Theory,” Ann. NY. Acad. Sci., **121**(2), pp. 321–349.

[148] Davis B. J., 1964, “Disc electrophoresis-II Method and application to human serum proteins,” Ann. NY. Acad. Sci., **121**(2), pp. 404–427.

[149] Foret F., Szoko E., and Karger B. L., 1993, "Trace analysis of proteins by capillary zone electrophoresis with on-column transient isotachophoretic preconcentration," Electrophoresis, **14**(1), pp. 417–428.

[150] Křivánková L., Pantůčková P., and Bocek P., 1999, "Isotachophoresis in zone electrophoresis," J. Chromatogr. A, **838**(1–2), pp. 55–70.

[151] Xu Z., Nishine T., Arai A., and Hirokawa T., 2004, "Performance of electrokinetic supercharging for high-sensitivity detection of DNA fragments in chip gel electrophoresis," Electrophoresis, **25**(21-22), pp. 3875–3881.

[152] Stellwagen N. C., and Stellwagen E., 2009, "Effect of the matrix on DNA electrophoretic mobility," J. Chromatogr. A, **1216**(10), pp. 1917–1929.

[153] Singer V. L., Lawlor T. E., and Yue S., 1999, "Comparison of SYBR® Green I nucleic acid gel stain mutagenicity and ethidium bromide mutagenicity in the Salmonella/mammalian microsome reverse mutation assay (Ames test)," Mutat. Res.-Gen. Tox. En., **439**(1), pp. 37–47.

[154] New England Biolabs, http://www.neb.com/nebecomm/products/productn3232.asp.

[155] Bahga S. S., Han C. M., and Santiago J. G., 2013, "Integration of rapid DNA hybridization and capillary zone electrophoresis using bidirectional ITP," Analyst, **138**, pp. 87–90.

[156] Wang J., 2000, "Survey and summary. From DNA biosensors to gene chips," Nucl. Acids Res., **28**(16), pp. 3011–3016.

[157] Lazcka O., Campo F. J. D., and Muñoz F. X., 2007, "Pathogen detection: A perspective of traditional methods and biosensors," Biosens. Bioelectron., **22**(7), pp. 1205–1217.

[158] Wieder R., and Wetmur J. G., 1981, "One hundred-fold acceleration of DNA renaturation rates in solution," Biopolymers, **20**(7), pp. 1537–1547.

[159] Bercovici M., Han C. M., Liao J. C., and Santiago J. G., 2012, "Rapid hybridization of nucleic acids using isotachophoresis," P. Natl. Acad. Sci. USA, **109**(28), pp. 11127–11132.

[160] Persat A., and Santiago J. G., 2011, “MicroRNA profiling by simultaneous selective isotachophoresis and hybridization with molecular beacons,” Anal. Chem., **83**(6), pp. 2310–2316.

[161] Bercovici M., Kaigala G. V., Mach K. E., Han C. M., Liao J. C., and Santiago J. G., 2011, “Rapid detection of urinary tract infections using isotachophoresis and molecular beacons,” Anal. Chem., **83**(11), pp. 4110–4117.

[162] Tyagi S., and Kramer F. R., 1996, “Molecular beacons: Probes that fluoresce upon hybridization,” Nat. Biotechnol., **14**(3), pp. 303–308.

[163] Garcia-Schwarz G., Rogacs A., Bahga S. S., and Santiago J. G., 2012, “On-chip isotachophoresis for separation of ions and purification of nucleic acids,” J. Vis. Exp., (61), pp. e3890.

[164] Wei Chen J., Cohen A. S., and Karger B. L., 1991, “Identification of DNA molecules by pre-column hybridization using capillary electrophoresis,” J. Chromatogr. A, **559**(1–2), pp. 295–305.

[165] Bianchi N., Mischiati C., Feriotto G., and Gambari R., 1993, “Polymerase-chain reaction: analysis of DNA/DNA hybridization by capillary electrophoresis.,” Nucleic Acids Res., **21**(15), pp. 3595–3596.

[166] Southern E. M., 1975, “Detection of specific sequences among DNA fragments separated by gel electrophoresis,” J. Mol. Biol., **98**(3), pp. 503–517.

[167] Hruška V., Beneš M., Svobodová J., Zusková I., and Gaš B., 2012, “Simulation of the effects of complex- formation equilibria in electrophoresis: I. Mathematical model,” Electrophoresis, **33**(6), pp. 938–947.

[168] Ross D., and Locascio L. E., 2002, “Microfluidic Temperature Gradient Focusing,” Anal. Chem., **74**(11), pp. 2556–2564.

[169] Holmes D. L., and Stellwagen N. C., 1990, “The electric field dependence of DNA mobilities in agarose gels: a reinvestigation,” Electrophoresis, **11**(1), pp. 5–15.

[170] Botstein D., White R. L., Skolnick M., and Davis R. W., 1980, “Construction of a genetic linkage map in man using restriction fragment length polymorphisms.,” Am J Hum Genet, **32**(3), pp. 314–331.

[171] Mellars G., and Gomez K., 2011, “Mutation detection by Southern blotting,” Methods Mol. Biol., **688**, pp. 281–291.

[172] Datta S., and Ghosal S., 2008, "Dispersion due to wall interactions in microfluidic separation systems," Phys. Fluids, **20**(1), pp. 012103–012103–14.

A. Derivation of area-averaged species transport equations in variable cross-sectional area channels

In this section, we present lubrication theory analysis to derive cross-sectional area-averaged electromigration-diffusion equations for multispecies transport in channels with variable cross-sectional area. Figure A.1 shows a schematic of a variable cross-sectional channel considered in the current analysis. We assume that the channel axis is straight and aligned along the *x*-direction. Further, we assume that the characteristic length scale of variation of cross-sectional area and concentration in the axial direction, ℓ, is significantly greater than the characteristic height (or diameter) of the channel, *h*. This slenderness assumption of the channel allows us to perform asymptotic analysis based on the parameter $\epsilon = h/\ell \ll 1$.

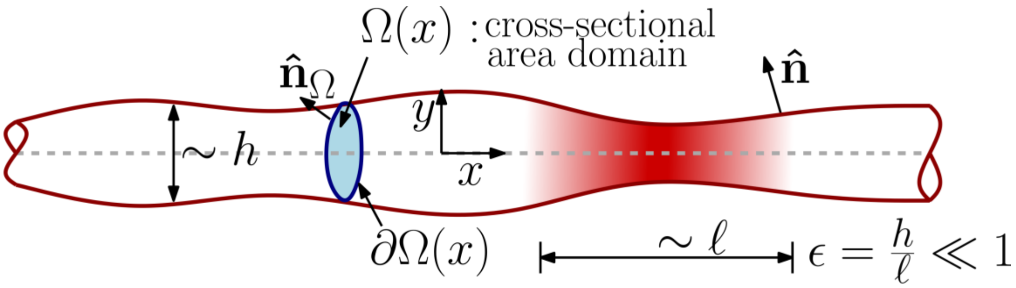
$\Omega(x)$: cross-sectional area domain
$\hat{\mathbf{n}}_\Omega$
$\hat{\mathbf{n}}$
y
$\sim h$
x
$\partial\Omega(x)$
$\sim \ell$
$\epsilon = \frac{h}{\ell} \ll 1$

Figure A.1: Schematic of a variable cross-section area channel considered for the lubrication theory analysis. The channel has a straight axis aligned along the x-direction and an arbitrarily varying cross-sectional area. The characteristic height (or diameter) of the channel is *h*, and the characteristic length scale over which the cross-sectional area and species concentrations vary is ℓ. In the current analysis we assume that $\epsilon = h/\ell \ll 1$, and we perform asymptotic analysis using ϵ as the smallness parameter. Here, $\Omega(x)$ denotes a cross-sectional area domain at a particular axial location x and $\partial\Omega$ denotes the boundary of this two-dimensional (2-D) domain. Vectors $\hat{\mathbf{n}}$ and $\hat{\mathbf{n}}_\Omega$ are outward-pointing unit vectors normal to the channel surface and the 2-D domain $\Omega(x)$, respectively.

The electric double layers which may be present on channel walls are outside our domain of interest. Thus, "channel surface" here can be interpreted as the bounding slip surface associated with the velocity “slip” of electroosmotic flow. Further, we note that non-uniform electroosmotic flow (EOF) can be decomposed into uniform length-averaged EOF (with no variation in spanwise direction) and non-uniform secondary flow (with variations in spanwise direction) due to internal pressure gradients. The uniform length-averaged flow does not cause Taylor-Aris type dispersion and is responsible for simple translation of species concentration profiles. On the other hand flows due to internal gradients are responsible for species dispersion. For this reason, below we present Taylor-dispersion type analysis for only pressure driven (internal and external) flows, as effects of uniform mean EOF can incorporated by simply adding a constant and uniform advection velocity to the system.

We begin with three-dimensional (3-D) advection-diffusion equations for concentrations of species i with valence z_i,

$$\frac{\partial c_i}{\partial t}+\nabla\cdot\left(\mathbf{u}c_i-\tilde{\mu}_i c_i\nabla\phi\right)=\nabla^2\left(\tilde{D}_i c_i\right),\quad i=1,\ldots,N,\quad \nabla=\frac{\partial}{\partial x}\hat{\mathbf{x}}+\frac{\partial}{\partial y}\hat{\mathbf{y}}+\frac{\partial}{\partial z}\hat{\mathbf{z}}. \tag{A.1}$$

Here c_i is the concentration, $\tilde{\mu}_i$ the electrophoretic mobility, and $\tilde{D}_i$ the molecular diffusivity of the corresponding species. The tilde signs in $\tilde{\mu}_i$ and $\tilde{D}_i$ denote dimensional quantities, as we reserve μ_i and D_i for non-dimensional mobility and diffusivity required later in this section. Vector field $\mathbf{u}=u\hat{\mathbf{x}}+v\hat{\mathbf{y}}+w\hat{\mathbf{z}}=u\hat{\mathbf{x}}+\mathbf{u}_\perp$ denotes the velocity of bulk fluid and ϕ denotes the electric potential. We assume that the species are fully ionized (strong electrolytes) and that the bulk fluid is electroneutral,

$$\sum_{i=1}^{N} z_i c_i = 0. \tag{A.2}$$

In the current analysis electrophoretic mobilities and molecular diffusivities are constants as the species are fully ionized. We discuss the extension of our analysis to weak electrolyte species later in Section S2. The boundary conditions for eq. (A.1) are,

$$\hat{\mathbf{n}}\cdot\nabla\phi=0,\quad \hat{\mathbf{n}}\cdot\nabla c_i=0,\quad \mathbf{u}=0,\quad \text{at boundary,} \tag{A.3}$$

where $\hat{\mathbf{n}}$ denotes the unit outward normal at the channel surface. Considering that the channel surface is defined by $f(x,y,z)=0,$ the unit normal $\hat{\mathbf{n}}$ is defined as,

$$\hat{\mathbf{n}} = \frac{\nabla f}{\|\nabla f\|_2} = \frac{\partial_x f}{\|\nabla f\|_2}\hat{\mathbf{x}} + \left(1 - \left(\frac{\partial_x f}{\|\nabla f\|_2}\right)^2\right)^{1/2} \hat{\mathbf{n}}_{\Omega}, \quad \|\nabla f\|_2 = \left(\left(\partial_x f\right)^2 + \left(\partial_y f\right)^2 + \left(\partial_z f\right)^2\right)^{1/2}, \tag{A.4}$$

where $\hat{\mathbf{n}}_{\Omega}$ denotes the unit normal at the boundary $\partial\Omega(x)$ of the two-dimensional (2-D) cross-sectional area domain $\Omega(x)$.

As is typical of lubrication theory analysis, we first non-dimensionalize the governing equations by using the following non-dimensional variables,

$$\begin{gathered} C_i = \frac{c_i}{c_0}, \quad X = \frac{x}{\ell}, \quad Y = \frac{y}{h}, \quad Z = \frac{z}{h}, \quad U = \frac{u}{u_0}, \quad \mathbf{U}_{\perp} = \frac{\mathbf{u}_{\perp}}{\epsilon u_0}, \\ \Phi = \frac{\phi}{E_0 \ell}, \quad T = \frac{t \mu_0 E_0}{\ell}, \quad \mu_i = \frac{\tilde{\mu}_i}{\tilde{\mu}_0}, \quad D_i = \frac{\tilde{D}_i}{\tilde{D}_0}. \end{gathered} \tag{A.5}$$

Here $c_0,\ u_0,\ E_0,\ \tilde{\mu}_0,$ and $\tilde{D}_0$ denote characteristic values of species concentration, axial bulk velocity, axial electric field, mobility, and diffusivity, respectively. The governing equations, eq. (A.1), in non-dimensional form are given by,

$$\begin{aligned} \epsilon^2 \frac{\partial C_i}{\partial T} + \epsilon^2 \frac{\partial}{\partial X}\left(\frac{Pe_U}{Pe_E} U C_i - \mu_i C_i \frac{\partial \Phi}{\partial X}\right) + \nabla_{\Omega} \cdot \left(\epsilon^2 \frac{Pe_U}{Pe_E} \mathbf{U}_{\perp} C_i - \mu_i C_i \nabla_{\Omega} \Phi\right) \\ = \frac{\epsilon^3}{Pe_E} \frac{\partial^2}{\partial X^2}\left(D_i C_i\right) + \frac{\epsilon}{Pe_E} \nabla_{\Omega}^2 \left(D_i C_i\right), \end{aligned} \tag{A.6}$$

where $Pe_U = u_0 h / \tilde{D}_0$ and $Pe_E = \tilde{\mu}_0 E_0 h / \tilde{D}_0$ denote Peclet numbers corresponding to advection due to bulk flow and electromigration, respectively. In eq. (A.6) ∇_{Ω} is the two-dimensional gradient operator defined on the cross-sectional area domain $\Omega(X)$ as,

$$\nabla_{\Omega} = \frac{\partial}{\partial Y}\hat{\mathbf{y}} + \frac{\partial}{\partial Z}\hat{\mathbf{z}}. \tag{A.7}$$

The expression for unit outward normal $\hat{\mathbf{n}}$ at the channel surface, eq. (A.4), in non-dimensional terms is given by,

$$\hat{\mathbf{n}} = \epsilon l \hat{\mathbf{x}} + \sqrt{1-\epsilon^2 l^2}\,\hat{\mathbf{n}}_{\Omega}, \quad l = \partial_X f \,/ \left(\left(\epsilon \partial_X f\right)^2 + \left(\partial_Y f\right)^2 + \left(\partial_Z f\right)^2 \right)^{1/2} \tag{A.8}$$

Non-dimensionalizing the boundary conditions, eq. (A.3), and using the expression of $\hat{\mathbf{n}}$, given by eq. (A.8), we obtain

$$\begin{aligned} &\epsilon^2 l \frac{\partial \Phi}{\partial X} + \sqrt{1-\epsilon^2 l^2}\,\hat{\mathbf{n}}_{\Omega} \cdot \nabla_{\Omega} \Phi = 0, \\ &\epsilon^2 l \frac{\partial C_i}{\partial X} + \sqrt{1-\epsilon^2 l^2}\,\hat{\mathbf{n}}_{\Omega} \cdot \nabla_{\Omega} C_i = 0, U\hat{\mathbf{x}} + \epsilon \mathbf{U}_{\perp} = \mathbf{0} \quad \text{at boundary.} \end{aligned} \tag{A.9}$$

We now perform asymptotic analysis on the non-dimensionalized governing equations and boundary conditions by expanding the variables in powers of ϵ,

$$\begin{aligned} &C_i = C_i^{(0)} + \epsilon C_i^{(1)} + \epsilon^2 C_i^{(2)} + \ldots, \quad \Phi = \Phi^{(0)} + \epsilon \Phi^{(1)} + \epsilon^2 \Phi^{(2)} + \ldots, \\ &U = U^{(0)} + \epsilon U^{(1)} + \epsilon^2 U^{(2)} + \ldots \end{aligned} \tag{A.10}$$

and substituting these series in Eqs. (A.6) and (A.9). Collecting terms with like powers of ϵ results in a series of boundary value problems at different levels of approximation.

A.1 Order ϵ^0

Considering $\mathcal{O}(1)$ terms in eqs. (A.6) and (A.9) we obtain the following boundary value problem,

$$\nabla_{\Omega} \cdot \left(\mu_i C_i^{(0)} \nabla_{\Omega} \Phi^{(0)} \right) = 0, \tag{A.11}$$

$$\hat{\mathbf{n}}_{\Omega} \cdot \nabla_{\Omega} \Phi^{(0)} \Big|_{\partial\Omega} = 0, \quad \hat{\mathbf{n}}_{\Omega} \cdot \nabla_{\Omega} C_i^{(0)} \Big|_{\partial\Omega} = 0. \tag{A.12}$$

Multiplying eq. (A.11) by z_i and summing over all species results in,

$$\nabla_{\Omega} \cdot \left(\sigma^{(0)} \nabla_{\Omega} \Phi^{(0)} \right) = 0, \quad \sigma = \sum_{i=1}^{N} z_i \mu_i C_i, \tag{A.13}$$

where σ is the non-dimensional electrical conductivity. Since electrical conductivity is positive throughout the domain, eq. (A.13) resembles the steady heat equation with non-uniform conductivity. Along with Neumann boundary condition, eq. (A.12), (which resembles adiabatic boundary condition for the steady heat equation) we infer that, $\Phi^{(0)}$ does not depend on the spanwise coordinates Y and Z. That is, $\Phi^{(0)} = \overline{\Phi}^{(0)}\left(X,T\right)$, where overbar indicates cross-sectional area-averaged quantity over the domain, $\Omega\left(X\right)$.

A.2 Order ϵ^1

At $\mathcal{O}\left(\epsilon^1\right)$ we have

$$\nabla_{\Omega}\cdot\left(-\mu_i C_i^{(0)}\nabla_{\Omega}\Phi^{(1)}\right) = \frac{1}{Pe_E}\nabla_{\Omega}^2\left(D_i C_i^{(0)}\right), \tag{A.14}$$

$$\hat{\mathbf{n}}_{\Omega}\cdot\nabla_{\Omega}\Phi^{(1)} = 0, \quad \hat{\mathbf{n}}_{\Omega}\cdot\nabla_{\Omega}C_i^{(0)} = 0, \quad \text{on } \partial\Omega. \tag{A.15}$$

Dividing both sides of eq. (A.14) by D_i and using electroneutrality assumption, eq. (A.2) , we transform eq. (A.14) to,

$$\nabla_{\Omega}\cdot\left(\underbrace{-\sum_{i=1}^{N} z_i \frac{\mu_i}{D_i} C_i^{(0)}}_{>0}\nabla_{\Omega}\Phi^{(1)}\right) = \frac{1}{Pe_E}\nabla_{\Omega}^2\underbrace{\sum_{i=1}^{N} z_i C_i^{(0)}}_{=0} = 0, \tag{A.16}$$

From eq. (A.16) and arguments similar to those in Section A.1 we infer that $\Phi^{(1)} = \overline{\Phi}^{(1)}\left(X,T\right)$. Substituting this form of $\Phi^{(1)}$ back into eq. (A.14) we obtain an explicit boundary value problem for $C_i^{(0)}$,

$$\nabla_{\Omega}^2 C_i^{(0)} = 0, \quad \mathbf{n}_{\Omega}\cdot\nabla_{\Omega}C_i^{(0)}\Big|_{\partial\Omega} = 0. \tag{A.17}$$

Equation (A.17) does not have a unique solution. However, it does suggest that the leading order of species concentrations is not a function of spanwise coordinates Y and Z, i.e., $C_i^{(0)} = \overline{C_i}^{(0)}\left(X,T\right)$. To obtain a unique solution for $\overline{C}_i^{(0)}$ we now consider the boundary value problem at the next order.

A.3 Order ϵ^2

Considering $\mathcal{O}\left(\epsilon^2\right)$ terms and noting that $C_i^{(0)} = \overline{C}_i^{(0)},\ \mathit{\Phi}^{(0)} = \overline{\mathit{\Phi}}^{(0)},\ \mathit{\Phi}^{(1)} = \overline{\mathit{\Phi}}^{(1)}$ we obtain,

$$\begin{aligned}\frac{\partial \overline{C}_i^{0}}{\partial T} + U^{(0)}\frac{\partial}{\partial X}\left(\frac{Pe_U}{Pe_E}\overline{C}_i^{(0)}\right) + \frac{\partial}{\partial X}\left(-\mu_i \overline{C}_i^{(0)}\frac{\partial \overline{\mathit{\Phi}}^{(0)}}{\partial X}\right)& \\ +\nabla_{\mathit{\Omega}}\cdot\left(-\mu_i\overline{C}_i^{(0)}\nabla_{\mathit{\Omega}}\mathit{\Phi}^{(2)}\right) = \frac{D_i}{Pe_E}\nabla_{\mathit{\Omega}}^2 C_i^{(1)}.&\end{aligned} \tag{A.18}$$

Here we have used the continuity of bulk flow to simplify the advection terms. Boundary conditions at this order of approximation are,

$$l\frac{\partial \mathit{\Phi}^{(0)}}{\partial X} + \hat{\mathbf{n}}_{\mathit{\Omega}}\cdot\nabla_{\mathit{\Omega}}\mathit{\Phi}^{(2)} = 0,\quad \hat{\mathbf{n}}_{\mathit{\Omega}}\cdot\nabla_{\mathit{\Omega}}C_i^{(1)} = 0,\quad U^{(0)} = 0,\quad \mathbf{U}_{\perp}^{(0)} = \mathbf{0}\quad \text{on } \partial\mathit{\Omega}. \tag{A.19}$$

A.3.1 Solvability Condition

Equations (A.18) and (A.19) have no solution unless the lower order solution satisfies a solvability condition. The required solvability condition is obtained by integrating eq. (A.18) over the cross-sectional area domain $\mathit{\Omega}\left(X\right)$ and using the boundary conditions, eq. (A.19). This condition is the governing equation for area-averaged species concentration at the leading order,

$$\frac{\partial}{\partial T}\left(A\left(X\right)\overline{C}_i^{(0)}\right) + A\left(X\right)\overline{U}^{(0)}\frac{\partial}{\partial X}\left(\frac{Pe_U}{Pe_E}\overline{C}_i^{(0)}\right) + \frac{\partial}{\partial X}\left(-A\left(X\right)\mu_i\overline{C}_i^{(0)}\frac{\partial \overline{\mathit{\Phi}}^{(0)}}{\partial X}\right) = 0. \tag{A.20}$$

We note that for integration over the cross-sectional area domain $\mathit{\Omega}\left(X\right)$, we have used an intermediate geometrical result [172],

$$\frac{\partial}{\partial X}\int_{\mathit{\Omega}} F\mathrm{d}A = \int_{\mathit{\Omega}}\frac{\partial}{\partial X}F\mathrm{d}A - \oint_{\partial\mathit{\Omega}} Fl\mathrm{d}S. \tag{A.21}$$

The solvability condition, eq. (A.20), can also be written in conservative form by employing the continuity of bulk fluid, $\left(A\overline{U}^{(0)}\right)_X = 0$, as

$$\frac{\partial}{\partial T}\left(A(X)\bar{C}_i^{(0)}\right)+\frac{\partial}{\partial X}\left(\frac{Pe_U}{Pe_E}A(X)\overline{U}^{(0)}\bar{C}_i^{(0)}-\mu_i A(X)\bar{C}_i^{(0)}\frac{\partial\overline{\Phi}^{(0)}}{\partial X}\right)=0. \tag{A.22}$$

The governing equation for $\overline{\Phi}^{(0)}$ is obtained by using the electroneutrality assumption, eq. (A.2), along with eq. (A.20),

$$\frac{\partial}{\partial X}\left(A(X)\bar{\sigma}^{(0)}\frac{\partial\overline{\Phi}^{(0)}}{\partial X}\right)=0. \tag{A.23}$$

Equations (A.20) and (A.23) describe the evolution of zeroth-order species concentrations and electric potential. These equations are the necessary conditions for existence of non-trivial solutions of eqs. (A.18) and (A.19).

A.3.2. Solution for $C_i^{(1)}$

To solve for $C_i^{(1)}$ we now multiply eq. (A.18) by $A(X)$ and eliminate the time derivate term using eq. (A.20). This yields a boundary value problem for $C_i^{(1)}$,

$$\begin{aligned}\frac{Pe_U}{Pe_E}A(X)\left(U^{(0)}-\overline{U}^{(0)}\right)\frac{\partial\bar{C}_i^{(0)}}{\partial X}+\mu_i\bar{C}_i^{(0)}A'(X)\frac{\partial\overline{\Phi}^{(0)}}{\partial X}-A(X)\mu_i\bar{C}_i^{(0)}\nabla_\Omega^2\Phi^{(2)}\\ =A(X)\frac{D_i}{Pe_E}\nabla_\Omega^2 C_i^{(1)}.\end{aligned} \tag{A.24}$$

Next, we eliminate $\bar{\Phi}^{(0)}$ and $\Phi^{(2)}$ in eq. (A.24) to obtain an explicit boundary value problem in terms of the species concentrations. For this, we first use the electroneutrality assumption along with eq. (A.24) to obtain,

$$A'(X)\frac{\partial\overline{\Phi}^{(0)}}{\partial X}-A(X)\nabla_\Omega^2\Phi^{(2)}=\frac{A(X)}{\bar{\sigma}^{(0)}}\sum_{k=1}^{N}\frac{z_k D_k}{Pe_E}\nabla_\Omega^2 C_k^{(1)}. \tag{A.25}$$

Eliminating the left hand side of eq. (A.25) using eq. (A.24) and then solving for $\nabla_\Omega^2 C_i^{(1)}$, we obtain an explicit equation for $C_i^{(1)}$,

$$\nabla_{\Omega}^{2} C_i^{(1)} = \overline{U}^{(0)} \frac{Pe_U}{D_i}\left(\frac{U^{(0)}}{\overline{U}^{(0)}}-1\right)\left\{\frac{\partial \overline{C}_i^{(0)}}{\partial X} - \mu_i \overline{C}_i^{(0)}\left(\sum_{k=1}^{N} \frac{z_k}{D_k}\frac{\partial \overline{C}_k^{(0)}}{\partial X}\right)\left(\sum_{k=1}^{N} \frac{z_k \mu_k \overline{C}_k^{(0)}}{D_k}\right)^{-1}\right\}. \tag{A.26}$$

Following Datta and Ghosal [172] we define $g^{(0)}$ as a solution to the following boundary value problem,

$$\nabla_{\Omega}^{2} g^{(0)} = \frac{U^{(0)}}{\overline{U}^{(0)}} - 1, \quad \mathbf{n}_{\Omega} \cdot \nabla_{\Omega} g^{(0)}\Big|_{\partial\Omega} = 0, \quad \overline{g}^{(0)} = 0. \tag{A.27}$$

Therefore, solution to eq. (A.26) satisfying boundary condition eq. (A.19) can be written as,

$$C_i^{(1)} = \overline{C}_i^{(1)} + \overline{U}^{(0)} \frac{Pe_U}{D_i} g^{(0)} \left\{\frac{\partial \overline{C}_i^{(0)}}{\partial X} - \mu_i \overline{C}_i^{(0)}\left(\sum_{k=1}^{N} \frac{z_k}{D_k}\frac{\partial \overline{C}_k^{(0)}}{\partial X}\right)\left(\sum_{k=1}^{N} \frac{z_k \mu_k \overline{C}_k^{(0)}}{D_k}\right)^{-1}\right\}. \tag{A.28}$$

However, it remains to solve for $\overline{C}_i^{(1)}$ so as to determine $C_i^{(1)}$ uniquely. For this, we need to consider the boundary value problem at the next order.

A.4 Order ϵ^3

Considering $\mathcal{O}\left(\epsilon^3\right)$ terms in eqs. (A.6) and (A.9), and using the results from previous sections we obtain a boundary value problem for $C_i^{(2)}$,

$$\begin{aligned} &\frac{\partial C_i^{(1)}}{\partial T} + \frac{\partial}{\partial X}\left(\frac{Pe_U}{Pe_E} U^{(0)} C_i^{(1)} - \mu_i C_i^{(1)} \frac{\partial \overline{\Phi}^{(0)}}{\partial X} + \frac{Pe_U}{Pe_E} U^{(1)} \overline{C}_i^{(0)} - \mu_i \overline{C}_i^{(0)} \frac{\partial \overline{\Phi}^{(1)}}{\partial X}\right) + \\ &\nabla_{\Omega} \cdot \left(\frac{Pe_U}{Pe_E} \mathbf{U}_{\perp}^{(0)} C_i^{(1)} + \frac{Pe_U}{Pe_E} \mathbf{U}_{\perp}^{(1)} \overline{C}_i^{(0)} - \mu_i C_i^{(1)} \nabla_{\Omega} \overline{\Phi}^{(2)} - \mu_i \overline{C}_i^{(0)} \nabla_{\Omega} \overline{\Phi}^{(3)}\right) \\ &\qquad = \frac{D_i}{Pe_E} \frac{\partial^2 \overline{C}_i^{(0)}}{\partial X^2} + \frac{D_i}{Pe_E} \nabla_{\Omega}^{2} C_i^{(2)}, \end{aligned} \tag{A.29}$$

$$\begin{gathered} l \frac{\partial \overline{\Phi}^{(1)}}{\partial X} + \hat{\mathbf{n}}_{\Omega} \cdot \nabla_{\Omega} \Phi^{(3)} = 0, \quad l \frac{\partial \overline{C}_i^{(0)}}{\partial X} + \hat{\mathbf{n}}_{\Omega} \cdot \nabla_{\Omega} C_i^{(2)} = 0, \\ U^{(1)} = 0, \quad \mathbf{U}_{\perp}^{(1)} = \mathbf{0} \quad \text{on } \partial\Omega. \end{gathered} \tag{A.30}$$

A.4.1 Solvability Condition

Similar to Section A.3, we integrate eq. (A.29) over the cross-sectional area domain $\mathit{\Omega}(X)$ and use the boundary conditions, eq. (A.30), to obtain the solvability condition for eqs. (A.29) and (A.30),

$$\begin{gathered}\frac{\partial}{\partial T}\left(A(X)\bar{C}_i^{(1)}\right)+\frac{\partial}{\partial X}\left(\frac{Pe_U}{Pe_E}A(X)\left(\overline{U^{(0)}C_i^{(1)}}+\bar{U}^{(1)}\bar{C}_i^{(0)}\right)\right)\\ +\frac{\partial}{\partial X}\left(-\mu_i A(X)\bar{C}_i^{(0)}\frac{\partial\bar{\mathit{\Phi}}^{(1)}}{\partial X}-\mu_i A(X)\bar{C}_i^{(1)}\frac{\partial\bar{\mathit{\Phi}}^{(0)}}{\partial X}\right)=\frac{D_i}{Pe_E}\frac{\partial}{\partial X}\left(A(X)\frac{\partial\bar{C}_i^{(0)}}{\partial X}\right).\end{gathered} \tag{A.31}$$

Equation (A.31) is cross-sectional area-averaged transport equation for first-order variation in species concentration in terms of area-averaged quantities. However, the term $\overline{U^{(0)}C_i^{(1)}}$ remains to be simplified in terms of area-averaged velocity and species concentration. Evaluating $\overline{U^{(0)}C_i^{(1)}}$ by using eq. (A.28) yields,

$$\begin{gathered}\overline{U^{(0)}C_i^{(1)}}=\bar{U}^{(0)}\bar{C}_i^{(1)}-\\ \mathit{\Gamma}\bar{U}^{(0)2}\frac{Pe_U}{D_i}\left\{\frac{\partial\bar{C}_i^{(0)}}{\partial X}-\mu_i\bar{C}_i^{(0)}\left(\sum_{k=1}^{N}\frac{z_k}{D_k}\frac{\partial\bar{C}_k^{(0)}}{\partial X}\right)\left(\sum_{k=1}^{N}\frac{z_k\mu_k\bar{C}_k^{(0)}}{D_k}\right)^{-1}\right\}.\end{gathered} \tag{A.32}$$

where $\mathit{\Gamma}$ is defined as,

$$\mathit{\Gamma}\bar{U}^{(0)}=-\overline{U^{(0)}g^{(0)}}. \tag{A.33}$$

A.5 Reconstruction

We now combine the species transport equations for $\bar{C}_i^{(0)}$ and $\bar{C}_i^{(1)}$ to obtain a single equation for cross-sectional area-averaged concentration, $\bar{C}_i=\bar{C}_i^{(0)}+\epsilon\bar{C}_i^{(1)}+\mathcal{O}\left(\epsilon^2\right)$. We multiply eq. (A.31) with ϵ and add it to eq. (A.22) to obtain the required governing equation for $\bar{C}_i$,

$$\begin{aligned}&\frac{\partial}{\partial T}\left(A\left(\overline{C}_i^{(0)}+\epsilon\overline{C}_i^{(1)}\right)\right)+\frac{\partial}{\partial X}\left(A\left(\overline{C}_i^{(0)}+\epsilon\overline{C}_i^{(1)}\right)\left(\frac{Pe_U}{Pe_E}\left(\overline{U}^{(0)}+\epsilon\overline{U}^{(1)}\right)-\mu_i\frac{\partial}{\partial X}\left(\overline{\Phi}^{(0)}+\epsilon\overline{\Phi}^{(1)}\right)\right)\right)\\&\quad=\frac{\epsilon}{Pe_E}\frac{\partial}{\partial X}\left(AD_i\frac{\partial}{\partial X}\left(\overline{C}_i^{(0)}+\epsilon\overline{C}_i^{(1)}\right)\right)\\&\quad+\frac{\epsilon Pe_U^2}{Pe_E}\frac{\partial}{\partial X}\left(\frac{\Gamma\overline{U}^{(0)2}}{D_i}\left\{A\frac{\partial\overline{C}_i^{(0)}}{\partial X}-\mu_i\overline{C}_i^{(0)}A\left(\sum_{k=1}^{N}\frac{z_k}{D_k}\frac{\partial\overline{C}_k^{(0)}}{\partial X}\right)\left(\sum_{k=1}^{N}\frac{z_k\mu_k\overline{C}_k^{(0)}}{D_k}\right)^{-1}\right\}\right).\end{aligned}\tag{A.34}$$

Note that, to obtain eq. (A.34) we have added extra $\mathcal{O}\left(\epsilon^2\right)$ terms $\epsilon^2 Pe_U\left(A\overline{U}^{(1)}\overline{C}_i^{(1)}\right)_X/Pe_E$, $-\epsilon^2\left(A\mu_i\overline{C}_i^{(1)}\overline{\Phi}_X^{(1)}\right)_X$, and $\epsilon^2 D_i\left(A\overline{C}_X^{(1)}\right)_X/Pe_E$. Adding these $\mathcal{O}\left(\epsilon^2\right)$ terms does not affect the validity of eq. (A.34) up to $\mathcal{O}(\epsilon)$. Also, in the last term of eq. (A.34) we can replace $\overline{U}^{(0)}$ and $\overline{C}_i^{(0)}$ by $\overline{U}$ and $\overline{C}_i$, respectively, without altering the validity of eq. (A.34) up to $\mathcal{O}(\epsilon)$. The final cross-sectional area-averaged species transport equation in non-dimensional variables is given by,

$$\begin{aligned}&\frac{\partial}{\partial T}\left(A\overline{C}_i\right)+\frac{\partial}{\partial X}\left(A\overline{C}_i\left(\frac{Pe_U}{Pe_E}\overline{U}-\mu_i\frac{\partial\overline{\Phi}}{\partial X}\right)\right)=\frac{\epsilon}{Pe_E}\frac{\partial}{\partial X}\left(AD_i\frac{\partial\overline{C}_i}{\partial X}\right)\\&\quad+\frac{\epsilon Pe_U^2}{Pe_E}\frac{\partial}{\partial X}\left(\frac{\Gamma\overline{U}^2}{D_i}\left\{A\frac{\partial\overline{C}_i}{\partial X}-A\mu_i\overline{C}_i\left(\sum_{k=1}^{N}\frac{z_k}{D_k}\frac{\partial\overline{C}_k}{\partial X}\right)\left(\sum_{k=1}^{N}\frac{z_k\mu_k\overline{C}_k}{D_k}\right)^{-1}\right\}\right).\end{aligned}\tag{A.35}$$

Converting eq. (A.35) into dimensional form yields,

$$\begin{aligned}&\frac{\partial}{\partial t}\left(A\overline{c}_i\right)+\frac{\partial}{\partial x}\left(A\overline{c}_i\left(\overline{u}-\tilde{\mu}_i\frac{\partial\overline{\phi}}{\partial x}\right)\right)=\frac{\partial}{\partial x}\left(A\tilde{D}_i\frac{\partial\overline{c}_i}{\partial x}\right)\\&\quad+\frac{\partial}{\partial x}\left(\frac{\Gamma h^2\overline{u}^2}{\tilde{D}_i}\left\{A\frac{\partial\overline{c}_i}{\partial x}-\tilde{\mu}_i\overline{c}_iA\left(\sum_{k=1}^{N}\frac{z_k}{\tilde{D}_k}\frac{\partial\overline{c}_k}{\partial x}\right)\left(\sum_{k=1}^{N}\frac{z_k\tilde{\mu}_k\overline{c}_k}{\tilde{D}_k}\right)^{-1}\right\}\right).\end{aligned}\tag{A.36}$$

Here Γ is given by,

$$\Gamma\overline{u}=-\overline{gu},\tag{A.37}$$

where g is the solution of following boundary value problem,

$$\frac{\partial^2 g}{\partial y^2}+\frac{\partial^2 g}{\partial z^2}=\frac{u}{\overline{u}}-1,\quad \hat{\mathbf{n}}_{\Omega}\cdot\left(\frac{\partial g}{\partial y}\hat{\mathbf{y}}+\frac{\partial g}{\partial z}\hat{\mathbf{z}}\right)\bigg|_{\partial\Omega}=0,\quad \overline{g}=0. \tag{A.38}$$

The value of Γ depends on the channel shape and the nature of flow field. For example, $\Gamma = 1/192$ for Poiseuille flow in a cylindrical channel and $\Gamma = 1/210$ for Poiseuille flow between two parallel plates.

Lastly, we use electroneutrality assumption to derive the governing equation for electric potential. We multiply eq. (A.36) with $z_i F$ and perform a summation over all species to obtain the required equation for electric potential ϕ,

$$\frac{\partial}{\partial x}\left(A\tilde{\sigma}\frac{\partial\overline{\phi}}{\partial x}+A\sum_{i=1}^{N} z_i D_i F\frac{\partial\overline{c}_i}{\partial x}\right)=0. \tag{A.39}$$

where $\tilde{\sigma}$ is the dimensional electrical conductivity defined as,

$$\tilde{\sigma}=\sum_{i=1}^{N} z_i c_i \tilde{\mu}_i F. \tag{A.40}$$

Note that $\overline{\phi}$ does not depend on the bulk flow field as advection current is absent due to bulk electroneutrality.

A.6 Further simplifications of the governing equations

Having obtained the area-averaged species transport equations, eqs. (A.36) and (A.39), we now discuss specific simplifications of the governing equations for three cases: (i) for symmetric binary electrolytes, (ii) when bulk fluid is stationary, and (iii) when all species have comparable molecular diffusivities.

A.6.1 Symmetric Binary Electrolyte

For this subsection, we consider a symmetric binary electrolyte consisting for cationic and anionic species with valence z and $-z$, respectively. In this case, it is sufficient to solve for concentration of any one of the species, as $c_+ = c_-$. Setting $i = +$ and in eq. (A.36) and eliminating $\overline{\phi}$ using eq. (A.39) yields,

$$\frac{\partial}{\partial t}\left(A\bar{c}_+\right)+\frac{\partial}{\partial x}\left(A\bar{c}_+\bar{u}\right)=\frac{\partial}{\partial x}\left(A\left(\tilde{D}_b+\frac{\Gamma h^2\bar{u}^2}{\tilde{D}_b}\right)\frac{\partial\bar{c}_+}{\partial x}\right),\quad \tilde{D}_b=\frac{2\tilde{D}_-\tilde{D}_+}{\tilde{D}_-+\tilde{D}_+}. \tag{A.41}$$

Therefore, for a symmetric binary electrolyte, the effective diffusivity for Taylor-Aris type dispersion is given by,

$$\tilde{D}_{eff}=\tilde{D}_b+\frac{\Gamma h^2\bar{u}^2}{\tilde{D}_b}. \tag{A.42}$$

A.6.2 No bulk flow

In the absence of bulk flow, the Taylor-Aris type dispersion terms vanish altogether and eq. (A.36) simplifies to,

$$\frac{\partial}{\partial t}\left(A\bar{c}_i\right)+\frac{\partial}{\partial x}\left(-\tilde{\mu}_i\bar{c}_i A\frac{\partial\bar{\phi}}{\partial x}\right)=\frac{\partial}{\partial x}\left(A\tilde{D}_i\frac{\partial\bar{c}_i}{\partial x}\right). \tag{A.43}$$

Note that, variation in electric field due to non-uniform cross-section does not cause additional dispersion of species up to $\mathcal{O}(\epsilon)$ accuracy. This is because, for slow axial variations in channel cross-section and species concentrations, the electric field is locally axial. Also, the transverse components of electric field are only $\mathcal{O}(\epsilon)$ or smaller. Hence, dispersive effects of non-uniform electric field which result from coupling of perturbation electric field and perturbation species concentration field are $\mathcal{O}(\epsilon^2)$ or smaller.

A.6.3 Species with comparable molecular diffusivities

If all species in the system have comparable molecular diffusivities (i.e., values of diffusivities which are roughly equal to each other), the Taylor-Aris dispersion term in eq. (A.36) can be simplified by noting that,

$$\begin{aligned}&\frac{\Gamma h^2\bar{u}^2}{\tilde{D}_i}\left\{A\frac{\partial\bar{c}_i}{\partial x}-\tilde{\mu}_i\bar{c}_i A\left(\sum_{k=1}^{N}\frac{z_k}{\tilde{D}_k}\frac{\partial\bar{c}_k}{\partial x}\right)\left(\sum_{k=1}^{N}\frac{z_k\tilde{\mu}_k\bar{c}_k}{\tilde{D}_k}\right)^{-1}\right\}\\ &\approx\frac{\Gamma h^2\bar{u}^2}{\tilde{D}_i}\left\{A\frac{\partial\bar{c}_i}{\partial x}-\frac{\tilde{\mu}_i\bar{c}_i A}{\tilde{D}_i}\frac{\partial}{\partial x}\underbrace{\left(\sum_{k=1}^{N}z_k\bar{c}_k\right)}_{=0}\left(\sum_{k=1}^{N}\frac{z_k\tilde{\mu}_k\bar{c}_k}{\tilde{D}_k}\right)^{-1}\right\}=\frac{\Gamma h^2\bar{u}^2}{\tilde{D}_i}A\frac{\partial\bar{c}_i}{\partial x}.\end{aligned} \tag{A.44}$$

Therefore, for the current case, eq. (A.36) simplifies to,

$$\frac{\partial}{\partial t}\left(A\bar{c}_i\right)+\frac{\partial}{\partial x}\left(A\bar{c}_i\left(\bar{u}-\tilde{\mu}_i\frac{\partial\bar{\phi}}{\partial x}\right)\right)=\frac{\partial}{\partial x}\left(A\tilde{D}_{i,t}\frac{\partial\bar{c}_i}{\partial x}\right),\quad \tilde{D}_{i,t}=\tilde{D}_i+\frac{\Gamma h^2\bar{u}^2}{\tilde{D}_i}. \tag{A.45}$$

In other words, when diffusivities of all species are similar, dispersion due to non-uniform flow can be taken into account by using Taylor-Aris diffusivity $\tilde{D}_{i,t}$ for individual species.

A.7 Extension to weak electrolyte species

While deriving the cross-sectional area-averaged species transport equations in Section A.1 we assumed that the species were fully ionized (strong electrolytes). Therefore, the analysis above assumed that mobilities and molecular diffusivities are constant and uniform. However, many practical electrokinetics experiments involve weak electrolyte species whose mobility and diffusivity depend on the local value of p*H*. The formulation for strong electrolyte species discussed in Section S1 can be extended to well-buffered systems with weak electrolytes. This is because, in well-buffered electrolyte systems, variation in local composition of electrolytes has negligible effect on the local p*H* value. Since variations in species concentrations in the transverse direction are small ($\mathcal{O}(\epsilon)$ or smaller) we can safely assume that, in well-buffered systems, mobility and diffusivity of species are uniform over the channel cross-section. With this assumption, we can perform asymptotic analysis for weak electrolyte species on same lines as that for strong electrolytes presented in Section A1. Below we provide cross-sectional area-averaged species transport equations for weak electrolyte species in well-buffered systems.

$$\frac{\partial}{\partial t}\left(A\bar{c}_i\right)+\frac{\partial}{\partial x}\left(A\bar{c}_i\left(\bar{u}-\tilde{\mu}_i\frac{\partial\bar{\phi}}{\partial x}\right)\right)=\frac{\partial}{\partial x}\left(A\frac{\partial}{\partial x}\left(\tilde{D}_{i,t}\bar{c}_i\right)\right),\quad \tilde{D}_{i,t}=\tilde{D}_i+\frac{\Gamma h^2\bar{u}^2}{\tilde{D}_i}, \tag{A.46}$$

$$\frac{\partial}{\partial x}\left(A\tilde{\sigma}\frac{\partial\bar{\phi}}{\partial x}+A\frac{\partial S}{\partial x}\right)=0,\quad S=\sum_{i=1}^{N}\sum_{z=n_i}^{z=p_i}z\tilde{D}_{i,z}g_{i,z}\bar{c}_iF. \tag{A.47}$$

Here, c_i is the total concentration, $\tilde{\mu}_i$ the effective mobility, and $\tilde{D}_i$ the effective diffusivity of species family i. In eq. (A.47) the $A\partial_x S$ term represents diffusive current. Note that, compared to eq. (A.36), in eq. (A.46) we have only accounted for order-of-magnitude, $\mathcal{O}(\epsilon)$, dispersive effects of non-uniform flow.

B. Necessary conditions for the stability of SLIP scheme

In Section 2.3.2, we described in detail the spatial discretization of the cross-sectional area-averaged species transport equations. Our numerical scheme stabilizes the solution by adding limited amount of numerical dissipation flux to the actual flux of species. The limited numerical dissipation flux for species family $i,$ at grid point j is given by,

$$d_{i,j+1/2} = \alpha_{j+1/2}\left(\Delta c_{i,j+1/2} - L\left(\Delta c_{i,j+3/2}, \Delta c_{i,j-1/2}\right)\right), \quad \Delta c_{i,j+1/2} = c_{i,j+1} - c_{i,j}. \tag{B.1}$$

In Section 2.3.2, we mentioned that $\alpha_{j+1/2}$ is a scalar parameter that regulates amount of numerical dissipation added to the solution. If $\alpha_{j+1/2}$ is smaller than the required value, it can result in oscillations in the solution. On the other hand, very high values of $\alpha_{j+1/2}$ can result in artificial broadening of peaks and zone boundaries in the numerical solution. We here derive an appropriate expression for $\alpha_{j+1/2}$ which provides unconditional stability to our numerical scheme without adding unnecessarily high amount of numerical dissipation.

We begin our analysis with a general hyperbolic system of equations,

$$\frac{\partial w_i}{\partial t} + \frac{\partial}{\partial x} f_i\left(w\right) = 0, \quad i = 1,\ldots,N. \tag{B.2}$$

This system of equations can be formulated in terms of the Jacobian matrix K_{ik} as,

$$\frac{\partial w_i}{\partial t} + K_{ik}\frac{\partial c_k}{\partial x} = 0, \quad K_{ik} = \frac{\partial f_i}{\partial c_k}. \tag{B.3}$$

Jameson [82] showed that the SLIP scheme guarantees non-oscillatory solutions when $\alpha_{j+1/2} > 0.5\max\left|\lambda_{j+1/2}\right|,$ where $\lambda_{j+1/2}$ are the eigenvalues of Jacobian matrix K_{ik}, evaluated at the cell edge-(*j+1/2*). Therefore, an appropriate choice of $\alpha_{j+1/2}$, requires correct estimate of the largest eigenvalue (largest by magnitude) of the corresponding Jacobian matrix.

To derive a guideline for choosing $\alpha_{j+1/2}$ for electrokinetics problems, we omit the molecular diffusion flux and consider the resulting hyperbolic system of equations. Doing so does not affect the choice of $\alpha_{j+1/2}$ for ensuring stability, as the molecular diffusion flux only tends to stabilize the simulation further. The governing equations (without molecular diffusion flux) in computational domain are,

$$JA\frac{\partial \bar{c}_i}{\partial t} - VA\frac{\partial \bar{c}_i}{\partial \xi} + \frac{\partial}{\partial \xi}\left(A\bar{u}_x\bar{c}_i + A\mu_i\bar{c}_i\bar{E}_x\right) = 0, \quad i = 1,\ldots,N. \tag{B.4}$$

Reformulating eq. (B.4) in terms of the Jacobian matrix and substituting the expression for electric field (without diffusion current), $\bar{E}_x = I/\left(A\bar{\sigma}\right)$, yields

$$JA\frac{\partial \bar{c}_i}{\partial t} + K_{ik}\frac{\partial \bar{c}_k}{\partial x} = 0, \quad K_{ik} = \left(-VA + A\bar{u}_x\right)\delta_{ik} + \frac{\partial}{\partial \bar{c}_k}\left(\frac{\mu_i\bar{c}_i I}{\bar{\sigma}}\right), \tag{B.5}$$

where δ_{ik} is the Kronecker delta, I the current and $\bar{\sigma}$ the area-averaged electrical conductivity. The electric conductivity depends on the species concentration as,

$$\bar{\sigma} = \sum_{i=1}^{N}\omega_i\bar{c}_i, \quad \omega_i = \sum_{z=n_i}^{p_i} z\mu_{i,z}F\frac{\bar{c}_{i,z}}{\bar{c}_i}. \tag{B.6}$$

In the current analysis, we assume that ω_i, defined in eq. (B.6), is locally constant. This assumption holds for strong electrolyte systems where species are fully ionized and hence the ionization fraction $\bar{c}_{i,z}/\bar{c}_i = 1.$ The same assumption is also valid for well buffered electrolyte systems, as they resist change to pH and ionization fraction $\left(\bar{c}_{i,z}/\bar{c}_i\right)$. Assuming ω_i is not a strong function of species concentrations the Jacobian K_{ik} can be written as,

$$K_{ik} = \left(-VA + A\bar{u}_x\right)\delta_{ik} + M_{ik}, \quad M_{ik} = \frac{\mu_i I}{\bar{\sigma}}\delta_{ik} - \frac{\mu_i\bar{c}_i\omega_k I}{\bar{\sigma}^2}. \tag{B.7}$$

Here we have defined a new matrix M_{ik} which is the Jacobian matrix for system with only electromigration and no bulk flow and grid adaptation. The eigenvalues λ of matrices K_{ik} and M_{ik} are related by,

$$\lambda\left(K_{ik}\right) = -VA + A\bar{u}_x + \lambda\left(M_{ik}\right). \tag{B.8}$$

The characteristic equation $\det\left(M_{ik} - \lambda\delta_{ik}\right) = 0$ for eigenvalues λ of matrix M_{ik} is given by,

$$P\left(\lambda\right) = 1 + \sum_{i=1}^{N} \frac{\mu_i \bar{c}_i \omega_i I}{\bar{\sigma}^2} \frac{1}{\lambda - \mu_i I / \bar{\sigma}} = 0. \tag{B.9}$$

Figure B.1 shows a schematic of $P\left(\lambda\right)$ for an arbitrary electrolyte system. As depicted in Figure B.1, in general, one root of $P\left(\lambda\right)$ is identically zero and the remaining roots necessarily lie between adjacent values of $\mu_i I / \bar{\sigma}$. Therefore, all eigenvalues of matrix M_{ik} have smaller magnitude than $\max_i |\mu_i I / \bar{\sigma}|$. Physically, this upper bound on the magnitude of eigenvalues of M_{ik} exists because the speed of fastest ionic species in an electrolyte solution is given by $\max_i |\mu_i I / \bar{\sigma}|$, and any disturbance or wave in species concentrations cannot travel faster than this speed.

Since eigenvalues of matrices K_{ik} and M_{ik} are related by eq. (B.8), we also obtain an upper bound on the magnitude of eigenvalues of the Jacobian matrix K_{ik},

$$\left|\lambda\left(K_{ik}\right)\right| = \left|-VA + A\bar{u}_x + \lambda\left(M_{ik}\right)\right| < \max_i \left|-VA + A\bar{u}_x + \frac{\mu_i I}{\bar{\sigma}}\right|. \tag{B.10}$$

Therefore, choosing $\alpha_{j+1/2} \geq 0.5 \max_i \left|-VA + A\bar{u}_x + \mu_i I / \bar{\sigma}\right|_{j+1/2}$, satisfies the required stability criterion of $\alpha_{j+1/2} > 0.5 \max\left|\lambda_{j+1/2}\right|$.

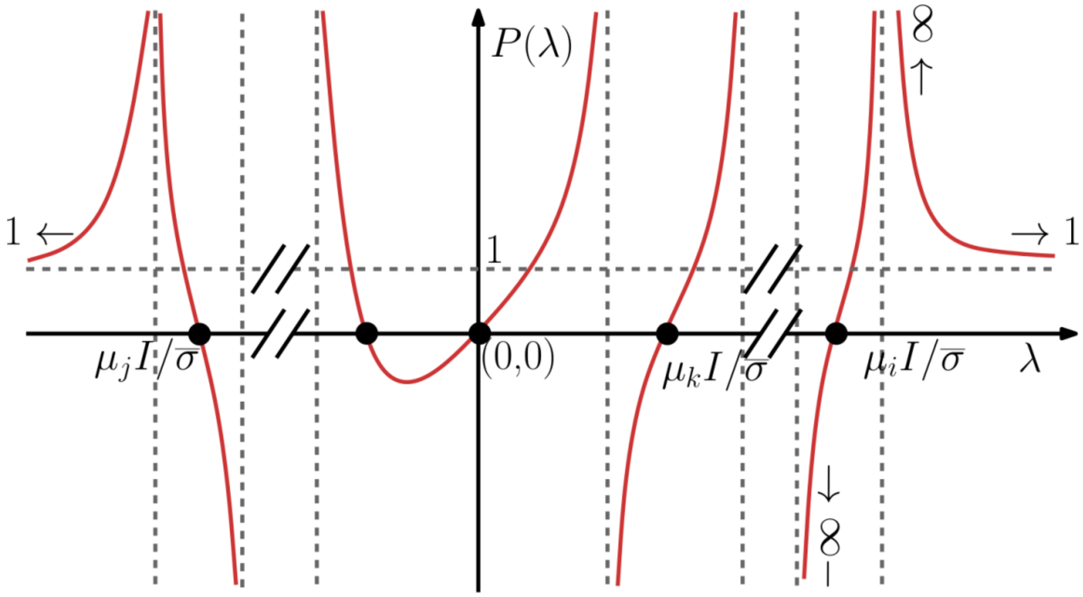

Figure B.1: Schematic showing characteristic equation for eigenvalues of an arbitrary electrokinetics system. The plot shows variation of $P(\lambda)$, defined in eq. (B.9), with λ and the zeros of this function (shown by solid, black circles) are the eigenvalues of matrix M_{ik}. The general variation of $P(\lambda)$ is the same for all electrolyte systems. One root of $P(\lambda)$ (eigenvalue of M_{ik}) is identically zero while others lie between adjacent values of $\mu_i I / \bar{\sigma}$ (denoted by vertical dashed lines).

C. Guidelines for choosing parameters for adaptive grid refinement

We here present a scaling analysis to derive simple guidelines for choosing parameters γ_1 and γ_2 for the adaptive grid refinement algorithm discussed in Section 2.3.3. Briefly, our adaptive grid scheme minimizes the cost functional,

$$K(x)=\int_0^L w(\xi)J\mathrm{d}x, \quad J=\frac{\partial x}{\partial \xi}. \tag{C.1}$$

Here $w(\xi)$ is the weighting function defined as,

$$w_j(\xi)=\gamma_1 w_j^* + \gamma_2 w_j^{**} + J_j, \quad w_j^* = \frac{\max\limits_i \left| d_{i,j+1/2} - d_{i,j-1/2} \right|}{\max\limits_{i,j} \left| d_{i,j+1/2} - d_{i,j-1/2} \right|}, \quad w_j^{**} = \frac{\left.\partial A/\partial \xi\right|_j}{\max\limits_j \left.\partial A/\partial \xi\right|_j}. \tag{C.2}$$

We first consider the case of uniform cross-sectional area channels. In this case, the weighting function does not depend on the cross-sectional area, i.e., $w^{**}=0.$ The optimal grid density therefore results from a tradeoff between the Jacobian, $J,$ and the numerical dissipation (accounted by w^*). We roughly divide the computational domain of length *L* into regions with high and low numerical dissipation. The high numerical dissipation region has length L_D and the remaining domain with combined length $L_{ND}=(L-L_D)$ has low numerical dissipation. Subscripts *D* and *ND* denote properties in regions with dissipation and no dissipation, respectively.

As discussed in Section 3.3, the optimal grid density is achieved when,

$$w(\xi)J = const. \quad \Rightarrow \quad \left(\gamma_1 w_j^* + J_j\right)J_j = const. \tag{C.3}$$

Applying eq. (C.3) to regions with high and low dissipation we obtain a relation between grid densities in the two regions,

$$\left(\gamma_1 w_D^* + J_D\right)J_D = \left(\gamma_1 w_{ND}^* + J_{ND}\right)J_{ND}. \tag{C.4}$$

Noting that, the grid density is high $\left(J_D \ll 1\right)$ in the region with high dissipation and $\gamma_1 w_{ND} \ll 1$ in region with low dissipation, eq. (C.4) simplifies to

$$\gamma_1 w_D^* J_D = J_{ND}^2. \tag{C.5}$$

Assuming that out of total N grid points, N_D grid points cluster in the high dissipation region, J_D and J_{ND} can be approximated as,

$$J_D = \frac{\Delta x_D}{\Delta \xi} \approx \frac{L_D / N_D}{L / N}, \quad J_{ND} = \frac{\Delta x_{ND}}{\Delta \xi} \approx \frac{L_{ND} / \left(N - N_D\right)}{L / N} = \frac{1 - L_D / L}{1 - N_D / N}. \tag{C.6}$$

Substituting expressions of J_D and J_{ND} in eq. (C.5) yields a scaling for the parameter γ_1,

$$\gamma_1 = \left(\frac{1 - L_D / L}{1 - N_D / N}\right)^2 \frac{N_D L}{N L_D w_D^*}. \tag{C.7}$$

In typical electrokinetics problems, $L_D \ll L$, and $N_D \ll N$ and $w_D^* \approx 1$ (since w^* is normalized by its maximum value). Therefore, scaling of γ_1 given by eq. (C.7) can be simplified to,

$$\gamma_1 = \frac{N_D L}{N L_D}. \tag{C.8}$$

For many non-linear electrokinetics problems, such as ITP, numerical dissipation is primarily limited to sharp zone boundaries. Hence, L_D can be approximated as the characteristic length scale of the zone boundary, $L_D = \delta \sim RT\sigma / \left(jF\right).$ Here R is the universal gas constant, T the temperature, j the current density, F the Faraday's constant, and σ the local electrical conductivity. Typical simulation parameters for ITP problems are $N \sim \mathcal{O}(100)$, $N_D \sim \mathcal{O}(10)$, $L \sim \mathcal{O}(10 \text{ mm})$, and $L_D = \delta \sim \mathcal{O}\left(10^{-3}\text{-}10^{-2} \text{ mm}\right)$. Therefore, γ_1 is $\mathcal{O}\left(10^2 - 10^3\right)$ in majority of ITP simulations. Analogously, for problems with variable cross-sectional area where the area varies over relatively small distance compared to the total length of the domain, γ_2 is $\mathcal{O}\left(10^2-10^3\right)$. For problems involving both sharp concentration boundaries and cross-sectional variation, γ_1 and γ_2 are each $\mathcal{O}\left(10^2-10^3\right)$ and the relative magnitude of γ_1 and γ_2 determine whether grid points preferentially aggregate in regions with high dissipation or large variations in channel cross-section.

To confirm the latter order of magnitude estimate of the adaptive grid parameter γ_1, we performed numerical experiments based on a single-interface ITP problem consisting of three strong electrolyte species, leading electrolyte ion (LE), trailing electrolyte ion (TE) and counter-ion (CI). For these set of simulations, we assumed that all species were fully ionized and we did not include chemical equilibrium and ionic strength effects in our calculations. Hence mobilities of all species were constant throughout the simulation; the mobilities of LE, TE, and CI are -8×10^{-8}, -4×10^{-8} and 5×10^{-8} $\mathrm{m^2V^{-1}s^{-1}}$, respectively. We performed simulations for 10 mM LE concentration and a current density of 255 $\mathrm{Am^{-2}}$. The computational domain length was 10 mm and we discretized the domain using 100 grid points. Simulations were performed in the frame of reference moving with ITP interface.

This model problem is interesting because it allows comparison of simulation results with an analytical expression of the ratio of LE to TE concentration. As shown by Saville and Palusinski [60], the ratio of LE to TE concentration for the current problem is given by,

$$\frac{c_{LE}}{c_{TE}}=\exp\left(-\frac{x}{\delta}\right),\quad \delta=RTz_{LE}\frac{\mu_{TE}\left(\mu_{LE}-\mu_{CI}\right)}{\mu_{LE}-\mu_{TE}}\frac{c_{LE}^0}{j},\tag{C.9}$$

where subscripts *LE*, *TE*, and *CI* denote properties related to the leading electrolyte ion, the trailing electrolyte ion and the counter-ion. In eq. (C.9) δ denotes the characteristic length of the diffusive ITP interface, *R* is the universal gas constant, *T* is the temperature (assumed to be 298 K) and *j* is the current density. For the current problem, eq. (C.9) yields $\delta=12.6$ µm.

We performed simulations using the SLIP scheme (with $\gamma_1=0$, 10, 100) and the non-dissipative sixth-order compact scheme [69], and compared the simulation results with the analytical expression given by eq. (C.9). In Figure C.1 we plot the computed and analytical ratio of LE to TE concentration versus the axial coordinate (non-dimensionalized with δ). The SLIP scheme without adaptive grid refinement $\left(\gamma_1 = 0\right)$ results in significantly diffused interface. The accuracy of SLIP scheme improves when adaptive grid refinement is used $\left(\gamma_1 = 10, 100\right)$. For $\gamma_1 = 100$, the numerical solution shows good agreement with the analytical result. Furthermore, as shown in Figure C.1, the SLIP scheme with $\gamma_1 = 100$ has similar resolution as the non-dissipative sixth-order compact scheme (with adaptive grid refinement). These simulation results suggest that $\gamma_1 \sim \mathcal{O}\left(10^2\right)$ is a good choice for obtaining high resolution solutions using the SLIP scheme.

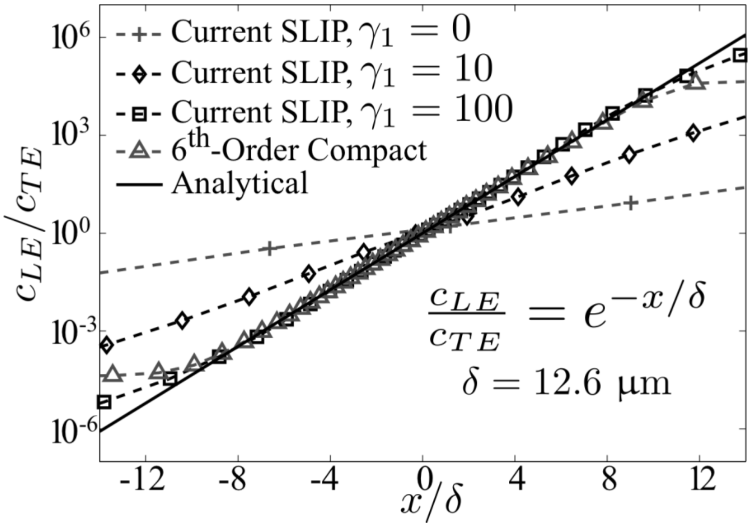

Figure C.1: Comparison of the accuracy of SLIP scheme with varying degree of grid adaptation and the sixth-order compact scheme with analytical solution of a model single-interface ITP problem. The plot shows variation of the ratio of LE to TE concentration (c_{LE} / c_{TE}) versus the axial coordinate. The axial coordinate x is non-dimensionalized using the characteristic length of the diffusive zone boundary δ. The solid straight line shows the analytical solution by Saville and Palusinski [60] in log-linear coordinates. The current SLIP schemes yields artificially diffused solution when adaptive grid refinement is not used $(\gamma_1 = 0)$. The solution obtained using the SLIP scheme approaches the analytical solution as higher amount of grid adaptation is employed (corresponding to higher values of grid adaptation parameter γ_1). At $\gamma_1 = 100$ the solution obtained by the SLIP scheme closely resembles the analytical solution. Also, in the current case, the accuracy of SLIP scheme with $\gamma_1 = 100$ is equivalent to the accuracy of sixth-order compact scheme coupled with adaptive grid refinement.

D. Derivation of regulating functions for weak univalent electrolyte systems

We here summarize the key assumptions and steps involved in the derivation of Jovin [43] and Alberty [44] regulating functions for weak univalent electrolyte systems. We also describe a combined Jovin-Alberty function and apply it for calculating species concentrations in ITP.

D.1 Jovin function

The Jovin function is valid for electrolyte systems consisting of weak univalent acid and bases, under the safe pH conditions (5<pH<9, [134]). The safe pH range ensures that the contribution of hydronium and hydroxyl ions to the local electrical conductivity is negligible. Starting with the species transport equations given by eq. (2.2), and neglecting hydrodynamic flow and molecular diffusion we obtain,

$$\frac{\partial c_i}{\partial t} + \nabla \cdot \left(\mu_i c_i \mathbf{E} \right) = 0, \quad i = 1, \ldots, N. \tag{D.1}$$

Here c_i and μ_i respectively denote the total concentration and the effective mobility of species *i*. Multiplying eq. (D.1) with $z_i = \{\pm 1\}$ and performing summation over all species yields,

$$\frac{\partial}{\partial t}\left(\sum_{i=1}^{N} z_i c_i \right) + \nabla \cdot \left(\sum_{i=1}^{N} z_i \mu_i c_i \mathbf{E} \right) = 0. \tag{D.2}$$

Noting that for univalent electrolytes, conductivity $\sigma = \sum_i z c_{i,z} \mu_{i,z} F$ (from eq. (2.7)), eq. (D.2) can be simplified as,

$$\frac{\partial}{\partial t}\left(\sum_{i=1}^{N} z_i c_i \right) + \frac{1}{F} \nabla \cdot \left(\sigma \mathbf{E} \right) = 0. \tag{D.3}$$

In absence of diffusive fluxes, the second term on the left hand side of eq. (D.3) is exactly zero as a consequence of Ohm’s law. Therefore, eq. (D.3) simplifies to,

$$\begin{gathered}\frac{\partial}{\partial t}\left(\sum_{i=1}^{N} z_i c_i\right)=0,\\ J\left(x,t\right)=\sum_{i=1}^{N} z_i c_i\left(x,t\right)=J\left(x,0\right).\end{gathered}\tag{D.4}$$

The time invariant function $J(x,t)$ in eq. (D.4) is termed the Jovin function [43]. Since the above derivation neglects the diffusive fluxes, the Jovin function is only valid at locations far from sharp concentration gradients. We also note that the Jovin function differs from the electroneutrality assumption as c_i here denotes the total concentration of species. Unlike the electroneutrality relation the Jovin function in general is not equal to zero.

D.2 Alberty function

The Alberty function applies for electrolyte systems consisting of weak univalent acid and bases, under the assumption that hydronium and hydroxyl ion concentrations are significantly smaller than other species concentrations. The latter assumption is less restrictive than the safe pH condition (5<pH<9) [49] used to derive the Jovin function in Section D.1. We begin by multiplying eq. (D.1) with $z_i / \mu_{i,z}$ followed by summation over all species to obtain,

$$\frac{\partial}{\partial t}\left(\sum_{i=1}^{N}\frac{z_i c_i}{\mu_{i,z}}\right)+\nabla\cdot\left(\sum_{i=1}^{N} z_i \frac{\mu_i}{\mu_{i,z}} c_i \mathbf{E}\right)=0. \tag{D.5}$$

Using the electroneutrality assumption, $\sum_{i=1}^{N} z_i c_{i,z}=0,$ and noting that for weak univalent electrolyte species $\mu_i c_i / \mu_{i,z}=g_{i,z} c_i=c_{i,z}$, eq. (D.5) can be simplified as following,

$$\begin{gathered}\frac{\partial}{\partial t}\left(\sum_{i=1}^{N}\frac{z_i c_i}{\mu_{i,z}}\right)+\nabla\cdot\left(\sum_{i=1}^{N} z_i c_{i,z}\mathbf{E}\right)=0,\\ \frac{\partial}{\partial t}\left(\sum_{i=1}^{N}\frac{z_i c_i}{\mu_{i,z}}\right)=0,\\ A\left(x,t\right)=\sum_{i=1}^{N}\frac{z_i c_i\left(x,t\right)}{\mu_{i,z}}=A\left(x,0\right).\end{gathered}\tag{D.6}$$

The function $A(x,t)$ in eq. (D.6) is termed the Alberty function [44], and is the counterpart of Kohlrausch function [42] for weak univalent electrolytes.

D.3 Combined Jovin-Alberty function

The Jovin and Alberty functions relate total concentrations of all species in an electrokinetic system to the initial species concentrations. For a system of N univalent weak electrolyte species, Jovin and Alberty relations provide two coupled, linear, algebraic equations for N variables (the species concentrations). Instead of solving these two linear equations for every problem, it is convenient to formulate a single equation by eliminating one variable (*e.g.*, concentration of Nth species) from the Jovin and Alberty functions. Multiplying the Jovin function $J(x,t)$ by $1/\mu_{N,z}$ and subtracting it from the Alberty function $A(x,t)$ yields a combined Jovin-Alberty function $F(x,t)$,

$$\begin{aligned} F(x,t) &= A(x,t) - \frac{1}{\mu_{N,z}} J(x,t), \\ &= \sum_{i=1}^{N} \frac{z_i c_i}{\mu_{i,z}} - \frac{1}{\mu_{N,z}} \sum_{i=1}^{N} z_i c_i, \\ &= \sum_{i=1}^{N-1} z_i c_i \left(\frac{1}{\mu_{i,z}} - \frac{1}{\mu_{N,z}} \right) = F(x,0). \end{aligned} \tag{D.7}$$

Note that the combined Jovin-Alberty function $F(x,t)$, defined in eq. (D.7), is a linear combination of Jovin and Alberty functions, and should not be treated as a separate regulating function for weak univalent electrolyte systems. Since the combined Jovin-Alberty function is based on the Jovin function, it is only applicable for safe pH conditions ($5 < \text{pH} < 9$). We also note that using electroneutrality assumption in addition to the combined Jovin-Alberty function provides no extra information about the total concentrations of species. This is because Alberty function is itself derived using the electroneutrality assumption (see eq. (D.6)). However, knowing the total concentrations of species, electroneutrality assumption can be used in conjunction with chemical equilibrium equations to obtain concentrations of various ionization states of weak electrolyte species.

D.4 Example showing use of combined Jovin-Alberty function for calculating analyte concentration in plateau mode ITP

The combined Jovin-Alberty function is particularly useful for calculating species concentrations in ITP zones for weak univalent electrolyte systems. In typical ITP experiments, the separation channel is initially filled with LE having a spatially uniform concentration. Therefore, the initial LE concentration sets a constant value of Jovin-Alberty function for later times. To calculate the total concentration of an analyte focused in a purified, plateau zone in anionic ITP, we choose background counter-ion (C) as the Nth species in eq. (D.7) to obtain,

$$\begin{aligned} F(x,t) &= -c_{A,l}\left(\frac{1}{\mu_{A,-1}} - \frac{1}{\mu_{C,+1}}\right) \\ &= F(x,0) = -c_{L,l}\left(\frac{1}{\mu_{L,-1}} - \frac{1}{\mu_{C,+1}}\right). \end{aligned} \tag{D.8}$$

Here first subscripts A and L denote analyte and LE ion, respectively, and second subscripts a and l denote analyte and LE zones, respectively. Simplifying eq. (D.8) yields total concentration of focused analyte as a function of LE ion concentration and species mobilities,

$$c_{A,a} = c_{L,l}\left(\frac{1-\mu_{C,+1}/\mu_{L,-1}}{1-\mu_{C,+1}/\mu_{A,-1}}\right). \tag{D.9}$$

E. Benchmark of ionic strength correction calculations with PeakMaster

Table E.1: Benchmark of ionic strength correction calculation of SPRESSO with PeakMaster. Calculations for HEPES-NaOH buffer for different ionic strengths. Concentrations of HEPES and NaOH are varied for varying ionic strength, with fixed concentration ratio HEPES:NaOH equal to 2:1.

Ionic Strength (mM)	PeakMaster					
	pH	Mobility HEPES $(\times 10^{-9})$ $m^2V^{-1}s^{-1}$	Mobility Sodium $(\times 10^{-9})$ $m^2V^{-1}s^{-1}$	pH	Mobility HEPES $(\times 10^{-9})$ $m^2V^{-1}s^{-1}$	Mobility Sodium $(\times 10^{-9})$ $m^2V^{-1}s^{-1}$
10	7.457	-10.15	48.13	7.457	-10.16	48.14
20	7.443	-9.60	46.84	7.443	-9.61	46.86
30	7.433	-9.22	45.94	7.433	-9.23	45.96
40	7.426	-8.92	45.23	7.426	-8.93	45.25
50	7.420	-8.67	44.64	7.420	-8.68	44.67
60	7.415	-8.45	44.14	7.415	-8.47	44.16
70	7.411	-8.26	43.69	7.411	-8.28	43.72
80	7.407	-8.10	43.30	7.407	-8.11	43.32
90	7.404	-7.94	42.93	7.404	-7.96	42.96
100	7.401	-7.80	42.61	7.401	-7.82	42.63

Results agree with maximum error of 0.2%. This may be because PeakMaster uses slightly different values of the basic properties of the solvent as they appear in the Onsager-Fuoss relation. We do not know the values used by Peakmaster, and they are not listed in [101]. For our calculations we use assume a value of 78.36 for the relative permittivity of water, and assume a viscosity of water = 0.8903×10^{-3} Pa.s at 25°C.

F. Calculation of species concentrations in ITP zones using diffusion-free model

In Section 4.2.1, we presented an unsteady, diffusion-free model to calculate species concentrations and shock speeds in ITP. We also showed (in Figure 4.2) comparison of our model with detailed one-dimensional simulations using SPRESSO [58,63,118]. Here we describe the numerical procedure to calculate species concentrations in different ITP zones using our diffusion-free model. In Section 4.2.1 we derived Hugoniot jump conditions relating concentrations of each species across ITP shocks,

$$\frac{dx}{dt}(c_i^+ - c_i^-) = \frac{J}{A(x)}\left(\frac{\mu_i^+ c_i^+}{\sigma^+} - \frac{\mu_i^- c_i^-}{\sigma^-}\right), \quad \sigma = \sum_{i=1}^{N} \alpha_i c_i, \quad \alpha_i = \sum_{i=1}^{N} \sum_{z=n_i}^{p_i} z\mu_{i,z} c_{i,z} F / c_i. \qquad \text{(F.1)}$$

where c_i, μ_i denote the concentration and effective mobility of species i, and σ denotes the electrical conductivity. Here J denotes the current, A the cross-sectional area and dx/dt the shock speed. In eq. (F.1) $-$ and $+$ denote the evaluation of a property behind and in front of a shock, respectively.

Here we consider an ITP experiment with a leading electrolyte (LE), a trailing electrolyte (TE), an analyte (initially mixed with the TE) and a background electrolyte. In this case, two propagating shocks form corresponding to the adjusted-TE-to-analyte interface and the analyte-to-LE interface. Whereas the interface between the TE well and the adjusted TE zone remains stationary. See Zhukov [7] for more discussion on existence of propagating and stationary interfaces. The concentrations of species in the LE zone and the TE well are set by the initial conditions (when samples are loaded onto the chip). Whereas the species concentrations in the (plateau mode) analyte and the adjusted-TE zones matches the Jovin and Alberty functions [43,44] established by the LE. We therefore solve for the species concentrations in the analyte and the adjusted-TE zones.

For computing the analyte zone composition the unknowns are: (i) analyte concentration, $c_{a,A}$, (ii) counter-ion concentration, $c_{c,A}$, and (iii) local pH (or hydronium ion concentration, $c_{H+,A}$) of analyte zone. In our notation, first subscripts *l*, *a*, *t*, and *c* denote LE, analyte, TE, and counter ions, respectively. The second subscripts *L*, *A*, and *T* denote LE, analyte, and adjusted TE zones. We solve for the species concentrations in the analyte zone by applying jump conditions, eq. (F.1), across the analyte-to-LE interface. Since analyte ions are not present in the LE zone (neglecting diffusion), and LE ions are not present in the analyte zone, eq. (F.1), for analyte and LE ions yields,

$$\frac{\mu_{a,A}}{\sigma_A} = \frac{\mu_{l,L}}{\sigma_L}, \tag{F.2}$$

which is the usual ITP condition. Next, using eq. (F.2) along with Hugoniot condition (eq. (F.1)) for counter-ions yields an explicit relation between the concentrations of counter-ions in LE and analyte zones,

$$c_{c,A}\left(1-\frac{\mu_{c,A}}{\mu_{a,A}}\right) = c_{c,L}\left(1-\frac{\mu_{c,L}}{\mu_{l,L}}\right). \tag{F.3}$$

The remaining equation for pH of analyte zone comes from the electroneutrality assumption, eq. (2.10). Equations (F.2) and (F.3) along with electroneutrality condition form a coupled set of nonlinear algebraic equations in terms of variables, $c_{a,A}$, $c_{c,A}$, and pH (or hydronium ion concentration, $c_{H+,A}$). The nonlinearity results from strong dependence of effective mobilities on $c_{H+,A}$. We employ an iterative approach to solve this set of nonlinear equations, wherein we first use concentrations, $c_{a,A}$ and $c_{c,A}$, from the previous iteration to compute pH. This satisfies the electroneutrality equation for analyte zone. Knowing the local pH of analyte zone, and hence the effective mobilities, eqs. (F.2) and (F.3) result in a solvable set of linear equations for $c_{a,A}$ and $c_{c,A}$. We repeat the above steps until solution converges. In practice, we found that updating the species concentrations using $c_i^{n+1} = \omega \tilde{c}_i^{n+1} + (1-\omega)c_i^n$ (i.e., by successive over-relaxation procedure) at every iteration improves the convergence rate. Here ω is a predefined scalar parameter. Choosing $0<\omega<1$ can stabilize otherwise unstable iteration, while $\omega>1$ can accelerate the convergence of otherwise stable iteration. For typical calculations we choose $\omega = 0.9$. To account for effects of ionic strength on electrophoretic mobilities and ionic activity (see Chapter 3), we correct mobilities and ionic activities at each iteration using the Onsager-Fuoss [80] and the Debye-Huckel model [81], respectively. We note that, to simplify calculations, ionic strength effects can be neglected while calculating sample accumulation for univalent ITP systems (see Section 3.3.2).

Next, we solve for the remaining unknowns, namely the concentrations of analyte, TE ion and counter-ion in the adjusted-TE zone. We apply eq. (F.1) across the adjusted-TE-to-analyte and the TE well-to-adjusted-TE interface to solve for the concentrations of analyte, TE and counter-ion in the adjusted TE zone. Using the jump conditions, eq. (1), across the adjusted-TE-to-analyte interface (which moves at a speed of $\mu_{t,T} J / (\sigma_T A)$) we obtain,

$$\frac{\mu_{t,T}}{\sigma_T}\left(c_{i,A} - c_{i,T}\right) = \left(\frac{\mu_{i,A}}{\sigma_A} c_{i,A} - \frac{\mu_{i,T}}{\sigma_T} c_{i,T}\right), \quad i = a, t, c. \tag{F.4}$$

Further, using the jump condition across the stationary interface between the TE well and the adjusted TE zone we obtain a relation between the species concentrations in the adjusted-TE zone and the TE well,

$$\frac{\mu_{i,well}}{\sigma_{well}} c_{i,well} = \frac{\mu_{i,T}}{\sigma_T} c_{i,T}, \quad i = a, t, c. \tag{F.5}$$

Combining eqs. (F.4) and (F.5) yields a set of three nonlinear equations for species concentrations in TE zone,

$$\frac{\mu_{t,T}}{\sigma_T}\left(c_{i,A} - c_{i,T}\right) = \left(\frac{\mu_{i,A}}{\sigma_A} c_{i,A} - \frac{\mu_{i,well}}{\sigma_{well}} c_{i,well}\right), \quad i = a, t, c. \tag{F.6}$$

The above set of equations along with the electroneutrality assumption then form a set of four coupled algebraic equations in $c_{a,T}$, $c_{t,T}$, $c_{c,T}$ and the pH of adjusted-TE zone. We solve this set of equations using an iterative procedure, similar to that described above for eqs. (F.2) and (F.3). Finally, knowing the species concentrations in all ITP zones, we evaluate the speeds of propagating interfaces. The analyte-to-LE interface propagates at a speed of $\mu_{l,L} J/\left(\sigma_L A\right) = \mu_{a,A} J/\left(\sigma_A A\right)$ while the adjusted-TE-to-analyte interface propagates at a speed of $\mu_{t,T} J/\left(\sigma_T A\right)$.

G. Dependence of sensitivity and assay time on geometry of variable cross-sectional area channels

In Section 4.2.2, we showed that the plateau zone length of an analyte, Δ_P, is proportional to both the concentration of the analyte in the well, c_a^0, and to the geometric parameter $A_L L_L / A_D$,

$$\Delta_p = \left(1 - \frac{\mu_{t,T}}{\mu_{a,T}}\right) \frac{\mu_a^0}{\mu_{t,T}} \frac{\sigma_T}{\sigma^0} \left(\frac{A_L L_L}{A_D}\right) \frac{c_a^0}{c_{a,A}}. \tag{G.1}$$

Recall that A_L and L_L are the cross-sectional area and length of the loading (larger cross-section) region of the channel, and A_D is the cross-sectional area of the detection (smaller cross-section) region. We observe that the theoretical plateau zone length is independent of the applied voltage or current. We here derive analytical relations for the dependence of sensitivity (or SNR) and assay time on channel geometry. SNR and assay time have different functional dependences for the cases of fixed current and fixed voltage. We therefore derive the analytical expressions for SNR and assay time separately for fixed voltage and fixed current operation.

G.1 Fixed Voltage

To estimate the assay time for fixed voltage operation, we calculate the time taken by the analyte zone to travel from the trailing electrolyte (TE) well to the detection section. Let x denote the coordinate of the interface between the analyte and leading electrolyte (LE). In the absence of electroosmotic flow (EOF), the speed of the analyte-to-LE interface in the loading section is given by

$$\frac{dx}{dt} = \frac{\mu_{l,L}}{A_L} \frac{J(x)}{\sigma_L}, \tag{G.2}$$

where A_L is the cross-sectional area of the loading section, $\mu_{l,L}$ is the effective mobility of LE in the LE zone, σ_L is the conductivity of the LE zone and $J(x)$ is the current through the channel when the analyte-to-LE interface is at location x. We can approximately relate total current in the system to the applied voltage, ΔV, using Ohm's law,

$$\Delta V = JR, \quad R = \frac{x}{\sigma_T A_L} + \frac{L_L - x}{\sigma_L A_L} + \frac{L_D}{\sigma_L A_D}, \tag{G.3}$$

where σ_T is the conductivity of TE zone and A_D is the cross-sectional area of detection section. In eq. (G.3) we have neglected the contribution of analyte zone to the electrical resistance of the channel. This is a reasonable approximation because the analyte zone length is much smaller than the LE and the TE zones. Also, within interfaces between zones, the diffusive current is non-negligible and so Ohm's law does not apply locally. However, we also assume these interfaces also contribute negligible resistance to the total axial-length-averaged resistance in the channel. Combining eqs. (G.2) and (G.3) we obtain a differential equation relating time and the location of analyte-to-LE interface,

$$\frac{dt}{dx} = \frac{A_L}{\mu_{l,L}} \frac{\sigma_L}{\Delta V} \left(\frac{x}{\sigma_T A_L} + \frac{L_L - x}{\sigma_L A_L} + \frac{L_D}{\sigma_L A_D} \right). \tag{G.4}$$

To calculate the assay time, *T*, we integrate eq. (G.4) up to $x = L_L$ (where the detection section begins)

$$T = \int_0^{L_L} \frac{A_L}{\mu_{l,L}} \frac{\sigma_L}{\Delta V} \left(\frac{x}{\sigma_T A_L} + \frac{L_L - x}{\sigma_L A_L} + \frac{L_D}{\sigma_L A_D} \right) dx. \tag{G.5}$$

Evaluating the integral above, we obtain an algebraic expression for the assay time for fixed voltage operation,

$$T = \frac{L_L L_D}{\mu_{l,L} \Delta V} \left(\frac{A_L}{A_D} + \frac{1}{2} \left(1 + \frac{\sigma_L}{\sigma_T} \right) \frac{L_L}{L_D} \right). \tag{G.6}$$

Next, we derive the dependence of SNR on geometric parameters. SNR is given by the length of the analyte plateau zone normalized by the characteristic length of diffused zone boundaries,

$$\mathrm{SNR} = \frac{\varDelta_p}{\left(\delta_{te,an} + \delta_{an,le}\right)/2}. \tag{G.7}$$

Here $\delta_{te,an}$ and $\delta_{an,le}$ are, respectively, the characteristic widths of adjusted TE-to-analyte and analyte-to-LE interfaces in the detection section. For the characteristic width of an ITP interface, we use the analytical expression provided by Saville and Palusinski [60],

$$\delta_{1,2} = \frac{k_B T}{e} \frac{\mu_1 \sigma_2}{\left(\mu_2 - \mu_1\right) j}. \tag{G.8}$$

where subscripts 1 and 2 denote lower and higher mobility species corresponding to the zones adjoining a particular interface (*e.g.*, for analyte-to-LE zone subscript 1 refers to the analyte and 2 refers to the LE). Here k_B is the Boltzmann constant, T the temperature, e the unit elementary charge and j $\left(= J / A_D\right)$ the current density. To estimate the current, for eq. (G.8), we substitute $x = L_L$ in eq. (G.3). The corresponding current density is given by,

$$j = \frac{\varDelta V \sigma_L}{L_D \left(1 + \dfrac{L_L A_D \sigma_L}{L_D A_L \sigma_T}\right)}. \tag{G.9}$$

This is the current density in the detector section, when the analyte-to-LE interface is at the junction of loading and detection section. Combining eqs. (G.7), (G.8) and (G.9) we obtain the dependence of SNR on geometric parameters, A_L, A_D, L_L and L_D,

$$\mathrm{SNR} \propto \left(\frac{A_L L_L}{A_D L_D}\right)\left(1 + \frac{L_L A_D \sigma_L}{L_D A_L \sigma_T}\right)^{-1}. \tag{G.10}$$

Figure G.1 shows the dependence of zone length (dashed contours) and interface thickness (solid line contours) on L_L and A_L / A_D, for fixed voltage. Here, we choose values of L_D = 5 mm and an applied potential of 350 V as typical values of interest. We note that smaller L_D values are often impractical as the channel can then become overly sensitive to pressure differences due to small differences in chip well liquid levels. From eq. (G.1) zone length increases by increasing A_L / A_D and L_L. This is because, for larger cross-sectional area ratios and loading lengths, larger amounts of sample accumulates in the loading section. As a result, the zone length in the detection section increases. Additionally, Figure G.1 shows that the interface thickness decreases by increasing A_L / A_D and decreasing L_L. From eq. (G.9), we see that current density in the detection section increases on increasing the cross-section ratio and decreasing loading length. Therefore the interface thickness, which is inversely proportional to current density, decreases by using higher cross-sectional area ratio and smaller loading length (since each of these increase electric field in the detector region).

Figure G.2 shows the dependence of SNR (dashed contours) and assay time (solid line contours) on cross-sectional area ratio and the length of the loading section, for fixed voltage operation. SNR increases by increasing both the cross-section ratio and the length of loading section. On increasing A_L / A_D, the zone length increases (more accumulation) and the interface length decreases (more field in the detection region, as per Figure G.1). Therefore SNR, which we define as the ratio of plateau zone length and characteristic interface thickness, increases for larger cross-sectional area ratios. However, for a fixed cross-section ratio, increasing the loading length increases both the zone length and the interface thickness. Hence in Figure G.2, we observe a weak dependence of SNR on L_L, particularly at high A_L / A_D. Further, Figure G.2 shows that, using larger cross-section ratio and loading length leads to longer assay time. For larger A_L / A_D, smaller voltage is dropped across the loading section. As a result, by increasing the cross-sectional area ratio, electric field in the loading section decreases. At lower electric field, ITP zones propagate slower and take longer time to reach the detection section, thereby increasing the assay time. Also, the assay time increases for longer loading section, as ITP zones have to travel a longer distance to reach the detection section.

For fixed voltage and SNR, increase in cross-sectional area ratio decreases the required channel length and also reduces the assay time. However, for a fixed loading length, larger cross-sectional area ratio yields higher SNR, but at the expense of longer assay time. Thus for a fixed voltage operation, there is a trade-off between SNR and assay time.

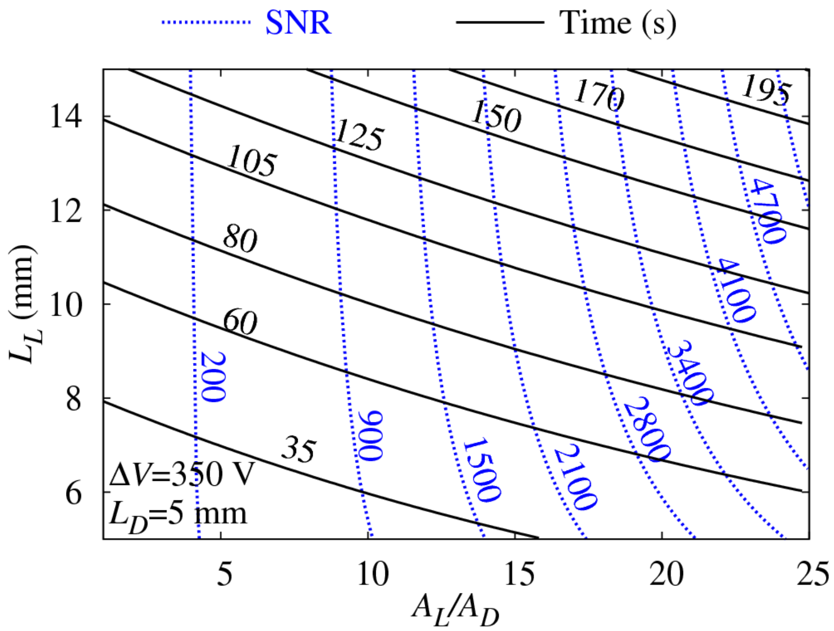

Figure G.1: Effect of cross-sectional area ratio (A_L / A_D) and the length of loading section (L_L) on plateau zone length and interface thickness for fixed voltage operation. Dashed lines show contours of constant zone length for varying A_L / A_D and L_L. Zone length increases by increasing both, A_L / A_D and L_L, since the amount of sample accumulated increases for larger A_L / A_D and L_L. Solid lines show the variation of diffusion-limited interface thickness (in the detection section) as a function of cross-section ratio and the length of loading section. Interface thickness decreases by increasing the cross-sectional area ratio and decreasing the loading length. For these calculations, we used a fixed voltage of 350 V and a detection section of length 5 mm. We calculated the values of conductivity of the LE and the adjusted TE zones, using our diffusion-free model, for ITP focusing of 2 µM Bistris (initially mixed with TE), with 10 mM NaOH as the LE, 10 mM Pyridine as the TE and 20 mM Hepes as the background counter-ion. The calculated conductivity of the LE zone is 7.28×10^{-2} S.m^{-1} and the conductivity of the adjusted TE zone is 4.7×10^{-3} S.m^{-1}.

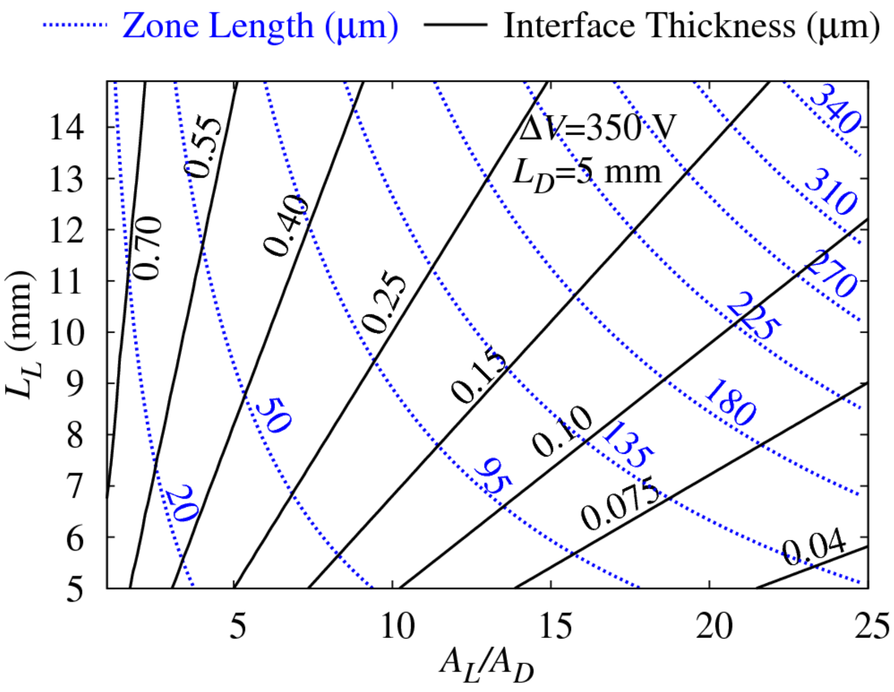

Figure G.2: Effect of cross-sectional area ratio (A_L / A_D) and length of loading section (L_L) on signal-to-noise ratio (SNR) and assay time, for fixed voltage operation. Dotted lines show the variation of SNR as a function of A_L / A_D and L_L. SNR increases by increasing both the cross-sectional area ratio and the loading length. However, increasing A_L / A_D yields greater improvements in SNR as compared to that only increasing L_L. This is because increasing A_L / A_D results in longer zone length and sharper interfaces; while increasing L_L yields longer zone length but thicker zone boundaries. Solid lines show the contours of constant assay time for different cross-sectional area ratios and loading lengths. The assay time increases by increasing the cross-sectional area ratio as well as the loading length. Therefore, for fixed voltage operation, higher SNR can be achieved with the same physical length of channel but this is accompanied by longer assay time. All calculations here are based on the parameters used in Figure G.1.

G.2 Fixed Current

We here estimate the dependence of assay time, interface thickness and SNR on channel geometry, for fixed current operation. To calculate the assay time, we integrate eq. (G.2) to obtain an analytical expression for assay time.

$$T = \frac{\sigma_L A_L L_L}{\mu_{l,L} J}. \tag{G.11}$$

In this case, the calculation of assay time is straightforward because the current is fixed and the shocks move at constant speeds in the loading section. To obtain the interface thickness we substitute current density $j = J / A_D$ in eq. (G.8) to obtain,

$$\delta_{1,2} = \frac{k_B T}{e} \frac{\mu_1 \sigma_2 A_D}{(\mu_2 - \mu_1) J}. \tag{G.12}$$

Using eq. (G.7) and (G.12) we see that when fixed current is applied across a varying cross-section channel,

$$\mathrm{SNR} \propto A_L L_L / A_D^2. \tag{G.13}$$

Figure G.3, shows the contours of constant zone length, assay time and SNR for varying A_L / A_D and L_L. For a fixed cross-sectional area of the detection section, zone length, assay time and SNR are all proportional to $A_L L_L$. Therefore in Figure G.3, the contours of constant zone length, assay time and SNR, are the same except for a multiplicative constant. Unlike the case of fixed voltage, SNR for fixed current operation increases significantly by increasing the loading length. This is because zone length increases for large L_L, while the interface thickness remains unaffected by changing L_L. Thus, SNR (which is the ratio of zone length and characteristic interface thickness) increases by using longer L_L, for fixed current systems.

Further, by using eqs. (G.7), (G.11) and (G.12) we note that,

$$\mathrm{SNR} \propto \frac{T}{A_D^2}. \tag{G.14}$$

The relation above shows that for a fixed assay time, T, we can obtain very high SNR by decreasing A_D. We note that such behavior is not observed for fixed voltage operation, where higher SNR is accompanied by longer assay time.

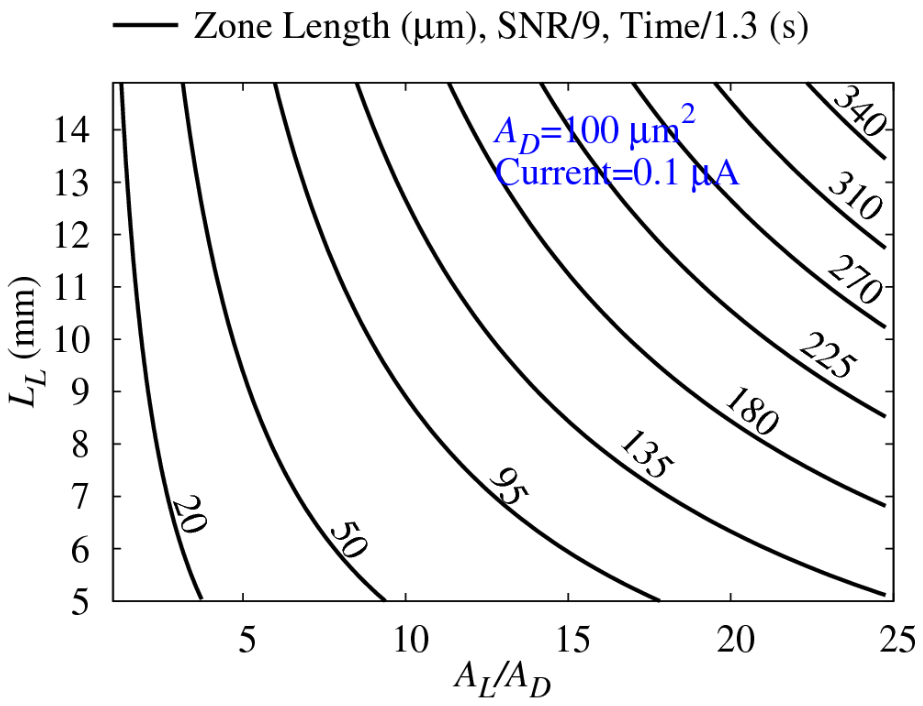

Figure G.3: Variation of zone length, SNR and assay time with cross-sectional area ratio (A_L / A_D) and loading length (L_L), for fixed current operation. Solid lines show the contours of constant zone length for varying cross-sectional area ratio and loading length. The contours of zone length are the same as those shown in Figure G.1, as zone length is independent of the applied voltage or current. For a fixed cross-section of the detection section, variation of SNR and assay time with A_L and L_L is similar to that of the zone length. Therefore, the contours of SNR and detection time have the same shape as those of zone length, except for a multiplicative constant. As an example, 50 µm zone length is equivalent to SNR = 450 and assay time of 66 s. For these calculations we used a fixed current of 0.1 µA and a detection section with 100 µm^2 cross-sectional area. ITP buffer chemistry for these calculations is the same as that used in Figure G.1.

H. Calculation of species concentrations in bidirectional ITP zones using diffusion-free model

Here we consider a bidirectional ITP experiment similar to that shown in Figure 5.4. In this case, finite amounts of anionic sample species, S1- and S2-, focus between anionic leading and trailing electrolyte ions (LE- and TE-, respectively). Simultaneously, a cationic ITP shock forms between cationic leading electrolyte (LE+) and trailing electrolyte (TE+) ions. The anionic and cationic shocks approach each other and later interact.

We solve the Hugoniot conditions across ITP shocks (given by eq. (F.1)) iteratively, using the approach described in Appendix E, to obtain the analyte zone concentrations before and after the shock interaction. The ratio of initial to final concentrations of an analyte zone then gives the gain in its zone length due to shock interaction. To obtain the initial and final analyte zone concentrations, we perform the following steps:

(a) *Anionic ITP before shock interaction*: We first solve for the concentrations of the sample analytes focused behind the LE-/LE+ zone (see Figure 5.4).

(b) *Cationic ITP before shock interaction*: We then solve for the concentration of LE- ions in the cationic TE (TE+/LE-) zone. Note that before shock interaction LE- is the background counter-ion for cationic ITP.

(c) *Anionic ITP after shock interaction*: After the shock interaction TE+/LE- mixture replaces LE+/LE- as the leading electrolyte for anionic ITP. Using the species concentrations in TE+/LE- zone, computed in step (b), we solve for the readjusted analyte zone concentrations behind the TE+/LE- zone.

H.1 Comparison of diffusion-free model with SPRESSO

We validated the calculations from the diffusion-free model with detailed one-dimensional simulations using SPRESSO [58,63]. We simulated a bidirectional ITP system similar to that shown in Figure 5.2 of the paper. For our simulations, we used

100 mM MOPS as LE-, 20 mM taurine as TE-, imidazole as LE+ (varying between 200-300 mM), 100 mM bistris as TE+, and HEPES and tricine as the model analytes. We varied the ratio of LE+ to LE- concentration by keeping LE- concentration fixed at 100 mM and varying LE+ concentration from 200 mM to 300 mM. The relative error between the species concentrations predicted by the steady state solver and SPRESSO was negligible (on the order of 0.001%). This is expected as steady state solver and SPRESSO solve respectively the integral and the differential forms of same species-transport equations. In Figure H.1, we show the gain in zone length due shock interaction predicted by the diffusion-free model and SPRESSO. The diffusion-free model and SPRESSO predict similar gains in zone length over wide range of LE+ to LE-concentration ratios, with and without ionic strength corrections.

H.2. Comparison of analytical model with SPRESSO and diffusion-free model

In Section 5.2.3, we presented an analytical model to predict the increase in zone length due to shock interaction in bidirectional ITP. The analytical model is valid for univalent ions at safe pH conditions (5< pH <9) and neglects the effect of ionic strength on species mobilities. In Figure H.1, we compare the gain in zone length predicted by the analytical model along with predictions using diffusion-free model and SPRESSO. Predictions using the analytical model agree well with those from diffusion-free model and SPRESSO when ionic-strength effects are neglected in both of the latter models. This shows that the assumption of safe pH in our model is valid for the conditions of our simulations (and experiments discussed in Section 5.4). However, the gains in zone length calculated using the analytical model do not agree with that obtained using SPRESSO and diffusion-free model with ionic strength corrections for species mobilities. This supports our conclusion that the error in prediction of gains in zone length by the analytical model (in Section 5.4.2) is solely due to our assumption of negligible dependence of ionic strength on species mobilities. Most importantly, the predictions resulting from the diffusion-free model including ionic strength effects and the SPRESSO predictions including ionic strength effects agree nearly exactly; successfully benchmarking the diffusion-free model *versus* SPRESSO.

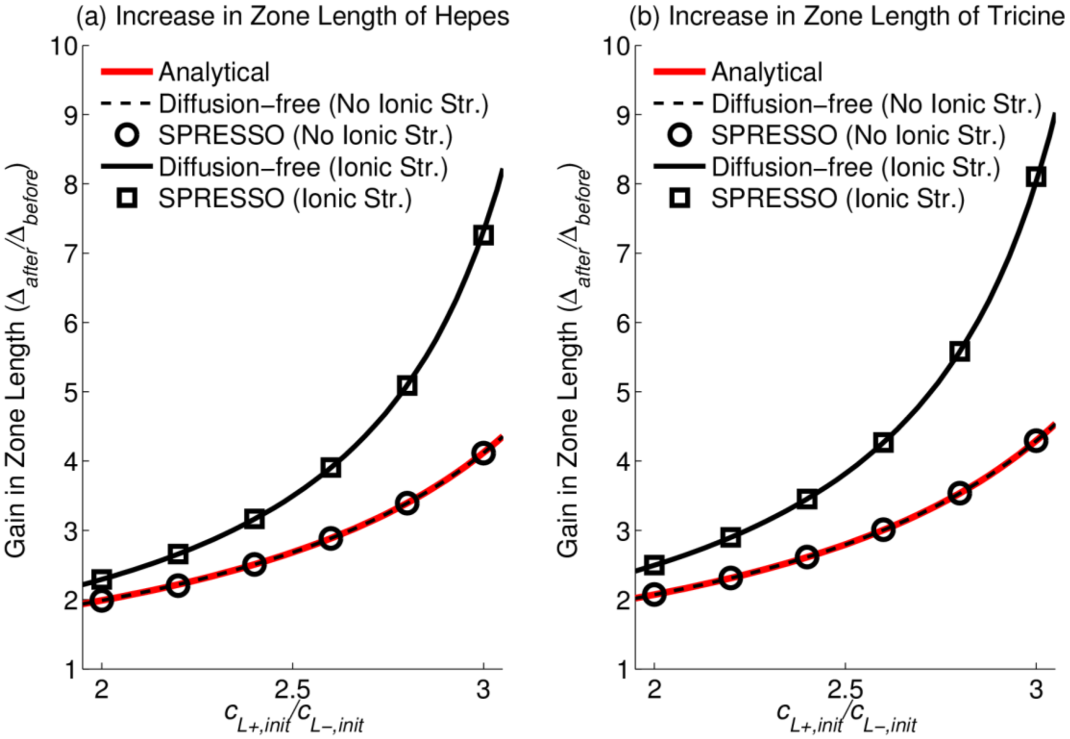

Figure H.1: Comparison of predicted gains in zone length due shock interaction using analytical model, diffusion-free model and SPRESSO. (a) and (b) show the variation of calculated gain in zone length $(\Delta_{after} / \Delta_{before})$ of two analytes (HEPES and tricine) versus the ratio of LE+ to LE- concentration in the initial LE+/LE- mixture $(c_{L+,init} / c_{L-,init})$. Both plots show that the predictions using diffusion-free model and SPRESSO agree well with each other, with and without ionic strength corrections for species mobilities. Whereas predictions using analytical model agree well with the simulations using diffusion-free model and SPRESSO only when ionic strength effects are neglected in both of the latter models. For these calculations, LE- is MOPS, LE+ is imidazole, TE- is 20 mM taurine and TE+ is 100 mM bistris. To vary the ratio $c_{L+,init} / c_{L-,init}$ we fixed the concentration of LE- at 100 mM and varied the concentration of LE+ from 200 to 320 mM.

I. Method for preconcentrating and separating weak acids using bidirectional ITP

In Section 6.2.1 we described a strategy for choosing electrolytes to couple ITP preconcentration and CE separation for the case of strongly ionized samples, such as nucleic acids. Here we describe the choice of buffers for weakly acidic analytes. For such analytes, we pursue a strategy wherein shock interaction decreases local pH of the anionic ITP zones, causing the effective mobility of analyte ions to drop below that of the TE- ions and thereby initiating electrophoretic separation. To this end, we can choose a relatively high pK_a base with high mobility as LE+ and a low mobility, weaker base as TE+. This creates a pH gradient across the cationic ITP shock, with a lower pH on the TE+ side. For the anionic ITP, we choose from relatively strong acids for LE-. We then choose a TE- with a lower pK_a than that of the analytes, but which also has low mobility. The latter is a key choice as we will use the shock interaction to titrate the anionic ITP zones to a lower pH, at which effective mobility of analytes decreases significantly compared to TE- ions, causing them to become slower than TE- ions.

Before the shock interaction, the pH of anionic ITP zones is high as the LE+ (a cation of weak base with relatively high pK_a) serves as the counter-ion. At high pH, weakly acidic analytes have high effective mobility and therefore focus ahead of slower TE- ions. When the cationic ITP shock interacts with the anionic ITP shock, TE+ (cation of relatively weak base) replaces LE+ (cation of a stronger base) as the counter-ion for anionic ITP. This decreases the local pH of anionic ITP zones and therefore decreases the local value of effective mobility of analyte ions. Whereas, the mobility of TE- ions does not decrease appreciably compared to analytes, as TE- is an anion of a stronger acid. If we make the choices of electrolytes correctly, the shock interaction causes the effective mobility of analyte anions to decreases to a value smaller than that of TE-. This then violates the ITP focusing conditions of analyte ions and initiates electrophoretic separation.

This scheme for preconcentrating and separating weakly acidic species differs from that for strongly acidic species in several aspects. Firstly, for weakly acidic species we use cationic ITP to titrate anionic ITP zones to a higher pH before the shock interaction and to a lower pH afterwards. This is in contrast to the scheme for strongly ionized anionic species, wherein the pH of anionic ITP zones increases after the shock interaction. Secondly, in the current scheme, electrophoretic separation occurs because the mobility of analyte ions decreases below the mobility of TE- ions after the shock interaction, while the mobility of TE- ions does not change appreciably. In contrast, in the case of strongly ionized anionic analytes, electrophoretic separation occurs because the mobility of TE- ions increases above that of the analytes after the shock interaction, but the mobility of analyte ions does not change appreciably.

We provide specific examples of viable electrolyte chemistries for extending our technique to anions of weak acids. Note that a key requirement is that LE+ should be a cation of a relatively stronger base with a pK_a higher than that of the TE+ and with a high fully-ionized mobility. While TE+ should be a cation of a weaker base with low fully-ionized mobility. Typically stronger bases have relatively high fully-ionized mobility compared to weak bases. Table H.1 shows three choices each for cationic LE and TE (nine usable combinations of LE+ and TE+) which satisfy our requirements. Another requirement is that the effective mobility of analyte ions should be more than that of TE- ions when the buffering counter-ion is LE+ and otherwise when the counter-ion is TE+. In order to effect a substantial increase in the effective mobility of analyte ions after the shock interaction, TE+ and LE+ should be chosen such that $\mathrm{p}K_{a,TE+} < \mathrm{p}K_{a,S-} < \mathrm{p}K_{a,LE+}$. On the other hand, TE- should belong to an acid with a pK_a lower than that of the analyte ions, so that the mobility of TE- ions does not change appreciably, after the shock interaction, compared to the mobility of analyte ions. For example, in our simulations shown below in Figure I.1, we used HEPES ($\mathrm{p}K_{a,TE-} = 7.5$) as TE-, ethanonamine ($\mathrm{p}K_{a,LE+}$ = 9.5) as LE+, bistris ($\mathrm{p}K_{a,TE+} = 6.4$) as TE+ and serine ($\mathrm{p}K_{a,-1} = 9.3$, $\mathrm{p}K_{a,+1} = 2.2$) as one of the analytes. Lastly, the choice LE- is straight forward, and any fast anion will serve such as Cl^- or SO_4^{2-}.

I.1 Simulation of coupled preconcentration and separation of amino acids using bidirectional ITP

To demonstrate the applicability of our technique for weakly acidic analyte species we performed simulations of coupled ITP focusing and electrophoretic separation of two amino acids (cysteine and serine) using bidirectional ITP. For our simulation we used the SPRESSO simulation tool [58,63] to solve one-dimensional species transport equations. We used 75 mM HCl as LE-, 20 mM HEPES as TE-, 150 mM ethanolamine as LE+ and 150 mM bistris as TE+. Initialy two analytes, cysteine (S1-) and serine (S2-), are mixed with the LE-/LE+ mixture each at a concentration of 80 µM. Figures I.1a-b show the initial conditions of the simulation. When electric field is applied, LE-/TE- and LE+/TE+ shocks propagate towards the right and the left, respectively. Prior to shock interaction, S1- and S2- focus between the LE- and TE- ions, as shown in Figure I.1d. When the LE+/TE+ and LE-/TE- shocks interact (Figures I.1e-f) the effective mobility of cysteine and serine ions decreases below the mobility of TE- ions. This initiates electrophoretic separation of the analyte ions. Figures I.1g-h show the final state where both analyte ions, S1- and S2-, are fully separated. We note that, for electrophoretic separation to occur it is necessary for TE- ions to overtake the focused analytes. However, TE- ions need not overtake LE- ions and the LE-/TE- shock may persist, as shown in Figure I.1g.

Table I.1: Possible cationic buffer systems for coupled preconcentration and separation of weakly acidic anions using bidirectional ITP.

cationic LE (LE+)	$\mu_{+1}\left(\times 10^{-9}\ \mathrm{m}^2.\mathrm{V}^{-1}.\mathrm{s}^{-1}\right)$	$\mathrm{p}K_{a,+1}$
Ethanolamine	44.3	9.5
Ammonium	76.2	9.25
Amediol	33.5	8.78
cationic TE (TE+)	$\mu_{+1}\left(\times 10^{-9}\ \mathrm{m}^2.\mathrm{V}^{-1}.\mathrm{s}^{-1}\right)$	$\mathrm{p}K_{a,+1}$
Bistris	26	6.4
Pyridine	30	5.18
Creatinine	37.2	4.83

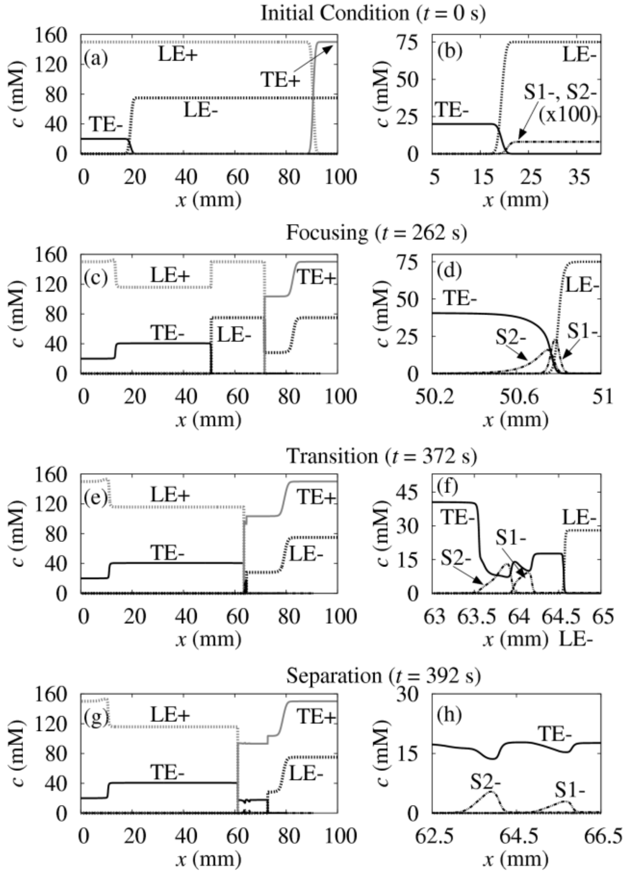

Figure I.1: Simulation showing focusing and separation of two amino acids (cysteine and serine) using bidirectional ITP. Plots in second column are detailed views of the distributions in the first column. (a-b) show the initial distribution of chemical species in the separation channel, prior to activating current. (c-d) show LE-/TE- and LE+/TE+ shocks after the electric field is applied. (c) shows an LE-/TE- shock (*x* = 50.5 mm) propagating rightward and a LE+/TE+ shock (*x* = 70 mm) propagating leftward. (d) shows anionic analytes cysteine (S1-) and serine (S2-) focused between LE- and TE-. (e-f) show the transition from focusing to separation upon the interaction of LE-/TE-and LE+/TE+ ITP shocks. The low pH TE+ zone washes over the focused anionic analytes, decreasing the effective mobility of S1- and S2-, while only negligibly affecting the mobility of TE-, which is a stronger acid. Here, the effective mobility of S1- and S2- decreases below that of TE-, thereby initiating separation. (f) shows TE- overtaking focused S1- and S2-, thus initiating electrophoretic separation. (g-h) show the final state, in which analytes S1- and S2- are fully separated. (h) shows fully separated peaks of S1- and S2- in the CE mode. Simulations were performed using our open source code SPRESSO. Chemistry is described in text. We assumed a constant current of 1.4 µA, and a D-shaped, wet-etched channel 74 µm wide and 12 µm deep. We approximately account for electroosmotic flow using a constant and uniform electroosmotic mobility of 2×10^{-9} $m^2V^{-1}s^{-1}$.

J. User's Manual to the Stanford Public Release Electrophoretic Separation Solver (SPRESSO)

J.1 Download and Installation

1) SPRESSO is a MATLAB based open source, nonlinear electrophoresis solver. The source code and its executable binary file can be downloaded for free at: http://microfluidics.stanford.edu/spresso.

2) Download the code and unzip the file to a desired directory. To run SPRESSO using the source code, first navigate to the directory containing the file `Spresso.m`. Then run `Spresso.m` by opening the file in MATLAB editor and hitting the run command (F5). Alternatively, SPRESSO can be run by giving Spresso command on the MATLAB command line. Running SPRESSO will cause a graphical user interface (GUI) to appear, as shown in Figure J.1.

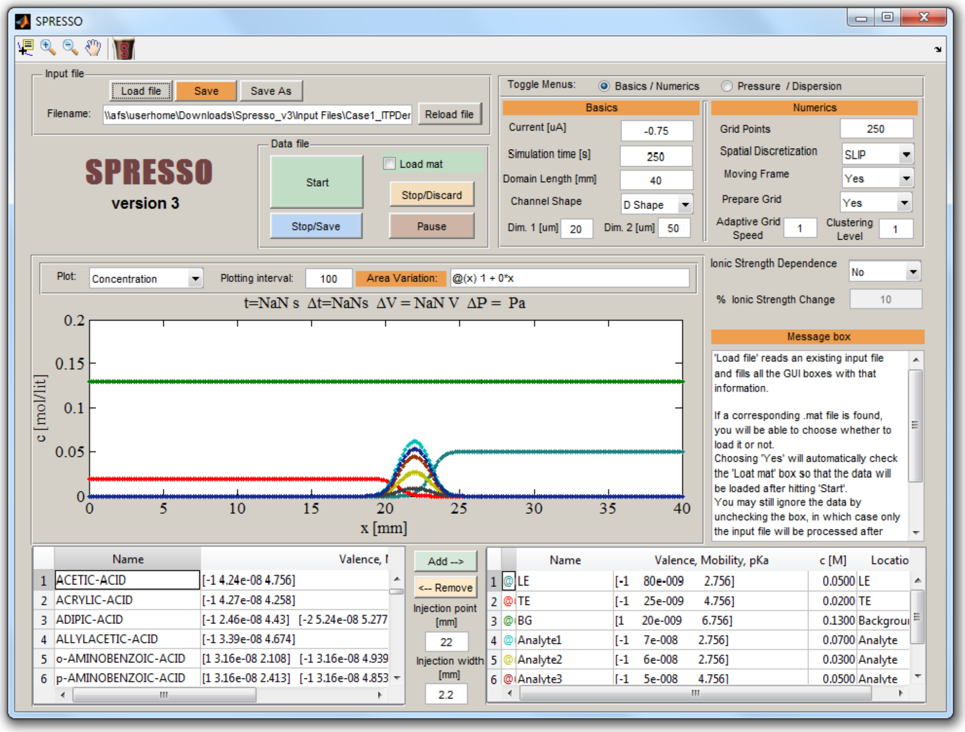

Filename: \\afs\userhome\Downloads\Spresso_v3\Input Files\Case1_ITPDer

☐ Load mat

Toggle Menus: ● Basics / Numerics ○ Pressure / Dispersion

Current [uA]: -0.75

Simulation time [s]: 250

Domain Length [mm]: 40

Channel Shape: D Shape

Dim. 1 [um]: 20 Dim. 2 [um]: 50

Grid Points: 250

Spatial Discretization: SLIP

Moving Frame: Yes

Prepare Grid: Yes

Adaptive Grid Speed: 1 Clustering Level: 1

Plot: Concentration Plotting interval: 100 Area Variation: @(x) 1 + 0*x

Ionic Strength Dependence: No

% Ionic Strength Change: 10

'Load file' reads an existing input file and fills all the GUI boxes with that information.

If a corresponding .mat file is found, you will be able to choose whether to load it or not.
Choosing 'Yes' will automatically check the 'Loat mat' box so that the data will be loaded after hitting 'Start'.
You may still ignore the data by unchecking the box, in which case only the input file will be processed after

	Name	Valence, I
1	ACETIC-ACID	[-1 4.24e-08 4.756]
2	ACRYLIC-ACID	[-1 4.27e-08 4.258]
3	ADIPIC-ACID	[-1 2.46e-08 4.43] [-2 5.24e-08 5.277
4	ALLYLACETIC-ACID	[-1 3.39e-08 4.674]
5	o-AMINOBENZOIC-ACID	[1 3.16e-08 2.108] [-1 3.16e-08 4.939
6	p-AMINOBENZOIC-ACID	[1 3.16e-08 2.413] [-1 3.16e-08 4.853

Injection point [mm]: 22

Injection width [mm]: 2.2

		Name	Valence, Mobility, pKa	c [M]	Locatio
1	@	LE	[-1 80e-009 2.756]	0.0500	LE
2	@	TE	[-1 25e-009 4.756]	0.0200	TE
3	@	BG	[1 20e-009 6.756]	0.1300	Backgrou
4	@	Analyte1	[-1 7e-008 2.756]	0.0700	Analyte
5	@	Analyte2	[-1 6e-008 2.756]	0.0300	Analyte
6	@	Analyte3	[-1 5e-008 4.756]	0.0500	Analyte

Figure J.1: Graphical user interface of SPRESSO code. The screenshot was taken after loading a sample input file `Case1_ITPDemo.m` provided in `Input Files` directory.

3) To run SPRESSO using the executable version, double click on Spresso.exe file. Executable version of the code works only on the Microsoft Windows platform. Note that, for running the executable version it is necessary to install the Matlab Component Runtime (MCR) library. MCR is available for free download on the SPRESSO download page. Whenever possible, we suggest running the code using the source code so as to avoid machine and operating system specific issues.

J.2. Introduction to GUI and input variables

As described in Section J.1, running SPRESSO causes a GUI to appear on the computer screen. The GUI can be used to create and run input files, and visualize simulation results in real time. We provide several example cases in the Input Files directory, to help users familiarize with GUI and the input parameters. Throughout this manual we will refer to a model ITP problem described in the `Case1_ITPDemo.m` file in the Input Files directory. To load the input file, click Load file on GUI and select the above mentioned input file. Loading the input file populates various fields in the GUI. Figure J.1 shows screenshot of the GUI after loading `Case1_ITPDemo.m` input file. The input file can also be viewed by opening it in the MATLAB editor. Below we discuss various simulation parameters in a typical input file, and the corresponding fields in GUI.

1) `IonicEffectFlag`

- *Description*: Determines whether ionic strength corrections on electrophoretic mobility and ionic activity are applied or not. See Chapter 3 for detailed discussion on ionic strength effects.
- *Usage*: Takes on values 0 (ionic strength corrections disabled), or 1 (ionic strength corrections enabled).
- *GUI*: Select `Yes` or `No` from the `Ionic Strength Correction` drop down menu to switch between 1 and 0, respectively.

2) `PcentIonicChange`

- *Description*: Controls the change in local ionic strength during simulation after which ionic strength corrections are applied. This option is applicable only if ionic strength effects are activated using `IonicEffectFlag`.
- *Usage:* Takes on non-negative values in terms of percentage change. For example, `PcentIonicChange=10`, indicates that ionic strength effects will be evaluated if ionic strength of solution changes by more than 10% during simulation.
- *GUI*: Input value in the `% Ionic Strength Change` box. Input is available only if Yes is selected in the Ionic Strength Dependence drop down menu.

3) `L1`

- *Description*: Leftmost coordinate of the computational domain.
- *Usage:* Default value is 0, and we suggest not changing this parameter in the input file.
- *GUI*: Not available in GUI.

4) `L2`

- *Description*: Rightmost coordinate of the computational domain.
- *Usage:* Value corresponds to the length of computational domain in meter unit.
- *GUI*: Input value in the `Domain Length` box.

5) `N`

- *Description*: Number of grid points.
- *Usage:* Takes on non-negative integer values. Typical values range from 100 to 1000 grid points.
- *GUI*: Input value in the `Grid Points` box.

6) `DChannel`

- *Description*: Width of the separation channel for D-shaped cross-section, and diameter for circular cross-section.
- *Usage:* Takes on non-negative values in meter unit.
- *GUI*: Input value in the `Dim 2` box.

7) `hChannel`

- *Description*: Depth of the separation channel for D-shaped cross-section, and diameter for circular cross-section
- *Usage:* Takes on non-negative values in meter unit.
- *GUI*: Input value in the `Dim 1` box.

8) `ChannelShape`

- *Description*: Describes whether channel cross-section is D-shaped or circular.
- *Usage:* Takes on values 1 for circular channel, and 2 for D-shaped channel.
- *GUI*: Choose the cross-section shape in the `Channel Shape` drop down menu.

9) `Current`

- *Description*: Current applied through the system.
- *Usage:* Takes on positive and negative values in ampere unit. Positive values of Current signify rightwards pointing electric field, and negative values for electric leftward pointing electric field.
- *GUI*: Input value in the `Current` box.

10) `tEnd`

- *Description*: Physical time for which problem is simulated.
- *Usage:* Takes on positive values in seconds.
- *GUI*: Input value in the `Simulation time` box.

11) `SteadyStateFlag`

- *Description*: Indicates whether simulation is solved in a moving reference frame or stationary laboratory frame.
- *Usage*: Takes on values 0 and 1. The value 1 indicates that simulation is solved in a frame of reference moving with the first species mentioned in the `InputTable`. The value 0 indicates that simulation is performed in a stationary laboratory frame.
- *GUI*: Choose `Yes` or `No` from the `Moving Frame` drop down menu.

12) `PrepareGridStage`

- *Description*: Indicates whether grid should be refined prior to the application of electric field.
- *Usage:* Takes on values 0 and 1. The value 1 enables adaptive grid refinement, and value 0 disables grid refinement. The adaptive grid scheme is discussed in detail in Chapter 2.
- *GUI*: Choose `Yes` or `No` from the `Prepare Grid` drop down menu.

13) `AdaptGrid.Coeff`

- *Description*: Controls the speed of grid adaptation.
- *Usage:* Takes on non-negative values. Speed of grid adaptation increases with increase in value of `AdaptGrid.Coeff`. Typical values range from 0-10. The value 0 indicates no grid adaptation. Typical value for ITP problems is 1, and for CZE problems is 0.1. This parameter is used to compute problem specific adaptive grid parameters as described in Appendix C.
- *GUI*: Input value in the `Adaptive Grid Speed` box.

14) `AdaptGrid.PointsAtInterface`

- *Description*: Controls the clustering of grid points during adaptive grid refinement.

- *Usage:* Takes on non-negative values. Higher values lead to greater clustering of grid points at regions with large gradients. Typical values range from 0-10. The value 0 indicates no grid adaptation. Typical value for ITP problems is 1, and for CZE problems is 0.1. This parameter is used to compute problem specific adaptive grid parameters as described in Appendix C.
- *GUI*: Input value in the `Clustering Level` box.

15) `DeltaCounterNextPlot`

- *Description*: Controls the number of simulation time steps after which data are saved and plotted on GUI. Data are saved in the directory containing the input file. The data file has the same name as input file but with .mat extension.
- *Usage:* Takes on positive integer values. Typical value is 100. Smaller values will slow the simulation as more resources will be required for plotting the data.
- *GUI*: Input value in the `Plotting Interval` box.

16) `SpatialDiscFlag`

- *Description*: Indicates the spatial discretization scheme.
- *Usage:* Use `'SLIP'` for finite volume SLIP scheme discussed in Chapter 2; `'Compact'` for sixth-order compact scheme described by Bercovici *et al.* [69]; `'Upwind'` for first order upwind scheme; and `'2nd'` for centered second order scheme. Note that only the SLIP scheme allows solving problems with variable cross-sectional area channels.
- *GUI*: Select desired numerical scheme from the `Spatial Discretization` box.

17) `InjLen`

- *Description*: Thickness of the initial concentration boundary at the sample injection point.
- *Usage*: Takes on positive values in millimeter. The value must be chosen to ensure that the concentration boundary lies completely inside the computation

domain, and there are no concentration gradients at the domain boundaries. This ensures proper imposition of boundary conditions.

- *GUI*: Input value in the `Injection width` box. Note that the GUI allows only one injection point. However, multiple sample injection points can be inserted by manually customizing the input file, e.g., using the MATLAB text editor.

18) `InjLoc`

- *Description*: Location of the initial concentration boundary.
- *Usage*: Takes on positive values in millimeter. The value must be chosen to ensure that the concentration boundary lies completely inside the computation domain, and there are no concentration gradients at the domain boundaries. This ensures proper imposition of boundary conditions.
- *GUI*: Input value in the `Injection width` box. Note that the GUI allows only one injection point. However, multiple sample injection points can be inserted by manually customizing the input file, e.g., using the MATLAB text editor.

19) `Pressurehead`

- *Description*: Pressure head across the length of computational domain to include hydrodynamic flow.
- *Usage*: Takes on negative and positive values in millimeters of water column.
- *GUI*: Click the `Pressure/Dispersion` button and then input the value in `Pressure head` box.

20) `bPressure`

- *Description*: Hydraulic resistance coefficient in Poiseuille's Law.
- *Usage*: Dimensionless parameter that takes on positive values. Use value of 32 for channels with circular cross-section.

- *GUI*: Click the `Pressure/Dispersion` button and then input the value in `b (coeff)` box.

21) `betaDispersion`

- *Description*: Taylor-Aris dispersion coefficient described by Bercovici *et al.* [63]
- *Usage*: Dimensionless parameter that takes on positive values.
- *GUI*: Click the `Pressure/Dispersion` button and then input the value in `beta (coeff)` box.

22) `zVec, phiVec, AnalyteVec, TEVec, LEVec, BackgroundVec`

- *Description*: Vectors that define initial distribution of analytes, trailing electrolyte and leading electrolyte.
- *Usage*: Vectors normalized with the highest term, i.e., maximum term should be 1. User can change these vectors and save the input file using a text editor. Saving the input file from GUI will overwrite the user defined vectors with default values.
- *GUI*: Default values are used when the input file is saved from GUI.

23) `AreaFunctionText`

- *Description*: Function defining axial variation of channel cross-sectional area.
- *Usage*: The function must be defined in the following format: `'@(x) f(x)'`. Here `f(x)` is a user-defined function written in a form to allow vectorized arithmetic operations. Default value is `'@(x) 1 + 0*x'` which corresponds to axially uniform cross-section. This function is later automatically scaled such that the cross-sectional area of left channel inlet is that given by `DChannel` and `hChannel` dimensions.
- *GUI*: Input the desired function in the `Area Variation` box.

24) `A and AreaRatio`

- *Description*: Variables to evaluate cross-sectional area variation defined by `AreaFunctionText`.
- *Usage*: Use the values initialized by GUI. We suggest not changing these parameters.
- *GUI*: Default values are used when the input file is saved from GUI. These variables cannot be changed though the GUI.

25) `InputTable`

- *Description*: Describes chemical species, their ionization states, mobilities, acid dissociation constants, and concentrations.
- *Usage*: Example input from `Case1_ITPDemo.m` is as follows:

```
InputTable =
{'LE','[-1    80e-009      2.756]',0.05,'LE';
'TE','[-1     25e-009      4.756]',0.02,'TE';
'BG','[1      20e-009      6.756]',0.13,'Background';
'Analyte1','[-1 7e-008     2.756]',0.07,'Analyte';
'Analyte2','[-1 6e-008     2.756]',0.03,'Analyte';
'Analyte3','[-1 5e-008     4.756]',0.05,'Analyte';
'Analyte4','[-1 4e-008     4.756]',0.01,'Analyte';
'Analyte5','[-1 3e-008     4.756]',0.06,'Analyte';};
```

The first entry in every row of `InputTable` is the name of chemical species. The species names are shown in GUI to aid data visualization, but they do not affect the actual simulation. The second entry in each row should be in the following format:

`'[valence mobility  (acid dissociation constant)]'.`

Multivalent species can be handled using the following format:

`'[...] [...]'`

The third entry in each row of the `InputTable` is the species concentration in molar units. The last entry of each row describes the initial concentration distribution of species. The available options for concentration distributions are: `'LE'`, `'TE'`, `'Background'` and `'Analyte'`.

- *GUI*: `InputTable` can be generated using the GUI by either manually inputting the table rows in the above mentioned format, or by using `Add` and `Remove` buttons to insert required species from the chemical database.

26) `cMat(:,1),` etc.

- *Description*: Initial concentration distribution of all species constructed using the values defined in `InputTable` and vectors discussed in (21).
- *Usage*: Use default values determined by the GUI. Unless customized species distributions are required, we suggest not editing these lines in the input file.
- *GUI*: Default values are used when input file is saved from the GUI. These variables cannot be changed though GUI.

27) Miscellaneous features available in GUI

- `Load mat`: Checking this option allows starting simulation from the point where last simulation ended.
- `Stop/Save`: Stops the simulation and saves the data. The data are automatically saved if the simulation reaches time `tEnd`.
- `Stop/Discard`: Stops the simulation without saving the data.
- `Pause`: Temporarily stops the simulation to allow data visualization. Hitting the *Pause* button for the second time will restart the simulation from the point where it was paused.
- `Plot`: This drop down menu allows visualization of axial variations in species concentration, pH, effective mobility, electric field, conductivity, grid density, and cross-sectional area.
- Caution: Saving the input file through GUI will overwrite any manual changes made to the input file. For manually customized input file, the GUI can still be used to run and visualize the simulation as usual.

J.3 Using SPRESSO to explore electrolyte chemistries for ITP

SPRESSO allows fast simulations of ITP and thereby minimizes the time required for selection of optimal electrolyte chemistries. When the goal of simulations is to explore LE-TE electrolyte systems for focusing given analytes in ITP, we suggest using the dissipative SLIP scheme without adaptive grid refinement. Although, this approach yields relatively dispersed concentration gradients, it correctly predicts zone orders and sample accumulation. Moreover, the SLIP scheme being unconditional stable, even without adaptive grid refinement, yields significant reduction in computational time. Below, we provide guidelines for performing fast and approximate ITP simulations to explore electrolyte chemistries.

Step 1: One of the simplest methods for setting up SPRESSO simulation is by loading and editing an existing input file in the GUI. In this example, we will use the input file named `Case1_ITPDemo.m`. Figure J.1 shows screenshot of GUI after loading this input file.

Step2: Edit the input file by choosing the following simulation parameters on GUI:

`Grid Points = 250`
`Spatial Discretization = SLIP`
`Moving Frame = Yes`
`Prepare Grid = No`
`Adaptive Grid Speed = 0`
`Clustering Level = 0`

These are the typical numerical parameters that are required for fast, but approximate ITP simulations. Disabling adaptive grid refinement yields significant reduction in computation time. Also simulating ITP in moving frame of reference allows use of smaller computational domain and lesser number of grid points.

Step 3: Save the input parameters to a different input file by clicking the `Save As` button, and then click `Start` to run the simulation. Figure J.2 shows the GUI with updated simulation parameters along with simulated concentration profiles. This simulation took less than 15 s on a standard desktop computer. Note that the zone boundaries are significantly diffused. Nevertheless, the simulation shows that the model electrolyte chemistry enables focusing of analytes ITP.

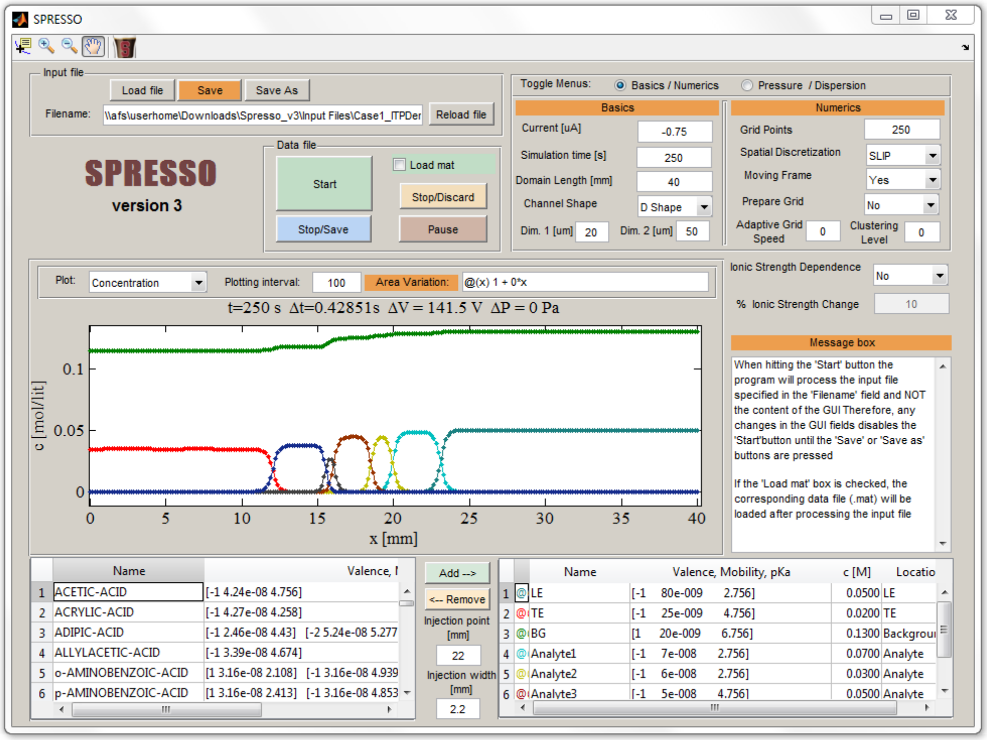

Filename: \\afs\userhome\Downloads\Spresso_v3\Input Files\Case1_ITPDer

☐ Load mat

Toggle Menus: ● Basics / Numerics ○ Pressure / Dispersion

Current [uA]: -0.75
Simulation time [s]: 250
Domain Length [mm]: 40
Channel Shape: D Shape
Dim. 1 [um]: 20
Dim. 2 [um]: 50

Grid Points: 250
Spatial Discretization: SLIP
Moving Frame: Yes
Prepare Grid: No
Adaptive Grid Speed: 0
Clustering Level: 0

Ionic Strength Dependence: No
% Ionic Strength Change: 10

Plot: Concentration
Plotting interval: 100
Area Variation: @(x) 1 + 0*x

t=250 s Δt=0.42851s ΔV = 141.5 V ΔP = 0 Pa

When hitting the 'Start' button the program will process the input file specified in the 'Filename' field and NOT the content of the GUI Therefore, any changes in the GUI fields disables the 'Start'button until the 'Save' or 'Save as' buttons are pressed

If the 'Load mat' box is checked, the corresponding data file (.mat) will be loaded after processing the input file

	Name	Valence, I
1	ACETIC-ACID	[-1 4.24e-08 4.756]
2	ACRYLIC-ACID	[-1 4.27e-08 4.258]
3	ADIPIC-ACID	[-1 2.46e-08 4.43] [-2 5.24e-08 5.277
4	ALLYLACETIC-ACID	[-1 3.39e-08 4.674]
5	o-AMINOBENZOIC-ACID	[1 3.16e-08 2.108] [-1 3.16e-08 4.939
6	p-AMINOBENZOIC-ACID	[1 3.16e-08 2.413] [-1 3.16e-08 4.853

Injection point [mm]: 22
Injection width [mm]: 2.2

	Name	Valence, Mobility, pKa	c [M]	Locatio
1	@ LE	[-1 80e-009 2.756]	0.0500	LE
2	@ TE	[-1 25e-009 4.756]	0.0200	TE
3	@ BG	[1 20e-009 6.756]	0.1300	Backgrou
4	@ Analyte1	[-1 7e-008 2.756]	0.0700	Analyte
5	@ Analyte2	[-1 6e-008 2.756]	0.0300	Analyte
6	@ Analyte3	[-1 5e-008 4.756]	0.0500	Analyte

Figure J.2: Screenshot of SPRESSO GUI showing typical parameters for performing fast and approximate ITP simulations, discussed in Section J.3. Such simulations yield dispersed zone boundaries but correctly predict ITP zone orders and sample accumulation.

J.4 Using SPRESSO for high-fidelity simulations of ITP

There are two approaches to obtain high-accuracy numerical solutions using SPRESSO: (1) using the dissipative SLIP scheme with adaptive grid refinement to minimize numerical diffusion, and (2) using the non-dissipative sixth-order compact scheme with adaptive grid refinement to avoid non-physical oscillations. While SLIP scheme yields robust simulations with no oscillations, it requires careful choice grid density to minimize numerical diffusion. Whereas, the non-dissipative compact scheme yields high-resolution solutions with minimal numerical diffusion, provided that a non-oscillatory solution is achieved. Unlike the SLIP scheme, the sixth-order compact scheme is not unconditionally stable, and therefore it is necessary to vary the grid density (by changing the number of grid points, and/or varying adaptive grid parameters) to ensure a non-oscillatory solution.

For unsteady ITP problems either of the above approach can be used. Whereas, for steady state ITP problems, a hybrid approach based on SLIP and compact schemes can allow faster simulations. In this hybrid approach, we first simulate the ITP problem using the SLIP scheme (without adaptive grid) in a moving frame of reference. Once an approximate steady state is attained, we stop the simulation, save the data, and restart the simulation using the compact scheme. This approach yields faster simulations because the first step involving the SLIP scheme (without adaptive grid) gets past the initial transients with relative ease. Simulating such transients with compact scheme would take significantly longer duration. Whereas, the second step involving compact scheme starts with an initial condition resembling the actual steady state solution. Better initial starting condition for the steady state simulation speedup up convergence to actual solution.

Below, we discuss an example of steady state ITP simulation using hybrid SLIP and compact scheme approach:

Step 1: Follow the steps outlined in Section J.3 to solve the required ITP problem with SLIP scheme and no adaptive grid refinement. Figure J.2 shows screenshot of the GUI with necessary simulation parameters and simulated concentration profiles. Next, save the simulation data by clicking the `Stop/Save` button. The simulation data are automatically saved if the simulation reaches completion.

Step2: Edit the input file by choosing the following simulation parameters on GUI:

```
Grid Points = 250
Spatial Discretization = Compact
Moving Frame = Yes
Prepare Grid = Yes
Adaptive Grid Speed = 2
Clustering Level = 2
```

Step 3: Save the input parameters to the same input file by clicking `Save`. Also, turn on the `Load mat` option on GUI to load data saved from the previous simulation. The simulated data from Step 1 will then be used as the initial condition for next simulation. Next, click `Start` to run the simulation.

Figure J.3 shows screenshot of the GUI with simulation parameters discussed in Step 2, along with simulated concentration profiles. This simulation took approximately

60 s to attain steady state on a standard desktop computer. Combined with 15 s of computational time taken by Step 1, the hybrid approach leveraging the SLIP and compact schemes takes approximately 75 s of computational time. Whereas, simulating the same problem with compact scheme alone takes over 120 s. We note that for simulations involving complex transients, the hybrid approach will yield further speed enhancement.

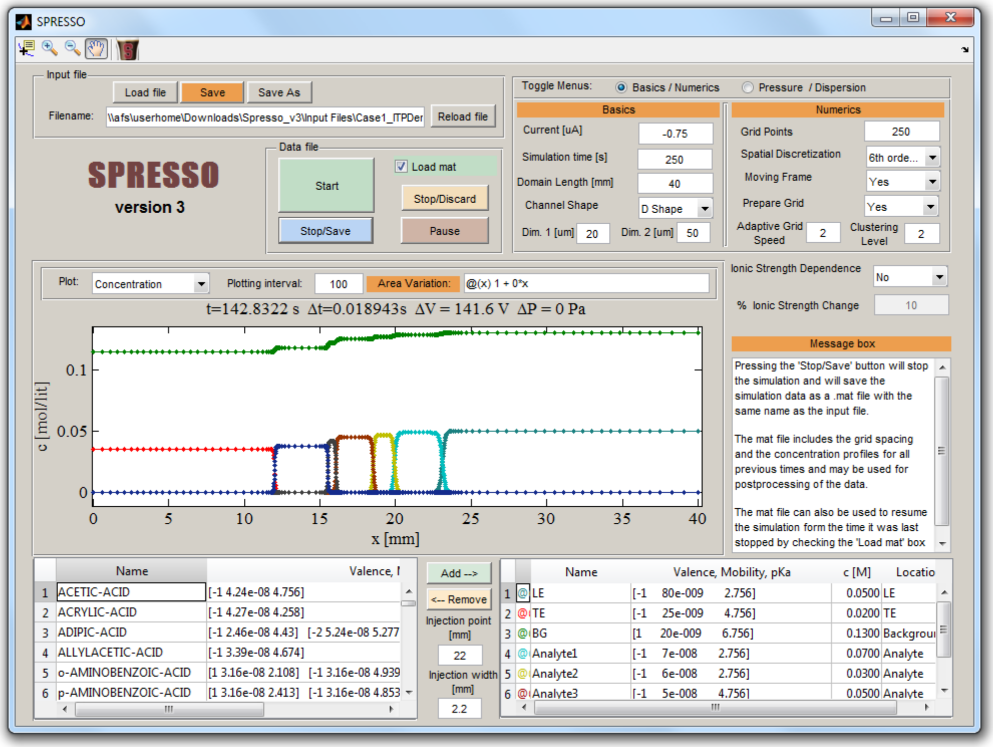

Filename: \\afs\userhome\Downloads\Spresso_v3\Input Files\Case1_ITPDer

☑ Load mat

Toggle Menus: ● Basics / Numerics ○ Pressure / Dispersion

Current [uA] -0.75
Simulation time [s] 250
Domain Length [mm] 40
Channel Shape D Shape
Dim. 1 [um] 20 Dim. 2 [um] 50

Grid Points 250
Spatial Discretization 6th orde...
Moving Frame Yes
Prepare Grid Yes
Adaptive Grid Speed 2 Clustering Level 2

Plot: Concentration Plotting interval: 100 Area Variation: @(x) 1 + 0*x

Ionic Strength Dependence No
% Ionic Strength Change 10

t=142.8322 s Δt=0.018943s ΔV = 141.6 V ΔP = 0 Pa

Pressing the 'Stop/Save' button will stop the simulation and will save the simulation data as a .mat file with the same name as the input file.

The mat file includes the grid spacing and the concentration profiles for all previous times and may be used for postprocessing of the data.

The mat file can also be used to resume the simulation form the time it was last stopped by checking the 'Load mat' box

	Name	Valence, I
1	ACETIC-ACID	[-1 4.24e-08 4.756]
2	ACRYLIC-ACID	[-1 4.27e-08 4.258]
3	ADIPIC-ACID	[-1 2.46e-08 4.43] [-2 5.24e-08 5.277
4	ALLYLACETIC-ACID	[-1 3.39e-08 4.674]
5	o-AMINOBENZOIC-ACID	[1 3.16e-08 2.108] [-1 3.16e-08 4.939
6	p-AMINOBENZOIC-ACID	[1 3.16e-08 2.413] [-1 3.16e-08 4.853

Injection point [mm] 22
Injection width [mm] 2.2

		Name	Valence, Mobility, pKa	c [M]	Locatio
1	@	LE	[-1 80e-009 2.756]	0.0500	LE
2	@	TE	[-1 25e-009 4.756]	0.0200	TE
3	@	BG	[1 20e-009 6.756]	0.1300	Backgrou
4	@	Analyte1	[-1 7e-008 2.756]	0.0700	Analyte
5	@	Analyte2	[-1 6e-008 2.756]	0.0300	Analyte
6	@	Analyte3	[-1 5e-008 4.756]	0.0500	Analyte

Figure J.3: Screenshot of SPRESSO GUI showing typical parameters for performing a high-fidelity simulation of ITP using compact scheme. For this particular simulation data from the simulation shown in Figure J.2 was used as the initial condition. Simulating a steady state ITP problem with an initial condition resembling the final solution yields significant computational efficiencies.

J.5 Analyzing simulation data

Simulation data is saved by SPRESSO in MAT-file format of MATLAB. For a simulation based on an input file named `Input.m`, simulation data are saved as `Input.mat` in the directory containing the corresponding input file. Data are usually saved automatically at the completion of simulation. However, users can also terminate the simulation before completion, and save the data by clicking `Stop/Save` button.

Table J.1 describes the variables in data file corresponding to different physicochemical quantities.

Table J.1: Important variables in SPRESSO data file corresponding to various physicochemical quantities. Data are saved at all `N` grid points and different time steps. The number of times steps at which data are saved is given by `Ntimes=length(tVecOut)`, and the number of species is given by `Nspecies`.

Variable in Data File	Physicochemical Quantity	Data Type and Usage
`phiVecAllTimes`	*Coordinates of grid points in physical domain* at different time steps.	• Matrix Size: `N×2×Ntimes` • Coordinates in moving frame `= phiVecAllTimes(:,1,:)` • Coordinates in stationary frame `= phiVecAllTimes(:,2,:)`
`tVecOut`	*Physical time* at which data are saved	Vector Length: `N`
`pHVecAllTimes`	*pH* at all grid points at different time steps	Matrix Size: `N×Ntimes`
`SigVecAllTime`	*Electrical conductivity* at all grid points at different time steps	Matrix Size: `N×Ntimes`
`cMatAllTimes`	*Species concentrations* at all grid points at different time steps	• Matrix Size: `N×(Nspecies+1)×Ntimes` • Concentration of species `j={1,2,...,Nspecies}` `=cMatAllTimes(:,j,:)` • Hydronium ion concentration `=cMatAllTimes(:,end,:)`

J.6 Routinely encountered issues with SPRESSO

Several runtime issues with SPRESSO have been reported over the past, and we have done our best to address them in the latest version of code. Issues with SPRESSO often stem from erroneous user inputs. We here document routinely committed input errors, and their remedies.

1) *Problem*: The most commonly committed error is to input the species concentrations in millimolar (mM) units in the `InputTable`. This might be the due to common usage of millimolar units in electrophoresis community.
   Solution: Input species concentrations in molar (M) units.

2) *Problem*: MATLAB gives the following error on clicking GUI buttons:
   ```
   Undefined function 'SpressoGUI' for input arguments of
   type 'struct'. Error in guidemfile/@(hObject,eventdata)
   SpressoGUI ('StartButton_Callback' ,hObject,eventdata,
   guidata(hObject))
   Error while evaluating uicontrol Callback.
   ```
   Solution: Such runtime errors are caused when users navigate to a different working directory in MATLAB and try using SPRESSO GUI. To run SPRESSO, it is necessary that the present working directory in MATLAB is the one containing `Spresso.m` file.

3) *Problem*: ITP zones are not stationary while simulating in a moving frame of reference.
   Solution: SPRESSO uses the electromigration speed of the first species defined in `InputTable` to define the speed of moving frame of reference. Therefore, for ITP simulations with moving frame of reference, the first species in the `InputTable` should be the leading electrolyte (LE).

4) *Problem*: Simulation of ITP shows zone boundaries dispersing over time, and not sharpening as expected.
   Solution: Switch the current direction by changing the sign of input current.

5) *Problem:* Simulations take extremely long time to complete. *Solution*: This issue usually results while using large number of points (1000 or more). SPRESSO includes adaptive grid refinement scheme which enables faster simulations with order 100 grid points, without compromising accuracy. Also, using extreme grid adaptation (i.e., with high grid adaptation parameters) can decrease simulation speed. We encourage users to run numerical experiments to find optimal number of grid points and adaptive grid refinement parameters to achieve shorter simulation times. Numerical parameters are often problem specific and we provide typical values of these parameters in Section J.1.

6) *Problem*: Simulations with sixth-order compact scheme yield oscillatory solutions. *Solution*: The sixth-order compact scheme is not unconditionally stable and can yield oscillatory solutions due to insufficient grid density. Oscillatory solutions can be avoided by increasing the number of grid points, or increasing the value of adaptive grid parameters. Also, for fast and approximate simulations we suggest using the unconditionally stable SLIP scheme which does not yield oscillations.

7) *Problem*: GUI overwrites manually customized input file. *Solution*: When input file is saved through GUI, the code uses input values in GUI to write a new input file. This overwrites manual changes made to the input file. Therefore, we suggest saving the customized input file through a text editor and not the GUI.

8) *Problem:* While using a customized input file, GUI plots incorrect initial conditions. *Solution*: The code in its current form uses the inputs from GUI to plot initial conditions using a set of predefined concentration distributions. However, this does not affect simulations or real time data visualization. While using manually customized input files, the GUI plots correct concentration profiles upon starting the simulation.

K. Practically useful electrolyte buffers for anionic and cationic ITP

ITP employs discontinuous electrolyte system consisting of a leading electrolyte (LE) and a trailing electrolyte (TE) for preconcentration and separation of ionic species. To focus analytes in ITP, co-ions of LE (termed LE ions) should have high effective mobility and co-ions of TE (termed TE ions) should have low effective mobility. ITP experiments are usually performed in well buffering conditions to avoid run-to-run variability. Also, to minimize interference from hydronium and hydroxyl ions in the preconcentration and separation process, we recommend to perform ITP under safe pH conditions ($5 < pH < 9$). We here provide a list of electrolyte chemistries that we have found to be practically useful for anionic and cationic ITP experiments.

K.1 Electrolyte buffers for anionic ITP

LE ion: Anions of strong acids, such hydrochloric acid (HCl) and sulfuric acid, are often good choices for LE ions. Strong acids are almost fully ionized at all pH values, which results in pH independent effective mobility of their anions. We suggest using univalent ions (e.g., chloride ion) over multivalent ions (e.g, sulphate ion) for LE ion, as the mobility of multivalent ions is affected strongly by ionic strength compared with that of univalent ions (see Chapter 3). Other choices of LE ions include anions of lactic, acetic, citric, caproic, nicotinic, benzoic, and phosphoric acids.

Besides strong acids, anions of weak acids such as MES and MOPS can also be used as LE ions, provided that the working pH is high. Using weakly acidic species as LE ions allow indirect visualization of ITP zones with over-speeding fluorescent nonfocusing tracers (NFT), such as Alexa Fluor and fluorescein.

TE ion: Anions of weak acids are good choices for TE ions. Effective mobility of weakly acidic species is strongly dependent on the pH of solution. Therefore, TE mobility can be easily tuned by varying the pH of electrolyte buffer. This is particularly helpful while using semi-infinite sample injection (see Section 1.3.3) as low effective mobility TE ions allow higher sample focusing. In certain applications where selective focusing of analytes is required, tuning mobility of weakly acidic species allows exclusion of low mobility analytes. Practical choices for TE ions include MOPS, HEPES, tricine, taurine, serine, histidine, and asparagine. Note that taurine, serine, histidine, and asparagine have relatively low (order 100 mM) solubility.

For focusing high mobility species, anions of nicotinic, caproic, benzoic, and lactic acids can also be used as TE ions. These ions have higher mobility than fluorescein. Therefore, fluorescein can be used as an under-speeding NFT to visualize ITP zones.

Counter-ion: Selecting an appropriate counter-ion is essential for ITP as counter-ionic species often govern the pH and the effective mobility of TE ions. For anionic ITP, weakly basic species are preferred as counter-ions so as to maintain good buffering conditions and control effective mobility of TE ions. A variety of weakly basic species can be used as counter-ions to achieve different working pHs. These include pyridine ($pK_a = 5.18$), bistris ($pK_a = 6.4$), imidazole ($pK_a = 7.15$), tris ($pK_a = 8.1$), amediol ($pK_a = 8.78$) and ethanolamine ($pK_a = 9.5$).

Electrolyte buffers: In well-buffered ITP experiments, pH of various ITP zones closely resembles the pH of LE buffer. Therefore, pH of LE buffer is a good thumb rule for selecting appropriate TE ions. A straightforward method for making LE buffers for anionic ITP involves titrating a weak base with a strong acid. For such kind of buffers, titrating 2× weak base with 1× strong acid yields a buffer solution with pH equal to the pK_a of weak base. For example, 200 mM imidazole ($pK_a = 7.15$) titrated with 100 mM hydrochloric acid yields a buffer with pH of 7.15. Below, we provide a list of common LE buffers for anionic ITP, along with some guidelines for using them.

1) 1× HCl and 2× pyridine (pH = 5.1)

- Preferred TE ions: MES, MOPS, and HEPES.
- Low pH results in significant reduction in EOF, and also eliminates unwanted zones due to carbonic acid.

- Tricine, taurine, and serine have very low mobility at these conditions, and should not be used as TE ions.
- Pyridine is a foul smelling liquid.

2) 1× HCl and 2× bistris (pH = 6.4)

- Preferred TE ions: MOPS, HEPES, and tricine.
- Low pH reduces EOF and minimizes the effects of carbonic acid.
- MES has relatively high effective mobility at these conditions. Using MES as TE with this LE buffer, without EOF suppression, causes ITP interface to become stationary midway of the glass channel due to opposing EOF. We have observed that a stationary zone of Alexa Fluor focused between chloride (LE ion) and MES (TE ion) can remain stable for over 1 hr. This chemistry can be used for large amount of sample focusing using EOF based counter-flow.
- Taurine and serine have very low effective mobility at these conditions and they should not be used as TE ions.

3) 1× HCl and 2× imidazole (pH = 7.15)

- Preferred TE ions: MOPS, HEPES, tricine, taurine, and serine.
- Imidazole has relatively high mobility among all weak bases. Therefore, it can be used as cationic LE for bidirectional ITP.

4) 1× HCl and 2× tris (pH = 8.1)

- Preferred TE ions: HEPES, tricine, histidine, and serine.
- At these conditions, tricine has higher effective mobility than HEPES. This is unlike the case for LE buffers 1-3.
- Relatively high EOF is observed if taurine and serine are used as TE ions. In absence of strong EOF suppression, using serine as TE ion may cause EOF to push the ITP zone back into the TE well.
- Carbonic acid can interfere at this pH. Adding barium hydroxide to TE reduces adverse effects of carbonic acid.

5) 1× HCl and 2× amediol (pH = 8.8);
1× HCl and 2× ethanolamine (pH = 9.5)

- We suggest not using these LE buffers unless high pH is required.
- High pH results in strong EOF, focusing of carbonic acid, and possible interference from hydroxyl ions.
- High concentration (> 3%) of PVP is required to suppress EOF. In the adjusted TE zone where pH is higher, PVP might not even be effective to suppress EOF.

K.2 Electrolyte buffers for cationic ITP

LE ion: Analogous to the case of anionic ITP, cations of strong bases, such as sodium hydroxide (NaOH) and potassium hydroxide, are usually good choices for LE ions. Effective mobility of sodium and potassium ions is effectively independent of the pH. Therefore these ions can be used as LE ions under any pH conditions. Besides strong bases, relatively weak bases having high actual mobility, such as imidazole, ethanolamine, and amediol can also be used as LE ions for cationic ITP.

TE ion: Cations of weak bases are good choices for TE ions. These include tris, bistris, pyridine, and creatinine. As discussed in Chapter 6, arginine can also be used as cationic TE despite being relatively strong base. This is because of low actual mobility of arginine. Using arginine as TE ion also allows indirect visualization of cationic ITP zones using rhodamine 6G as the under-speeding NFT.

Counter-ion: For cationic ITP, weakly acidic species serve as good counter-ions as they allow good buffering conditions and precise control over effective mobility of TE ions. A variety of weakly acidic species can be used as counter-ions to achieve different working pHs. These include anions of acetic acid ($pK_a = 4.75$), MES ($pK_a = 6.1$), MOPS ($pK_a = 7.2$), HEPES ($pK_a = 7.5$), and tricine ($pK_a = 8.1$).

Electrolyte buffers: Titrating a weak acid with a strong base is a convenient method of making LE buffers for cationic ITP. For such buffers, titrating 2× weak acid with 1× acid yields a buffer solution with pH equal to the pK_a of weak acid. For example, 200 mM HEPES (pK_a = 7.5) titrated with 100 mM sodium hydroxide yields a buffer with pH of 7.5. Below, we provide a list of common LE buffers for cationic ITP, along with some guidelines for using them.

1) 1× NaOH and 2× acetic acid (pH = 4.75)

- Preferred TE ions: creatinine, pyridine, bistris, and tris have mobiltites around 20 $m^2V^{-1}s^{-1}$.
- Low pH also allows using β-alanine as TE ion.
- High mobility of TE ions allows use of rhodamine 6G as an under-speeding NFT for indirect visualization of ITP zones.
- Small differences in mobilities of weakly basic analytes at low pH may result in lower separation resolution in plateau mode ITP.
- Relatively low EOF at these conditions.

2) 1× NaOH and 2× MES (pH = 6.1);
1× NaOH and 2× MOPS (pH = 7.2);
1× NaOH and 2× HEPES (pH = 7.5)

- Preferred TE ions: bistris, pyridine, and creatinine.
- Tris has relatively high mobility at this pH and β-alanine has very low mobility. Thus, tris and β-alanine should be avoided as TE ions at these conditions.
- For cationic ITP in glass channels, EOF acts to speedup ITP zones. This allows smaller time for analytes to focus and separate in ITP. However, EOF can be effectively suppressed at these pH conditions using 2% PVP.

3) Excess imidazole titrated with HCl

- Unlike the above buffers, here LE ion is the buffering ion.
- Preferred TE ions: bistris and pyridine
- As discussed in Chapter 5, increasing the ratio of imidazole to HCl concentration results in very low concentration of chloride ion in the TE zone. High ratios of

cationic LE to counter-ion concentration (> 3.5) therefore result in very low conductivity TE zone. High conductivity ratio of LE and TE zones in such cases can yield an unstable ITP shock wave.